

Jinkui Tang · Peng Zhang

Lanthanide Single Molecule Magnets

 Springer

Lanthanide Single Molecule Magnets

Jinkui Tang · Peng Zhang

Lanthanide Single Molecule Magnets

 Springer

Jinkui Tang
Changchun Institute of Applied Chemistry
Chinese Academy of Sciences
Changchun
China

Peng Zhang
Changchun Institute of Applied Chemistry
Chinese Academy of Sciences
Changchun
China

ISBN 978-3-662-46998-9

ISBN 978-3-662-46999-6 (eBook)

DOI 10.1007/978-3-662-46999-6

Library of Congress Control Number: 2015937526

Springer Heidelberg New York Dordrecht London

© Springer-Verlag Berlin Heidelberg 2015

This work is subject to copyright. All rights are reserved by the Publisher, whether the whole or part of the material is concerned, specifically the rights of translation, reprinting, reuse of illustrations, recitation, broadcasting, reproduction on microfilms or in any other physical way, and transmission or information storage and retrieval, electronic adaptation, computer software, or by similar or dissimilar methodology now known or hereafter developed.

The use of general descriptive names, registered names, trademarks, service marks, etc. in this publication does not imply, even in the absence of a specific statement, that such names are exempt from the relevant protective laws and regulations and therefore free for general use.

The publisher, the authors and the editors are safe to assume that the advice and information in this book are believed to be true and accurate at the date of publication. Neither the publisher nor the authors or the editors give a warranty, express or implied, with respect to the material contained herein or for any errors or omissions that may have been made.

Printed on acid-free paper

Springer-Verlag GmbH Berlin Heidelberg is part of Springer Science+Business Media
(www.springer.com)

Foreword

Magnetic materials play an important role in our modern civilization and have driven great advances in the field of information technology. However, the storage densities are still limited by the superparamagnetic effect of conventional magnetic materials, and hence, advanced magnetic materials are requisite to increase the storage density or to develop new memory devices such as quantum computer based on the Grover algorithm. Therefore, magnets on the scale of individual molecule/atom exhibiting rich quantum behavior are expected to record and process digital information and are very promising to tackle the problems of traditional materials. Herein, single-molecule magnets (SMMs), named for its magnetic behavior of purely molecular origin below blocking temperature (T_B), provide potential applications for such ultra-high-density data storage media, quantum computations, and spintronics devices. The rapid developments in this field represent a significant innovation in magnetic materials since the 1990s, opening new door for information technology. In particular, the extensive application of lanthanide elements with large inherent anisotropy since 2003 has resulted in huge breakthrough not only in improving T_B but also in theoretical prediction and device design, bringing the goals of molecule-based information storage and processing closer to reality.

To date, some specialist books have been published in the field of molecular magnetism. Some of them are concerned only with the particular physical aspect of the subject. Others are usually very comprehensive, covering a wide range of molecule-based magnetic materials and hence rather formidable to someone seeking a succinct introduction to lanthanide SMMs. This book concentrates on the research developed in the fascinating and challenging field of lanthanide SMMs in recent years with particular focus on how recent studies tend to address the issue of enhancing SMM properties in these systems from the viewpoint of a chemist. It describes the basic issues in the interpretation of the experiments and the potential developments in this field. In particular, some important relationships between the structural features and magnetic performances are discussed in detail based on the combined experimental and theoretical explorations, representing an essential step for the rational design of lanthanide-based SMMs, thus enhancing

the understanding crucial to the advancement of single-molecule data storage and processing technologies.

I believe that researchers should highly benefit from the reading of this book, especially for the newcomers expecting to grasp ongoing trends and explore new directions in this exciting field.

Song Gao
CAS Member
Professor of Chemistry
Peking University

Contents

1 A Basis for Lanthanide Single-Molecule Magnets	1
1.1 Magnetism of Lanthanides	2
1.1.1 Magnetism of Free Lanthanide Ions	2
1.1.2 Spin–Orbital Coupling and Anisotropy of Free Lanthanide Ions	6
1.1.3 Lanthanide Magnetism in Ligand Fields	8
1.2 Single-Molecule Magnets (SMMs)	11
1.2.1 Effective Barrier (U_{eff})	11
1.2.2 Blocking Temperature (T_B) and Hysteresis	18
1.2.3 Relaxation Dynamics	19
1.3 Lanthanide Single-Molecule Magnets	26
1.3.1 Angle-Resolved Magnetometry	27
1.3.2 Ab Initio Calculations	32
References	34
2 Lanthanide Single-Ion Molecular Magnets	41
2.1 Single-Ion Anisotropy and QTM	42
2.2 $[\text{LnPc}_2]$ and LnPOM SIMMs	46
2.2.1 Phthalocyanine-Type Ligands and the $[\text{LnPc}_2]$ Structure	46
2.2.2 The Magnetism of Seminal $[\text{LnPc}_2]^- \cdot \text{TBA}^+$	48
2.2.3 The Enhanced SMMs from the Redox Reactions	53
2.2.4 The Substituted $[\text{LnPc}_2]$ SIMMs	57
2.2.5 The $[\text{LnPc}_2]$ -like SIMMs	60
2.2.6 The LnPOM SIMMs	62
2.3 Lanthanide β -diketone Systems	64
2.3.1 The Magnetism of $[\text{Dy}(\text{acac})_3(\text{H}_2\text{O})_2]$	66
2.3.2 The Modulations of Auxiliary Ligands	67
2.3.3 Chiral β -diketone Dy SIMMs	72
2.3.4 The SIMMs with Large Capping Ligands	73
2.3.5 The SIMMs with Radical Ligands	77

2.4	Organometallic SIMMs	80
2.5	Conclusion	84
	References	84
3	Dinuclear Lanthanide Single-Molecule Magnets	91
3.1	Magnetic Interactions	92
3.2	The Coupling of Two SIMMs	97
3.2.1	Triple-Decker Lanthanide Phthalocyanine System	98
3.2.2	Dinuclear β -Diketone SMMs	102
3.2.3	Dinuclear Lanthanide Radical SMMs	108
3.2.4	Organometallic Multidecker Ln-COT SMMs	110
3.3	The Choice of Bridging Ligands	112
3.4	Dinuclear SMMs with O-Bridges	116
3.4.1	Carboxylato-Bridged Dy ₂ SMMs	118
3.4.2	Phenoxido-Bridged Dy ₂ SMMs	120
3.4.3	Alkoxido-Bridged Dy ₂ SMMs	122
3.5	Conclusion	123
	References	124
4	Single-Molecule Toroids and Multinuclear Lanthanide Single-Molecule Magnets	127
4.1	Single-Molecule Toroid	128
4.1.1	The Seminal Dy ₃ SMT	130
4.1.2	New Dy ₃ -SMTs Systems	132
4.1.3	Cyclic Dy ₄ and Dy ₆ SMT Systems	135
4.1.4	Coupled Dy ₃ -SMTs Systems	137
4.1.5	Other Dy ₃ Examples	142
4.2	High-Performance Multinuclear Lanthanide SMMs	144
4.2.1	Building Block Approach	145
4.2.2	Organometallic Approach	147
4.2.3	Multidentate Ligand Approach	150
	References	163
5	Hydrazone-Based Lanthanide Single-Molecule Magnets	167
5.1	Hydrazone Ligands	168
5.2	Two Model Complexes for Two-Step Relaxation	170
5.3	Hydrazone Ligands Based on Different Hydrazone Parts	172
5.3.1	Benzhydrazone Ligands	172
5.3.2	Isonicotinohydrazone Ligands	175
5.3.3	Picolinohydrazone Ligands	177
5.3.4	Pyrazine Acylhydrazone Ligands	179
5.3.5	Hydroxymethyl Picolinohydrazone Ligands	181
5.3.6	<i>o</i> -Vanilloyl Hydrazone Ligands	183

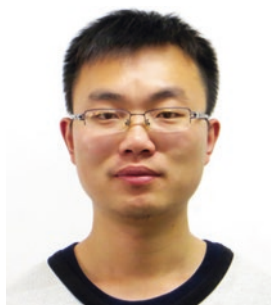
5.3.7	Hydrazone–Oxime Ligands	186
5.3.8	Hydrazone Ligands from Bis-Acylhydrazide.	188
	References	191
6	Conclusion and Perspective	195
6.1	New Type of Lanthanide SMM— $\text{Dy}_n\text{Sc}_{3-n}\text{N}@C_{80}$ ($n = 1, 2, 3$)	196
6.2	The Organization of SMMs on Surfaces	198
6.2.1	Transition Metal SMMs on Au Surface	199
6.2.2	[LnPc ₂] SMMs on Surfaces	201
6.3	Molecular Spintronics	204
	References	208

About the Authors



Jinkui Tang received his Ph.D. degree in 2001 from Nankai University under the supervision of Prof. Dai-Zheng Liao and then worked as a postdoctoral fellow at Universität Karlsruhe (TH) in the research group of Prof. Annie K. Powell and Universiteit Leiden with Prof. Jan Reedijk, before initiating his independent career at Changchun Institute of Applied Chemistry, Chinese Academy of Sciences in 2007. His current research focuses on the synthesis and characterization of new molecular magnetic materials (including single molecule-magnets and single-

molecule toroids) based on highly anisotropic lanthanide ions. His work has resulted in about 150 peer-reviewed publications.



Peng Zhang obtained his B.Sc. in chemistry from Inner Mongolia University, China, in 2010. Now he is a Ph.D. student supervised by Prof. Jinkui Tang at Changchun Institute of Applied Chemistry, Chinese Academy of Sciences (CAS). His current work focuses on lanthanide-based molecular magnetism.

Chapter 1

A Basis for Lanthanide Single-Molecule Magnets

Abstract The basic information on lanthanide single-molecule magnets (SMMs) has been introduced systematically in this chapter covering the magnetism of lanthanide, the characterization and relaxation dynamics of SMMs, and advanced means of studying lanthanide SMMs. In particular, the brief introduction to the single-crystal magnetic measurements and ab initio calculations of lanthanide SMMs demonstrate the up-to-date progresses on elucidating the magnetic anisotropy and relaxation mechanism of highly anisotropic lanthanide SMMs. Such basic knowledge is very essential for the readers to grasp the subject of this book.

Keywords Single-molecule magnet · Lanthanide ions · Magnetic anisotropy · Relaxation dynamics · Ab initio calculations

This chapter will provide a basis for lanthanide single-molecule magnets [1, 2] (SMMs) ranging from the magnetism of lanthanide and the magnetic relaxation theory to advanced means for characterizing SMMs. We believe this basis is very essential for the readers to grasp the subject of this book. In 2011, Long et al. depicted the requisite electronic structure for a lanthanide complex to exhibit single-molecule magnetic behavior by applying a simple model [3]. Herein, the free-ion and crystal-field contributions to the $4f$ electronic structure are highlighted. Considering the complexity and specialty of the $4f$ -element electronic structure, we will introduce the magnetic properties of lanthanide ions in the first section of this chapter. The second part focuses on the characterization and relaxation dynamics of SMMs, which is a foundation for understanding and grasping this field for new and current researchers. Finally, lanthanide SMMs are discussed with an emphasis on the specialty in contrast to transition metal SMMs, especially the advanced means, such as angle-resolved magnetometry and ab initio calculations, which can provide a direct detection for the relationship between the crystal structure and magnetic properties, are introduced.

1.1 Magnetism of Lanthanides

Lanthanide elements contain a total of 15 elements with atomic numbers ranging from 57 to 71 (La to Lu), which are referred to as rare earth elements with inclusion of 21 (Sc) and 39 (Y). For lanthanide atoms, two types of electronic configurations are present, $[\text{Xe}]4f^n6s^2$ and $[\text{Xe}]4f^{n-1}5d^16s^2$, where n represents a number from 1 to 14. Generally speaking, lanthanide atoms tend to lose three electrons and exhibit a 3+ valence state (Ln^{III}) in coordination complexes. It is remarkable that $4f$ orbitals show the extremely strong angular dependence (Fig. 1.1 inset) and lie deeply buried in core electron density (Fig. 1.1) [3–5]. Therefore, Ln^{III} ions with $4f$ electrons except Gd^{III} ($4f^7$, half-filled) and Lu^{III} ($4f^{14}$, full-filled) all present the large unquenched orbital angular momentum and effective spin–orbital coupling under ligand field, which give rise to their strong single-ion anisotropies. In contrast to transition metal SMMs, such strong anisotropies of Ln^{III} ions are very crucial for their SMM behavior, which can be seen from the discoveries of numerous lanthanide SMMs with high effective barriers surpassing that of transition metal SMMs [2, 6].

1.1.1 Magnetism of Free Lanthanide Ions

The initial point to understand the magnetism of lanthanide complexes is the description of the electronic structures of the $4f$ electrons in free lanthanide ions. The radial components and angular dependences of $4f$ wave functions have been

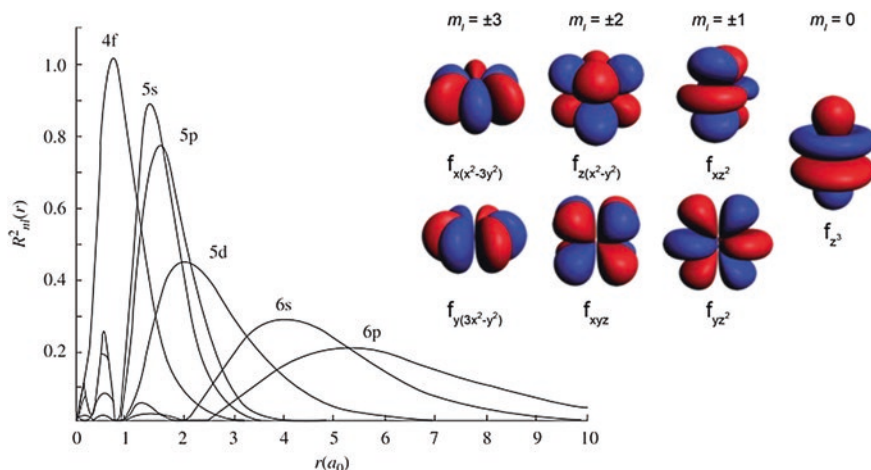


Fig. 1.1 Radial distribution functions of $4f$, $5s$, $5p$, $5d$, $6s$, and $6p$ electrons for cerium. Reprinted from Ref. [5] Copyright 1978, with permission from Elsevier. *Inset* the $4f$ orbitals from highest magnitude m_l (most oblate shape) to lowest magnitude m_l (most prolate shape). Reproduced from Ref. [3] by permission of The Royal Society of Chemistry

depicted in Fig. 1.1. The figure indicates that the $4f$ electrons are well shielded by the $5s$ and $5p$ states from the surroundings and their angular variation is very obvious with the changes in magnetic quantum number m_l , which leads to the strong spin-orbit interaction. To better describe the electronic structure of lanthanide ions, the L - S or Russell-Saunders coupling scheme [7] is adopted, giving a multiplet denoted by $^{2S+1}L_J$ ($|L - S| \leq J \leq |L + S|$), as shown in Fig. 1.2. Here, the total momentum J is derived from the sum of the total orbital momentum $L = \sum_i l_i$ and the total spin momentum $S = \sum_i s_i$ based on the *vector model*. $L = 0, 1, 2, 3, \dots$ is labeled by S, P, D, F, etc. The energies of multiplet levels $^{2S+1}L_J$ can be defined as follows:

$$E(^{2S+1}L_J) = (\lambda/2)[J(J+1) - L(L+1) - S(S+1)] \quad (1.1.1)$$

where λ is the spin-orbit coupling constant [8]. In the lowest multiplet ^{2S+1}L with J ranging from $(L - S)$, $(L - S + 1)$ to $(L + S - 1)$, $(L + S)$, the lowest lying J multiplet is called the ground-state multiplet level. In general, the ground-state multiplet level is well separated from the excited ones of the same multiplet because of the large spin-orbit coupling energies except two ions Eu^{III} and Sm^{III} , which are rarely studied in SMM field (Table 1.1). Therefore, for describing the magnetic properties of the ions, it may be sufficient to consider only the ground level characterized by the angular momentum quantum number J [7].

Fig. 1.2 Level scheme of the electronic structures of the Dy^{III} ion obtained after the electronic repulsion, spin-orbital coupling and crystal or magnetic field. Reproduced from Ref. [3] by permission of The Royal Society of Chemistry

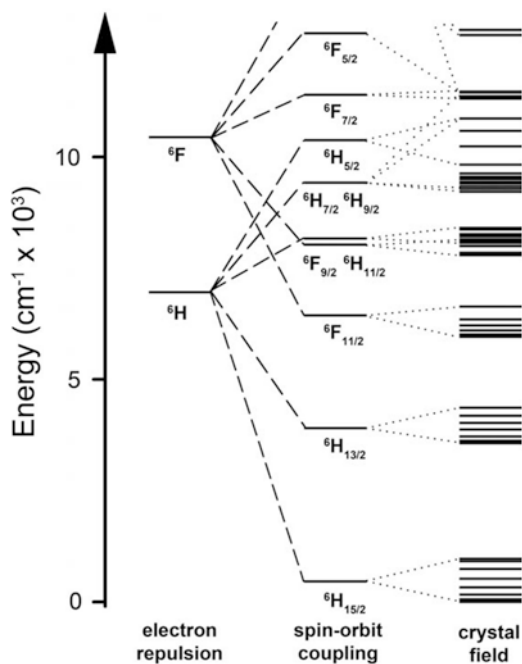


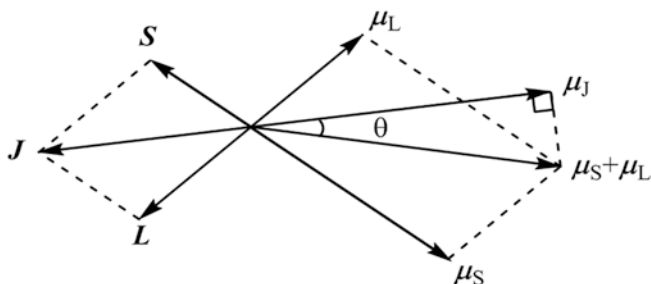
Table 1.1 Ground state, g values, room temperature χT values, and energy separation between ground state and the first excited state for trivalent lanthanide ions

Ln^{3+}	$4f^n$	Ground state	g_J	χT (emu mol $^{-1}$ K)	First excited state	Energy separation (cm $^{-1}$)
Ce	f^1	$^2F_{5/2}$	6/7	0.8	$^2F_{7/2}$	2200
Pr	f^2	3H_4	4/5	1.6	3H_5	2100
Nd	f^3	$^4I_{9/2}$	8/11	1.64	$^4I_{11/2}$	1900
Pm	f^4	5I_4	3/5	0.9	5I_5	1600
Sm	f^5	$^6H_{5/2}$	2/7	0.09	$^6H_{7/2}$	1000
Eu	f^6	7F_0	0		7F_1	300
Gd	f^7	$^8S_{7/2}$	2	7.88	$^6P_{7/2}$	30,000
Tb	f^8	7F_6	3/2	11.82	7F_5	2000
Dy	f^9	$^6H_{15/2}$	4/3	14.17	$^6H_{13/2}$	–
Ho	f^{10}	5I_8	5/4	14.07	5I_7	–
Er	f^{11}	$^4I_{15/2}$	6/5	11.48	$^4I_{13/2}$	6500
Tm	f^{12}	3H_6	7/6	7.15	3H_5	–
Yb	f^{13}	$^2F_{7/2}$	8/7	2.57	$^2F_{5/2}$	10,000

For a given lanthanide ion, the ground-state multiplet level can be easily determined through Hund's rules [7, 9]:

1. The value of S takes its maximum but must be compatible with the Pauli exclusion principle;
2. The value of L also takes its maximum as far as allowed by rule (1);
3. For ions with less-than-half-filled shells, the level with the lowest value of J lies lowest ($J = |L - S|$), while the opposite rule applies (highest J lies lowest) when a subshell is more than half full ($J = |L + S|$).

The ground states of all lanthanide ions based on above rules are listed in Table 1.1.

**Fig. 1.3** The J and μ_J from spin-orbital interaction between the angular momentum S and L

In addition, for a magnetic ion in an applied field \mathbf{H} , the orbital and spin moments are given by $\boldsymbol{\mu}_L = -\mu_B \mathbf{L}$ and $\boldsymbol{\mu}_S = -g_e \mu_B \mathbf{S} = -2\mu_B \mathbf{S}$, corresponding to the orbital and spin momentum, respectively. Therefore, it is important to realize that the total moment $\boldsymbol{\mu}_{\text{tot}} = \boldsymbol{\mu}_L + \boldsymbol{\mu}_S$ is not collinear with \mathbf{J} but is tilted toward the spin due to their different gyromagnetic factors or g-factor. As shown in Fig. 1.3, the vector $\boldsymbol{\mu}_{\text{tot}}$ makes an angle θ with \mathbf{J} and precesses around \mathbf{J} . It is thus necessary to project $\boldsymbol{\mu}_{\text{tot}}$ onto vector \mathbf{J} , so that $(\mathbf{L} + 2\mathbf{S}) \cdot \mathbf{J} = g_J J^2$. Since $2\mathbf{L} \cdot \mathbf{S} = \mathbf{J}^2 - \mathbf{L}^2 - \mathbf{S}^2 = J(J+1) - L(L+1) - S(S+1)$, thus,

$$\boldsymbol{\mu}_J = -g_J \mu_B \mathbf{J} \quad (1.1.2)$$

$$|\boldsymbol{\mu}_J| = \mu_J = g_J \sqrt{J(J+1)} \mu_B \quad (1.1.3)$$

$$g_J = \frac{1}{2} + \frac{3}{2} \frac{S(S+1) - L(L+1)}{J(J+1)} \quad (1.1.4)$$

Here, the factor g_J is called Landé factor, which denotes the components of L and S along the field direction by M_L and M_S and determines the amount of the separation of the levels in magnetic field [7, 10]. The factors of lanthanide ions are listed in Table 1.1.

Until now, the ground-state multiplet levels for lanthanide ions, their moments, and Landé factor have been determined, so the magnetic properties of a system consisting of N atoms can be described. For a free lanthanide ion, the ground-state multiplet $^{2S+1}L_J$ has $(2J+1)$ degenerate levels characterized by the magnetic quantum number $m_J = J, J-1, J-2, \dots, -J$ under zero applied field. The ground state of Dy ion, for example, is $^6\text{H}_{15/2}$, which has $(2 \times 15/2 + 1) = 16$ degenerate levels. Furthermore, the application of a direct current (dc) field can remove the $(2J+1)$ degenerate levels (Fig. 1.2). The corresponding energies of each level are given by

$$E_H = -\boldsymbol{\mu}_0 \boldsymbol{\mu} \cdot \mathbf{H} = -\mu_0 \mu_z H = -g_J m_J \mu_0 \mu_B H \quad (1.1.5)$$

Here, $\boldsymbol{\mu}$ and μ_z are the atomic moment and its quantization component along the direction of the applied field, respectively. In addition, $\mu_z = -g_J m_J \mu_B$ and $\mu_0 = 4\pi \times 10^{-7} \text{ T mA}^{-1}$. For the ground state of free ion, those levels are equally spaced with the energy difference between two adjacent levels $\Delta E = g_J \mu_0 \mu_B H$.

For a system containing N atoms, if the temperature and applied field reach such a condition that for all of the participating magnetic atoms, only the lowest level is occupied, the magnetization of the system will reach its saturated value:

$$M_s = -N\mu_J = Ng_J J \mu_B \quad (1.1.6)$$

However, in general, the excited levels are also populated at finite conditions and the relative population of the levels at a given temperature T and a given field strength H can be determined by assuming a Boltzmann distribution. Therefore, the magnetization of this system can be given by

$$M = N\bar{\mu} = N \frac{\sum_i \mu_i \exp(-E_i/kT)}{\sum_i \exp(-E_i/kT)} = N \frac{\sum_{m=-J}^J (-g_J m \mu_B) \exp(-g_J m \mu_0 \mu_B H/kT)}{\sum_{m=-J}^J \exp(-g_J m \mu_0 \mu_B H/kT)} \quad (1.1.7)$$

After a series of derivation following Eq. (1.1.7), the so-called Brillouin function can be given by

$$M = Ng_J \mu_B J \cdot B_J(y) \quad (1.1.8)$$

$$B_J(y) = \frac{2J+1}{2J} \coth \frac{(2J+1)y}{2J} - \frac{1}{2J} \coth \frac{y}{2J}$$

$$y = \frac{g_J J \mu_B \mu_0 H}{kT}$$

Furthermore, at high temperature and low field such as 298 K and 1000 Oe, y is far less than 1, and thus, the magnetic susceptibility will follow Curie's law:

$$\chi = \frac{M}{H} = \frac{N \mu_0 g^2 J(J+1) \mu_B^2}{3kT} = \frac{C}{T} \quad (1.1.9)$$

Here, the C is called Curie constant. Importantly, the χT values for lanthanide ions can be calculated through Eq. (1.1.9) and are listed in Table 1.1.

It is notable that all above equations are as a consequence of only considering the populations of $(2J+1)$ levels of the ground-state multiplet, which is also suitable for almost lanthanide ions. However, for Sm^{III} and Eu^{III} ions, the sublevels of the excited states also become populated at a relatively high temperature because of the small difference between the ground-state and excited multiplets. Consequently, deviations from Curie behavior may be expected [7].

1.1.2 Spin–Orbital Coupling and Anisotropy of Free Lanthanide Ions

Spin is isotropic, whereas the orbital component reflects the symmetry of the system and can be anisotropic. The magnitude of the magnetic anisotropy is thus determined by the quenching extent of the orbital moment, which depends on the electrostatic crystal-field interactions. Therefore, the magnetic anisotropy in solid is mainly a competed effect between spin–orbit coupling and electrostatic crystal-field interactions. Table 1.2 shows the order of magnitude of the crystal-field (CF) splitting relative to the electronic repulsion energies and the LS coupling in various groups of materials [7]. For iron-series $3d$ metal ions, the orbital moments are largely quenched due to the strong crystal-field interactions, while lanthanide ions show the larger spin–orbit coupling energy relative to the CF splitting which leads to the unquenched orbital moments and the further high magnetic anisotropy.

Table 1.2 The order of magnitude of the CF splitting relative to the electronic repulsion energies and the LS coupling (cm^{-1})

Group	Shell	Electronic repulsion	LS coupling	CF splitting
Fe	3d	10^5	10	10^3
Pd, Pt	4d, 5d	10^4	10^2	10^4
RE	4f	10^5	10^3	10^2

Spin–orbit coupling originates from the relativistic nature of rapidly moving electrons and is thus an important term in the relativistic Pauli expansion. It can be parameterized by the spin–orbit coupling constant λ [11]. For hydrogen-like orbitals,

$$\lambda = \frac{m_e}{2} Z^4 \alpha^4 c^2 \frac{1}{n^3 l \left(l + \frac{1}{2} \right) (l + 1)} \quad (1.1.10)$$

Here, Z is the effective nuclear charge and α is Sommerfeld’s fine-structure constant $1/137$. The Eq. (1.1.10) reveals that the heavier the element and the closer the electrons to the nucleus, the higher the Z and λ , i.e., the stronger the spin–orbital coupling. Compared with iron-series transition metal ions, the lanthanide ions, especially the late lanthanides ($4f^n$, $n > 7$), demonstrate stronger spin–orbital coupling interactions mainly due to their higher effective nuclear charge and the screening effects of outer $5d$ and $6s$ electrons. It is well known that the strong spin–orbit interactions in $4f$ -electron systems together with the weak crystal-field effect make the orbital moment largely unquenched and thus the total angular momentum J is regarded as a good quantum number. Here, lanthanide anisotropy can be described by the single-ion model of magnetic anisotropy, i.e., single-ion anisotropy, which is mainly derived from the internal nature of lanthanide ions, while the crystal-field interaction is only a small perturbation to spin–orbital coupling [3].

To quantify the single-ion anisotropy of lanthanide ions, we can see firstly the charge distribution of free lanthanide ions at the lowest J states, which can be identified as prolate, oblate, and spherical shape based on the quadrupole moment Q_2 [12, 13]. Here,

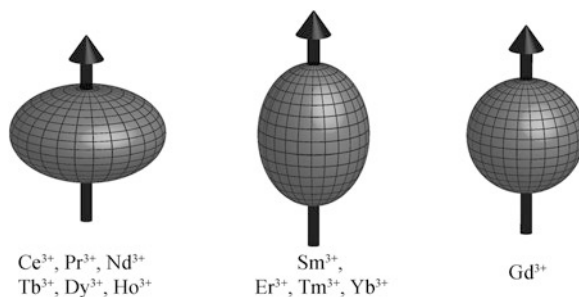
$$Q_2 = \alpha_J \langle r^2 \rangle_{4f} (2J^2 - J) \quad (1.1.11)$$

$\langle r^2 \rangle_{4f}$ is the squared $4f$ -shell radius and α_J is the second-order Stevens coefficient (Table 1.3), a quantity dependent only on the quantum numbers of the rare earth $4f$ shell, which determines the sign of Q_2 . For lanthanide ions, $Q_2 > 0$ indicates the prolate electron distribution, while $Q_2 < 0$ indicates the oblate electron distribution. Here, the value of each lanthanide ion can be calculated using Eq. (1.1.11) and the sign denotes their shape of electron distribution [11]. Lanthanide ions with negative Q_2 , Ce^{III} , Pr^{III} , Nd^{III} and Tb^{III} , Dy^{III} , Ho^{III} exhibit oblate $4f$ charge distributions, whereas the distributions of Pm^{III} , Sm^{III} , Eu^{III} and Er^{III} , Tm^{III} , Yb^{III} with positive Q_2 are prolate. Figure 1.4 provides a simple yet powerful visualization of the free-ion contribution to the $4f$ electronic structure. In fact, this shape variation in the

Table 1.3 The values of Stevens coefficient α_J , β_J , γ_J , and quadrupole moment Q_2

Ln^{3+}	Ground state	α_J	β_J	γ_J	Q_2
Ce	$^2F_{5/2}$	$\frac{-2}{5 \cdot 7}$	$\frac{2}{3^2 \cdot 5 \cdot 7}$	0	-0.686
Pr	3H_4	$\frac{-2^2 \cdot 13}{3^2 \cdot 5^2 \cdot 11}$	$\frac{-2^2}{3^2 \cdot 5 \cdot 11^2}$	$\frac{2^4 \cdot 17}{3^4 \cdot 5 \cdot 7 \cdot 11^2 \cdot 13}$	-0.639
Nd	$^4I_{9/2}$	$\frac{-7}{3^2 \cdot 11^2}$	$\frac{-2^3 \cdot 17}{3^3 \cdot 11^3 \cdot 13}$	$\frac{-5 \cdot 17 \cdot 19}{3^3 \cdot 7 \cdot 11^3 \cdot 13^2}$	-0.232
Pm	5I_4	$\frac{2 \cdot 7}{3 \cdot 5 \cdot 11^2}$	$\frac{2^3 \cdot 7 \cdot 17}{3^3 \cdot 5 \cdot 11^3 \cdot 13}$	$\frac{2^3 \cdot 17 \cdot 19}{3^3 \cdot 7 \cdot 11^2 \cdot 13^2}$	0.202
Sm	$^6H_{5/2}$	$\frac{13}{3^2 \cdot 5 \cdot 7}$	$\frac{2 \cdot 13}{3^3 \cdot 5 \cdot 7 \cdot 11}$	0	0.364
Eu	7F_0	0	0	0	-
Gd	$^8S_{7/2}$	0	0	0	0
Tb	7F_6	$\frac{-1}{3^2 \cdot 11}$	$\frac{2}{3^3 \cdot 5 \cdot 11^2}$	$\frac{-1}{3^4 \cdot 7 \cdot 11^2 \cdot 13}$	-0.505
Dy	$^6H_{15/2}$	$\frac{-2}{3^2 \cdot 5 \cdot 7}$	$\frac{-2^3}{3^3 \cdot 5 \cdot 7 \cdot 11 \cdot 13}$	$\frac{2^2}{3^3 \cdot 7 \cdot 11^2 \cdot 13^2}$	-0.484
Ho	5I_8	$\frac{-1}{2 \cdot 3^2 \cdot 5^2}$	$\frac{-1}{2 \cdot 3 \cdot 5 \cdot 7 \cdot 11 \cdot 13}$	$\frac{-5}{3^3 \cdot 7 \cdot 11^2 \cdot 13^2}$	-0.185
Er	$^4I_{15/2}$	$\frac{2^2}{3^2 \cdot 5^2 \cdot 7}$	$\frac{5}{3^2 \cdot 5 \cdot 7 \cdot 11 \cdot 13}$	$\frac{2^3}{3^3 \cdot 7 \cdot 11^2 \cdot 13^2}$	0.178
Tm	3H_6	$\frac{1}{3^2 \cdot 11}$	$\frac{2^3}{3^4 \cdot 5 \cdot 11^2}$	$\frac{-5}{3^4 \cdot 7 \cdot 11^2 \cdot 13}$	0.427
Yb	$^2F_{7/2}$	$\frac{2}{3^2 \cdot 7}$	$\frac{-2}{3 \cdot 5 \cdot 7 \cdot 11}$	$\frac{2^2}{3^3 \cdot 7 \cdot 11 \cdot 13}$	0.409

Fig. 1.4 The anisotropy of the $4f$ -shell electron distribution from quadrupole approximations for the tripositive lanthanides



f -electron charge cloud arises from the strong angular dependence of the f orbitals, because the orbitals with the largest m_l are oblate and lie in the $x - y$ basal plane, as shown in Fig. 1.1 inset, and further, the filling of the level starts with the state with the large m_l orbital according to Hund's rule. Such an estimation of charge cloud shape is necessary for predicting which type of crystal-field magnetism will lead to the strong easy-axis anisotropy requisite for strong single-molecule magnetism.

1.1.3 Lanthanide Magnetism in Ligand Fields

Even though the crystal-field interaction is small compared to the spin-orbit interaction for lanthanide ions, the crystalline electric field akin to magnetic field can also lift the $(2J + 1)$ -fold degeneracy of ground state and further play

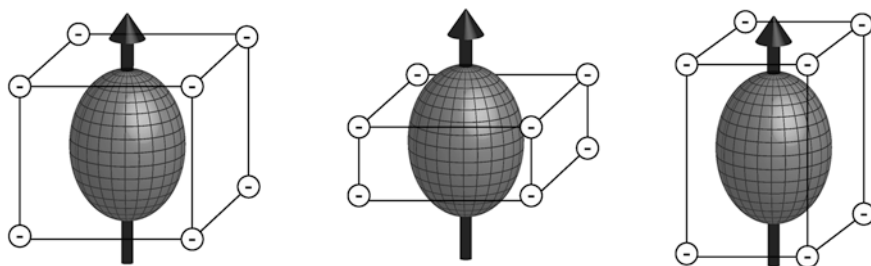
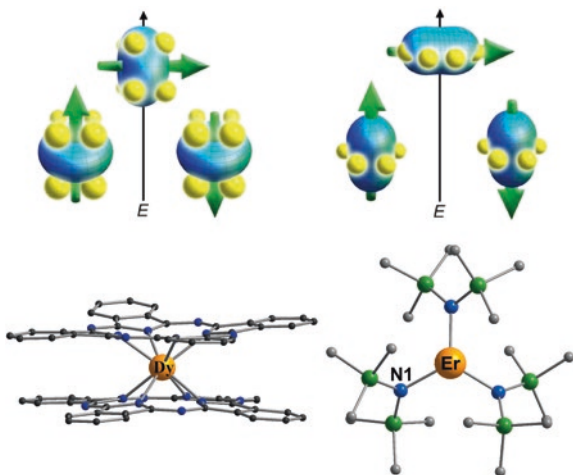


Fig. 1.5 The point-charge model in cubic crystal-field (*left*) and tetragonal crystal-fields with opposite crystal-field parameter A_2^0 (*middle* and *right*) for the lanthanide ions with the prolate electron distribution

a critical role in creating a highly anisotropic ground state. Simply, the crystal-field is the electrostatic field experienced by the unpaired electrons of a given magnetic ion from the surrounding coordinate atoms and can be described as the point-charge model [11], as shown in Fig. 1.5. Here, a given crystal-field is able to orient the electronic charge cloud to an energetically favorable direction and decides the type of the anisotropy (easy axis or easy plane) based on the shape of the lanthanide ions. For example, the compressed cubic crystal-field in Fig. 1.5 makes the lanthanide ions with the prolate electron distribution being easy-axis configuration, because the planar distribution of the negative crystal-field charges minimizes the repulsive contacts to f -electron charge clouds. Inversely, the anisotropy is easy plane for the lanthanide ions with the prolate electron distribution in elongated cubic crystal-field because of the large repulsive contacts between coordinate atoms and f -electron charge clouds. In contrast, the opposite is true for the lanthanide ion with oblate electron distribution, such as Dy^{III} and Tb^{III} . This effect was used to create and optimize permanent magnets in the past years. Remarkably, Long et al. expand the effect into the SMM field in 2011 and develop a simple model (Fig. 1.6) to predict the ligand architectures with high symmetry that will generate strong magnetic anisotropy for a variety of f -element ions [3]. In the example of the phthalocyanine double-decker lanthanide complexes [14], Fig. 1.6 (left) describes the interactions between the f -orbital electron density and the sandwich-type crystal-field, which create a bistable ground state with large m_j for the lanthanide ions with oblate electron density like Dy^{III} and Tb^{III} ions, because of the small contact between charge cloud and ligands. In contrast, for a prolate ion like Er^{III} ions, an equatorially coordinating geometry is preferable so as to minimize charge contact with the axial f -element electron density [15], as shown in Fig. 1.6 (right). In addition, recently, the model is also introduced into the Dy SMMs containing mono- and multinuclear complexes with low symmetry in a quantitative method based on a straightforward electrostatic energy minimization, which successfully predicts the orientation of the ground-state magnetic anisotropy axis of Dy^{III} ions consistent with that from *ab initio* CASSCF calculations [16].

Fig. 1.6 Depictions of low- and high-energy configurations of the f -orbital electron density with respect to the crystal-field environment for a $4f$ ion of oblate (*left*) and prolate (*right*) electron density. Two typical examples are also provided below. *Top* Reproduced from Ref. [3] by permission of The Royal Society of Chemistry



To quantitatively describe the fundamental magnetic behavior of lanthanide ions in ligand field, the simple crystal-field calculations based on an effective crystal-field Hamiltonian that assumes the point-charge electrostatic model can be performed, which permits us to estimate the whole set of crystal-field parameters and further gives the resulting states and their energies. Here, for the effective crystal-field Hamiltonian, the most commonly used one in molecular magnetism is the Stevens formalism [17, 18]:

$$H_{\text{CF}}(J) = \sum_{k=2,4,6} \sum_{q=-k}^k B_k^q O_k^q = \sum_{k=2,4,6} \sum_{q=-k}^k a_k A_k^q \langle r^k \rangle O_k^q \quad (1.1.12)$$

where k is the operator order (also called rank or degree) and must be even owing to inversion symmetry of the crystal-field potential, q is the operator range that varies between k and $-k$, $\langle r^k \rangle$ is the expectation value of r^k , and a_k are the α , β , and γ Stevens equivalent coefficients for $k = 2, 4, 6$, respectively. The O_k^q is the polynomials of the total angular momentum matrices, J^2 , J_z , J_- , and J_+ , called the operator equivalents of the crystal-field potential. The O_k^0 terms are predominant for determining the energy order of the m_J states, while the O_k^q ($q \neq 0$) terms are responsible for generating avoided level crossings through the couplings of the $|m_J\rangle$ and $|m_J \pm q\rangle$ basis wave functions, which usually considered as the main source of QTM [19]. The B_k^q or $A_k^q \langle r^k \rangle$ are called the crystal-field parameters, and the number of those parameters to be included in Eq. (1.1.12) is dictated by the point symmetry of the lanthanide center. For example, for tetragonal symmetry, only the $q = 0, \pm 4$ terms are different from zero, while the $q = \pm 4$ terms are also zero for D_{4d} , which thus represents an ideal coordinate geometry for designing the Dy SMMs. In addition, the B_k^q ($q \neq 0$) terms also vanish in some other highly symmetric geometries containing $C_{\infty v}$, $D_{\infty h}$, S_8 (I_4), D_{5h} , and D_{6d} , which provides significant insight for reducing the QTM through fine-tuning the local symmetry of lanthanide ions [20].

1.2 Single-Molecule Magnets (SMMs)

The study of SMMs (Fig. 1.7) started with the exploration of magnetism of famous Mn_{12} clusters since 1990s. Initially, it focuses on the determination of the ground states of those Mn_{12} clusters through alternating current susceptibility, high-field magnetization, and millimeter band EPR by Gatteschi and coworkers [21, 22]. Until 1993, the magnetic bistability of molecular origin is referred to explain the hysteresis effects of Mn_{12} molecule below blocking temperature (T_B), similar to those of a bulk ferromagnet [23]. Here, the bistability is derived from the large magnetic ground state (S) and negative anisotropy (D) of Mn_{12} molecule, which leads to the slow relaxation of magnetization, analogous to that used for superparamagnets, as a result of overcoming the anisotropy barrier (ΔE). Subsequently, this area of chemistry has experienced an almost unparalleled growth, as evidenced by not only the sheer number of SMMs reported with $3d$ (Mn [24–27], Fe [28, 29], Co [30] et al.), $4d$ (Mo) [31], $5d$ (Re) [32, 33], $4f$ (Dy [2, 6, 34, 35], Tb [14, 36], Er [15, 37] et al.), and $5f$ (U [38], Np [39]) ions but also the ever-expanding scope of the research [40]. Herein, two parameters, U_{eff} and T_B , are very critical to measure the success (or not) of an SMM.

1.2.1 Effective Barrier (U_{eff})

In general, the anisotropy barrier ΔE is referred to as an effective barrier (U_{eff}), as it can be determined by the relaxation times (τ) from the experiment-measured out-of-phase component χ'' of the alternating current (ac) susceptibility, following an exponential law

$$\tau = \tau_0 \exp(\Delta E/k_B T) \text{ or } \tau_0 \exp(U_{eff}/k_B T) \quad (1.2.1)$$

Here, τ_0 is pre-exponential factor, providing a quantitative measure of the attempt time of relaxation from the thermal phonon bath, and its value is within the range of 10^{-7} – 10^{-10} s expected for a molecular species [41]. k_B is the Boltzmann's constant.

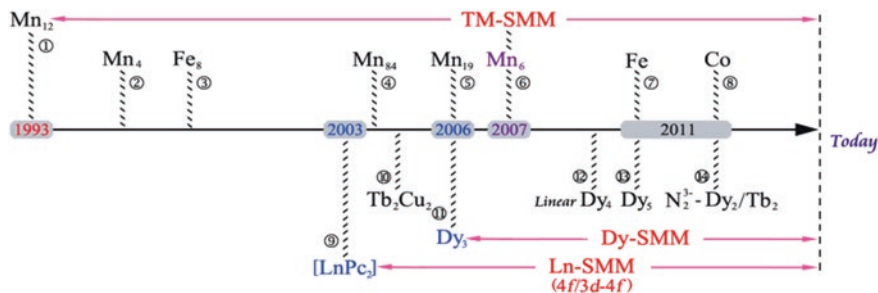


Fig. 1.7 Time axis of the development of SMMs. Reprinted from Ref. [2], Copyright 2013, with permission from Elsevier

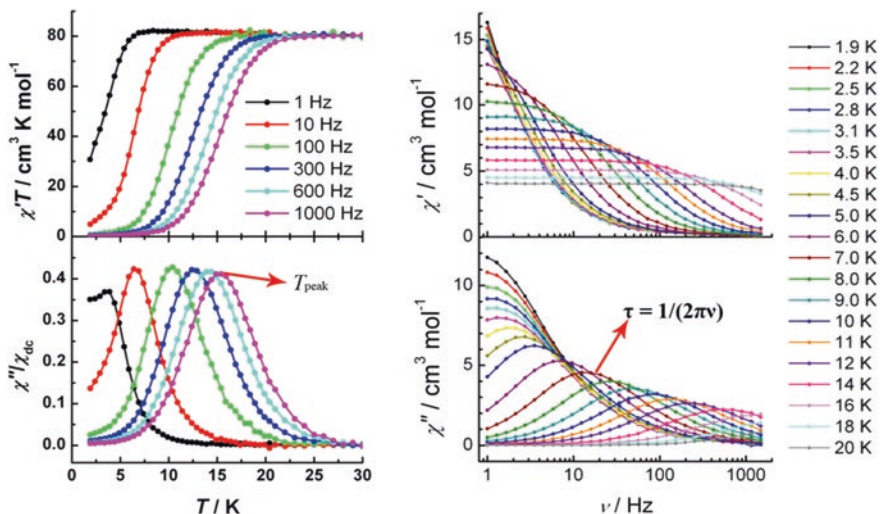


Fig. 1.8 Ac susceptibility contains the in-phase (χ') and the out-of-phase (χ'') components measured as a function of temperature (T) and as a function of the ac frequency (ν), respectively. The peak positions can be extracted from the two plots. Reprinted with permission from Ref. [34]. Copyright 2012 American Chemical Society

In the vast majority of cases, the relaxation times (τ) can be determined from ac magnetic measurements using a Quantum Design MPMS-XL SQUID magnetometer, where a small ac drive magnetic field (<10 Oe) is applied to a sample and the ac susceptibility reflecting information about magnetization dynamics is measured either in zero direct current (dc) field or in an applied dc field [42]. In general, the ac susceptibility contains the in-phase (χ') and the out-of-phase (χ'') components, which are measured as a function of temperature (T) and as a function of the ac frequency (ν), as shown in Fig. 1.8. The figure exhibits two different expressing fashions about ac susceptibility, one being χ' and χ'' versus T plots and the other being χ' and χ'' versus ν plots. However, both fashions can yield the relaxation times (τ) following $\tau = 1/(2\pi\nu)$ at a particular temperature (T) through extracting the peak positions of the ac out-of-phase (χ'') components. For the former case in Fig. 1.8 (left), the χ''/χ_{dc} versus T plots but not χ'' versus T plots were used to extract exactly the temperature maxima (T_{peak}) at a given ac frequency (ν), the reason for which is explained in Ref. [43]. For the second case in Fig. 1.8 (right), the frequency (ν) maxima at a given temperature can be easily extracted in χ'' versus ν plots. As a result, the value of U_{eff} is then extracted from the linear section of the Arrhenius plot of $\ln\tau$ versus $1/T$ (Fig. 1.9), which describes a region where the relaxation is a thermally activated process.

In addition, the relaxation time (τ) can be also deduced by direct measurements of the magnetization relaxation (magnetization decay experiments), which can measure the longer relaxation time than that in ac magnetic measurements [44, 45]. A strong dc magnetic field is applied to a sample, and then the sample is cooled down to the investigated temperature. After removing the field,

Fig. 1.9 The plot of magnetization relaxation time τ from two different fashions versus T^{-1} . The line is fitted with the Arrhenius law.

Reprinted with permission from Ref. [34]. Copyright 2012 American Chemical Society

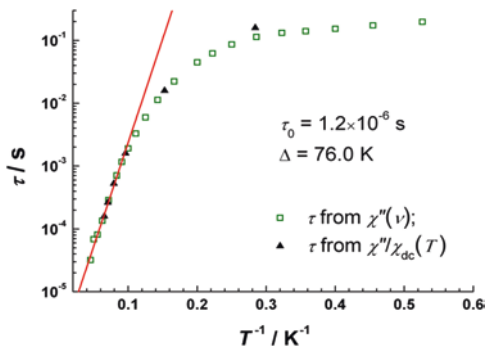
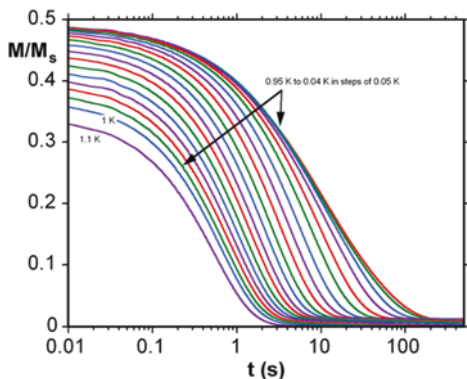


Fig. 1.10 Magnetization versus time decay plots for a single crystal at the indicated temperatures. Reprinted with permission from Ref. [45]. Copyright 2011 American Chemical Society



the magnetization (M) as a function of the time (t) was measured, as shown in Fig. 1.10. Here, the curve can be fitted by an exponential law [44]

$$M(t) = M_0 + M \exp[-(t - t_0)/\tau] \quad (1.2.2)$$

Here, τ is the relaxation time, M_0 the residual slower relaxation due to a small fraction of the crystal (less than 5 %), and t_0 the time error of the measurement using SQUID. As a result, the relaxation time (τ) was given by fitting the decay curve of magnetization.

For the systems with the strong exchange limit, such as in polynuclear transition metal SMMs Mn_{12} [23], Mn_4 [24], and Fe_8 [28], the anisotropy energy barrier (ΔE) to reorientation of the magnetization is related to D and S^2 , $\Delta E = DS^2$ or $D(S^2 - 1/4)$ for integer and half-integer spins, where D and S can be determined through ac susceptibility, high-field magnetization, and EPR data [21, 22]. Generally, the above value of the anisotropy energy (ΔE) agrees well with the U_{eff} value obtained from ac susceptibility measurements. In the case of Mn_{12} SMM, the barrier can be well described by a double-well scheme [46] (Fig. 1.11), where a negative axial zero-field splitting (D) stabilizes the largest spin states $m_s = -10$ (spin-up) and $m_s = +10$ (spin-down) lying lowest in energy, and thus, it needs to surmount the energy barrier to reorient the spin via the perpendicular $m_s = 0$ state

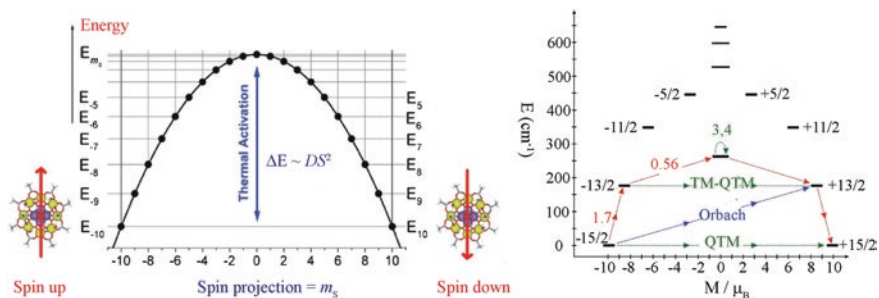


Fig. 1.11 *Left* Plot of the potential energy versus the magnetization direction for a Mn_{12} SMM with an $S = 10$ ground state experiencing axial zero-field splitting (D). Reproduced from ref. [46] by permission from John Wiley & Sons Ltd. *Right* The most efficient relaxation paths from a state with maximal magnetization in the ground-state doublet to the time-reversed state in lanthanide SMM. Reprinted with permission from Macmillan Publishers Ltd.: Ref. [35], Copyright 2014

upon being magnetized [1]. It is obvious that improving the spin ground state and anisotropy parameter is necessary to enhance the anisotropy barrier. Consequently, the initial study is focused on the synthesis of polynuclear transition metal complexes with ferromagnetic or ferrimagnetic interactions in order to obtain the largest possible spin of ground state (S), which is more predictable than the magnetic anisotropy parameter (D). However, a great number of examples indicate that those polynuclear clusters can have extremely large S values, but the accompanying D values tend to rapidly decrease, which will result in a low U_{eff} [47]. In 2004, Christou et al. reported the highest nuclearity SMM $[\text{Mn}_{84}\text{O}_{72}(\text{OAc})_{78}(\text{OMe})_{24}(\text{MeOH})_{12}(\text{H}_2\text{O})_{42}(\text{OH})_6 \cdot x\text{H}_2\text{O} \cdot y\text{CHCl}_3]$, which only possesses a molecular spin of $S = 6$ and exhibits a low energy barrier $U_{\text{eff}} = 18$ K [25]. In particular, the Mn_{19} cluster reported by Powell in 2006 exhibits dominant ferromagnetic interactions with the maximum spin ground state $S = 83/2$ to date, but the geometrical arrangement and the strong ferromagnetic interactions between spin carriers lead to a very low anisotropy and thus the disappearance of SMM behavior [26]. In addition, the largest anisotropy barrier claimed in a conventional polynuclear transition metal SMM to date is only 86.4 K (60 cm^{-1}), which was obtained in 2006 from studies of ferromagnetically coupled Mn_6 complex, $[\text{Mn}_6\text{O}_2(\text{Etsao})_6(\text{O}_2\text{CPh}(\text{Me})_2(\text{EtOH})_6)]$ (saoH₂ = salicylaldehyde) [48]. Importantly, from the first SMM discovered in 1993 to present, the highest energy barrier increases by only ~ 15 K for polynuclear transition metal SMMs. As a result, it became apparent that the strategy might not necessarily produce the desired SMM with high U_{eff} . Furthermore, it has to be noticed that the magnetic anisotropy is a key factor in creating highly efficient SMM. Recently, the mononuclear transition metal SMMs are of increasing interest because of their magnetic properties [41, 49–52]. In particular, the low-coordinate transition metal complexes have proven to be particularly useful for the isolation of efficient SMMs due to the large orbital contributions of transition metal ions (Table 1.4) [41, 52]. Nevertheless, to date, lanthanide ions with strong single-ion anisotropy still turn out to be most efficient tools to construct the SMM with high-energy barriers.

Table 1.4 The list of effective barriers for polynuclear and mononuclear transition metal SMMs as well as mononuclear and polynuclear lanthanide SMMs

Molecules	U_{eff} (H/Oe)	T_B /K	Years	Ref.
<i>Polynuclear transition metal SMMs</i>				
$\text{Mn}_{12}\text{O}_{12}(\text{O}_2\text{CMe})_{16}(\text{H}_2\text{O})_4$	61 K/42 cm^{-1}	3	1993	[23]
$\text{Mn}_4\text{O}_3\text{Cl}(\text{O}_2\text{CMe})_3(\text{dbm})_3$	18.7 K/13 cm^{-1}		1996	[24]
$[(\text{tacn})_6\text{Fe}_8\text{O}_2(\text{OH})_{12}]^{8+}$	24.5 K/17 cm^{-1}		1997	[28]
$[\text{Fe}_4(5\text{-Br-sae})_4(\text{MeO})_4] \cdot \text{MeOH}$	30 K/21 cm^{-1}	1.2	2004	[29]
$[\text{Mn}_{84}\text{O}_{72}(\text{OAc})_{78}(\text{OMe})_{24}(\text{MeOH})_{12}(\text{H}_2\text{O})_{42}(\text{OH})_6] \cdot x\text{H}_2\text{O} \cdot y\text{CHCl}_3$	18 K/12.5 cm^{-1}	1.5	2004	[25]
$[\text{Mn}_7^{\text{III}}\text{Mn}_7^{\text{II}}(\mu_4\text{-O})_8(\text{N}_3)_8(\text{HL})_{12}(\text{MeCN})_6]\text{Cl}_2 \cdot 10\text{MeOH} \cdot \text{MeCN}$	5.8 K/4 cm^{-1}		2006	[26]
$[\text{Mn}_{12}\text{O}_{12}(\text{O}_2\text{CCH}_2\text{Br})_{16}(\text{H}_2\text{O})_4]$	74.4 K/52 cm^{-1}	3.6 (40 Oe s^{-1})	2006	[27]
$[\text{Mn}_6^{\text{III}}\text{O}_2(\text{Et-sao})_6(\text{O}_2\text{CPh})_2(\text{EtOH})_6]$	86.4 K/60 cm^{-1}	4.5 (0.14 T s^{-1})	2007	[48]
<i>Mononuclear transition metal SMMs</i>				
$\text{K}[(\text{tpa}^{\text{Mes}})\text{Fe}]$	60 K/42 cm^{-1} (1500)		2010	[49]
$\text{Na}[(\text{tpa}^{\text{t-Bu}})\text{Fe}]$	94 K/65 cm^{-1} (1500)		2010	[50]
$[\text{Co}(\text{SPh})_4]^{2-}$	30 K/21 cm^{-1}		2011	[51]
$\text{Fe}[\text{N}(\text{SiMe}_3)(\text{Dipp})]_2$	260 K/181 cm^{-1} (500)		2012	[52]
$\text{Fe}[\text{C}(\text{SiMe}_3)_3]_2$	210 K/146 cm^{-1} (500)		2012	[52]
$\text{Fe}[\text{N}(\text{H})\text{Ar}']_2$	157 K/109 cm^{-1} (1800)		2012	[52]
$\text{Fe}[\text{N}(\text{H})\text{Ar}^*]_2$	150 K/104 cm^{-1} (875)		2012	[52]
$[\text{Fe}(\text{C}(\text{SiMe}_3)_3)_2]^-$	325 K/226 cm^{-1}	6.5 ($\text{H} \neq 0$ Oe)	2013	[41]
<i>Mononuclear lanthanide SMMs</i>				
$[\text{Pc}_2\text{Tb}]^- \cdot \text{TBA}^+$	331 K/230 cm^{-1}		2003	[14]
$[\text{Pc}_2\text{Tb}]^0$	590 K/410 cm^{-1}		2004	[53]
$[(\text{Pc}(\text{OEt})_8)_2\text{Tb}]^+(\text{SbCl}_6)^-$	792 K/550 cm^{-1}		2007	[54]
$[(\text{Pc}(\text{OEt})_8)_2\text{Dy}]^+(\text{SbCl}_6)^-$	79 K/55 cm^{-1}	1.8	2008	[55]
$[\text{Tb}((\text{O}-\text{C}_6\text{H}_4)\text{-}p\text{-}t\text{Bu})_8\text{Pc})(\text{Pc}')$	939 K/652 cm^{-1}	2.0 ($\text{H} \neq 0$ Oe)	2013	[56]
$[\text{ErW}_{10}\text{O}_{36}]^{9-}$	55 K/38 cm^{-1}		2008	[58]
$[\text{Dy}(\text{acac})_3(\text{H}_2\text{O})_2]$	64.3 K/44.7 cm^{-1}	0.5 ($\text{H} \neq 0$ Oe)	2010	[59]
$[\text{Dy}(\text{acac})_3(\text{phen})]$	64 K/44 cm^{-1}		2011	[62]
$[\text{Dy}(\text{acac})_3(\text{dpq})]$	136 K/94 cm^{-1}		2012	[60]
$[\text{Dy}(\text{acac})_3(\text{dpqz})] \cdot \text{CH}_3\text{OH}$	187 K/130 cm^{-1}	2 ($\text{H} \neq 0$ Oe)	2012	[60]

(continued)

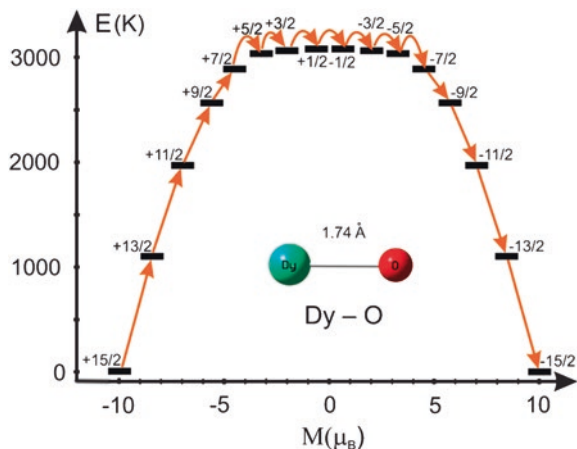
Table 1.4 (continued)

Molecules	U_{eff} (H/Oe)	T_B /K	Years	Ref.
(Cp*)Er(COT)	323 K/224 cm ⁻¹ 197 K/137 cm ⁻¹	5 K	2011	[44]
[K(18-crown-6)] [Er(COT) ₂]	216 K/150 cm ⁻¹	10 (7.8 Oe s ⁻¹)	2013	[37]
[Li(DME) ₃][Er(COT'') ₂]	187 K/130 cm ⁻¹	8 (22 Oe s ⁻¹)	2014	[63]
[Zn ₂ DyL ₂ (MeOH)]NO ₃ ·3MeOH·H ₂ O	439 K/305 cm ⁻¹	11 (200 Oe s ⁻¹)	2013	[20]
<i>Polynuclear lanthanide SMMs</i>				
[Dy ₃ (μ ₃ -OH) ₂ L ₃ Cl(H ₂ O) ₅]Cl ₃ ·4H ₂ O·2MeO H·0.7MeCN	61.7 K/43 cm ⁻¹	0.1	2006	[65]
[Dy ₂ (hmi) ₂ (NO ₃) ₂ (MeOH) ₂] _∞ ·MeCN	71 K/49 cm ⁻¹		2008	[66]
[Dy ₄ (μ ₃ -OH) ₂ (bmh) ₂ (msh) ₄ Cl ₂]	170 K/118 cm ⁻¹	7 (0.14 T s ⁻¹)	2009	[67]
[Dy ₄ (L) ₄ (MeOH) ₆] ₂ ·2MeOH	173 K/120 cm ⁻¹		2010	[68]
[Dy ₆ (μ ₃ -OH) ₄ L ₄ L' ₂ (H ₂ O) ₉ Cl]Cl ₅ ·15H ₂ O	200 K/139 cm ⁻¹		2010	[69]
[Dy ₅ O(OiPr) ₁₃]	528 K/367 cm ⁻¹	1.85	2011	[70]
[Dy ₂ (ovph) ₂ Cl ₂ (MeOH) ₃] ₂ ·MeCN	198 K/137.5 cm ⁻¹ 150 K/104 cm ⁻¹	1.5	2011	[45]
[K(18-crown-6)(THF) ₂] [[[(Me ₃ Si) ₂ N] ₂ (THF)Dy] ₂ (μ-η ² :η ² -N ₂)]	177 K/123 cm ⁻¹	8.0 (800 Oe s ⁻¹)	2011	[71]
[K(18-crown-6)(THF) ₂] [[[(Me ₃ Si) ₂ N] ₂ (THF)Tb] ₂ (μ-η ² :η ² -N ₂)]	327 K/227 cm ⁻¹	14 (9 Oe s ⁻¹)	2011	[36]
[(Cp* ₂ Dy(μ-SSiPh ₃) ₂)]	192 K/133 cm ⁻¹		2012	[73]
[(Cp* ₂ Dy) ₂ (μ-bpym•)](BPh ₄)	126 K/87.8 cm ⁻¹	7 (20 Oe s ⁻¹)	2012	[72]
[Dy ₄ K ₂ O(OrBu) ₁₂] ₂ ·C ₆ H ₁₄	692 K/481 cm ⁻¹ 316 K/219 cm ⁻¹	5 (0.14 T s ⁻¹)	2013	[74]

In 2003, the first class of SMMs containing lanthanide ions, phthalocyanine double-decker complexes [Pc₂Ln]⁻·TBA⁺ (Ln = Tb, Dy), was reported by Ishikawa and coworkers [14]. Remarkably, the Tb complex clearly exhibits magnetlike behavior of slow relaxation of the magnetization below 50 K, and the barrier U_{eff} is as high as 230 cm⁻¹ (331 K), which far surpasses that of Mn₁₂ SMM. Here, such a high barrier should benefit from their large unquenched orbital moments and strong spin-orbit coupling leading to the strong single-ion anisotropies. Further studies for redox, heteroleptic, and multidecker species of this class of complexes [53–57] were performed and thus created a high effective barrier record of SMM field, $U_{\text{eff}} = 652$ cm⁻¹ (938 K) [56], which surpasses by an order of magnitude that obtained for the original Mn₁₂ SMM. Remarkably, the interest in new kinds of mononuclear lanthanide SMMs [58] is continuing in recent years, and some of them show the very high effective barrier and blocking temperature, such as β-diketone [59–62], organometallic [35, 37, 44, 63],

and some low-symmetry [20, 64] lanthanide systems (Table 1.4). As such, the mononuclear SMMs are called single-ion magnets (SIMs) in some recent papers. However, the concept of SIM seems ambiguous, which may easily mislead the readers from other research fields. Here we call it single-ion molecular magnet (SIMM). In addition, since a triangular Dy₃ cluster with toroidal arrangement of magnetic moments on the dysprosium sites (spin chirality on the ground state) shows SMM behavior of thermally excited spin states [65], pure polynuclear Dy^{III}-based SMMs with different topologies have also attracted a large interest due to their peculiar properties and high U_{eff} . Particularly, in the last five years, the anisotropic barrier records have toppled like dominoes for polynuclear lanthanide SMMs [36, 45, 66–74], which is shown in Table 1.4. It is noteworthy that the magnetic relaxation pathways in SMMs involving strongly anisotropic lanthanide ions are distinct from those in strong exchange polynuclear transition metal SMMs. As depicted in Fig. 1.11, for most lanthanide SMMs, the relaxation of magnetization occurs through a spin–phonon mechanism via the first excited state. To date, there are only few examples reported with the relaxation via the second excited states [35, 74, 75]. Here, two reasons for this are presented [76]. Firstly, the real structure of the complexes is always distorted from the high-symmetry geometry, even in highly symmetric double-decker phthalocyanine complexes, which leads to the large transversal components of excited states and thus strong QTM between doublets, i.e., thermally activated QTM. Secondly, the low-symmetry components in structure will result in the non-coinciding anisotropy axes between the ground and the first excited Kramers doublets, which enhance the Orbach and Raman relaxation processes via the first excited doublets. Therefore, the effective barrier is usually related to the separation between the bistable ground state and the first excited state, while the relationship, $\Delta E = DS^2$, fails to represent accurately the observed barriers in lanthanide complexes. In order to improve the effective barrier, the suitable crystal-field should be designed to enlarge the separation between the bistable ground state and the first excited state and further to keep the coinciding anisotropy axes between the ground and excited Kramers doublets. To achieve the aim, a perfect axiality for lanthanide ion should be expected. Here, an ideal example, the diatomic complex [DyO]⁺ (Fig. 1.12) [76], was explored through the ab initio calculation by L. Ungur and L. F. Chibotaru. In this complex, all Kramers doublets show the perfect axiality up to the highest one, as indicated by $g_{\perp} = 0$ except $m_J = \pm 1/2$ states. As a result, the relaxation follows a path similar to that of the reversed double-well potential of Mn₁₂-Ac, as shown in Fig. 1.11, leading to the extremely high barrier ($U_{\text{eff}} > 3000$ K). However, such an example has not been prepared in experiment; nevertheless, the important breakthrough has been achieved, i.e., the relaxation passing through the second excited state (Fig. 1.11) in the organometallic lanthanide [35, 75] and the diluted Dy₄K₂ SMMs [74], where the axial strong chemical bond dominates over all other chemical bonds of the metal site, leading to basically axial nature of the total ligand field.

Fig. 1.12 Barrier for reversal of magnetization in $[\text{DyO}]^+$ at equilibrium geometry. The arrows show the path for the reversal of magnetization. Reproduced from Ref. [76] with permission from The Royal Society of Chemistry



1.2.2 Blocking Temperature (T_B) and Hysteresis

The other important parameter for evaluating the SMM performance is the magnetic blocking temperature (T_B). Here, three kinds of definitions can be given through referring to the papers on molecule-based magnets [3]: (a) the temperature at which a peak is observed in the out-of-phase susceptibility (χ'') at a given frequency, (b) the highest temperature at which hysteresis loop is observed in a plot of field (H) versus magnetization (M), and (c) the temperature at which a maximum is observed in the zero-field cooled magnetization. Usually, we adapt the second definition closest to the behavior of a bulk ferromagnet, but it must be careful when comparing the temperature since the value strongly depends on the sweep rate of the magnetic field [6]. It is noteworthy that the highest blocking temperature, $T_B = 14$ K (Table 1.4), under the slow sweep rate of the magnetic field is kept by the strong exchange coupling $\text{N}_2^{3-}\text{-Tb}_2$ complex [36], where the strong magnetic exchange coupling hinders zero-field fast relaxation pathways. Recently, the mononuclear lanthanide complexes were also reported to show the high blocking temperature. Impressively, the high-symmetry $[\text{Er}(\text{COT})_2]^-$ complex exhibits an open hysteresis loop to 10 K, which represents the highest blocking temperature yet observed for a mononuclear complex and the second highest for any single-molecule magnet [37, 75]. It appears to be clear that the lanthanide ions hold better promise for the design of new SMMs with higher blocking temperatures compared with other transition metal ions. In addition, to give a more quantitative description for the blocking temperature (T_B), Gatteschi et al. [42] proposed that T_B corresponds to the temperature at which $\tau = 100$ s. However, to date, very few SMMs could reach relaxation times in this domain due to the fast QTM in the low-temperature region [36].

1.2.3 Relaxation Dynamics

Relaxation phenomenon will occur when the equilibrium state in a system is influenced by an external field and the time for reaching a new equilibrium is so long after removing the external field. The studies for the process are important in many fields such as NMR processes, disordered solids, and dielectric and magnetic materials [77]. Here, we focus on the investigation of the magnetic relaxation dynamics in SMM field. Nowadays, the most important method identifying the SMM behavior is ac magnetic measurements, where the measured ac susceptibility or dynamic susceptibility in an alternating magnetic field reflects information about magnetization dynamics. The alternating magnetic field can be identified as follows:

$$H(t) = H_0 + h\cos(\omega t), \quad \omega = 2\pi\nu \quad (1.2.3)$$

where H_0 is zero or nonzero constant indicating the zero- or nonzero-dc magnetic field parallel to the oscillating field h , h is the amplitude of ac magnetic field, and ν indicates the oscillating frequency of ac magnetic field. Therefore, the measured ac susceptibility, χ_{ac} , at a given temperature is a complex value containing the real (χ') and imaginary (χ'') components as a function of the oscillating frequency (ν) of ac magnetic field, as shown in Fig. 1.13:

$$\chi_{ac}(\omega) = \chi'(\omega) - i\chi''(\omega) = |\chi|e^{-i\theta}, \quad \omega = 2\pi\nu \quad (1.2.4)$$

where $\chi'(\omega)$ and $\chi''(\omega)$ are often referred to as magnetic dispersion and magnetic absorption [10, 42]. In general, the decline in the in-phase component $\chi'(\omega)$ of the ac susceptibility will be concomitant with the appearance of peaks in the out-of-phase component $\chi''(\omega)$, clearly indicating slow magnetic relaxation behavior.

To better investigate the magnetic relaxation process, the plots of $\chi''(\omega)$ versus $\chi'(\omega)$ are usually performed, i.e., so-called Argand diagram similar to

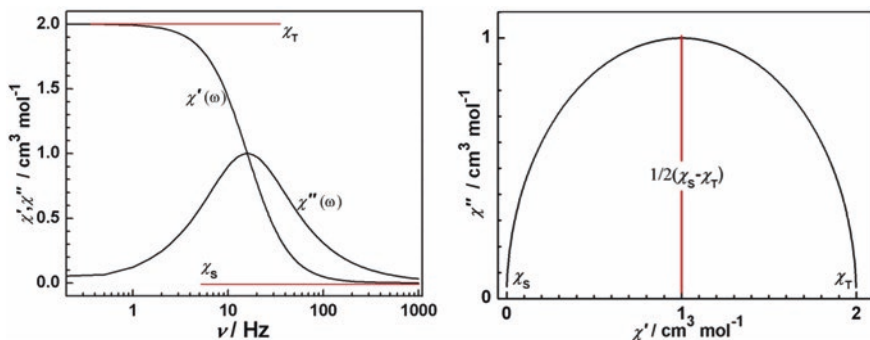


Fig. 1.13 *Left* The real (χ') and imaginary (χ'') components as a function of the oscillating frequency (ν) of ac magnetic field. *Right* the so-called Argand diagram with a single-relaxation process characterized by a single-relaxation time

the Cole–Cole plot used for dielectrics, which presents the results for various frequencies in the complex χ -plane (Fig. 1.13) [77]. In order to relate the measured susceptibility to the relaxation process in a magnetic system, Casimir and Du Pré in 1938 firstly proposed the thermodynamic model for spin–lattice relaxation [78]. Here, if the magnetic system experiences a single-relaxation process characterized by a single-relaxation time, $\tau = \omega^{-1} = 1/(2\pi\nu)$, the Argand diagram would show a semicircle with a center on the x -axis and the expression for the complex ac susceptibility can be derived in a mathematically analogous relations to dielectrics from Debye (Debye model):

$$\chi_{ac}(\omega) = \chi_S + \frac{\chi_T - \chi_S}{1 + i\omega\tau} \quad (1.2.5)$$

The quantities χ_T and χ_S are the isothermal and the adiabatic susceptibility, respectively. If the frequency ω of the ac field is low, $\omega\tau \ll 1$, for which the temperature equilibrium is obtained over the timescale of the experiment, the measured susceptibility is the isothermal susceptibility χ_T in the limit of the lowest field frequencies. On the other hand, if the oscillations of the ac field are fast compared to the time constant τ , $\omega\tau \gg 1$, the magnetic system remains isolated from its surroundings, and then the adiabatic susceptibility χ_S , lower than χ_T , is revealed [42, 79]. According to Eqs. (1.2.4) and (1.2.5), the real (χ') and imaginary (χ'') components can be split into

$$\chi'(\omega) = \chi_S + \frac{\chi_T - \chi_S}{1 + (\omega\tau)^2} \quad (1.2.6)$$

$$\chi''(\omega) = (\chi_T - \chi_S) \frac{\omega\tau}{1 + (\omega\tau)^2} \quad (1.2.7)$$

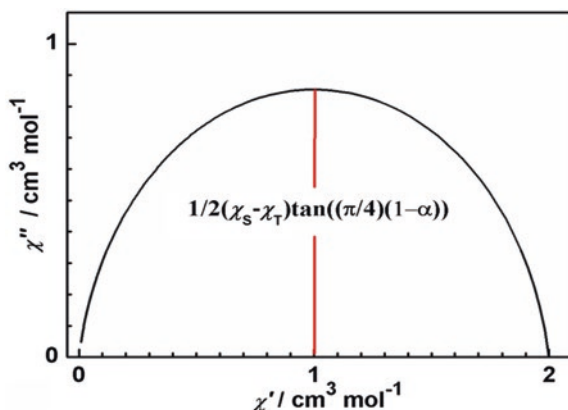
It should be stressed again that the above two equations are related to the relaxation process with a single-relaxation time τ . The frequency ω_{peak} , at which the absorption reaches its maximum, $\chi_{\text{max}} = 1/2(\chi_T - \chi_S)$, determines the relaxation time, $\tau = \omega^{-1} = (2\pi\nu)^{-1}$. However, for most magnetic samples, the relaxation process is not characterized by a single τ but rather by a distribution of relaxation times. The Argand plot is thus flatten, and the $\chi_{ac}(\omega)$ can be modified in the Cole–Cole expression [80, 81]:

$$\chi_{ac}(\omega) = \chi_S + \frac{\chi_T - \chi_S}{1 + (i\omega\tau)^{1-\alpha}} \quad (1.2.8)$$

Here, α is introduced to describe the distribution of relaxation times in a magnetic system, and its value changes between 0 and 1. The wider the distribution in relaxation times, the larger the value of α . When α value is equal to 0, the Eq. (1.2.8) is related to Debye process with a single τ . Further, the real (χ') and imaginary (χ'') components can be split into

$$\chi'(\omega) = \chi_S + (\chi_T - \chi_S) \frac{1 + (\omega\tau)^{1-\alpha} \sin\left(\frac{\pi}{2}\alpha\right)}{1 + 2(\omega\tau)^{1-\alpha} \sin\left(\frac{\pi}{2}\alpha\right) + (\omega\tau)^{2-2\alpha}} \quad (1.2.9)$$

Fig. 1.14 The so-called Argand diagram with a distribution of relaxation times characterized by α parameter



$$\chi''(\omega) = (\chi_T - \chi_S) \frac{(\omega\tau)^{1-\alpha} \cos\left(\frac{\pi}{2}\alpha\right)}{1 + 2(\omega\tau)^{1-\alpha} \sin\left(\frac{\pi}{2}\alpha\right) + (\omega\tau)^{2-2\alpha}} \quad (1.2.10)$$

Therefore, the real (χ') and imaginary (χ'') components for a given ac magnetic data can be fitted easily to the Eqs. (1.2.9) and (1.2.10), respectively. Importantly, the relation between χ'' and χ' can be yielded through combining Eqs. (1.2.9) and (1.2.10):

$$\chi'' = \frac{1}{2}(\chi_S - \chi_T) \tan\left(\frac{\pi}{2}\alpha\right) + \frac{1}{2} \sqrt{\left[(\chi_T - \chi_S) \tan\left(\frac{\pi}{2}\alpha\right)\right]^2 - 4\left[\chi'^2 - \chi'(\chi_T + \chi_S) + \frac{1}{4}(\chi_T + \chi_S)^2 - \frac{(\chi_T - \chi_S)^2}{4(\sin(\pi/2)(1-\alpha))^2} + \frac{1}{4}(\chi_T - \chi_S)^2 \left(\tan\left(\frac{\pi}{2}\alpha\right)\right)^2\right]} \quad (1.2.11)$$

The Argand diagram for a single-relaxation process with a narrow distribution of relaxation times can be fitted very well by the above Eq. (1.2.11). Nevertheless, the diagram exhibits a flattened semicircle with the χ'' maximum at $\chi' = \chi_S + 1/2(\chi_T - \chi_S)$, as shown in Fig. 1.14:

$$\chi''_{\max} = \frac{1}{2}(\chi_T - \chi_S) \tan\left(\frac{\pi}{4}(1-\alpha)\right) \quad (1.2.12)$$

Now, we have performed a detailed description for the single-relaxation process with a narrow distribution of relaxation times, which is suitable for the interpretation of relaxation behavior of most transition metal SMMs with a strong exchange limit. However, since 2006, the wide investigation into polynuclear lanthanide SMMs with weak intramolecular magnetic interactions reveals that the relaxation in a polynuclear system may thus become more complicated due to the presence of several weakly coupled spin centers, each showing intrinsic magnetic anisotropy which is characterized by its own spin temperature and characteristic τ value [68, 79]. So two or more relaxation processes would be present in such a

system, and thus, a further analysis of such processes is of utmost importance in order to better understand the relaxation dynamics of lanthanide-based SMMs.

In 2010, our group developed the two-step relaxation model through the sum of two modified Debye functions to successfully explain the multiple relaxation processes in the linear Dy₄ SMM with two crystallographically independent spin centers [68, 79]. The equation can be described as follows:

$$\chi_{ac}(\omega) = \chi_{S1} + \chi_{S2} + \frac{\chi_{T1} - \chi_{S1}}{1 + (i\omega\tau_1)^{1-\alpha_1}} + \frac{\chi_{T2} - \chi_{S2}}{1 + (i\omega\tau_2)^{1-\alpha_2}} \quad (1.2.13)$$

Because χ_{Si} of each relaxation phase cannot be determined, we define

$$\chi_{S,tot} = \chi_{S1} + \chi_{S2} \quad (1.2.14)$$

which represents the sum of the adiabatic susceptibility of the two relaxing species. Thus, let

$$\Delta\chi_1 = \chi_{T1} - \chi_{S1} \quad (1.2.15)$$

$$\Delta\chi_2 = \chi_{T2} - \chi_{S2} \quad (1.2.16)$$

where $\Delta\chi_i$ is the difference between the adiabatic susceptibility (χ_S) and the isothermal susceptibility (χ_T) of each magnetic species. Finally, we obtain the following equation:

$$\chi_{ac}(\omega) = \chi_{S,tot} + \frac{\Delta\chi_1}{1 + (i\omega\tau_1)^{1-\alpha_1}} + \frac{\Delta\chi_2}{1 + (i\omega\tau_2)^{1-\alpha_2}} \quad (1.2.17)$$

Splitting the Eq. (1.2.17) into the real and imaginary parts, one gets

$$\begin{aligned} \chi'(\omega) = & \chi_{S,tot} + \Delta\chi_1 \frac{1 + (\omega\tau_1)^{1-\alpha_1} \sin(\pi\alpha_1/2)}{1 + 2(\omega\tau_1)^{1-\alpha_1} \sin(\pi\alpha_1/2) + (\omega\tau_1)^{2-2\alpha_1}} \\ & + \Delta\chi_2 \frac{1 + (\omega\tau_2)^{1-\alpha_2} \sin(\pi\alpha_2/2)}{1 + 2(\omega\tau_2)^{1-\alpha_2} \sin(\pi\alpha_2/2) + (\omega\tau_2)^{2-2\alpha_2}} \end{aligned} \quad (1.2.18)$$

$$\begin{aligned} \chi''(\omega) = & \Delta\chi_1 \frac{1 + (\omega\tau_1)^{1-\alpha_1} \cos(\pi\alpha_1/2)}{1 + 2(\omega\tau_1)^{1-\alpha_1} \sin(\pi\alpha_1/2) + (\omega\tau_1)^{2-2\alpha_1}} \\ & + \Delta\chi_2 \frac{1 + (\omega\tau_2)^{1-\alpha_2} \cos(\pi\alpha_2/2)}{1 + 2(\omega\tau_2)^{1-\alpha_2} \sin(\pi\alpha_2/2) + (\omega\tau_2)^{2-2\alpha_2}} \end{aligned} \quad (1.2.19)$$

Because ac susceptibility is a complex quantity, the ac susceptibility $\chi_1(\omega)$ and $\chi_2(\omega)$ for two-relaxation phases may take the following forms:

$$\chi_1(\omega) = \chi'_1(\omega) - i\chi''_1(\omega) \quad (1.2.20)$$

$$\chi_2(\omega) = \chi'_2(\omega) - i\chi''_2(\omega) \quad (1.2.21)$$

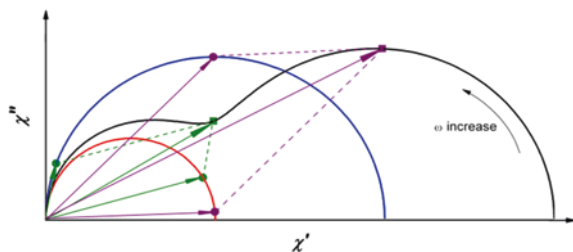


Fig. 1.15 Resolution of Cole–Cole plot for two-step relaxation applying parallelogram law as the frequency increases. The *black line* represents the experimental curve, and the *blue and red lines* are resolved two-relaxation processes. χ_{Si} are taken as the origin. $\tau_2/\tau_1 = 20$. Reproduced from Ref. [79] with permission from The Royal Society of Chemistry

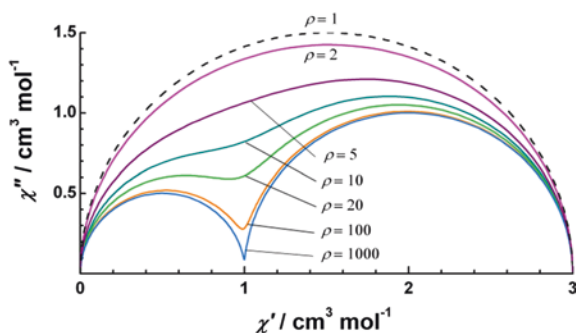


Fig. 1.16 Cole–Cole plot for the two-relaxation process for different ρ values, where ρ being defined as τ_2/τ_1 ($\rho = 1$ for a single-relaxation process). For the sake of simplicity, α_i and χ_{Si} are taken equal to zero, $\Delta\chi_2 = 2\Delta\chi_1$. Reproduced from Ref. [79] with permission from The Royal Society of Chemistry

Then, each of χ_1 and χ_2 represents a semicircle for each relaxation phase in Cole–Cole plot. The total ac susceptibility $\chi_{ac}(\omega)$ is being thought of the sum of two complex numbers:

$$\chi_{ac}(\omega) = \chi_1(\omega) + \chi_2(\omega) \quad (1.2.22)$$

The geometric construction of two vectors χ_1 and χ_2 by using parallelogram law for addition gives χ_{ac} , and conversely, χ_{ac} can be resolved into its components χ_1 and χ_2 . Thus, the operations described algebraically above can be visualized in Fig. 1.15. Such analysis reveals that the shape of the Cole–Cole plots for overall process is mainly determined by the different relaxation time of each process. We define ρ as $\rho = \tau_2/\tau_1$, such that $\rho = 1$ corresponds to the single-relaxation process. Figure 1.16 shows χ'' versus χ' curves for $\rho = 2, 5, 10, 20, 100$, and 1000. For the sake of simplicity, α_i and χ_{Si} are taken equal to zero. When ρ is small, the Cole–Cole plot exhibits an approximate semicircle or asymmetric semicircle, indicating the distribution of relaxation times of the material; when ρ lies between 10 and 100, two merged relaxation occurs as revealed by Cole–Cole plot, predicting the presence of two closely spaced relaxation phases; and finally, in case that one

relaxation is significantly slower than the other, as $\rho > 100$, two well-separated relaxation phases will be observed.

In order to explain the intrinsic relaxation mechanism in SMMs, the relaxation theories such as QTM and spin–lattice relaxation previously developed in the experiments on paramagnetic metal salts [82–84] can be also applied here. In particular, the spin–lattice relaxation theory arising from the energy exchanges between the paramagnetic ions and the phonon radiations plays a critical role in the extraction and interpretation of effective barrier (U_{eff}). Simply, a magnetic system could be seen as two parts, the spin system and the lattice system, and the thermal equilibrium is usually kept between two systems, but upon applying an oscillating field parallel to a constant field on the magnetic sample, the energy exchanges between them would take place and thus produce the magnetic relaxation effects [77]. In 1932, Waller firstly attempted the theoretical calculation of the spin–lattice relaxation times τ under the assumption that the lattice vibrations influence the spin only by modulating the spin–spin interaction [82, 85]. Even though the calculated results exhibited a great departure from experiments, he identified two types of relaxation effects affecting τ , i.e., the direct and Raman precesses. Further investigations from de Kronig [86] and Van Vleck [82] et al. indicate that the modulation of the ligand field by lattice vibrations is more important in spin–lattice relaxation in contrast to the spin–spin interactions. Here, the ligand field can produce a fluctuating electric field by lattice vibrations and thus modulate the orbital motion of the magnetic electron, which further affects the spin system through the spin–orbital coupling [84]. In addition, an extended work was performed by Orbach et al. [87], who proposed a new spin–lattice relaxation mechanism, i.e., the Orbach process showing the different temperature dependence from the direct and Raman processes. Figure 1.17 shows the illustration of the absorption and emission of phonon from lattice vibration for three types of spin–lattice relaxation processes. Furthermore, a quantitative formulation of relaxation times τ for three relaxation processes according to the above theory is usually applied in SMM field to model the magnetic data [52, 88]:

$$\tau^{-1} = AH^m T + CT^n + \tau_0^{-1} \exp(-U_{\text{eff}}/kT) \quad (1.2.23)$$

Here, the parameters A , C , and τ_0 are constant, and the three terms correspond to three different relaxation processes (direct, Raman, and Orbach), respectively, that contribute simultaneous to the relaxation rate τ^{-1} . Equation (1.2.23) and Fig. 1.17 allow one to distinguish the three relaxation processes:

- (a) Direct process, a single-phonon process involving the phonons with the same energy as the magnetic resonance quantum $h\nu$, which allows the spin to flip without traversing the energy barrier in SMM. Here, the τ^{-1} shows the temperature (T) and dc applied field (H) dependence as shown in the first term in Eq. (1.2.23) with $m = 4$ and 2 for Kramers and non-Kramers doublets, respectively.
- (b) Raman process, a two-phonon process with the scattering of phonons on spins, where all phonons can take part and the phonon frequencies are related to each other by $h(\nu_2 - \nu_1) = \Delta$, leading to the strong temperature dependence but the non-dependence on the applied magnetic field, as seen in the second term of Eq. (1.2.23). Theoretically, the exponent n corresponds to 7 for the

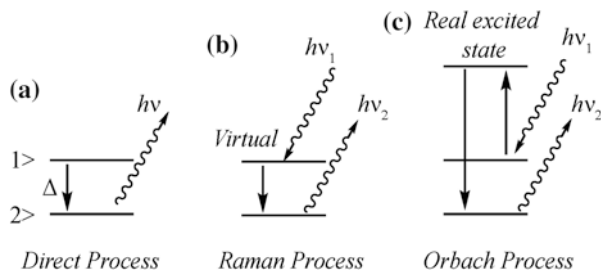


Fig. 1.17 Phonon-assisted relaxation. **a** Direct relaxation into the ground state under the emission of a phonon with energy $h\nu$. **b** The two-phonon Raman process involves the absorption of a phonon of energy $h\nu_1$ and a subsequent emission of another phonon of energy $h\nu_2$, relaxing the molecule into its ground state. **c** The two-phonon Orbach process

non-Kramers ions and 9 for the Kramers ions, but n may vary depending on the exact energies of the ground doublets, and thus, the value is reasonable for $n \geq 4$ [52].

- (c) Orbach process, a direct, resonant two-phonon process via a real intermediate state involving two phonons related to each other by $h(\nu_2 - \nu_1) = \Delta$. Here, the relaxation time is found to vary exponentially with T^{-1} with a slope Δ/k . In contrast to the above two processes, the presence of this process is more important in characterizing a SMM, because it allows a spin to reorient by climbing over the anisotropy barrier (U_{eff}), a key characteristic for SMM.

Contrary to the above magnetic relaxations arising from the energy exchanges between the paramagnetic ions and the phonon radiations, magnetic relaxations caused by transitions between ground doublets as a result of a transverse anisotropy induced by a distortion from the axial symmetry are referred to as a quantum tunneling of magnetizations (QTM) [19]. Generally, the QTM relaxation is very slow for polynuclear transition metal SMMs because of its strong exchange coupling interactions between metal ions. Here, we focus on the QTM relaxation behavior in lanthanide SMMs with strong single-ion anisotropy, and its length of the relaxation time mainly depends on the extent of the departure from a perfect axiality, which is very sensitive to the coordination environment. In fact, the real structure of the complexes is always slightly distorted from the highly axial symmetry geometry, thus leading to the occurrence of QTM even for highly symmetric molecules such as the double-decker phthalocyanine lanthanide complex [76]. In addition, the presence of hyperfine and nuclear quadrupole interactions between the $4f$ electrons and the nucleus and the dipole-dipole interactions between different molecules plays also an important role in opening the efficient QTM relaxation path [89]. Different from the above relaxation processes, the QTM relaxation is temperature independent and only shows the dependence for applied dc magnetic field (H) [19, 90].

In general, an efficient QTM, direct, or Raman process will shortcut the Orbach process at a given temperature, especially in the low-temperature region, and greatly reduce the anisotropic barrier. In order to extend the temperature region of Orbach process and effectively enhance the anisotropic barrier, the three processes, especially

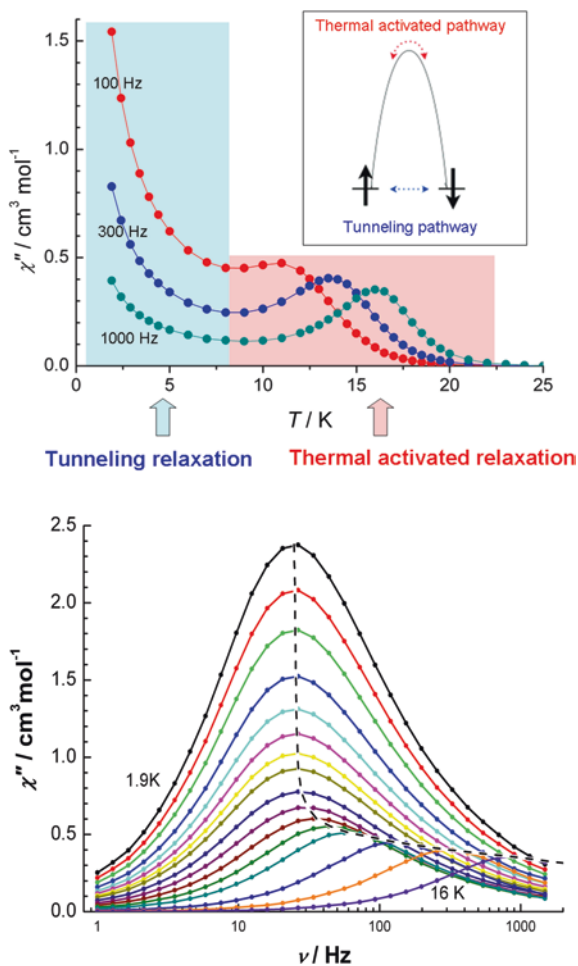
QTM, should be suppressed as efficiently as possible, which can be achieved by modulating the ligand field to enhance the axial anisotropy [75], applied dc magnetic field, or magnetic dilution [59]. The detailed information of those methods will be introduced in the chapter about “Lanthanide Single-Ion Molecular Magnets”.

1.3 Lanthanide Single-Molecule Magnets

The basic knowledge of lanthanide magnetism and SMMs has been introduced in the above sections. When the lanthanide ions are incorporated into SMMs, the effective barrier has been enhanced greatly in contrast to transition metal SMMs (Table 1.4), and further, many novel magnetic phenomena were discovered mainly because of the strong magnetic anisotropy of $4f$ electrons arising from the strong spin–orbital coupling interactions. Herein, the internal nature of lanthanide ions leads to the presence of its strong single-ion anisotropy in ligand field for not only mononuclear but also multinuclear lanthanide complexes. In mononuclear complexes, the single-ion anisotropy has been well proved by the angle-resolved magnetometry studies and ab initio calculations, as seen in the magnetic investigations of Dy-DOTA SMMs [91, 92]. Importantly, very weak magnetic coupling interactions occur between lanthanide centers in multinuclear cluster molecules except the example of N_2^{3-} -radical-bridged lanthanide complex owing to the limited radial extension of the $4f$ orbital [71], and thus, the relaxation barrier blocking the magnetization is mainly attributable to the single-ion anisotropy of individual lanthanide ion, the evidence for which has been provided in the magnetic dilution of an antiferromagnetic Dy_2 SMM reported by Murugesu [93]. Further, it is because of the strong single-ion anisotropy that the zero-field multiple-step relaxation process usually appears in the lanthanide cluster with different magnetic centers, each of which may function as a single-ion magnet characterized by its own spin temperature and characteristic t values [79]. The typical examples were provided by our group, i.e., the linear Dy_4 [68] and asymmetric Dy_2 [45] complexes with hydrazone ligands, both of which contain two different spin centers. More particularly, the triangular Dy_3 cluster reported by Powell shows toroidal arrangement of magnetic moments on the dysprosium sites (spin chirality on the ground state) and SMM behavior of thermally excited spin states [65], which originate from the non-collinearity of the single-ion easy axes of magnetization of the Dy^{III} ions, as revealed by single-crystal magnetic studies [94] and muon spin–lattice relaxation measurements [95] and corroborated by ab initio calculations. In addition, as mentioned in the above section, faster QTM relaxation occurs in the lanthanide SMMs in contrast to the transition metal SMMs, which allows us to directly detect the process within the investigated temperature domain of ac susceptibility measurements [79], as shown in Fig. 1.18.

Here, only a simple description is introduced about the lanthanide SMMs, and the detailed information will be provided in the following chapters. Finally, to obtain a good understanding of the correlation between the structure and magnetic properties of the molecules, some advanced means have been applied to study the

Fig. 1.18 $\chi''(T)$ (top) and $\chi''(\nu)$ (bottom) for a lanthanide SMM showing the fast QTM. Reproduced from Ref. [79] with permission from The Royal Society of Chemistry



lanthanide SMMs. Here, two critical techniques will be introduced simply with one being angle-resolved magnetometry developed by Sessoli et al. [91, 96] and the other being *ab initio* calculations from Chibotaru and coworkers [97]. They provide the experimental and theoretical evidences for the local magnetic anisotropy of lanthanide ions, respectively, and in particular, the *ab initio* calculations can also allow the determination of the complex electronic structures of lanthanide ions.

1.3.1 Angle-Resolved Magnetometry

Persistent axiality of lanthanide ions in lanthanide compounds is an important feature enabling them functioning as SMMs and responsible for the unusual magnetic behavior such as multiple relaxation processes and spin chirality due to the

non-collinearity of their single-ion anisotropic axes. Therefore, the accurate determination of axial anisotropy of lanthanide ion in a complex will provide vital information to aid our understanding of the magnetic relaxation mechanism. In particular, in the complexes with low-symmetry components, even though the local symmetry around lanthanide ions can be approximated by a higher one, the magnetic anisotropy of lanthanide ions is not directly related to the approximated high-symmetry environment and the simple analysis based on the idealized symmetry could be misleading [91]. Here, it should be noted that the anisotropy not only points to the magnitude of the axial component, but also contains the axis direction and its transverse components, which are very critical in explaining the tunneling relaxation. Even though now *ab initio* calculations could theoretically provide the detailed information for those parameters which will be introduced in the next part, the direct experimental confirmation of the presence of uniaxial anisotropy seems to be more convincing. In transition metal complexes, single-crystal EPR measurements can provide a full characterization of the magnetic anisotropy, while the EPR signal is silent or shows the broaden peaks for lanthanide complexes, especially Dy ion [96]. Here, Sessoli et al. [96] firstly developed single-crystal magnetic measurements into molecular magnetism in 2009 and thus provide accurate information on the magnetic anisotropy through angle-resolved magnetometry. In fact, the technique was initiated in the 1960s, but has scarcely been employed in molecular magnetism before because of its complex procedure and low sensitivity [98, 99]. Nevertheless, the problem was solved by the integration of horizontal sample rotator (Fig. 1.19) combined modern SQUID magnetometers with high sensitivity here [100].

The large enough single crystal should be grown firstly, and then, it is embedded in glue (or grease) on one face of a millimeter-sized Teflon cube to better handle the crystals which are air sensitive, susceptible to solvent loss, or with poor habit [69]. Most importantly, the crystal mounted on the Teflon cube is indexed on a single-crystal X-ray diffractometer, and in the experimental XYZ reference frame, the X, Y, and Z orthogonal axes can be defined as the normal to three faces of the cube, which can be indexed with non-integer Miller indices within the crystal lattice frame (*abc* reference frame or *ab'c** reference frame) [96]. Therefore, the relation between XYZ and *abc* reference frames is well defined, which confirms the accurate measurement of anisotropic axes. Three orthogonal faces of the cube were then employed to fix the sample on the sample holder of a horizontal sample rotator. Here, the horizontal sample rotator is shown in Fig. 1.19 with three main parts: internal and external rods, wire and spring, and sample holder, which allow the investigations of angle dependence over an angular range of more than 180° in three consecutive rotations in the experimental XYZ reference frame. Finally, the angular dependence of the magnetic susceptibility can be measured through three orthogonal rotations along X, Y, and Z axes, as shown in Fig. 1.19. The experimental data are simulated using Eq. (1.3.1) [91] taking into account that only the component of *M* along *H* is measured.

$$\chi^{\text{rot}}(\theta) = \chi_{\alpha\alpha}\cos^2(\theta) + \chi_{\beta\beta}\cos^2(\theta) + 2\chi_{\alpha\beta}\cos^2(\theta) \quad (1.3.1)$$

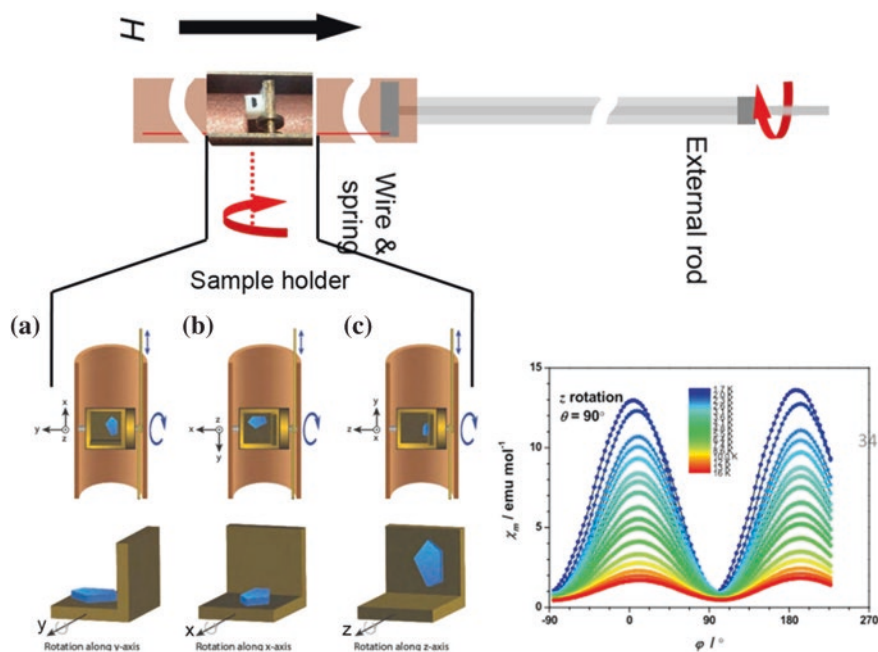


Fig. 1.19 The structure of horizontal sample rotator. The rotation axis is perpendicular to the static magnetic field direction. The rotation is performed via the stretching of the Cu–Be wire bonded on the pulley, which shares the rotation axis with the sample holder. The *lower row* is the orientation of an L-shaped Cu–Be support with respect to the three rotation axes. Reprinted from Ref. [100], with kind permission from Springer Science+Business Media

with cyclic permutation of the α , β , and γ indexes over the XYZ reference frame and θ the angle the magnetic field forms with the α -axis. Therefore, the susceptibility tensor can be extracted using

$$\chi = \begin{pmatrix} \chi_{\alpha\alpha} & \chi_{\alpha\beta} & \chi_{\alpha\gamma} \\ \chi_{\beta\alpha} & \chi_{\beta\beta} & \chi_{\beta\gamma} \\ \chi_{\gamma\alpha} & \chi_{\gamma\beta} & \chi_{\gamma\gamma} \end{pmatrix} \rightarrow \begin{pmatrix} \chi_x & 0 & 0 \\ 0 & \chi_y & 0 \\ 0 & 0 & \chi_z \end{pmatrix} \quad (1.3.2)$$

The above susceptibility tensor (χ) has been diagonalized, thus providing the principal values of the susceptibility (χ_x , χ_y , and χ_z) and their orientation. In addition, the largest principal value can provide the information about the ground state and the corresponding axial g -factor indicating the strong axial anisotropy for an effective spin $S_{\text{eff}} = 1/2$.

A remarkable example is the series of lanthanide complexes ($\text{Ln}^{\text{III}} = \text{Tb}^{\text{III}}, \text{Dy}^{\text{III}}, \text{Ho}^{\text{III}}, \text{Er}^{\text{III}}, \text{Tm}^{\text{III}}, \text{and Yb}^{\text{III}}$) with DOTA ligand ($\text{H}_4\text{DOTA} = 1, 4, 7, 10$ -tetraazacyclododecane N, N', N'', N''' -tetraacetic acid), the anisotropies of which were explored by Sessoli et al. [91] in 2012. The structure is shown in Fig. 1.20. Here, the coordination of a H_2O molecule breaks the square-antiprismatic coordination

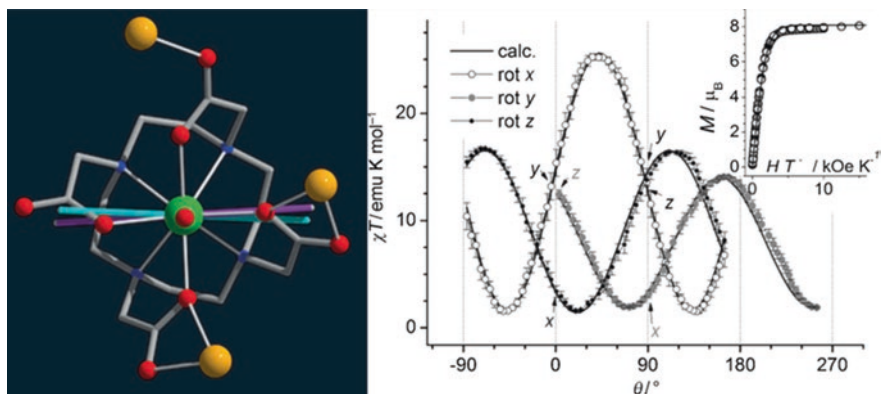


Fig. 1.20 The crystal structure of $\text{Dy}^{\text{III}}\text{-DOTA}$ (left, the violet rod represents the orientation of the experimental easy axis of the magnetization, while the pale blue rod represents the calculated one); angular dependence of the magnetic susceptibility of $\text{Dy}^{\text{III}}\text{-DOTA}$ (right). Reproduced from Ref. [91] with permission from John Wiley & Sons Ltd.

environment in the first coordination sphere, and the tetragonal symmetry is also suppressed in a larger coordination sphere due to the coordinated Na^+ ion. Thus, simple analysis based on the idealized symmetry of the lanthanide complex can be misleading. In the example of Dy-DOTA , the single-crystal magnetic measurements reveal the high angular dependence of the magnetization (Fig. 1.20), suggesting a strong magnetic anisotropy of Dy^{III} ion. The diagonalization of susceptibility tensor (χ) can provide the principal values of the susceptibility and their orientation: $g_{\parallel} = 17.0$ for an effective $S_{\text{eff}} = 1/2$, which confirms the Ising anisotropy of the Dy^{III} ion in the low-symmetry environment. The orientation of the easy axis (violet rod) is shown in Fig. 1.20 (left). To ensure the accuracy, ab initio calculations including all the atoms of the complex have been performed. The effective g -tensor of the ground-state doublet of the ${}^6\text{H}_{15/2}$ has also been estimated at 18.6, approaching the Ising limit. The orientation of anisotropy (pale blue rod) is close (10° , within experimental uncertainty) to the experimental one and is almost perpendicular to the idealized symmetry axis. In addition, the calculations were performed on several reduced models, revealing that the hydrogen bonds on coordinated water molecule play a key role in the unexpected orientation of the easy axis. Other late lanthanide derivatives were further investigated through the angle-resolved magnetometry and ab initio calculations to get a deeper insight into the anisotropic properties of lanthanide ions. Figure 1.21 shows a reorientation of the easy axis of magnetization from perpendicular to parallel to the Ln-O bond of the apical water molecule upon going from Tb^{III} to Yb^{III} centers in the complexes [92].

In addition, the single-ion anisotropy of Dy^{III} ion in Dy^{III} -radical complex $[\text{Dy}(\text{hfac})_3\text{-(NIT-R)}_2]$ has been investigated as early as 2009 [96], which is shown in Fig. 1.22. The complex crystallizes in the triclinic space group with only one Dy ion located in a distorted square-antiprismatic environment. The analytic outcomes of angle-resolved magnetic measurements show a strong Ising-type

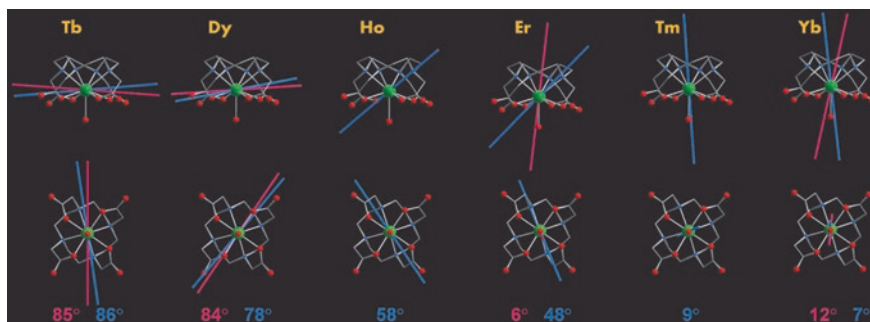


Fig. 1.21 Experimental (*pink*) and calculated (*blue*) magnetization easy axis at $T = 2$ K for the series viewed perpendicular (*top*) and parallel (*bottom*) to the pseudo-fourfold symmetry axis of the molecules. Reproduced from Ref. [92] with permission from John Wiley & Sons Ltd.

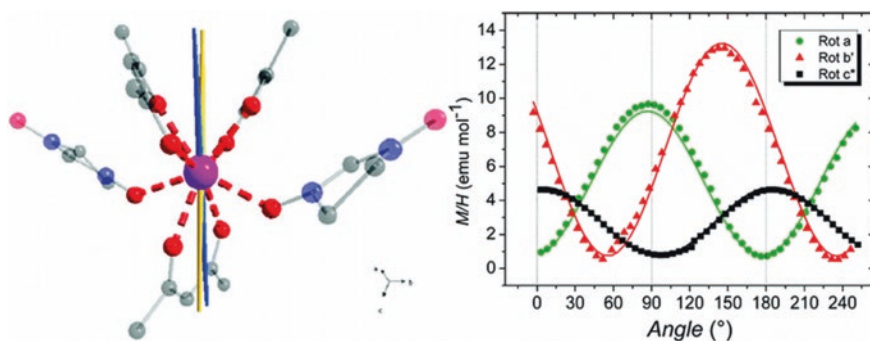


Fig. 1.22 The crystal structure of $[\text{Dy}^{\text{III}}(\text{hfac})_3\text{-(NIT-R)}_2]$ (*left*, the *yellow rod* represents the orientation of the experimental easy axis of the magnetization, while the *blue rod* represents the calculated one); angular dependence of the magnetic susceptibility of $[\text{Dy}^{\text{III}}(\text{hfac})_3\text{-(NIT-R)}_2]$ (*right*). Reprinted with permission from Ref. [96]. Copyright 2009 American Chemical Society

anisotropy for the complex. The largest g component of ground-state doublet obtained from *ab initio* calculations is about 18, and its orientation is calculated to be very close (7°) to the experimental one.

It should be noted that the above magnetometry is not a local probe. When the site symmetry of the magnetic molecules is lower than that of the space group like in the monoclinic system, the molecules in the lattice will be structurally identical but oriented differently, and thus, the observed magnetization is the average of those molecules in the crystal [96]. Therefore, until now, the application of this technique is almost limited in triclinic system with only one magnetically independent site, which reduces significantly its application. Nevertheless, recently Sessoli et al. [101] have proposed a way to extend single-crystal magnetic investigations to non-triclinic SMMs (i.e., those that contain more than one orientation of the molecules in the crystal) by exploiting the reconstruction of the molecular anisotropy tensor from out-of-equilibrium magnetization data.

1.3.2 *Ab Initio Calculations*

In order to explore in depth the origin of SMM behavior, especially the correlation between the electronic structure resulting from the crystal-field splitting and the magnetic relaxation dynamics, and further effectively direct the design of target SMMs incorporating 4f elements, some theoretical approaches or models have been developed into molecule magnetism, such as ligand field calculations [18], density functional theory (DFT) [102] calculations, and ab initio calculations [97]. Nevertheless, in contrast to the ligand field analysis via CONDON [59] or other approaches, the ab initio CASSCF/RASSI/SINGLE_ANISO calculations with MOLCAS package based on the complex multiconfigurational approach can provide more comprehensive and accurate information for the magnetic properties of lanthanide SMMs. A detailed calculating procedure of the ab initio method is available in Supporting Information of some references [35, 45, 75], and herein, we intend to provide an overview of the final calculation results associated with the SMM properties of the corresponding lanthanide complexes. On the basis of the resulting spin-orbital multiplets from the CASSCF and RASSI methods, the SINGLE_ANISO program can compute local magnetic properties of magnetic centers in lanthanide complexes including g -tensors, main magnetic axes, local magnetic susceptibility, and crystal-field parameters, the reliability of which is confirmed by the well fitting of dc magnetic susceptibility data, that is, the temperature- and field-dependent magnetic properties (Van Vleck susceptibility tensor and function, molar magnetization vector and function) [45, 103]. It is noteworthy that no geometry optimization has been done here, all atomic coordinates being taken from the single-crystal X-ray analysis in the calculation process. The resultant magnetic parameters from the real crystal structure are directly related to the magnetic relaxation dynamics of the corresponding lanthanide complexes, which is undoubtedly of great importance for gaining an insight into the structure-property relationship and further guiding the design of lanthanide SMMs with the enhanced properties. For Kramers ions such as Dy^{III} or Er^{III} ion, the strong axiality is characterized by a large axial component of g -tensor, g_z or $g_{//}$, while the transversal components, g_x and g_y or g_{\perp} , provide the quantitative description of the low symmetry of the ligand field [76], which is of great importance in explaining the relaxation dynamics in the low-temperature region such as the occurrence of QTM. When the Kramers doublet is perfectly axial, g_x and g_y are equal to zero. However, in general, even though the transversal components, g_x and g_y (<1), only show a small divergence from zero and far less than the axial g_z , it is enough to open the QTM pathway and further to affect the low-temperature relaxation dynamics, as indicated in some Dy SMMs [6, 73]. The case is different for non-Kramers ions because of $g_x, g_y = 0$ for them according to the Griffith's theorem [104], and thus, the direct QTM is due to an intrinsic tunneling gap (Δ_{tun}) present without any applied field [76]. Here, the QTM is reduced with the decreasing of the tunneling splitting (Δ_{tun}), which can be directly related to the symmetry of lanthanide complex. A highly symmetric coordination environment can confirm the small

tunneling splitting (Δ_{tun}) between the ground Ising doublets for non-Kramers ions and further promotes the SMM behavior, as observed in double-decker phthalocyanine Tb^{III} complexes [14]. More importantly, the most efficient relaxation paths from a state with maximal magnetization in the ground-state doublet to the time-reversed state with reversed magnetization can be accessed by calculating the matrix elements of transversal magnetic moments or the intrinsic tunneling gaps between different states [35, 105], which will be presented in examples below. In addition, the exchange interactions between metal sites in polynuclear lanthanide complexes can be calculated within the Lines model using the routine POLY_ANISO program [45, 103]. It is noteworthy that here the pure exchange (J_{exch}) and dipolar (J_{dip}) contributions to magnetic interactions are able to be given by the program. Traditionally, it is difficult to separate exchange coupling contributions from ligand field/Zeman level thermal depopulation effects in orbitally degenerate lanthanide systems, and thus, Chibotaru has pioneered these developments.

The above aspects can be well exemplified in a valence-localized carbon coordinated Dy SMM [35], showing a high effective barrier due to the unprecedented relaxation mediated via the second excited state. As shown in Fig. 1.23, the anisotropic orientations and energy of eight Kramers doublets of Dy center, as well as their corresponding anisotropic factors, were revealed by ab initio calculations,

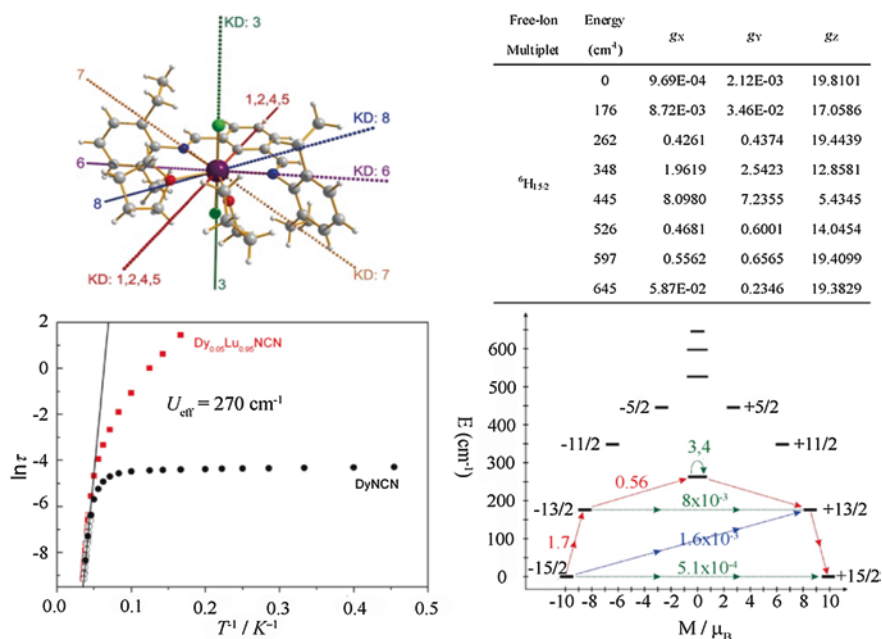


Fig. 1.23 The energy levels of the ground multiplet in DyNCN SMM, the corresponding anisotropic directions and factors for each Kramers doublet, as well as the experimental and theoretical anisotropy barriers. Reprinted with permission from Macmillan Publishers Ltd., Ref. [35], Copyright 2014

which allow us to gain an insight into the origin of strong SMM behavior. First of all, the ground and first excited doublets both possess the strong axial anisotropy indicated by the small transversal components, g_x and g_y , and importantly, their anisotropic axes are parallel along C_2 direction, which greatly reduces the Orbach and Raman relaxation processes via the first excited state. Secondly, the calculated energy gap between the ground and the first excited state is 262 cm^{-1} , which is well in agreement with the effective barrier of 270 cm^{-1} extracted by the ac susceptibility data. As a result, the unprecedented relaxation pathway via the second excited state is present in the current organometallic complex.

References

1. Christou G, Gatteschi D, Hendrickson DN et al (2000) Single-molecule magnets. *MRS Bull* 25(11):66–71. doi:[10.1557/mrs2000.204](https://doi.org/10.1557/mrs2000.204)
2. Zhang P, Guo Y-N, Tang J (2013) Recent advances in dysprosium-based single molecule magnets: structural overview and synthetic strategies. *Coord Chem Rev* 257(11–12):1728–1763. doi:[10.1016/j.ccr.2013.01.012](https://doi.org/10.1016/j.ccr.2013.01.012)
3. Rinehart JD, Long JR (2011) Exploiting single-ion anisotropy in the design of f-element single-molecule magnets. *Chem Sci* 2(11):2078–2085. doi:[10.1039/C1SC00513H](https://doi.org/10.1039/C1SC00513H)
4. Huang C (2010) Rare earth coordination chemistry: fundamentals and applications. Wiley, Singapore
5. Goldschmidt ZB (1978) Atomic properties (free atom) Chap. 1. In: Gschneidner KA Jr, Eyring LR (eds) Handbook on the physics and chemistry of rare earths, vol 1. Elsevier, Amsterdam, pp 1–171. doi:[10.1016/S0168-1273\(78\)01005-3](https://doi.org/10.1016/S0168-1273(78)01005-3)
6. Woodruff DN, Winpenny REP, Layfield RA (2013) Lanthanide single-molecule magnets. *Chem Rev* 113:5110–5148. doi:[10.1021/cr400018q](https://doi.org/10.1021/cr400018q)
7. Buschow KHJ, Boer FRd (2003) Physics of magnetism and magnetic materials. Kluwer Academic/Plenum Publishers, New York
8. Benelli C, Gatteschi D (2002) Magnetism of lanthanides in molecular materials with transition-metal ions and organic radicals. *Chem Rev* 102(6):2369–2388. doi:[10.1021/cr010303r](https://doi.org/10.1021/cr010303r)
9. Getzlaff M (2008) Fundamentals of magnetism. Springer, Berlin
10. Morrish AH (1965) The physical principles of magnetism. Wiley, New York
11. Skomski R (2008) Simple models of magnetism. Oxford University Press, New York
12. Skomski R, Sellmyer DJ (2009) Anisotropy of rare-earth magnets. *J Rare Earth* 27(4):675–679. doi:[10.1016/S1002-0721\(08\)60314-2](https://doi.org/10.1016/S1002-0721(08)60314-2)
13. Sievers J (1982) Asphericity of 4f-shells in their Hund's rule ground states. *Zeitschrift für Physik B Condensed Matter* 45(4):289–296. doi:[10.1007/bf01321865](https://doi.org/10.1007/bf01321865)
14. Ishikawa N, Sugita M, Ishikawa T et al (2003) Lanthanide double-decker complexes functioning as magnets at the single-molecular level. *J Am Chem Soc* 125(29):8694–8695. doi:[10.1021/ja029629n](https://doi.org/10.1021/ja029629n)
15. Zhang P, Zhang L, Wang C et al (2014) Equatorially coordinated lanthanide single ion magnets. *J Am Chem Soc* 136(12):4484–4487. doi:[10.1021/ja500793x](https://doi.org/10.1021/ja500793x)
16. Chilton NF, Collison D, McInnes EJJ et al (2013) An electrostatic model for the determination of magnetic anisotropy in dysprosium complexes. *Nat Commun* 4:2551. doi:[10.1038/ncomms3551](https://doi.org/10.1038/ncomms3551)
17. Stevens KWH (1952) Matrix elements and operator equivalents connected with the magnetic properties of rare earth ions. *Proc Phys Soc A* 65:209–215
18. Sorace L, Benelli C, Gatteschi D (2011) Lanthanides in molecular magnetism: old tools in a new field. *Chem Soc Rev* 40(6):3092–3104. doi:[10.1039/C0CS00185F](https://doi.org/10.1039/C0CS00185F)

19. Fukuda T, Matsumura K, Ishikawa N (2013) Influence of intramolecular f-f interactions on nuclear spin driven quantum tunneling of magnetizations in quadruple-decker phthalocyanine complexes containing two terbium or dysprosium magnetic centers. *J Phys Chem A* 117(40):10447–10454. doi:[10.1021/jp406009m](https://doi.org/10.1021/jp406009m)
20. Liu J-L, Chen Y-C, Zheng Y-Z et al (2013) Switching the anisotropy barrier of a single-ion magnet by symmetry change from quasi-D_{5h} to quasi-O_h. *Chem Sci* 4(8):3310–3316. doi:[10.1039/c3sc50843a](https://doi.org/10.1039/c3sc50843a)
21. Caneschi A, Gatteschi D, Sessoli R et al (1991) Alternating current susceptibility, high field magnetization, and millimeter band EPR evidence for a ground S = 10 state in [Mn₁₂O₁₂(CH₃COO)₁₆(H₂O)₄·2CH₃COOH·4H₂O]. *J Am Chem Soc* 113(15):5873–5874. doi:[10.1021/ja00015a057](https://doi.org/10.1021/ja00015a057)
22. Sessoli R, Tsai HL, Schake AR et al (1993) High-spin molecules: [Mn₁₂O₁₂(O₂CR)₁₆(H₂O)₄]. *J Am Chem Soc* 115(5):1804–1816
23. Sessoli R, Gatteschi D, Caneschi A et al (1993) Magnetic bistability in a metal-ion cluster. *Nature* 365(6442):141–143. doi:[10.1038/365141a0](https://doi.org/10.1038/365141a0)
24. Aubin SMJ, Wemple MW, Adams DM et al (1996) Distorted Mn^{IV}Mn₃^{III} Cubane Complexes as Single-Molecule Magnets. *J Am Chem Soc* 118(33):7746–7754. doi:[10.1021/ja960970f](https://doi.org/10.1021/ja960970f)
25. Tasiopoulos AJ, Vinslava A, Wernsdorfer W et al (2004) Giant single-molecule magnets: a Mn₈₄ torus and its supramolecular nanotubes. *Angew Chem Int Ed* 116(16):2169–2173. doi:[10.1002/ange.200353352](https://doi.org/10.1002/ange.200353352)
26. Ako AM, Hewitt IJ, Mereacre V et al (2006) A ferromagnetically coupled Mn₁₉ aggregate with a record S = 83/2 ground spin state. *Angew Chem Int Ed* 118(30):5048–5051. doi:[10.1002/ange.200601467](https://doi.org/10.1002/ange.200601467)
27. Chakov NE, Lee S-C, Harter AG et al (2006) The properties of the [Mn₁₂O₁₂(O₂CR)₁₆(H₂O)₄] single-molecule magnets in truly axial symmetry: [Mn₁₂O₁₂(O₂CCH₂Br)₁₆(H₂O)₄]·4CH₂Cl₂. *J Am Chem Soc* 128(21):6975–6989. doi:[10.1021/ja060796n](https://doi.org/10.1021/ja060796n)
28. Sangregorio C, Ohm T, Paulsen C et al (1997) Quantum tunneling of the magnetization in an iron cluster nanomagnet. *Phys Rev Lett* 78(24):4645–4648
29. Oshio H, Hoshino N, Ito T et al (2004) Single-molecule magnets of ferrous cubes: structurally controlled magnetic anisotropy. *J Am Chem Soc* 126(28):8805–8812. doi:[10.1021/ja0487933](https://doi.org/10.1021/ja0487933)
30. Murrie M (2010) Cobalt(II) single-molecule magnets. *Chem Soc Rev* 39(6):1986–1995
31. Qian K, Huang X-C, Zhou C et al (2013) A single-molecule magnet based on heptacyanomolybdate with the highest energy barrier for a cyanide compound. *J Am Chem Soc* 135(36):13302–13305. doi:[10.1021/ja4067833](https://doi.org/10.1021/ja4067833)
32. Pointillart F, Bernot K, Sessoli R et al (2010) Field induced 4f-5d [Re(salen)]₂O₃ [Dy(hfac)₃(H₂O)]₂ single molecule magnet. *Inorg Chem* 49(9):4355–4361. doi:[10.1021/ic1003287](https://doi.org/10.1021/ic1003287)
33. Schelter EJ, Prosvirin AV, Dunbar KR (2004) Molecular cube of Re^{II} and Mn^{II} that exhibits single-molecule magnetism. *J Am Chem Soc* 126(46):15004–15005. doi:[10.1021/ja047088r](https://doi.org/10.1021/ja047088r)
34. Guo Y-N, Chen X-H, Xue S et al (2012) Molecular assembly and magnetic dynamics of two novel Dy₆ and Dy₈ aggregates. *Inorg Chem* 51(7):4035–4042. doi:[10.1021/ic202170z](https://doi.org/10.1021/ic202170z)
35. Guo Y-N, Ungur L, Granroth GE et al (2014) An NCN-pincer ligand dysprosium single-ion magnet showing magnetic relaxation via the second excited state. *Sci Rep* 4:5471. doi:[10.1038/srep05471](https://doi.org/10.1038/srep05471)
36. Rinehart JD, Fang M, Evans WJ et al (2011) A N₂³⁻ radical-bridged terbium complex exhibiting magnetic hysteresis at 14 K. *J Am Chem Soc* 133(36):14236–14239. doi:[10.1021/ja206286h](https://doi.org/10.1021/ja206286h)
37. Meihaus KR, Long JR (2013) Magnetic blocking at 10 K and a dipolar-mediated avalanche in salts of the Bis(η⁸-cyclooctatetraenide) complex [Er(COT)₂]⁻. *J Am Chem Soc* 135(47):17952–17957. doi:[10.1021/ja4094814](https://doi.org/10.1021/ja4094814)
38. Rinehart JD, Long JR (2009) Slow magnetic relaxation in a trigonal prismatic uranium(III) complex. *J Am Chem Soc* 131(35):12558–12559. doi:[10.1021/ja906012u](https://doi.org/10.1021/ja906012u)

39. Magnani N, Apostolidis C, Morgenstern A et al (2011) Magnetic memory effect in a transuranic mononuclear complex. *Angew Chem Int Ed* 50(7):1696–1698. doi:[10.1002/anie.201006619](https://doi.org/10.1002/anie.201006619)
40. Dei A, Gatteschi D (2011) Molecular (Nano) magnets as test grounds of quantum mechanics. *Angew Chem Int Ed* 50(50):11852–11858. doi:[10.1002/anie.201100818](https://doi.org/10.1002/anie.201100818)
41. Zadrozny JM, Xiao DJ, Atanasov M et al (2013) Magnetic blocking in a linear iron(I) complex. *Nat Chem* 5(7):577–581. doi:[10.1038/nchem.1630](https://doi.org/10.1038/nchem.1630)
42. Gatteschi D, Sessoli R, Vallain J (2006) *Molecular nanomagnets*. Oxford University Press, New York
43. Ishikawa N, Sugita M, Ishikawa T et al (2004) Mononuclear lanthanide complexes with a long magnetization relaxation time at high temperatures: a new category of magnets at the single-molecular level. *J Phys Chem B* 108(31):11265–11271. doi:[10.1021/jp0376065](https://doi.org/10.1021/jp0376065)
44. Jiang S-D, Wang B-W, Sun H-L et al (2011) An organometallic single-ion magnet. *J Am Chem Soc* 133(13):4730–4733. doi:[10.1021/ja200198v](https://doi.org/10.1021/ja200198v)
45. Guo Y-N, Xu G-F, Wernsdorfer W et al (2011) Strong axiality and Ising exchange interaction suppress zero-field tunneling of magnetization of an asymmetric Dy₂ single-molecule magnet. *J Am Chem Soc* 133(31):11948–11951. doi:[10.1021/ja205035g](https://doi.org/10.1021/ja205035g)
46. Rogez G, Donnio B, Terazzi E et al (2009) The quest for nanoscale magnets: the example of [Mn₁₂] single molecule magnets. *Adv Mater* 21(43):4323–4333. doi:[10.1002/adma.200803020](https://doi.org/10.1002/adma.200803020)
47. Ruiz E, Cirera J, Cano J et al (2008) Can large magnetic anisotropy and high spin really coexist? *Chem Commun* 1:52–54. doi:[10.1039/B714715E](https://doi.org/10.1039/B714715E)
48. Milios CJ, Vinslava A, Wernsdorfer W et al (2007) A record anisotropy barrier for a single-molecule magnet. *J Am Chem Soc* 129(10):2754–2755. doi:[10.1021/ja068961m](https://doi.org/10.1021/ja068961m)
49. Freedman DE, Harman WH, Harris TD et al (2010) Slow magnetic relaxation in a high-spin Iron(II) complex. *J Am Chem Soc* 132(4):1224–1225. doi:[10.1021/ja909560d](https://doi.org/10.1021/ja909560d)
50. Harman WH, Harris TD, Freedman DE et al (2010) Slow magnetic relaxation in a family of trigonal pyramidal iron(II) pyrrolide complexes. *J Am Chem Soc* 132(51):18115–18126. doi:[10.1021/ja105291x](https://doi.org/10.1021/ja105291x)
51. Zadrozny JM, Long JR (2011) Slow magnetic relaxation at zero field in the tetrahedral complex [Co(SPh)₄]²⁻. *J Am Chem Soc* 133(51):20732–20734. doi:[10.1021/ja2100142](https://doi.org/10.1021/ja2100142)
52. Zadrozny JM, Atanasov M, Bryan AM et al (2013) Slow magnetization dynamics in a series of two-coordinate iron(II) complexes. *Chem Sci* 4(1):125–138. doi:[10.1039/c2sc20801f](https://doi.org/10.1039/c2sc20801f)
53. Ishikawa N, Sugita M, Tanaka N et al (2004) Upward temperature shift of the intrinsic phase lag of the magnetization of bis(phthalocyaninato)terbium by ligand oxidation creating an S = 1/2 spin. *Inorg Chem* 43(18):5498–5500. doi:[10.1021/ic049348b](https://doi.org/10.1021/ic049348b)
54. Takamatsu S, Ishikawa T, Koshihara S et al (2007) Significant increase of the barrier energy for magnetization reversal of a single-4f-ionic single-molecule magnet by a longitudinal contraction of the coordination space. *Inorg Chem* 46(18):7250–7252. doi:[10.1021/ic700954t](https://doi.org/10.1021/ic700954t)
55. Ishikawa N, Mizuno Y, Takamatsu S et al (2008) Effects of chemically induced contraction of a coordination polyhedron on the dynamical magnetism of bis(phthalocyaninato)disprosium, a single-4f-ionic single-molecule magnet with a kramers ground state. *Inorg Chem* 47(22):10217–10219. doi:[10.1021/ic8014892](https://doi.org/10.1021/ic8014892)
56. Ganivet CR, Ballesteros B, de la Torre G et al (2013) Influence of peripheral substitution on the magnetic behavior of single-ion magnets based on homo- and heteroleptic Tb^{III} bis(phthalocyaninate). *Chem Eur J* 19(4):1457–1465. doi:[10.1002/chem.201202600](https://doi.org/10.1002/chem.201202600)
57. Ishikawa N, Otsuka S, Kaizu Y (2005) The effect of the f-f interaction on the dynamic magnetism of a coupled 4f⁸ system in a dinuclear terbium complex with phthalocyanines. *Angew Chem Int Ed* 44(5):731–733. doi:[10.1002/anie.200461546](https://doi.org/10.1002/anie.200461546)
58. AlDamen MA, Clemente-Juan JM, Coronado E et al (2008) Mononuclear lanthanide single-molecule magnets based on polyoxometalates. *J Am Chem Soc* 130(28):8874–8875. doi:[10.1021/ja801659m](https://doi.org/10.1021/ja801659m)

59. Jiang SD, Wang BW, Su G et al (2010) A mononuclear dysprosium complex featuring single-molecule-magnet behavior. *Angew Chem Int Ed* 7448–7451. doi:[10.1002/anie.201004027](https://doi.org/10.1002/anie.201004027)
60. Chen G-J, Guo Y-N, Tian J-L et al (2012) Enhancing anisotropy barriers of dysprosium(III) single-ion magnets. *Chem Eur J* 18(9):2484–2487. doi:[10.1002/chem.201103816](https://doi.org/10.1002/chem.201103816)
61. Bi Y, Guo Y-N, Zhao L et al (2011) Capping ligand perturbed slow magnetic relaxation in dysprosium single-ion magnets. *Chem Eur J* 17(44):12476–12481. doi:[10.1002/chem.201101838](https://doi.org/10.1002/chem.201101838)
62. Chen G-J, Gao C-Y, Tian J-L et al (2011) Coordination-perturbed single-molecule magnet behaviour of mononuclear dysprosium complexes. *Dalton Trans* 40:5579–5583
63. Le Roy JJ, Korobkov I, Murugesu M (2014) A sandwich complex with axial symmetry for harnessing the anisotropy in a prolate erbium(III) ion. *Chem Commun* 50(13):1602–1604. doi:[10.1039/c3cc48557a](https://doi.org/10.1039/c3cc48557a)
64. Watanabe A, Yamashita A, Nakano M et al (2011) Multi-path magnetic relaxation of mono-dysprosium(III) single-molecule magnet with extremely high barrier. *Chem Eur J* 17(27):7428–7432. doi:[10.1002/chem.201003538](https://doi.org/10.1002/chem.201003538)
65. Tang J, Hewitt I, Madhu NT et al (2006) Dysprosium triangles showing single-molecule magnet behavior of thermally excited spin states. *Angew Chem Int Ed* 45(11):1729–1733. doi:[10.1002/anie.200503564](https://doi.org/10.1002/anie.200503564)
66. Lin P-H, Burchell TJ, Clérac R et al (2008) Dinuclear dysprosium(III) single-molecule magnets with a large anisotropic barrier. *Angew Chem Int Ed* 47(46):8848–8851. doi:[10.1002/anie.200802966](https://doi.org/10.1002/anie.200802966)
67. Lin P-H, Burchell TJ, Ungur L et al (2009) A polynuclear lanthanide single-molecule magnet with a record anisotropic barrier. *Angew Chem Int Ed* 48(50):9489–9492. doi:[10.1002/anie.200903199](https://doi.org/10.1002/anie.200903199)
68. Guo Y-N, Xu G-F, Gamez P et al (2010) Two-step relaxation in a linear tetranuclear dysprosium(III) aggregate showing single-molecule magnet behavior. *J Am Chem Soc* 132(25):8538–8539. doi:[10.1021/ja103018m](https://doi.org/10.1021/ja103018m)
69. Hewitt IJ, Tang J, Madhu NT et al (2010) Coupling Dy₃ triangles enhances their slow magnetic relaxation. *Angew Chem Int Ed* 49(36):6352–6356. doi:[10.1002/anie.201002691](https://doi.org/10.1002/anie.201002691)
70. Blagg RJ, Muryn CA, McInnes EJJ et al (2011) Single pyramid magnets: Dy₅ pyramids with slow magnetic relaxation to 40 K. *Angew Chem Int Ed* 50(29):6530–6533. doi:[10.1002/anie.201101932](https://doi.org/10.1002/anie.201101932)
71. Rinehart JD, Fang M, Evans WJ et al (2011) Strong exchange and magnetic blocking in N₂³⁻-radical-bridged lanthanide complexes. *Nat Chem* 3(7):538–542. doi:[10.1038/nchem.1063](https://doi.org/10.1038/nchem.1063)
72. Demir S, Zadrozny JM, Nippe M et al (2012) Exchange coupling and magnetic blocking in bipyrimidyl radical-bridged dilanthanide complexes. *J Am Chem Soc* 134(45):18546–18549. doi:[10.1021/ja308945d](https://doi.org/10.1021/ja308945d)
73. Tuna F, Smith CA, Bodensteiner M et al (2012) A high anisotropy barrier in a sulfur-bridged organodysprosium single-molecule magnet. *Angew Chem Int Ed* 51(28):6976–6980. doi:[10.1002/anie.201202497](https://doi.org/10.1002/anie.201202497)
74. Blagg RJ, Ungur L, Tuna F et al (2013) Magnetic relaxation pathways in lanthanide single-molecule magnets. *Nat Chem* 5(8):673–678. doi:[10.1038/nchem.1707](https://doi.org/10.1038/nchem.1707)
75. Ungur L, Le Roy JJ, Korobkov I et al (2014) fine-tuning the local symmetry to attain record blocking temperature and magnetic remanence in a single-ion magnet. *Angew Chem Int Ed* 53(17):4413–4417. doi:[10.1002/anie.201310451](https://doi.org/10.1002/anie.201310451)
76. Ungur L, Chibotaru LF (2011) Magnetic anisotropy in the excited states of low symmetry lanthanide complexes. *Phys Chem Chem Phys* 13(45):20086–20090. doi:[10.1039/C1CP22689D](https://doi.org/10.1039/C1CP22689D)
77. Haase W, Wróbel S (2003) *Relaxation phenomena*. Springer, Germany
78. Casimir HBG, du Pré FK (1938) Note on the thermodynamic interpretation of paramagnetic relaxation phenomena. *Physica* 5(6):507–511. doi:[10.1016/S0031-8914\(38\)80164-6](https://doi.org/10.1016/S0031-8914(38)80164-6)

79. Guo Y-N, Xu G-F, Guo Y et al (2011) Relaxation dynamics of dysprosium(III) single molecule magnets. *Dalton Trans* 40(39):9953–9963. doi:[10.1039/C1DT10474H](https://doi.org/10.1039/C1DT10474H)
80. Cole KS, Cole RH (1941) Dispersion and absorption in dielectrics I. Alternating current characteristics. *J Chem Phys* 9(4):341–351. doi:[10.1063/1.1750906](https://doi.org/10.1063/1.1750906)
81. Dekker C, Arts AFM, de Wijn HW et al (1989) Activated dynamics in a two-dimensional Ising spin glass: $\text{Rb}_2\text{Cu}_{1-x}\text{Co}_x\text{F}_4$. *Phys Rev B* 40(16):11243–11251. doi:[10.1103/PhysRevB.40.11243](https://doi.org/10.1103/PhysRevB.40.11243)
82. Van Vleck JH (1940) Paramagnetic relaxation times for titanium and chrome alum. *Phys Rev* 57(5):426–447. doi:[10.1103/PhysRev.57.426](https://doi.org/10.1103/PhysRev.57.426)
83. Shrivastava KN (1983) Theory of spin–lattice relaxation. *Phys Stat Sol (b)* 117(2):437–458. doi:[10.1002/pssb.2221170202](https://doi.org/10.1002/pssb.2221170202)
84. Abragam A, Bleaney B (1970) *Electron paramagnetic resonance of transition ions*. Clarendon Press, Oxford
85. Waller I, Zeits F (1932) *Physik* 79:370
86. de Kronig RL (1939) On the mechanism of paramagnetic relaxation. *Physica* 6(1):33–43. doi:[10.1016/S0031-8914\(39\)90282-X](https://doi.org/10.1016/S0031-8914(39)90282-X)
87. Finn CBP, Orbach R, Wolf WP (1961) Spin-lattice relaxation in cerium magnesium nitrate at liquid helium temperature: a new process. *Proc Phys Soc* 77:261–268. doi:[10.1088/0370-1328/77/2/305](https://doi.org/10.1088/0370-1328/77/2/305)
88. Carlin RL (1986) *Magnetochemistry*. Springer, Berlin
89. Ishikawa N, Sugita M, Wernsdorfer W (2005) Quantum tunneling of magnetization in lanthanide single-molecule magnets: bis(phthalocyaninato)terbium and bis(phthalocyaninato) dysprosium anions. *Angew Chem Int Ed* 44(19):2931–2935. doi:[10.1002/anie.200462638](https://doi.org/10.1002/anie.200462638)
90. Gatteschi D, Sessoli R (2003) Quantum tunneling of magnetization and related phenomena in molecular materials. *Angew Chem Int Ed* 42(3):268–297. doi:[10.1002/anie.200390099](https://doi.org/10.1002/anie.200390099)
91. Cucinotta G, Perfetti M, Luzon J et al (2012) Magnetic anisotropy in a dysprosium/DOTA single-molecule magnet: beyond simple magneto-structural correlations. *Angew Chem Int Ed* 51(7):1606–1610. doi:[10.1002/anie.201107453](https://doi.org/10.1002/anie.201107453)
92. Boulon M-E, Cucinotta G, Luzon J et al (2013) Magnetic anisotropy and spin-parity effect along the series of lanthanide complexes with DOTA. *Angew Chem Int Ed* 52(1):350–354. doi:[10.1002/anie.201205938](https://doi.org/10.1002/anie.201205938)
93. Habib F, Lin P-H, Long J et al (2011) The use of magnetic dilution to elucidate the slow magnetic relaxation effects of a Dy_2 single-molecule magnet. *J Am Chem Soc* 133(23):8830–8833. doi:[10.1021/ja2017009](https://doi.org/10.1021/ja2017009)
94. Luzon J, Bernot K, Hewitt IJ et al (2008) Spin chirality in a molecular dysprosium triangle: the archetype of the noncollinear ising model. *Phys Rev Lett* 100(24):247205. doi:[10.1103/PhysRevLett.100.247205](https://doi.org/10.1103/PhysRevLett.100.247205)
95. Salman Z, Giblin SR, Lan Y et al (2010) Probing the magnetic ground state of the molecular dysprosium triangle with muon spin relaxation. *Phys Rev B* 82(17):174427. doi:[10.1103/PhysRevB.82.174427](https://doi.org/10.1103/PhysRevB.82.174427)
96. Bernot K, Luzon J, Bogani L et al (2009) Magnetic anisotropy of dysprosium(III) in a low-symmetry environment: a theoretical and experimental investigation. *J Am Chem Soc* 131(15):5573–5579. doi:[10.1021/ja8100038](https://doi.org/10.1021/ja8100038)
97. Chibotaru LF, Ungur L (2012) Ab initio calculation of anisotropic magnetic properties of complexes. I. Unique definition of pseudospin Hamiltonians and their derivation. *J Chem Phys* 137(6):064112–064122. doi:[10.1063/1.4739763](https://doi.org/10.1063/1.4739763)
98. Figgis BN, Gerloch M, Mason R (1964) The paramagnetic anisotropies and ligand fields of the tetrahedral cobaltous chlorides and thiocyanate. *Proc R Soc Lond A* 279(1377):210–228. doi:[10.1098/rspa.1964.0099](https://doi.org/10.1098/rspa.1964.0099)
99. Gregson AK, Mitra S (1968) Magnetic susceptibility, anisotropy, and ESR studies on some copper dialkyldithiocarbamates. *J Chem Phys* 49(8):3696–3703. doi:[10.1063/1.1670654](https://doi.org/10.1063/1.1670654)
100. Jiang S-D, Wang B-W, Gao S (2014) Advances in lanthanide single-ion magnets. In: *Structure and bonding*. Springer, Berlin, pp 1–31. doi:[10.1007/430_2014_153](https://doi.org/10.1007/430_2014_153)

101. Boulon M-E, Cucinotta G, Liu S-S et al (2013) Angular-resolved magnetometry beyond triclinic crystals: out-of-equilibrium studies of Cp*ErCOT single-molecule magnet. *Chem Eur J* 19(41):13726–13731. doi:[10.1002/chem.201302600](https://doi.org/10.1002/chem.201302600)
102. Layfield RA, McDouall JJW, Sulway SA et al (2010) Influence of the N-bridging ligand on magnetic relaxation in an organometallic dysprosium single-molecule magnet. *Chem Eur J* 16(15):4442–4446. doi:[10.1002/chem.201000158](https://doi.org/10.1002/chem.201000158)
103. Long J, Habib F, Lin P-H et al (2011) Single-molecule magnet behavior for an antiferromagnetically superexchange-coupled dinuclear dysprosium(III) complex. *J Am Chem Soc* 133(14):5319–5328. doi:[10.1021/ja109706y](https://doi.org/10.1021/ja109706y)
104. Griffith JS (1963) Spin Hamiltonian for even-electron systems having even multiplicity. *Phys Rev* 132(1):316–319. doi:[10.1103/PhysRev.132.316](https://doi.org/10.1103/PhysRev.132.316)
105. Ungur L, Thewissen M, Costes J-P et al (2013) Interplay of strongly anisotropic metal ions in magnetic blocking of complexes. *Inorg Chem* 52(11):6328–6337. doi:[10.1021/ic302568x](https://doi.org/10.1021/ic302568x)

Chapter 2

Lanthanide Single-Ion Molecular Magnets

Abstract The most important lanthanide single-ion molecular magnets (SIMMs) reported to date including the lanthanide phthalocyanine, lanthanide β -diketone, and organometallic lanthanide systems are systematically investigated in this chapter. In particular, some important relationships between the structural features and magnetic performances are discussed in detail based on the theoretical results, presenting a guideline for the effective design of lanthanide SIMMs.

Keywords Single-ion molecular magnet · Quantum tunneling · Uniaxial anisotropy · Phthalocyanine · β -diketone · Organometallic

Over the past few years, molecular magnetic materials have flourished and ranged from the pioneering 2D/3D magnetic networks [1, 2] to 1D single-chain magnets (SCMs) [3, 4], 0D polynuclear metal [5] and metal-radical [6, 7] SMMs, and finally the smallest magnet-like molecules including only one single magnetic ion usually called single-ion magnet (SIM) [8–10]. In particular, the development of the latter class of molecules, i.e., SIMs, has been one of the hottest topics in SMM research in recent years, the reason for which is that their simple structure compared with polynuclear complexes allows us to have a better understanding for the correlation between structures and magnetic properties and further to fine-tune their SMM properties [10]. As mentioned in Chap. 1, to avoid misleading the readers from other research fields, we use the term single-ion molecular magnet (SIMM) in the following sections. The first example of such nanomagnets was reported by Ishikawa et al. in 2003 in a family of complexes of general formula $[\text{LnPc}_2]^-$ with a “double-decker” structure [11], where the Tb species demonstrates a high effective barrier, $U_{\text{eff}} = 230 \text{ cm}^{-1}$, far surpassing that of Mn_{12} SMM. This discovery further stimulated the successful design of a growing number of lanthanide SIMM systems, the most typical examples being lanthanide polyoxymetalates (LnPOM) [12], lanthanide β -diketone [8, 13], and organometallic double-decker [9, 14] lanthanide complexes. It is noteworthy that, recently, the SIMM family has been extended into the mononuclear *d*-transition metal [15–17]

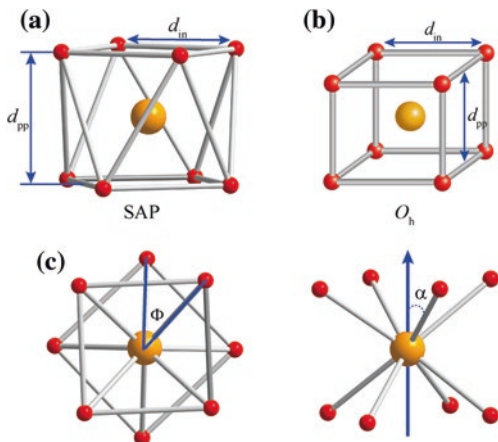
and actinoid [18, 19] complexes with several successful examples being achieved. Nevertheless, to date it is still heavily dominated by lanthanide-based SIMMs, where not only the complexes with high axial symmetry behave as the effective SMMs [11, 20, 21], but also the magnetic relaxation behavior can be observed in some low-symmetry lanthanide complexes [9, 22], mainly because the strong internal single-ion anisotropy of lanthanide ion arising from the large unquenched orbital angular moments greatly facilitates the design of SIMMs, while the subordination of the crystal field to the spin–orbit interaction makes it a minor factor in the overall electronic structure [23]. However, our goal is not to simply synthesize such magnetic molecules, but to achieve a SMM with high effective barrier and blocking temperature and retain its functionality in a more readily accessed temperature regime. Therefore, the role of crystal field must be highlighted, because a suitable crystal field is of critical importance in producing the electronic structure requisite for strong single-molecule magnets, which can be seen in the simple model developed by Long in Chap. 1 [23]. In particular, the effect is very sensitive in SIMMs, where a minor structural alteration may lead to drastic effects on the magnetism. For example, *ab initio* calculations show that the changes of the coordinated water molecule—removal of the water molecule and the positioning of hydrogen atoms—have great impact on the orientation of the anisotropy axis in Dy-DOTA complex [24, 25]. In addition, the impact of ligand donor strength within a given coordination geometry was also explored recently by Long through comparing two isostructural trigonal prismatic complexes with pyrazolate and N-heterocyclic carbene ligands, respectively [26]. The results reveal that, like molecular symmetry, ligand-donating ability is a variable that can be controlled to the advantage of the synthetic chemist in the design of SMMs with enhanced relaxation barriers. As a result, it is of vital importance to fine-tune the interaction between the single-ion electron density and the crystal field environment to make the magnetic moment of individual ion in a SIMM to be blocked as efficient as possible [23]. In this chapter, we focus on the synthetic strategies developed from the synthetic chemists providing a tailored chemical environment to modify the crystal field around lanthanide ion and the theoretical interpretations for magnetism from theoreticians, aiming at better guiding the SIMM design and finally obtaining highly effective SMMs.

2.1 Single-Ion Anisotropy and QTM

In SIMMs where magnetic exchange interactions are absent, the uniaxial anisotropy requisite for strong SMM behavior is mainly deriving from two aspects, one being single-ion contribution from unquenched first-order orbital moments and the other being crystal field contribution. In contrast to transition metal ions, a preeminent feature of lanthanide ions in the design of SIMM is their inherent strong single-ion contribution to anisotropy from the unquenched orbital moments and strong spin–orbital coupling interactions [27, 28], which provide a foundation to

achieve a strongly uniaxial anisotropy necessary for the magnetic moment of individual ions in molecule to be blocked. Further, crystal field turns out to be more crucial factor in making the best of the inherent anisotropy to obtain a robust SMM [23]. As stated in the model of J.R. Long in Chap. 1, a suitable crystal field can effectively enhance the single-ion anisotropy of lanthanide ions and further stabilize the high-magnitude m_j as ground state, which provides the underlying conditions to achieve a SMM. Here, a great number of the reported lanthanide SIMMs have indicated that it is easy to obtain a SIMM using a lanthanide ion, especially the Dy ion whose large magnetic moment and odd-electron configuration make it the most prolific lanthanide ions to date [29]. Nevertheless, it must be stressed that the fast QTM under zero-dc field occurs in most lanthanide SIMMs, especially in the low-symmetry complexes, as evidenced by the butterfly-shaped magnetic hysteresis and the rapidly increasing χ'' components with the decreasing of temperature in χ'' versus T plots [8, 13]. The presence of such fast QTM is very unfavorable to enhancing their SMM properties and the coercive fields (H_c) in the hysteresis loops denoting the strength of a magnet can be significantly reduced [20]. The transversal anisotropic components (g_x, g_y) in Kramers ions or the intrinsic tunneling gap (Δ_{tun}) in non-Kramers ions is the main factor that induces QTM and is extremely sensitive to the asymmetric factors in the structure of mononuclear complexes [30]. In addition, the intermolecular magnetic interactions and the hyperfine interactions between the electron and nuclear spins are also important sources of QTM in lanthanide SIMMs [11, 31]. To suppress the QTM, a series of measures can be adopted, such as applying a dc magnetic field on samples [8], measuring the dynamic properties of frozen solution [32], and magnetic dilution, but the most important is to modify the local crystal field around the lanthanide ions to improve single-ion anisotropy while reducing the g_x and g_y or Δ_{tun} . Here, an important superiority of mononuclear lanthanide magnets is their tenability [33], which allows for increased control over crystal field, and therefore magnetic properties, when compared to multinuclear species. Therefore, alongside the remarkable synthetic and theoretical progresses has come the development of several ways of achieving a high degree of axiality of single-ion anisotropy. One way is to achieve only one very strong chemical bond with the metal ion, which dominates over all other chemical bonds of the metal site, leading to the intrinsically axial nature of the total ligand field felt by the metal center [20]. To date, only a handful of such examples were discovered, but showing the strongly blocking of magnetization. Typically, the DyNCN complex mentioned in Chap. 1 exhibits the high U_{eff} for the reorientation of the magnetic moment and the particular relaxation path via the second excited state [34], which is still fairly sparse in lanthanide SIMMs. The more conventional route for obtaining the strong single-ion anisotropy is to modify the coordination geometry to reach as perfect an axial symmetry as possible, which is very important in reducing the possible mixing of the m_j levels, further confirming a pure high- m_j state as ground state [35]. Here, according to strict group-theoretical rules, an ideal axial symmetry can be achieved in point groups $C_{\infty v}$, $D_{\infty h}$, S_8 , D_{4d} , D_{5h} , D_{6d} , which show the vanishing off-diagonal crystal field parameters B_k^q ($q \neq 0$) responsible for generating the mixing m_j levels [36].

Fig. 2.1 Schematic structures of SAP (a) and cubic (b) geometries. (c) The relevant angular parameters in SAP geometry: Φ , the angle between the diagonals of the two squares (*skew angle*); α , the angle between the C_4 axis and a RE–L direction

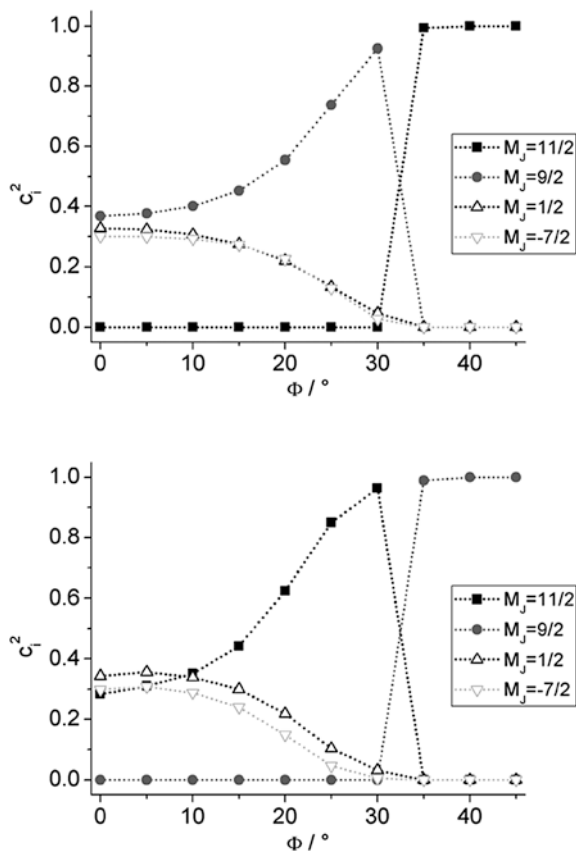


In fact, a great number of SIMM examples with such coordination geometries have been reported, showing very high energy barriers. Here, we take the example of the well-known square antiprismatic (SAP) geometry (D_{4d}), highlighting the key geometrical parameters in the definition of the electronic structure of the metal ion [35, 37], which directly affect the SMM performance.

The SAP geometry has been shown in Fig. 2.1 with several important parameters being labeled. The relevant geometrical parameters are d_{pp} , the distance between the L4 squares; d_{in} , the shorter L–L distance in the L4 square; Φ , the angle between the diagonals of the two squares (*skew angle*); and α , the angle between the C_4 axis and a RE–L direction. Eight identical RE–L distances define the highest symmetry D_{4d} corresponding to $d_{pp} = d_{in}$, $\Phi = 45^\circ$ and $\alpha = 54.74^\circ$, i.e., an axially non-distorted antiprism. Here, the D_{4d} symmetry ($\Phi = 45^\circ$) is taken as a distorted case of the O_h symmetry ($\Phi = 0^\circ$) when the two squares are staggered (Fig. 2.1). The deviation of Φ from 45° will result in the disappearance of D_{4d} symmetry, thus leading to the presence of nonzero B_4^4 and B_6^4 crystal parameters and further an extensive mixing of functions with different m_j values, which are of fundamental importance to promote the quantum tunneling of the magnetization in these systems. The simple calculations performed by D. Gatteschi demonstrate the great impact of a variation of angle Φ on the electronic structure of metal ions due to the introduction of nonzero B_4^4 and B_6^4 , as shown in Fig. 2.2, where the first excited state at $\Phi = 45^\circ$ for the SAP becomes the ground state for distortions of about 15° from pure SAP geometry [35]. The effects are well present in a series of lanthanide β -diketone SMMs showing the enhanced QTM with the deviation of Φ , which will be introduced in the below sections.

Another important factor of affecting the electronic structures of metal ions is the effect of the compression/elongation along the C_4 axis associated with α . Wider α angle corresponds to compression ($\alpha > 54.74^\circ$) and smaller to elongation ($\alpha < 54.74^\circ$) along the tetragonal axis. The main qualitative difference in the calculated parameters is the change of B_2^0 sign on passing from compressed

Fig. 2.2 Variation of the composition of the ground (*top*) and first excited (*bottom*) states on passing from a cube to a square antiprism, calculated by Gatteschi group on the basis of the AOM parameters. Reproduced from Ref. [35] by permission of The Royal Society of Chemistry



to elongated SAP for a given lanthanide ion. For α_J -negative lanthanide ions, Tb^{III} , Dy^{III} , Ho^{III} , Pr^{III} , and Nd^{III} , the B_2^0 sign will change from negative to positive with the variation from elongated to compressed SAP, while the reverse trend is observed in the α_J -positive lanthanide ions, Er^{III} , Tm^{III} , and Yb^{III} , as seen in Fig. 2.3 ($B_2^0 \sim \alpha_J B_0^2$, $\alpha_J < 0$ for Tb^{III} , Dy^{III} et al., while $\alpha_J > 0$ for Er^{III} , Tm^{III} et al.) [38]. Here to achieve a strong SMM, a negative uniaxial anisotropy associated with negative B_2^0 parameters is required to stabilize a high- m_J ground-state doublet. Therefore, the elongated SAP is much more favorable for Dy ion in the design of SMM, and the opposite for Er ion, which is consistent with the real case present in $[\text{LnPc}_2]$ and LnPOM systems.

In this section, we have discussed how to suppress the QTM through enhancing the single-ion anisotropy of lanthanide ions and further take the example of the well-known SAP geometry to show how to fine-tune the local geometry around lanthanide ions favorable for the strong SMM behavior. The following sections focus on the typical lanthanide SIMM systems discovered to date, highlighting their tunability through tailoring their organic ligands, which allows for increased control over structure and therefore magnetic properties.

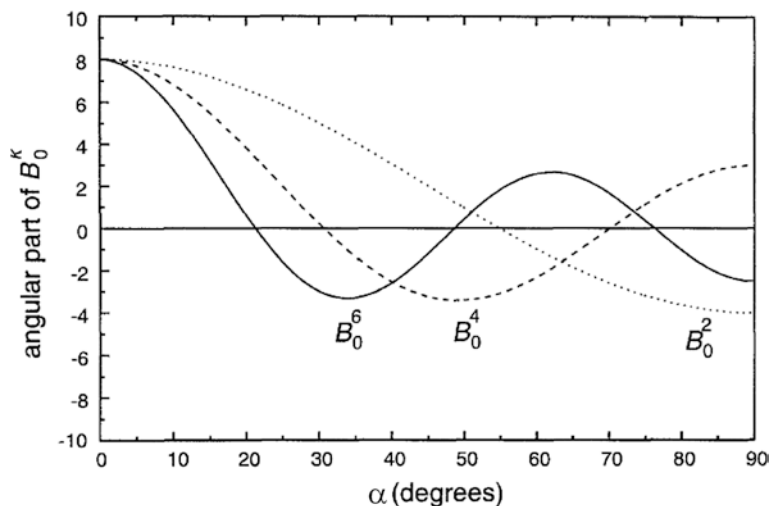


Fig. 2.3 Angular α -dependence of the B_0^k crystal field parameters in a D_{4h} symmetry. It should be noted that the parameter B_0^k in this figure is different from the B_k^0 in the text which contains B_0^k and Stevens equivalent coefficients. Reprinted from Ref. [38]. Copyright 1996, with permission from Elsevier

2.2 [LnPc₂] and LnPOM SIMMs

As seen in Fig. 2.4, both phthalocyanine (Pc) and polyoxometalates (POM) [39] ligands demonstrate the high local symmetry and the rigid characteristic with the coplanar coordinate atoms, which are favorable for the assembly of double-decker sandwich geometry with lanthanide ions ([LnPc₂]). In general, the two coordinate planes are staggered rather than eclipsed, leading to the typical SAP geometry (Fig. 2.1), which thus seems to be very helpful for the design with enhanced SMM properties. In particular, the tunability of substituent groups of Pc ligand (Fig. 2.5) and its redox ability enable us to easily optimize the coordination geometry around lanthanide ions to enhance the single-ion anisotropy as efficient as possible.

2.2.1 Phthalocyanine-Type Ligands and the [LnPc₂] Structure

The phthalocyanine contains four isoindole nitrogen atoms, showing two-dimensional π -conjugated planar structure, which are able to complex with a range of metal ions from transition metal to lanthanide ions [40]. Here, the ionic size and

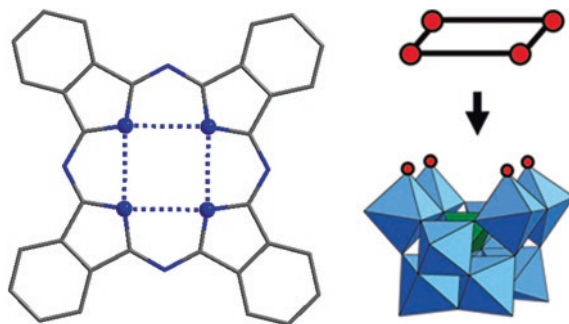


Fig. 2.4 The coplanar coordinate atoms of phthalocyanine (Pc) and polyoxometalates (POM) ligands. Reprinted with the permission from Ref. [39]. Copyright 2010 American Chemical Society

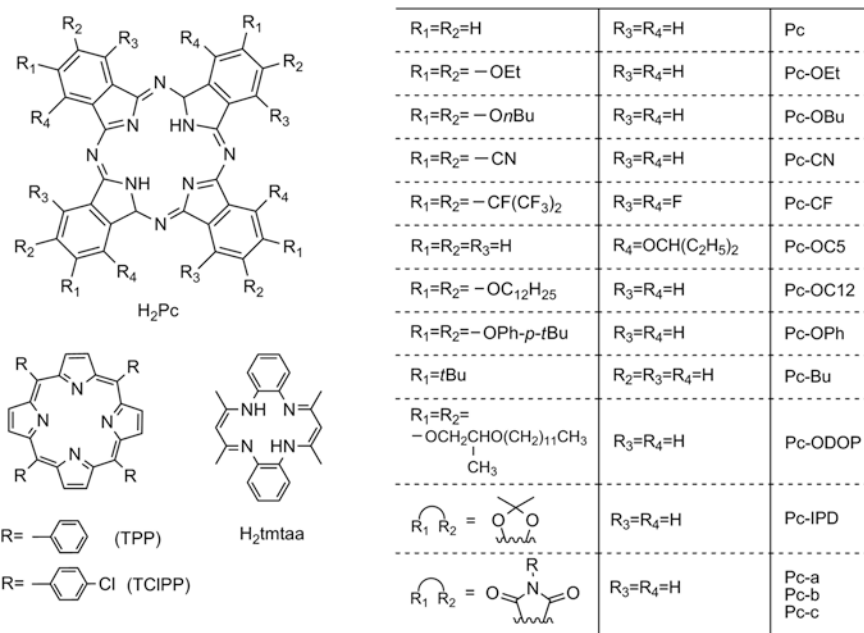
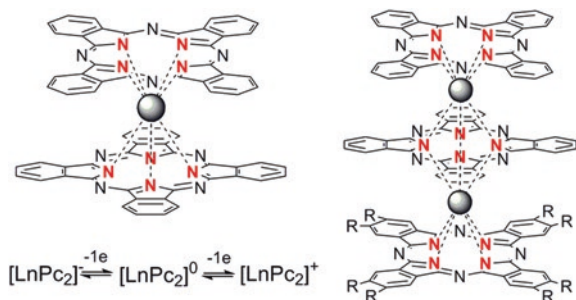


Fig. 2.5 Phthalocyanine (Pc) ligands with different substituent groups and the ligands showing the similar structure to Pc ligand used in lanthanide SIMMs

valence of metal ion is a critical factor in determining the structure of coordinate complexes. Pc and divalent *3d* transition metal ion such as Mn^{2+} , Fe^{2+} , Ni^{2+} , and Cu^{2+} can form planar molecules with no axial ligand [41], while the double-decker and even triple-decker sandwich-type structures (Fig. 2.6) are supported in the lanthanide phthalocyanine complexes with the increasing ion radius. It is noteworthy that various crystalline forms of bis(phthalocyaninato) lanthanide

Fig. 2.6 Schematic structures of double-decker and triple-decker sandwich-type structures with Pc ligands

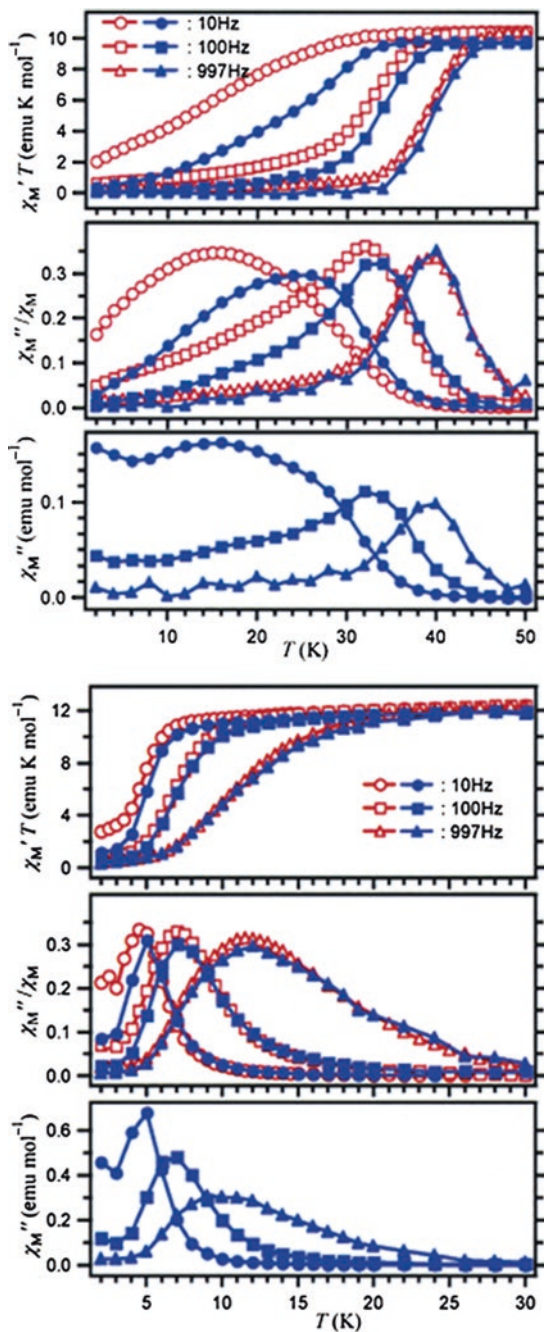


double-decker complexes including neutral, cationic, and anionic species can be obtained by controlling a redox reaction on the ligand side (Fig. 2.6), which thus allow us to better modulate the electronic structure of the complex and further control their dynamic magnetism without introducing any additional magnetic site or spin system [42]. Importantly, a great number of phthalocyanine derivatives are obtained through substituting some or all of the hydrogen atom(s) of the benzene rings, as seen in Fig. 2.5. The various modifications of substituent groups in Pc ligand provide a good condition for exploring the relaxation dynamics of different $[LnPc_2]$ species and isolating lanthanide SMM with high effective barrier.

2.2.2 The Magnetism of Seminal $[LnPc_2]^- \cdot TBA^+$

The early research interest of lanthanide phthalocyanine complexes can date back to 1960s [40], but the exploration for their SMM properties was just started in 2003 [11], when Ishikawa firstly demonstrated phthalocyanine Tb^{III} and Dy^{III} complexes functioning as magnets at the single-molecular level. Their structures have been well established by the prior investigations, showing an elongated SAP with $d_{pp} > d_{in}$ [43]. Importantly, the consistent binding mode of the phthalocyanine macrocycles to lanthanide metal center leads to the very small deviation from the SAP symmetry in the first coordination sphere for the late lanthanide ions with smaller ion radii. Such a high symmetry SAP is favorable of an isolated ground-state doublet with the large m_J value well separated in energy from the first excited state, necessary for achieving a high-performance SMM, for the lanthanide ions with oblate electron density such as Tb^{III} , Dy^{III} , and Ho^{III} in spite of the non-Kramers ion properties of Tb^{III} and Ho^{III} ions. Figure 2.7 shows ac magnetic susceptibilities as a function of temperature of polycrystalline powder sample of $[LnPc_2]^- \cdot TBA^+$ ($Ln = Tb^{III}$ and Dy^{III} , $TBA^+ = (C_4H_9)_4N^+$) [11]. The maximum of χ''/χ_{dc} , typical feature of SMM behavior, was observed at 15, 32, and 40 K with ac frequency of 10, 100, and 997 Hz, respectively, for undiluted Tb complex. In the diluted samples in diamagnetic $[YPc_2]^- \cdot TBA^+$, the shifts to

Fig. 2.7 The ac susceptibility data of Tb (*top*) and Dy (*bottom*) complexes in [LnPc₂]⁻·TBA⁺, with the open marks for the undiluted samples and the filled marks for the diluted samples. Reprinted with the permission from Ref. [11]. Copyright 2003 American Chemical Society



higher temperature of χ''/χ_{dc} peaks clearly indicate that slow relaxation of magnetization is single-molecule origin. In addition, it is remarkable that the Tb^{III} complex demonstrates the higher blocking temperature than Dy^{III} analogue, as seen in Fig. 2.7, which could be directly associated with their distinct electronic sublevel structures of the ground-state multiplets of the complexes discussed in the following sections.

For lanthanide phthalocyanine complexes, the fluorescence and absorption spectra associated with lanthanide centers are unavailable in obtaining the sublevel structures of the ground-state multiplet, because the low-lying Pc-centered energy levels quench the lanthanide fluorescence and the extremely intense Pc-centered absorption bands conceal the lanthanide-centered bands. In 2003, Ishikawa et al. determined their sublevel structures using a simultaneous fitting of paramagnetic NMR shifts and magnetic susceptibility data by the set of LF parameters from a multidimensional nonlinear minimization algorithm. Figure 2.8 shows the theoretical and observed $\chi_m T$ values and paramagnetic shifts ($\Delta\delta$) of the ¹H NMR signal, and substructures of the ground multiplets [44]. Here, the energy diagram for the ground multiplets (Fig. 2.8c) reveals that the Tb^{III}, Dy^{III}, and Ho^{III} complexes possess the well-isolated ground-state doublet with large m_J values, which are favorable of the presence of their SMM behaviors. In particular, the Tb complex shows the ground state with largest m_J values and a separation of more than 400 cm⁻¹

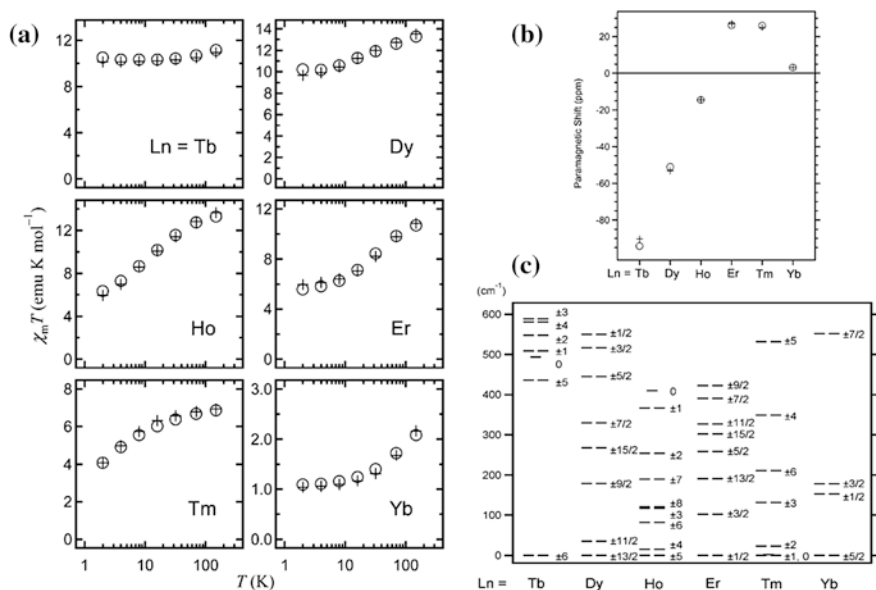


Fig. 2.8 **a** The comparisons of theoretical and experimental temperature dependence of the $\chi_m T$ values. **b** The theoretical and experimental paramagnetic shifts of the ¹H NMR signal of the α -proton on the Pc ligands. **c** The obtained energy diagram for the ground-state multiplets. Reprinted with the permission from Ref. [44]. Copyright 2003 American Chemical Society

between the ground state and the first excited state, which are well in agreement with its very high effective barrier of 230 cm⁻¹ surpassing several times of that of Mn₁₂ SMM. In the Dy complex, the ground state shows the quantum number of $m_J = \pm 13/2$ larger than that of the first excited state ($m_J = \pm 11/2$), still suggesting the strong Ising-type anisotropy, even though the doublet substates with the largest m_J do not lie in the lowest state. Here, the separation of 35 cm⁻¹ between the ground state and the first excited state is close to the effective energy barrier (28 cm⁻¹) determined experimentally in the diluted samples of Dy complex, suggesting that relaxation will take place by thermal-activated quantum tunneling through the first excited state. In addition, for the Er and Tm complexes the state with the smallest quantum number lies in the lowest energy states, indicating the easy-plane anisotropy, thus leading to the disappearance of SMM behavior.

Another important characterization for SMM is the observation of hysteresis loops. In known transition metal SMMs, the stepwise hysteresis loop was usually observed at low temperature, which is mainly ascribed to the QTM allowed by the avoided level crossing of different electronic levels m_S under an appropriate magnetic field [45]. Here, the Tb^{III}, Dy^{III}, and Ho^{III} complexes also show the staircase-like hysteresis loops at the relatively low magnetic field [31, 46], but it seems to be insufficient to explain them through the simple level crossing of different m_J states, because the separations between two adjacent m_J states are so high, up to a few hundred wave numbers surpassing that of transition metal cluster by an order of magnitude, that such level crossings occur only at very high fields. Therefore, Ishikawa et al. applied the new theoretical model with the nuclear spins terms to successfully explain the step structures of hysteresis observed around nonzero magnetic fields [31].

$$H_{Ln} = H_{LF} + \mu_B(\mathbf{L} + 2\mathbf{S}) \times \mathbf{H} + A_{hf}J \times I + P\left\{I_z^2 - 1/3I(I+1)\right\}$$

$$H_{LF} = A_2^0\langle r^2 \rangle \alpha O_2^0 + A_4^0\langle r^4 \rangle \beta O_4^0 + A_4^4\langle r^4 \rangle \beta O_4^4 + A_6^0\langle r^6 \rangle \gamma O_6^0 + A_6^4\langle r^6 \rangle \gamma O_6^4$$

For H_{Ln} , the H_{LF} , \mathbf{L} , and \mathbf{S} are operator equivalents of the LF potential on the f -system, orbital angular momentum, and spin angular momentum operators, respectively. The third and fourth terms represent the hyperfine and nuclear quadrupole interactions, respectively, in which the A_{hf} and P are coupling constants. The interactions between the $4f$ electrons and the nucleus spin lead to a $[(2J+1)(2I+1) \times (2J+1)(2I+1)]$ matrix. In the case of the Tb complex (Fig. 2.9a, b), terbium possesses a nucleus with $I = 3/2$ spin in a natural abundance of 100 %. The ground-state doublet, $m_J = \pm 6$, splits into eight states denoted as $|m_J\rangle|I_z\rangle$, where $I_z = \pm 3/2$ and $\pm 1/2$. Figure 2.9b shows the Zeeman diagram for the eight states with the $16 = 4^2$ crossing points but only 13 magnetic-field positions, which clearly explains the positions of staircase in the hysteresis loop of diluted [TbPc₂]⁻ samples. In addition, such staircase-like hysteresis loops are also observed in the diluted Dy and Ho samples, as seen in Fig. 2.9c, d, respectively. For the sample containing Ho ions possessing a nucleus with $I = 7/2$ spin in a natural abundance of 100 %, the same explanation

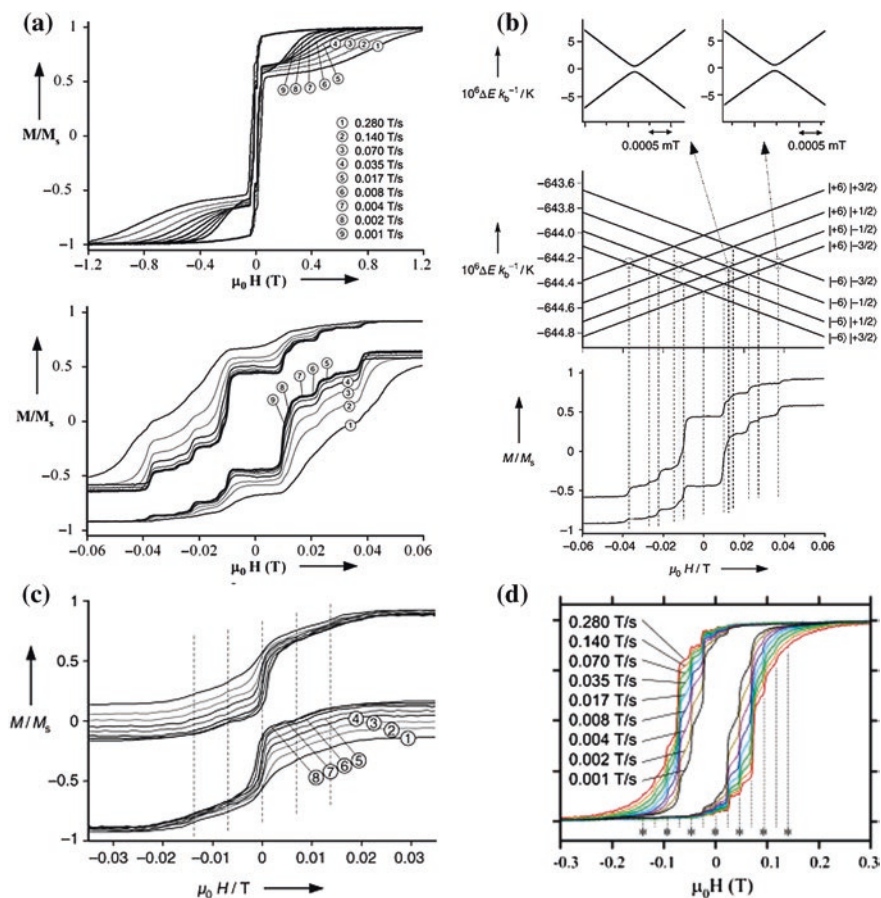


Fig. 2.9 Hysteresis loops at 0.04 K for the Tb (a), Dy (c) and Ho (d) complexes of $[\text{LnPc}_2]^-$. **b** Zeeman diagrams of Tb complex for the lowest $m_J = \pm 6$ substates combined with the $I = 3/2$ nucleus state calculated with the ligand-field parameters. **a–c** Reproduced from Ref. [31] by permission of John Wiley & Sons Ltd. **d** Reprinted with the permission from Ref. [46]. Copyright 2005 American Chemical Society

is given to the observed step positions in its hysteresis loops. However, for Dy there are seven naturally occurring isotopes, showing two different nuclear spins, $I = 0$ and $5/2$. For $I = 0$, no tunneling should occur because of the Kramers theorem of spin parity, while the coupling between $I = 5/2$ and $4f$ electrons leads to an integer total spin and further the avoided level crossings in the Zeeman diagram, which interpret the small step in the hysteresis loops of diluted Dy sample.

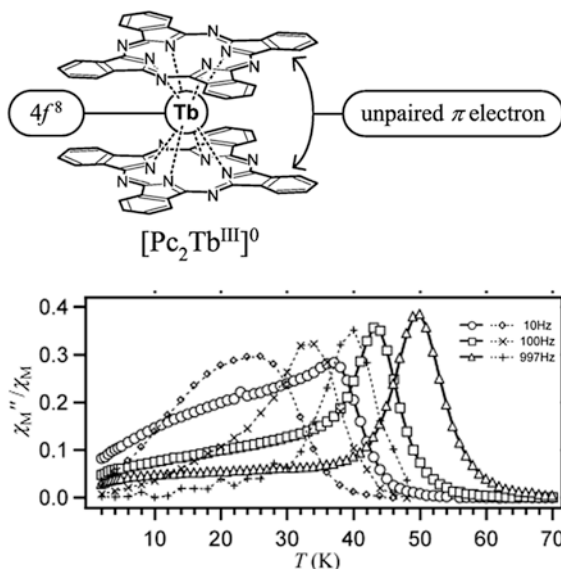
2.2.3 The Enhanced SMMs from the Redox Reactions

In the above section, we discussed the magnetism and electronic structures of the anionic form of bis(phthalocyaninato)terbium, where the Pc ligands have a formal charge of 2- with a closed shell π electronic system. However, it has been well known that one/two-electron oxidation of [LnPc₂]⁻ can occur on the ligand side, resulting in the neutral and cationic [LnPc₂]^{0/+} species (Fig. 2.6), which provide a great platform for studying the modulation of relaxation dynamic by controlling a redox reaction on the ligand side in pursuit of the envisaged SMM properties. In particular, the previous theoretical studies have indicated that the highest occupied molecular orbital (HOMO) and the next HOMO of [LnPc₂]⁻ are the antibonding and bonding linear combinations, respectively, of the highest occupied π orbitals of the component Pc²⁻ ligands [47, 48]. The removal of the two electrons from the HOMO orbital will thus shorten the Pc–Pc distance and the height of the coordination polyhedron of the lanthanide ion, which greatly strengthen the axial component of the ligand field and further lead to the possibly enhanced SMM behavior [49]. In fact, such several typical examples have been reported by Ishikawa and other groups, showing the significant increase of the barrier energy for magnetization reversal from the redox reaction on the ligand side.

In 2004, Ishikawa et al. reported the first example of π -radical [TbPc₂]⁰ SMM from the ligand oxidation of the anionic [TbPc₂]⁻ complex, which generates one unpaired π electron delocalized over two Pc ligands (Fig. 2.10) [49]. Clearly, the peaks of the out-of-phase component of the ac susceptibility are shifted to significantly higher temperatures in contrast to the values of the anionic complex, as seen in Fig. 2.10. Here, the effective barrier can be extracted to be 410 cm⁻¹, which is more than 100 cm⁻¹ higher than that of the seminal complex, indicating thus the enhanced SMM behavior. In order to eliminate the effect of intermolecular interactions, the peripheral H atoms of Pc ligands are substituted by the long-chain alkoxy groups in the [TbPc₂]⁰ complex, which can effectively increase the intermolecular distances and thus reduce the intermolecular interactions. Therefore, the ac susceptibility of [Tb(Pc-OC12)₂]⁰ in a frozen solution of eicosane shows the similar temperature range, where slow relaxation of magnetization is observed, to the [TbPc₂]⁰ complex, indicating that the magnetic relaxation phenomena is single-molecule origin, rather than resulting from intermolecular interactions and long-range magnetic order.

In 2007 and 2008, the cationic Tb and Dy phthalocyanine complexes arising from the two-electron oxidation of its corresponding anionic complexes were subsequently investigated by Ishikawa et al. [42, 50]. Here, the essential modifications for the seminal complex [LnPc₂]⁻ should be performed due to the extremely low solubility of [LnPc₂]⁺ to organic solvents. The substituted Pc-OEt ligand, 2,3,9,10,16,17,23,24-octaethoxyphthalocyanine, turns out to be effective in increasing the solubility of the cationic complex [LnPc₂]⁺ to organic solvents. Therefore, the cationic complex [Ln(Pc-OEt)₂]⁺(SbCl₆)⁻ (Ln = Tb and Dy) was isolated by oxidizing their neutral complexes with phenoxathiinium

Fig. 2.10 The schematic structure (*top*) and ac susceptibility data (*bottom, solid lines*) of π -radical $[\text{TbPc}_2]^0$. *Dotted lines* represent the ac susceptibility data of $[\text{TbPc}_2]^-$. Reprinted with the permission from Ref. [49]. Copyright 2004 American Chemical Society



hexachloroantimonate in dichloromethane. The changes of coordination geometry are demonstrated at the top of Fig. 2.11, showing a longitudinal contraction of the SAP polyhedron relative to the anionic complexes, which are predicted by DFT theoretical calculations. Comparing the alternating current (ac) susceptibility data of the cationic and the corresponding anionic complexes at the bottom of Fig. 2.11, we can see that the χ'' peaks clearly shift to the higher temperature, indicating the enhanced slow relaxation process. For the cationic Tb and Dy complexes, the χ'' peaks at 1000 Oe were observed at 52 and 25 K, which are 12 and 15 K higher than that of their anionic complexes, respectively. Naturally, their anisotropy barriers for the spin reversal of magnetization show also a corresponding increase. Here, the effective barrier of $[\text{Tb}(\text{Pc}-\text{OEt})_2]^+$ was estimated by Arrhenius analysis to be 550 cm^{-1} , showing an 8 % increase in contrast to that of the anionic complex [42]. More strikingly, the cationic Dy complex shows a 55-cm^{-1} effective barrier, about twice as large as that of its anionic complex, and the hysteresis loop at 1.8 K exhibits a large remnant magnetization at zero field [50]. The observations of the dynamic magnetism presented here are consistent with the longitudinal contraction of the SAP polyhedron, which is expected to increase the ligand-field splitting of the ground multiplet of lanthanide ions and further leads to the blocking of magnetic moments at higher temperature.

In addition, magnetic circular dichroism (MCD) spectroscopy was applied to further probe the magnetic properties of three interconvertible redox states in a family of new lanthanide phthalocyanine complexes, $[\text{Ln}(\text{Pc}-\text{IPD})_2]^{-/0/+}$ [51]. The MCD spectroscopy, showing a high sensitivity compared to the conventional

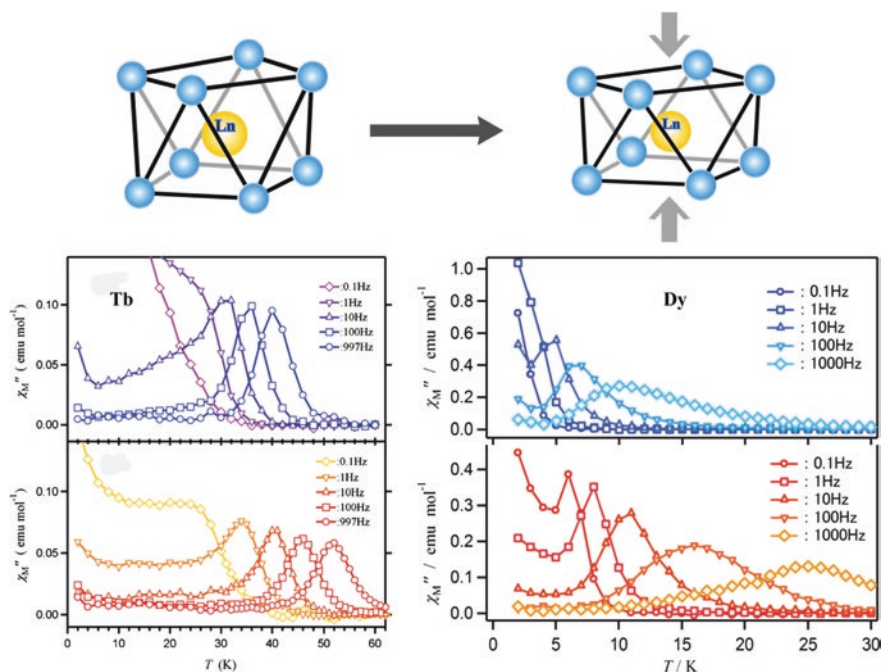


Fig. 2.11 Schematic diagram of the contraction of the coordination space and the changes of magnetic dynamics upon two-electron oxidation from [LnPc₂]⁻ to [LnPc₂]⁺ (Ln = Tb and Dy). Reprinted with the permission from Refs. [42, 50]. Copyright 2007 and 2008 American Chemical Society

magnetometer, has been viewed as a powerful tool for the optical detection of the magnetic behavior [52]. The field-dependent MCD intensity was recorded at 705, 664, and 631 nm for three samples as solutions in CH₂Cl₂ with 0.8 M [NBu₄][BF₄], as seen in Fig. 2.12 [51]. Therefore, the butterfly-shaped hysteresis was observed in both anionic and cationic samples, but the hysteresis of the cationic sample shows a larger coercive field and stronger remnant signal, which indicate that the cationic complex exhibits the larger ligand-field splitting of the ground multiplet and further behaves as a more effective SMM, in agreement with the above results presented by the ac susceptibility measurements. Nevertheless, the field-dependent MCD spectrum of the neutral complex demonstrates the different hysteresis behavior from their ionic complex. Here, the perfect hysteresis loop was observed without the clear steps indicating the QTM relaxation process around 0 T. In results, the neutral complex exhibits the greatest coercive field and least QTM at zero field, suggesting that the neutral complex is better suited to SMM applications.

In 2013, S.M. Gorun et al. firstly reported the magnetic study of the halogenated phthalocyanine double-decker lanthanide complex, [Tb(Pc-CF₂)₂]-H, showing

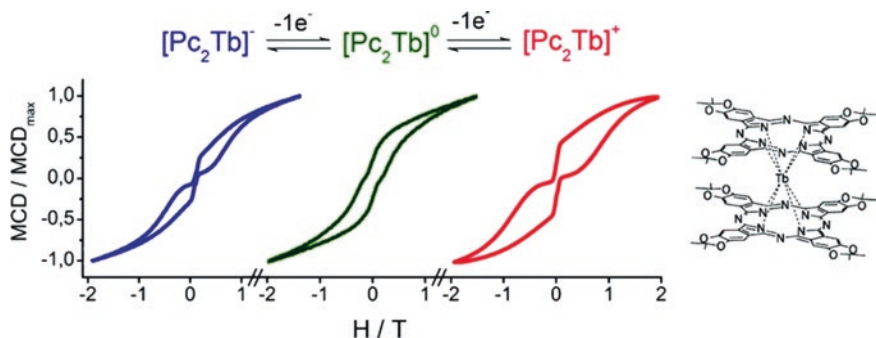


Fig. 2.12 Hysteresis curves of the normalized MCD intensity versus B recorded at 1.5 K and a sweep rate of $1 \text{ T}\cdot\text{min}^{-1}$ for the Q-band of $[\text{TbPc}_2]^-$, $[\text{TbPc}_2]^0$ to $[\text{TbPc}_2]^+$. Reprinted with the permission from Ref. [51]. Copyright 2010 American Chemical Society

the highly reduced states, i.e., the doubly and triply reduced states indicated by the cyclic voltammogram in Fig. 2.13 [53]. The complex contains two substituted Pc ligands, 1,4,8,11,15,18,22,25-octakis-fluoro and 2,3,9,10,16,17,23,24-octakis-perfluoro(isopropyl)phthalocyanine (Pc-CF in Fig. 2.5), where the fluorine-containing groups substitute all peripheral H atoms of Pc ligand, thus stabilizing the highly reduced states due to their strong electron-withdrawing effects. The single-crystal structure for the initial complex, $[\text{Tb}(\text{Pc-CF})_2]\text{-H}$, was obtained by single-crystal X-ray diffraction and shows the clear double-decker sandwiched structure, but one disordered H atom is present over eight nitrogen atoms of the Pc rings to balance the charge. Here, ac magnetic susceptibility measurements were performed for the complex, exhibiting the similar temperature-dependent ac signals to the unsubstituted $[\text{TbPc}_2]$ complex. The barrier was extracted by the Arrhenius fitting to be 365 cm^{-1} at the high-temperature region. Further, the sample solutions of $[\text{Tb}(\text{Pc-CF})_2]^-$, $[\text{Tb}(\text{Pc-CF})_2]^{2-}$, and $[\text{Tb}(\text{Pc-CF})_2]^{3-}$ were prepared by controlled electrolysis at potentials 0.37, -0.03 , and -0.47 V versus SCE, respectively, from the $[\text{Tb}(\text{Pc-CF})_2]\text{-H}$ solution in acetone. The field-dependent MCD spectra recorded at 562, 494, and 705 nm for three samples, respectively, all exhibit the clear hysteresis loops, as seen in Fig. 2.13. Differently, the butterfly-shaped hysteresis was observed in $[\text{Tb}(\text{Pc-CF})_2]^-$ and $[\text{Tb}(\text{Pc-CF})_2]^{3-}$ due to the QTM induced by the hyperfine interactions, while the hysteresis of $[\text{Tb}(\text{Pc-CF})_2]^{2-}$ does not display the narrowing of the loops around zero-dc field. The case is very similar to that occurred in the above $[\text{Ln}(\text{Pc-IPD})_2]^{-/0/+}$ examples. We can draw a key conclusion that the Tb phthalocyanine species with single radical should behave as the better SMMs at zero field due to the suppression of QTM by the coupling interactions between the ground spin ($m_J = \pm 6$) of Tb ion and the ligand spin ($S = 1/2$).

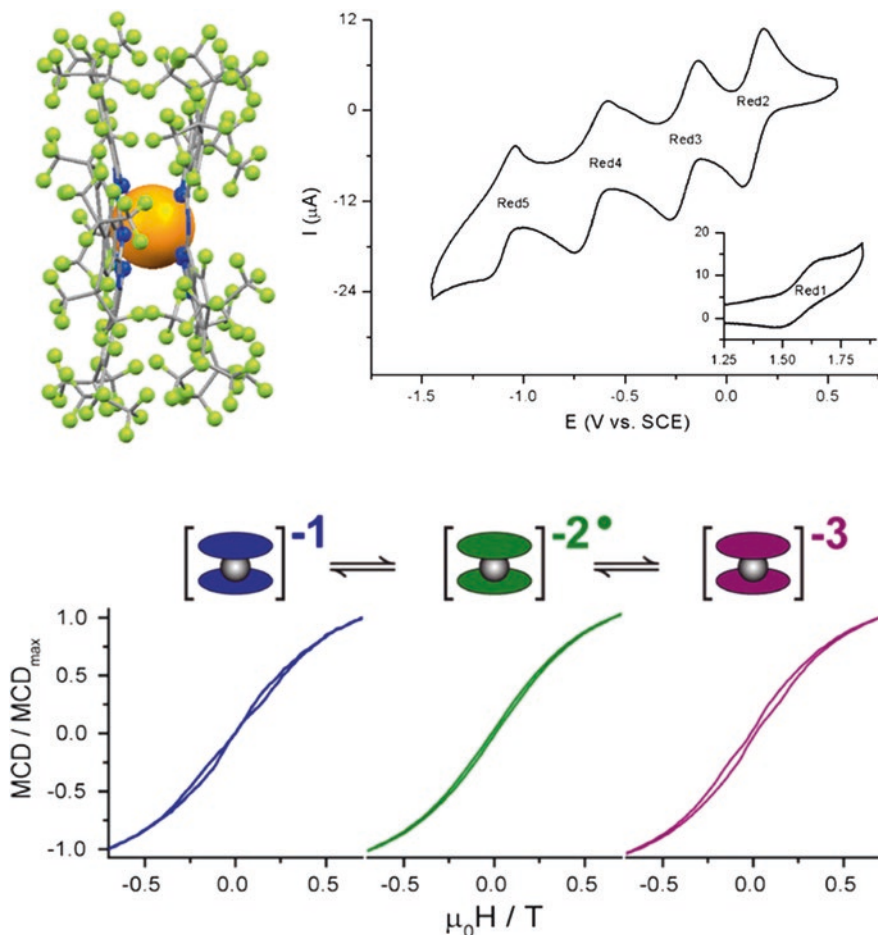


Fig. 2.13 The molecular structure of [Tb(Pc-CF₂)₂]-H, and cyclic voltammogram at 100 mV s⁻¹ of its solution in acetone, as well as hysteresis curves of the normalized MCD intensity recorded at 1.8–1.9 K and at a sweep rate of 1 T min⁻¹. Reprinted with the permission from Ref. [53]. Copyright 2013 American Chemical Society

2.2.4 The Substituted [LnPc₂] SIMMs

To date, a great number of bis(phthalocyaninato) lanthanide double-decker complexes with different substituents at the peripheral positions of the phthalocyanine ring have been synthesized and show the strong SMM behavior, as listed in Table 2.1 [54–59]. In fact, some previous experimental and theoretical investigations have indicated that the electron-donating and electron-withdrawing nature of various substituents have significant effects on the electronic structure, spectroscopic and electrochemistry properties of metal-free phthalocyanines, and, importantly,

Table 2.1 The effective barriers of some typical substituted [LnPc₂] species

Molecule	$U_{\text{eff}}/\text{cm}^{-1}$	τ_0/s	Ref.
[Tb(Pc-OPh) ₂]	504	2.16×10^{-11}	[54]
[Tb(Pc-Oph) ₂] ⁻ N(Me) ₄ ⁺	442	8.2×10^{-11}	[54]
[Tb(Pc-Oph) ₂] ⁻ N(Bu) ₄ ⁺	394	3.45×10^{-10}	[54]
[Tb(Pc)(Pc-Oph)]	652	1.1×10^{-11}	[54]
[Tb(Pc)(Pc-Oph)] ⁻ N(Me) ₄ ⁺	450	3.0×10^{-10}	[54]
[Tb(Pc)(Pc-Oph)] ⁻ N(Bu) ₄ ⁺	487	7.8×10^{-11}	[54]
[Tb(Pc)(Pc-Bu)]	642	2.21×10^{-11}	[54]
[Tb(Pc)(Pc-Bu)] ⁻ N(Bu) ₄ ⁺	400	4.78×10^{-10}	[54]
[Tb(Pc-ODOP) ₂] (order)	480		[55]
[Tb(Pc-ODOP) ₂] (disorder)	422		[55]
[Tb(Pc-a) ₂] ⁻ N(Bu) ₄ ⁺	445	6.35×10^{-11}	[56]
[Tb(Pc-b) ₂] ⁻ N(Bu) ₄ ⁺	428	1.34×10^{-10}	[56]
[Tb(Pc-c) ₂] ⁻ N(Bu) ₄ ⁺	463	2.22×10^{-11}	[56]
[Tb(Pc-OBu) ₂] ₂	230	1.1×10^{-10}	[57]
[Dy(Pc-OBu) ₂] ₂	44	1.3×10^{-5}	[58]
[Dy(Pc-CN) ₂]	40		[59]

further affect the properties of the corresponding coordination complexes with the phthalocyanine ligands. Therefore, such those peripheral modifications for phthalocyanine ligands seem to be critical for finding the SMMs with higher effective barriers.

In 2013, E. Coronado et al. reported a new series of homoleptic and heteroleptic bis(phthalocyaninato) Tb complexes with different peripheral substitution patterns, as seen in Table 2.1 and Fig. 2.14 [54]. The structures of their corresponding neutral radical and anionic forms can be confirmed by the various spectroscopic methods. Here, ¹H NMR spectra were obtained for all complexes and further identified the neutral radical and their reduced forms (Fig. 2.14 top). The magnetic investigations for them demonstrated that all complexes behave as the robust SMMs with the high effective barriers, which were listed in Table 2.1. As a representative example, the neutral heteroleptic [Tb(Pc)(Pc-OPh)] complex shows the well-resolved out-of-phase ac susceptibility maxima that vary with frequency, and the temperature of the χ'' peak at 10,000 Hz reaches up to 58 K, as shown at the bottom of Fig. 2.14. The effective barrier was given according to the Arrhenius formula to be up to 652 cm⁻¹, which represents the highest barrier recorded in the SMM field to date. Several clear trends can be drawn through comparing the magnetic properties of those several complexes. First, all neutral radical complexes exhibit higher barriers than their corresponding anionic complexes, which is consistent with the conclusions in the above section. Second, higher barriers were observed in the heteroleptic phthalocyanine Tb complexes than that in homoleptic complexes. One possible explanation was given by the authors to be that the

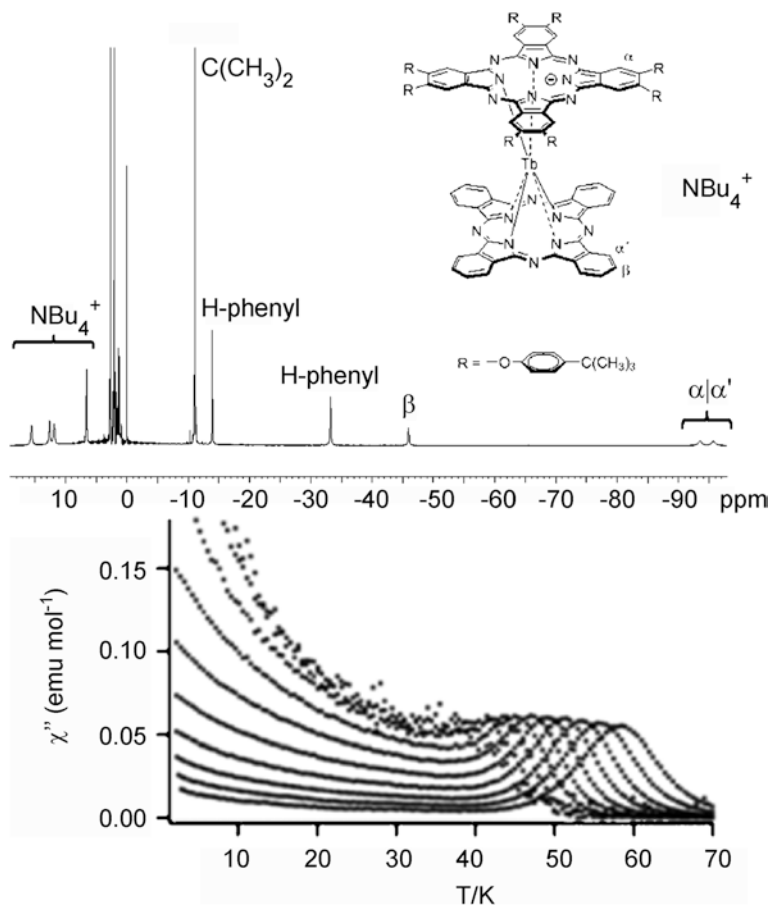


Fig. 2.14 Schematic structure and ^1H NMR spectrum of $[\text{Tb}(\text{Pc})(\text{Pc-Oph})]^- \text{N}(\text{Bu})_4^+$ and ac susceptibility data of its neutral species $[\text{Tb}(\text{Pc})(\text{Pc-Oph})]$ showing the highest effective barrier. Reproduced from Ref. [54] by permission of John Wiley & Sons Ltd.

presence of electron-donating groups on just one of the Pc rings makes the N–Tb distance of the substituted ring larger and, therefore, pushes the metal ion toward the bare Pc ring, thereby enhancing the ligand field of the latter ring [54].

In addition, some other modifications reported have been also presented in Table 2.1, where the very high barriers were demonstrated for the Tb complexes. In particular, the liquid-crystalline terbium double-decker phthalocyanine complex was synthesized in 2010 by using a long chiral alkyl chains to functionalize the $[\text{TbPc}_2]$ core, and further, the complex keeps the strong SMM behaviors of the original core in the disordered and ordered crystalline state [55].

2.2.5 The $[LnPc_2]$ -like SIMMs

Porphyrin, as the structural analogs of phthalocyanine ligand, shows the similar planar tetrapyrrole structure (Fig. 2.5), which thus leads to the assembly of the analogous double-decker structure to the lanthanide ions. The first bis(porphyrinato) double-decker rare earth complex was reported in 1983, but the SMM properties of the Tb complex were firstly explored until recently by Ishikawa and coworkers [60]. Here, the complex can be isolated into two forms, one being the protonated form $[TbH(TPP)_2]$ while the other being the anionic form $[Tb(TPP)_2]^- (H-DBU)^+$ (DBU = 1,8-diazabicyclo[5.4.0] undec-7-ene), which can be determined by the combinations of single-crystal X-ray analysis, NMR, and IR study. For the protonated form, the proton was proved to be located on the nitrogen atom of the TPP pyrrole ring, which thus leads to the different coordination geometry between two forms, as shown in Fig. 2.15. Importantly, the investigations of ac magnetic susceptibilities were indicative of the distinct SMM behaviors for the two forms. Here, no SMM behavior was observed in the protonated form, while the anionic form demonstrated the strongly blocking behavior of magnetization as evidenced by the well-resolved χ'' maxima in Fig. 2.15. Further, the application of a 2000-Oe dc field led to the similar results for them, and the effective barrier can extracted to be 283 cm^{-1} for the anionic complex. This represents a typical example of the double-decker complex whose SMM properties can be reversibly switched by only a single proton.

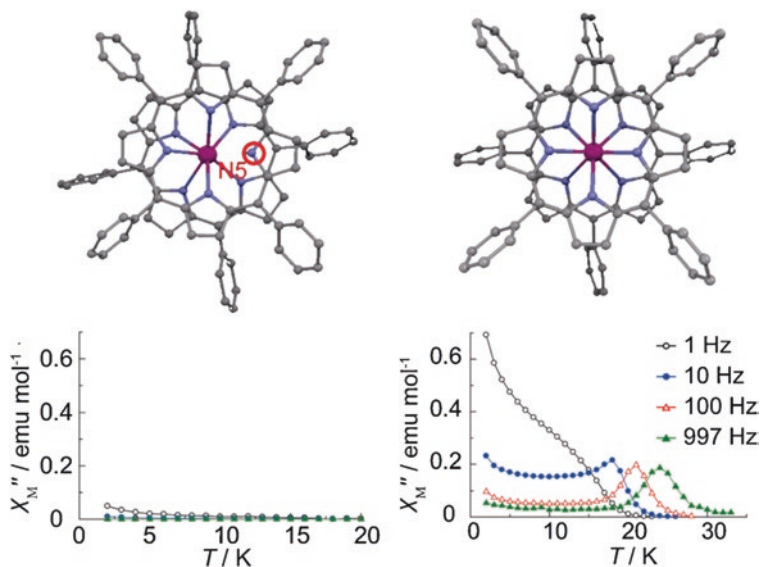


Fig. 2.15 The crystal structure and relaxation dynamics of protonated $[TbH(TPP)_2]$ and deprotonated $[Tb(TPP)_2]^- (H-DBU)^+$. Reproduced from Ref. [60] by permission of The Royal Society of Chemistry

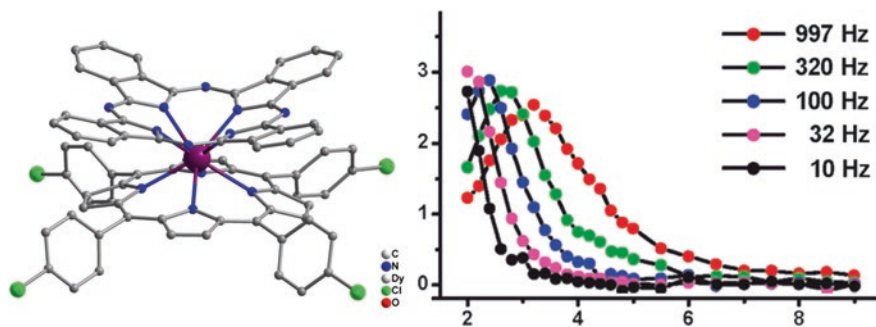


Fig. 2.16 The crystal structure and relaxation dynamics of unprotonated Dy(Pc)(TCIPP). Reproduced from Ref. [61] by permission of The Royal Society of Chemistry

In 2012, J. Jiang et al. reported the magnetic properties of three mixed (phthalocyaninato)(porphyrinato) Dy double-decker complexes, i.e., neutral unprotonated Dy(Pc)(TCIPP) and Dy(Pc-OC5)(TCIPP) and neutral protonated DyH(Pc-OC5)(TCIPP), showing similar sandwich-type double-decker structures to phthalocyanine lanthanide complexes (Fig. 2.16) [61]. A closer look at the crystal structure of three complexes reveals that the complex Dy(Pc)(TCIPP) possesses a SAP geometry with twist angles $\Phi = 43.6^\circ$ closer to the ideal SAP than the other two complexes containing the Pc ligand with non-peripheral substituents. Therefore, obvious temperature-dependent ac signals with χ'' maxima (Fig. 2.16) were observed in the Dy(Pc)(TCIPP) samples, while the other two Dy samples do not show any χ'' peaks under zero-dc field, indicating the presence of slower QTM rates in Dy(Pc)(TCIPP). The magnetic results are well in agreement with the structural changes mainly associated with the twist angle, which provides a typical example to explore correlation between their single-crystal structures and magnetic properties.

In 2012, E.J. Schelter displayed two new double-decker SMMs containing the tetradentate macrocyclic ligands, H₂tmtaa (6,8,15,17-tetramethyl-dibenzotetraaza [14]annulene), which retain the key structural and chemical characteristics of phthalocyanine and porphyrin ligands, as shown in Fig. 2.5 [62]. The double-decker structures were demonstrated in Fig. 2.17. Here, the coordination of tmtaa²⁻ to lanthanide ion leads to a typical saddle conformation, but clearly the double-decker structure is still kept for the two complexes, [Dy(tmtaa)₂K(DME)₂] and [K(DME)(18-crown-6)][Dy(tmtaa)₂]. Nevertheless, the twist angles seem to be so large for the SAP geometry that the geometry is closer to the cube geometry. Therefore, under zero-dc field the fast QTM relaxation is present in both two undiluted complexes, as indicated by the increasing χ'' signals with the decreasing of temperature, which is as a result of the increased transversal anisotropy from the decreased symmetry for the coordination geometry around Dy ion. Further, the combinations of the magnetic dilution in the isostructural Y complexes and the application of a 100-Oe dc field lead to the occurrence of the thermally activated relaxation in a wider temperature range, as seen in Fig. 2.17. The barriers were able to be extracted to be 28.4 and 34.6 K, respectively, for two diluted samples.

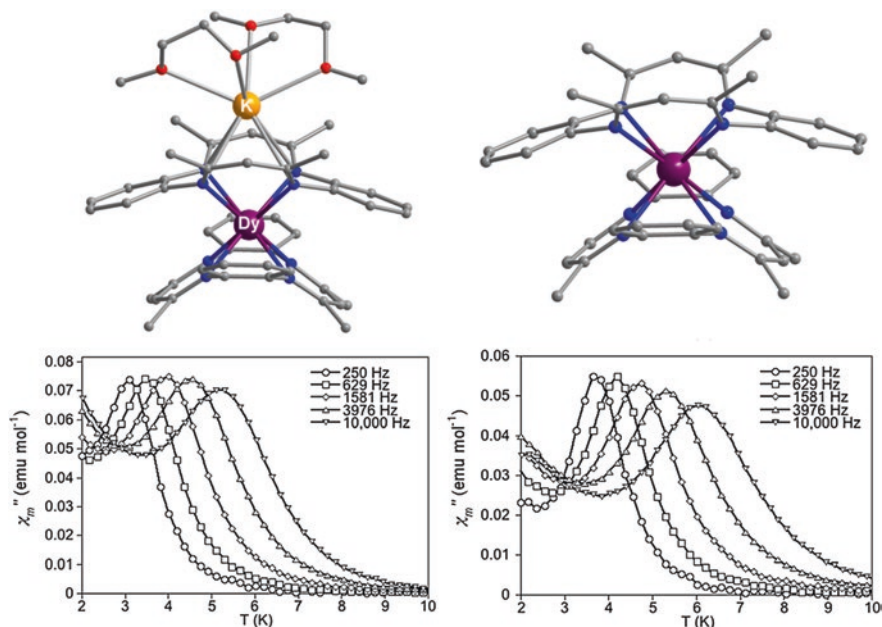


Fig. 2.17 The crystal structure and relaxation dynamics of $[\text{Dy}(\text{tmtaa})_2\text{K}(\text{DME})_2]$ and $[\text{K}(\text{DME})(18\text{-crown-6})][\text{Dy}(\text{tmtaa})_2]$. Reproduced from Ref. [62] by permission of The Royal Society of Chemistry

Consequently, the magnetic exploration into the porphyrin and other double-decker lanthanide complexes further expand the field of phthalocyanine lanthanide SIMMs and open the door to new experiments, potentially allowing the discovery of lanthanide SIMMs with higher effective barriers.

2.2.6 The LnPOM SIMMs

Polyoxometalates (POM) are built from the connection of $[\text{MO}_x]$ polyhedrons with M being a *d*-block element in high oxidation state, usually $\text{V}^{\text{IV,V}}$, Mo^{VI} , or W^{VI} [39]. In the past few years, the POM-based complexes have been investigated extensively for use in various applications from catalysis, medicine, electrochemistry, photochromism, to magnetism. The lanthanide POM complex (LnPOM) was firstly investigated to show the SMM behavior in 2008 [12] and they are seen as the second lanthanide SIMM family discovered following the $[\text{LnPc}_2]$ SIMMs. Figure 2.18 shows the structure features of LnPOM and the electronic levels of lanthanide ions under the crystal field constructed from the POM ligands [63]. The coordination geometry around lanthanide ions, at a first glance, is very similar to the SAP geometry of phthalocyanine lanthanide complexes with the twist angle of

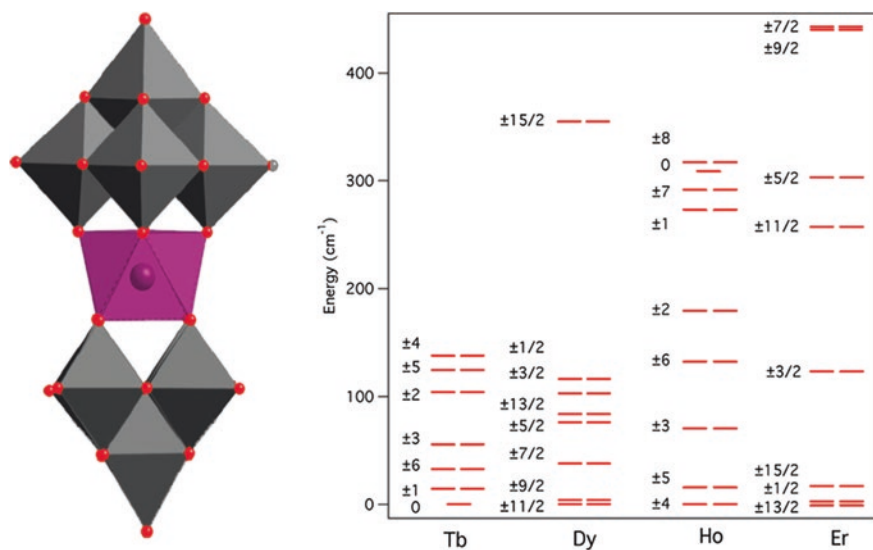


Fig. 2.18 The structure features of LnPOM and the electronic levels of lanthanide ions under the crystal field constructed from the POM ligands. Reprinted with the permission from Ref. [63]. Copyright 2009 American Chemical Society

44.2°, but a detailed analysis for their structures reveals a certain axial compression of the SAP geometry around lanthanide ions indicated by $d_{pp} < d_{in}$, which is opposite to that of the phthalocyanine lanthanide complexes. As predicted by the calculations in Sect. 2.1, these geometrical differences in the crystal fields, although small, seem to be sufficient to completely change the electronic structures of lanthanide ions as shown in Fig. 2.18. Contrary to the phthalocyanine lanthanide complexes (Fig. 2.8), the Tb, Dy, and Ho complexes show the ground state with the relatively small m_J value, while a large spin ground state $m_J = \pm 13/2$ is discovered in ErPOM. Therefore, the distinct electronic structures from [LnPc₂] complexes result in the different relaxation dynamics for them.

As indicated by the electronic levels diagram (Fig. 2.18), the ErPOM behaves as the best SMM in the series of lanthanide complexes. Ac magnetic susceptibility measurements show the typical features associated with the SMM behavior, i.e., the temperature-dependent peaks of the out-of-phase component of the ac susceptibility between 1000 and 10,000 Hz (Fig. 2.19). The effective barrier was given to be 55.2 K by the linear fitting of $\ln\tau$ versus $1/T$. For Tb, Dy, and Ho ions, only Ho complex shows the weak χ'' signal with a shoulder, indicating the fast competing QTM relaxation.

In addition, a new LnPOM family showing the unusual C_5 axial symmetry was explored in magnetism by Coronado et al. [64]. Here, the Dy and Ho derivatives show the weak slow relaxation of magnetization, which will not be introduced in detail.

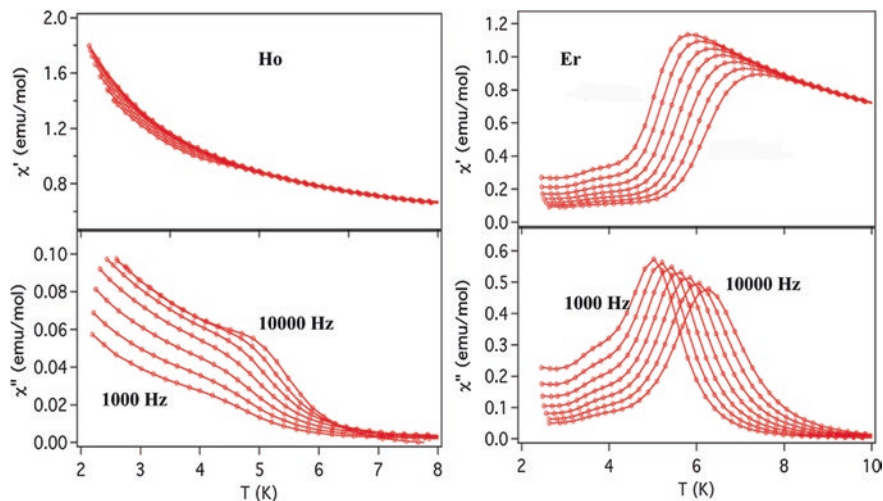


Fig. 2.19 The temperature-dependent out-of-phase component of the ac susceptibility signals between 1000 and 10,000 Hz for HoPOM and ErPOM. Reprinted with the permission from Ref. [63]. Copyright 2009 American Chemical Society

Up to now, the $[\text{LnPc}_2]$ and LnPOM SIMMs have been reviewed from a viewpoint of achieving the high-performance SMMs for the envisaged technological applications of these molecules as classical or quantum bits. It is well known that the two species, especially the $[\text{LnPc}_2]$, play an outstanding role in the development of SMM, because they open the door to lanthanide SMM field and the good performances stimulate the successful development of other following SMMs.

2.3 Lanthanide β -diketone Systems

A β -diketone behaves as a monobasic acid in solutions or solids, as the keto-enol tautomerisms easily lead to the deprotonated form in an appropriate pH range, as seen in Fig. 2.20. Thus, the β -diketone can act as a mononegative bidentate ligand to coordinate to a lanthanide ion and forms stable lanthanide complexes. In fact, such complexes have been widely investigated in some other fields, especially for the photoluminescence, where β -diketones have been recognized as efficient sensitizers to achieving high-harvest lanthanide emissions [40]. In the field of molecular magnetism, the magnetic study for them should start with the lanthanide complexes containing radical ligands [6, 65], whose synthesis almost begin with the reactions between the fluorinated β -diketones lanthanide complexes and the corresponding radicals due to the high solubility of fluorinated β -diketones lanthanide complexes in organic solvents. However, the real development in magnetism for this kinds of complexes should date back to 2010, when S. Gao et al.

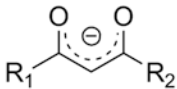
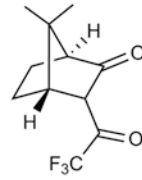
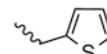
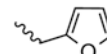
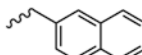
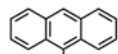
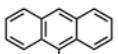
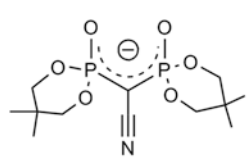
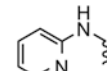
	R ₁	R ₂	abbreviation
L1	—CH ₃	—CH ₃	acac
	—CH ₃	—CH ₂ CH ₃	acec
	—CF ₃	—CF ₃	hfac
	Ph	Ph	Phacac
	Ph	—CF ₃	tfnb
		—CF ₃	tta
L2		—CF ₃	fta
		—CF ₃	nta
			accm
		—CH ₃	paaH
L3			

Fig. 2.20 β -diketone ligands with different substituent groups used in lanthanide SMMs

reported the tri(β -diketones) Dy complex, [Dy(acac)₃(H₂O)₂], functioning as the efficient SMM [8]. Here, three β -diketone ligands and two coordinating H₂O molecules form the eight coordinate quasi-SAP geometry close to the D_{4d} symmetry. Therefore, the authors attributed the SMM behavior to the high symmetry of this complex similar to the [LnPc₂] SMMs, and the CONDON calculations were performed based on the local D_{4d} symmetry, indicating the ground doublets with an Ising-type axial anisotropy. Such an idea further stimulated a series of magnetic investigations for this kind of β -diketone lanthanide complexes in expectation of obtaining the high-barrier SMMs [13]. In fact, some groundbreaking results have been achieved, which mainly benefit from the stable structures of this kind of complexes. It is noteworthy that the two H₂O molecules in seminal complex are easily substituted by other auxiliary ligands, especially the bidentate capping ligands as shown in Fig. 2.21, and thus, modifications can be easily incorporated into the coordination geometry in the β -diketone-based complexes. In addition, as

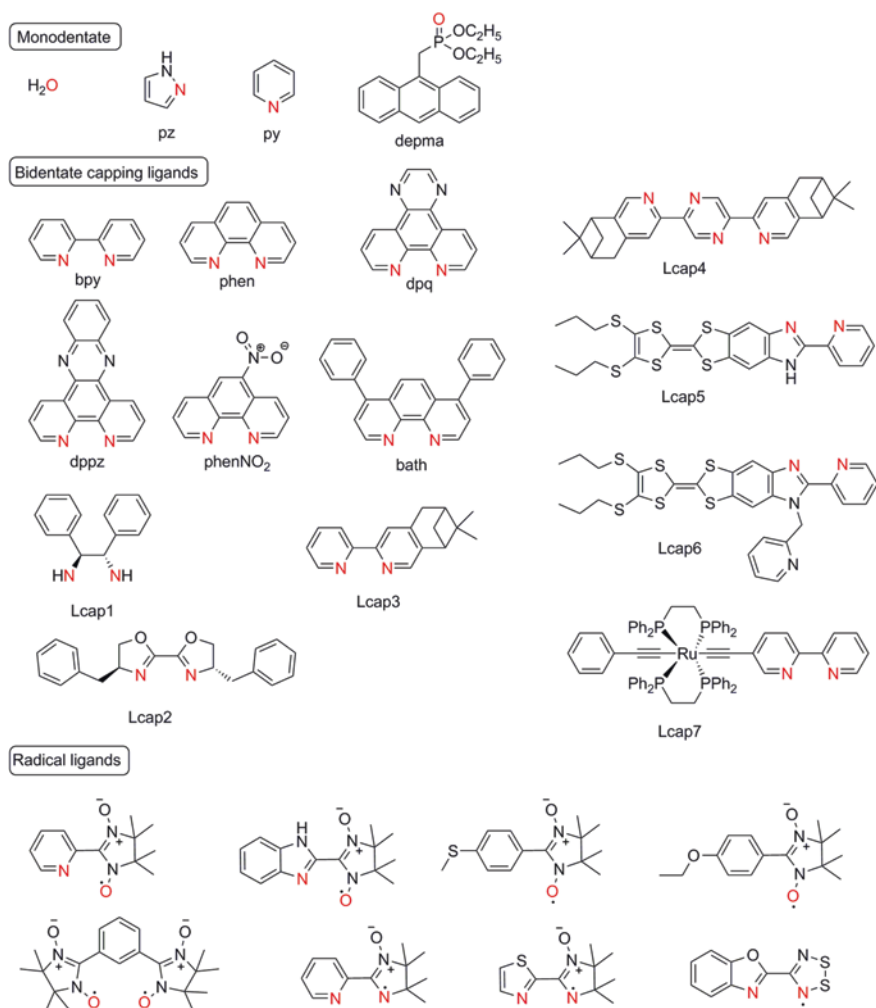


Fig. 2.21 Auxiliary ligands used in lanthanide β -diketonate systems

shown in Fig. 2.20, it is variety for β -diketonate ligands showing the different substituents at the R_1 and R_2 positions, which thus provides the advantage of systematically exploring the factors governing their magnetic properties.

2.3.1 The Magnetism of $[\text{Dy}(\text{acac})_3(\text{H}_2\text{O})_2]$

The structure has been described above as the quasi- D_{4d} symmetry in the first coordination sphere, which seems to be highly uniaxial symmetric, leading to the obvious slow relaxation of magnetization [8]. However, as seen in

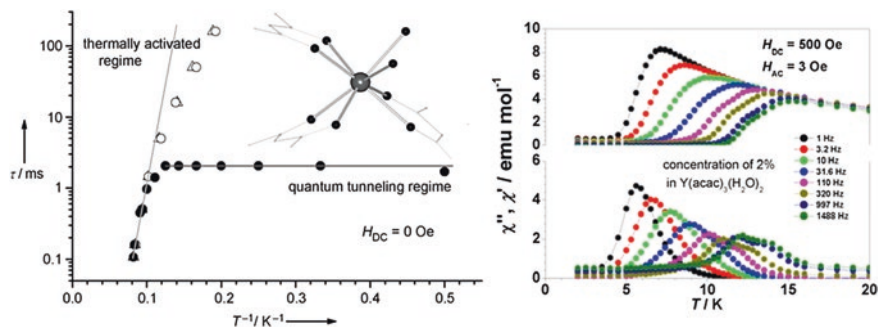


Fig. 2.22 *Left* The relaxation time (τ) of $[\text{Dy}(\text{acac})_3(\text{H}_2\text{O})_2]$ at different concentrations in $[\text{Y}(\text{acac})_3(\text{H}_2\text{O})_2]$ in the temperature range 2–12 K (*filled marks* undiluted samples; *open marks* diluted samples). *Right* The temperature dependence of the ac susceptibility from 1 to 1488 Hz for the 50 times diluted Dy by Y complex at a dc field of 500 Oe. Reproduced from Ref. [8] by permission of John Wiley & Sons Ltd.

Fig. 2.22, the temperature-independent region in the $\ln(\tau)$ versus $1/T$ plots is indicative of the presence of fast QTM relaxation pathway at low temperature, which should arise from some asymmetric factors in the local molecule or the relatively short intermolecular distances. To further get insight of the magnetic behavior and reduce QTM relaxation, magnetic dilutions were performed. The results show that the enhanced SMM behavior was observed, but an increasing χ'' signal with the decreasing temperature is still indicative of the occurrence of QTM at low temperature, i.e., the spin moments cannot be blocked completely. Further, the combination of magnetic dilution and the application of a dc field resulted in the perfect suppression of QTM relaxation, as evidenced by the nearly vanishing χ'' signals at low temperature in Fig. 2.22. The effective barrier was able to be fitted by the Arrhenius law to be 44.7 cm^{-1} (64 K). Here although the barrier seems to be not so high when compared to that of $[\text{TbPc}_2]$ complexes, the detailed investigations for magnetic properties of the complex initiated a new SIMM family after the $[\text{LnPc}_2]$ and LnPOM SIMMs.

2.3.2 The Modulations of Auxiliary Ligands

A successful modulation of SMM properties for the seminal complex was performed by J. Tang and coworkers [13]. Here, the two H_2O molecules in the seminal complex are replaced by 1,10-phenanthroline (phen) and its large aromatic derivatives (dpq and dppz in Fig. 2.21), which leads to the constructions of three new SIMMs keeping the nearly D_{4d} local symmetry of the similar complex. Here, the complex, $[\text{Dy}(\text{acac})_3(\text{phen})]$, displays the similar SMM properties with the almost same barrier to that of the seminal complex. Nevertheless, it is worth

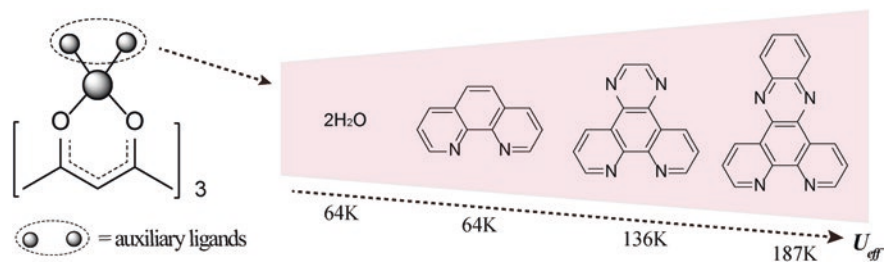


Fig. 2.23 Schematic structures and effective barriers of the Dy β -diketone complexes with different auxiliary ligands

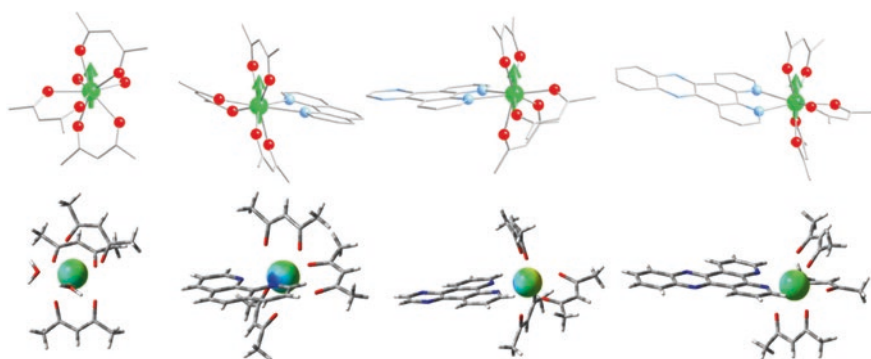


Fig. 2.24 *Top* The anisotropic axes of four Dy β -diketone complexes with auxiliary ligands H_2O , phen, dpq, and dppz. *Bottom* Their electrostatic potential originated from the ligand environment mapped into a sphere centered in the position of the Dy cation with radius 1.0 Å. The color scale between more (red) and less (blue) negative potential is always 0.065 a.u. Reprinted with the permission from Ref. [66]. Copyright 2013 American Chemical Society

noting that two another complexes with larger aromatic groups show the very high barriers, 136 and 187 K, which are two and three times larger than that of the seminal complex, as seen in Fig. 2.23.

A possible reason for their SMM behaviors was given as the strong uniaxial anisotropy arising from the nearly D_{4d} local symmetry, but it is difficult to explain the greatly increasing of effective barriers by replacing the auxiliary ligands. Significantly, the recent *ab initio* and electrostatic potential models calculations from E. Ruiz indicated that the anisotropy axis is not parallel to the quasi- S_8 axis of the local coordination geometry around Dy ion, but passes through the two trans- β -diketonate ligands for those complexes, as shown in Fig. 2.24 [66]. Therefore, it is more reasonable to explain the strong SMM behaviors through the electrostatic potential models for the series of lanthanide complexes. Here, the Dy ion is located in the plane constructed by the delocalized negative charge in two trans- β -diketonate ligands, leading to the strong repulsing interactions. Based on the rules of the electrostatic energy minimization, the radial plane of the oblate electron

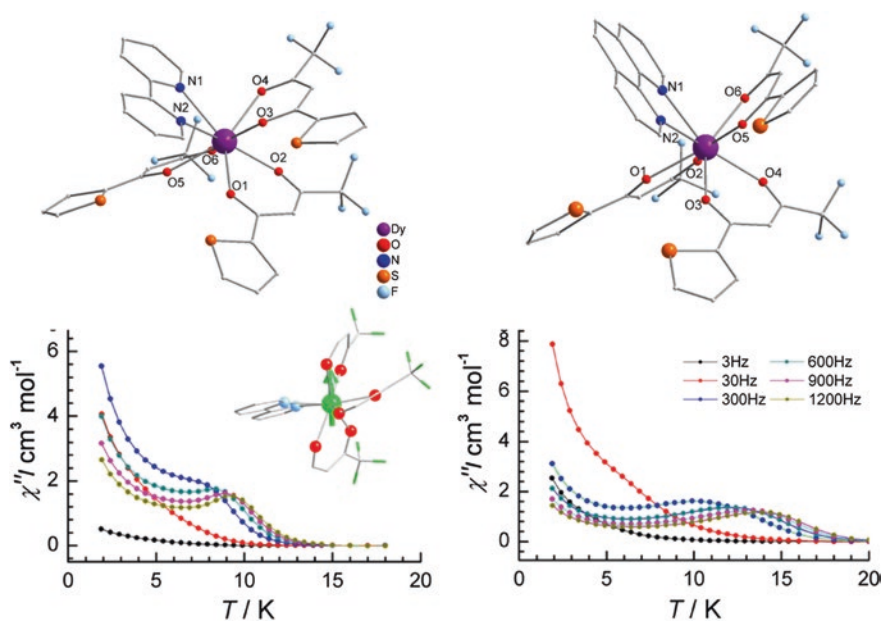


Fig. 2.25 The crystal structures and relaxation dynamics of Dy- β -diketones systems with tta and bpy/phen ligands. Reproduced from Ref. [68] by permission of John Wiley & Sons Ltd. *Inset*, Reprinted with the permission from Ref. [66]. Copyright 2013 American Chemical Society

density of Dy ion is thus coincident with the plane with only one charged ligand, and the anisotropy axis is parallel to the plane with two trans- β -diketonate ligands [67]. Electrostatic potential maps calculated for all four complexes show a similar electrostatic potential shape with a small less negative region originated by the neutral ligands and a more repulsive environment closer to the negative ligands, as shown in Fig. 2.24 [66]. Considering the above explanation for the magnetic anisotropy, we could deduce that the large delocalized effect in the neutral ligands may have a pronounced effect on reducing the repulsive interactions of their coordinate atoms at the plane perpendicular to the anisotropy axis, which, relatively, enhance the axial crystal effects. Consequently, it is possible to explain the increasing effective barriers by substituting the small ligands to the large aromatic derivatives with delocalized π -electrons. Nevertheless, it should note that the magnetic properties are extremely sensitive to small changes in the structure of the complexes, as shown by the experimental and theoretical study of the strong influence on magnetic anisotropic properties of the rotation of the hydrogen atoms in the water ligands in mononuclear Dy^{III} complexes [24], so further experimental and theoretical study should be performed for the better understanding of their magnetic properties.

Another Dy- β -diketone system with tta (tta = 4,4,4-trifluoro-1-(2-thienyl)-1,3-butanedionate) and bpy/phen has also been developed by our group with the goal of identifying features relevant to modulating relaxation dynamics of single-ion magnets, as shown in Fig. 2.25 [68]. Similarly, the O₆N₂ environment forms an

approximately SAP coordination polyhedron, with the similar α angles of 57.2 and 56.4° and remarkable difference in the skew angle of 39.7 and 42.1° for two complexes, respectively. The structures are still described as SAP geometry and the anisotropy axis also passes through the two trans- β -diketonate ligands (Fig. 2.25 inset) [66], consistent with that of the above examples. Their ac magnetic susceptibility signals were shown in Fig. 2.25, both showing the increasing out-of-phase χ'' signals with a shoulder indicative of the fast QTM at low temperature. At the linear regimes of $\ln(\tau)$ versus $1/T$ plots, the effective barriers were extracted to be 58 and 85 K, which are of the same order of magnitude as that of the seminal complex, for two complexes with bpy and phen ligands, respectively. The small increase in effective barriers for $[\text{Dy}(\text{tta})_3(\text{phen})]$ than $[\text{Dy}(\text{tta})_3(\text{bpy})]$ may be as a result of the stronger delocalized effects in the phen ligand than in the bpy ligand.

In addition, several typical Dy-based SIMMs based on hexafluoroacetylacetonate (hfac) were reported by the different research groups, as shown in Fig. 2.26 [69–71]. Compared with the seminal complex, for the first two complexes the

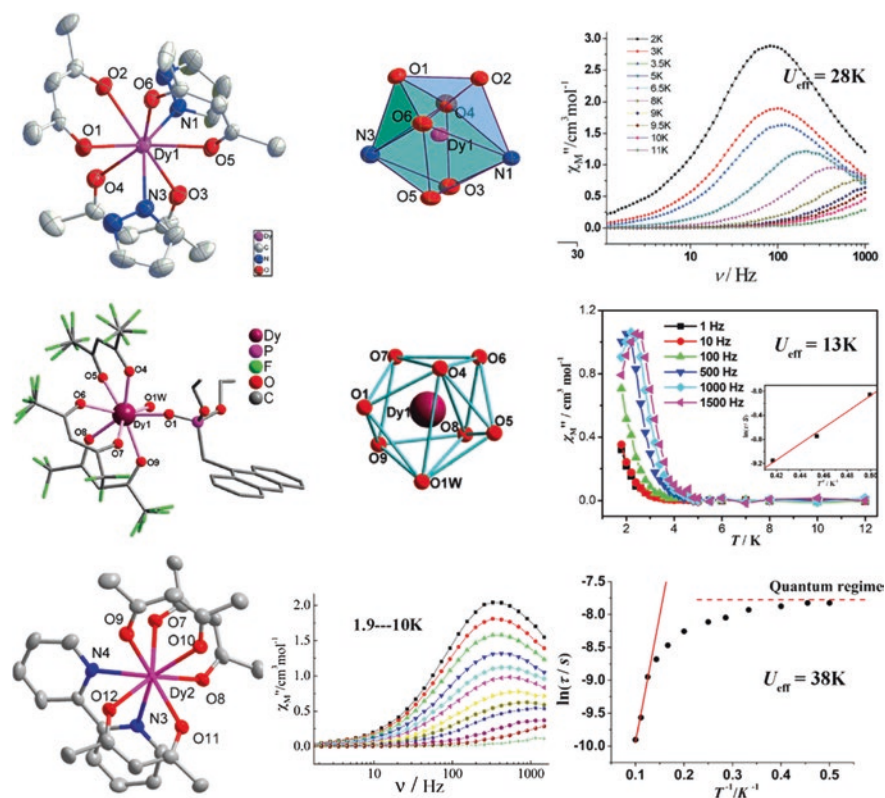


Fig. 2.26 Three Dy- β -diketonate systems with hfac ligands. *Top, Middle* Reproduced from Refs. [69, 70] by permission of The Royal Society of Chemistry. *Bottom* Reprinted with permission from Ref. [71]. Copyright 2013 American Chemical Society

H_2O was substituted by the larger monodentate ligands, leading to the low-symmetry coordination geometry around Dy ions, while the bidentate bpy ligand was applied to replace two H_2O in the third complexes and thus the complex keeps the quasi- D_{4d} geometry. Nevertheless, no obvious changes in SMM properties were observed for the three complexes, and their SMM properties were weakened in contrast to that of the seminal complex, as indicated by their small effective barriers labeled in Fig. 2.26. The reduced SMM behavior may be due to the lowered symmetry around Dy ions and the strong electron-withdrawing effects of fluorine atoms, which may greatly reduce the strength of the axial crystal field. Finally, it is worth noting that this kind of fluorinated β -diketones lanthanide complexes shows the enhanced luminescence behavior with reducing the acidity of the β -diketones compared with the conventional β -diketone ligands, which thus provide a promising approach to design multifunctional lanthanide SMMs.

To date, all the β -diketones lanthanide SIMMs discussed above are Dy-based complexes, which mainly depends on the electronic structures of Dy ions and its Kramers ion properties. In contrast, for another Kramers ion Er^{3+} with the distinct electronic structures from Dy ion, the magnetism of a series of β -diketones complexes was also explored recently by Silva [72], as shown in Fig. 2.27. Here, 2,4-hexanedione (acac) ligands and three bidentate capping ligands were applied to construct three complexes with the typical

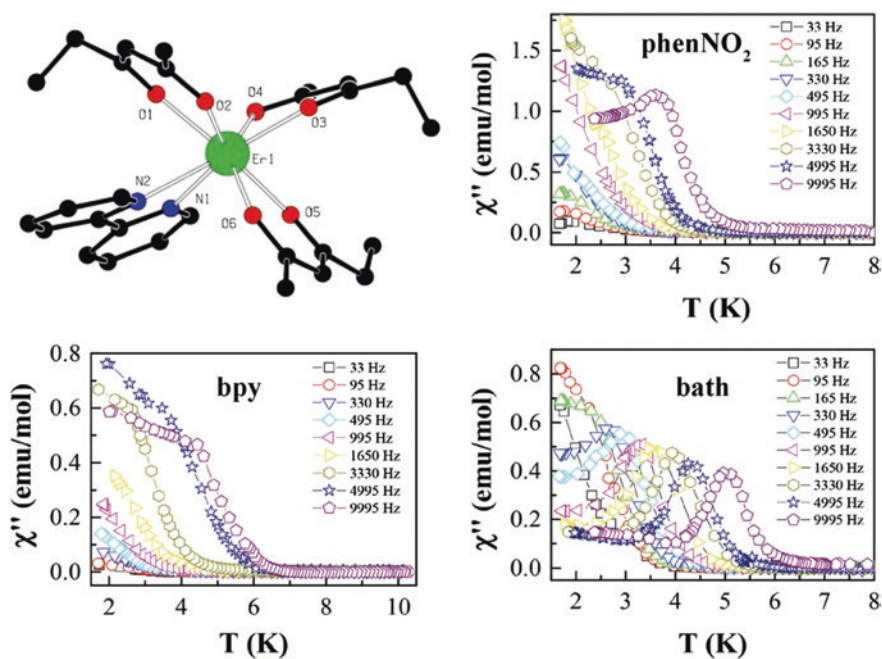


Fig. 2.27 The Er-based β -diketone systems with acac ligands and three different bidentate capping ligands. Reproduced from Ref. [72] by permission of The Royal Society of Chemistry

coordination geometry, $[\text{Er}(\text{acec})_3(\text{Lcap})]$ ($\text{Lcap} = \text{bpy}, \text{phenNO}_2$ and bath in Fig. 2.21). All three complexes display the typical field-induced slow relaxation of magnetization under a 1000-Oe dc field, as evidenced by the obvious χ'' signals shown in Fig. 2.27. In contrast to the other two complexes, the third complex with bath ligand behaves as the best SMM by introducing the larger auxiliary ligands. Nevertheless, the effective barriers for three complexes are still very low, only 8, 13, and 23 K, respectively, and thus the further modifications are necessary.

2.3.3 Chiral β -diketone Dy SIMMs

Due to the stable structures as seen above, some additional functions can be easily incorporated into the β -diketone lanthanide systems by the modifications of the auxiliary ligands or β -diketone ligands, while maintaining their typical structural features and the robust SMM behavior. The most typical examples are the design and assembly of chiral SMMs showing certain physical properties such as ferroelectricity, piezoelectricity, second harmonic generation (SHG), and magneto-chiral dichroism (MChD) effects [73], and to date several complexes have been reported containing the auxiliary ligands from Lcap1 to Lcap4 in Fig. 2.21 [73–77]. Here, only two typical examples were discussed below to present the useful synthetic approach of chiral SMMs for readers.

Figure 2.28 shows the crystal structures of the enantiomeric pair of Dy β -diketone complexes (R -1 and S -1), where the chirality is clearly introduced by transferring chiral information of auxiliary ligands (Lcap4 in Fig. 2.21) to the paramagnetic assemblies [73]. The two complexes crystallized in chiral space groups $P2_12_12_1$ and the solid-state CD spectra confirmed their chiroptical activity and enantiomeric nature. Here, the changes of β -diketone and auxiliary ligands lead to the bicapped trigonal prism geometry around Dy ions, diverging from the SAP geometry of the seminal complex. Even so obvious SMM behaviors were still observed below 20 K at zero-dc field for them, which was shown in Fig. 2.28. The effective barrier was extracted by Arrhenius law to be 47 K, slightly smaller than that of the seminal complex.

In addition, two enantiomeric pairs of β -diketone Dy SIMs were assembled in 2013 using a pair of homochiral β -diketonate ligands L2 in Fig. 2.20 [77]. It is worth noting that their SMM behaviors can be modified through changing the auxiliary ligands (bpy and phen in Fig. 2.21), as shown in Figs. 2.29 and 2.30. Similarly, both two complexes crystallized in chiral space groups and the solid-state CD spectra also confirmed their chiroptical activity and enantiomeric nature. For the complexes with bipyridine ligands, two types of homochiral stereoisomers are cocrystallized together in the crystal structure, as shown in Fig. 2.29. Here although two stereoisomers demonstrate the same molecular formula, the distinct structures are observed for them displaying the different distorted SAP geometries. The ac magnetic susceptibilities measurements display the weak ac signals with no peaks under zero-dc field,

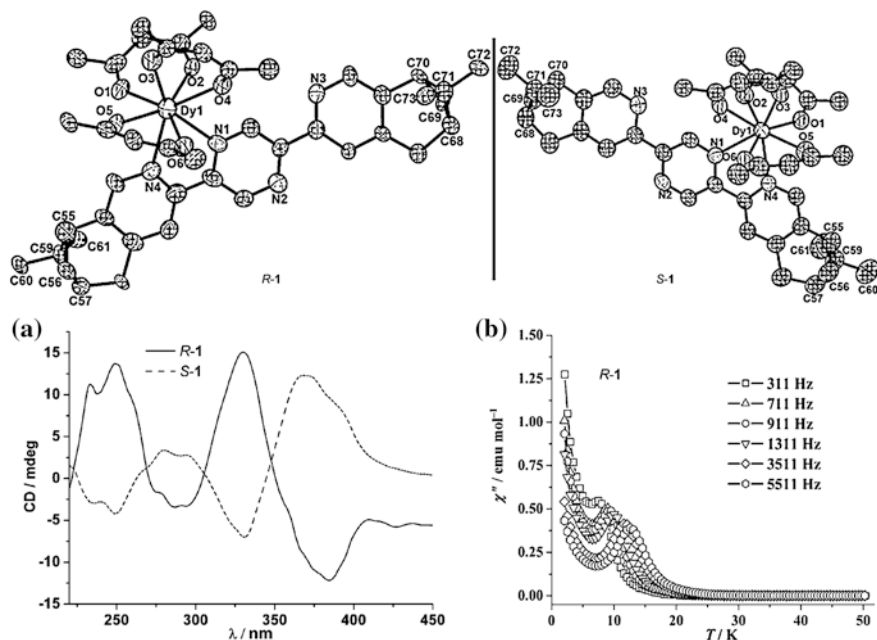


Fig. 2.28 The crystal structures, CD spectra, and relaxation dynamics of the enantiomeric pair of Dy β -diketone complexes with chiral auxiliary ligands Lcap4. Reproduced from Ref. [73] by permission of John Wiley & Sons Ltd.

indicating the onset of slow relaxation of magnetization. Further, the application of a 1000-Oe dc field leads to the occurrence of two thermally activated relaxation processes revealed by the presence of two distinct peaks for the out-of-phase ac signals in Fig. 2.29, which may be related to the presence of two crystallographically independent Dy^{III} centers in crystal structure. The effective barriers were given to be 36.5 and 46 K, respectively.

The complexes with phen ligands in Fig. 2.30 also adopt a distorted SAP coordination geometry with the phen capping ligand instead of the bpy capping ligand of the above complexes. Here, the SMM behavior was not observed under a zero-field, but the application of a 1000-Oe dc field leads to the occurrence of single relaxation process, as shown in Fig. 2.30. The effective barrier was given to be 30.5 K with $\tau_0 = 1.1 \times 10^{-7}$ s.

2.3.4 The SIMMs with Large Capping Ligands

In recent years, the synthesis and coordination chemistry of electro-active molecules functionalized by various mono- or polydentate groups have developed to be the focus of much attention. For example, the tetrathiafulvalene (TTF) derivatives

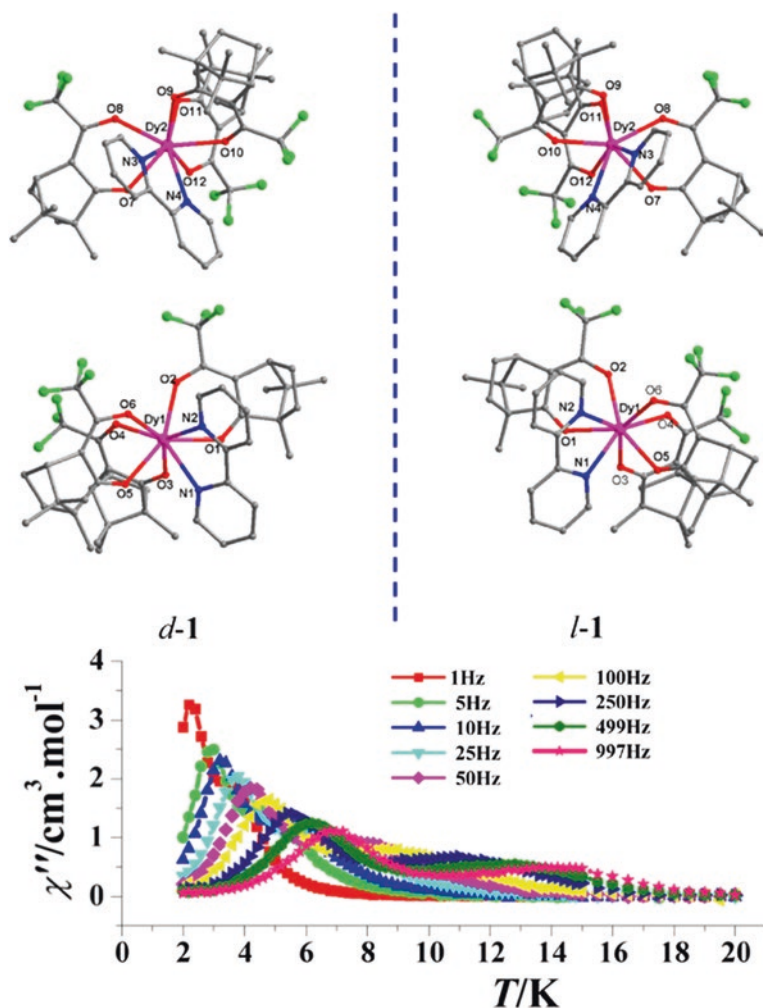


Fig. 2.29 The crystal structures, and relaxation dynamics of the enantiomeric pair of Dy β -diketone complexes with chiral β -diketone ligands L2 and auxiliary ligand bpy. Reprinted with the permission from Ref. [77]. Copyright 2013 American Chemical Society

with the delocalized π electrons showing the strong redox-active properties have been extensively studied in molecular conductors and superconductors [78, 79]. In particular, the redox-active TTF molecules coordinating heteroatom-based groups can be directly coupled with the localized unpaired electrons, which lead to the so-called π - d systems consisting of the delocalized π and localized d electrons, displaying some novel transport properties [80]. In addition, group 8 metal acetylacetonate complexes displaying strong ligand-mediated electronic effects are attractive redox-switchable building blocks for the realization of optical or conductive

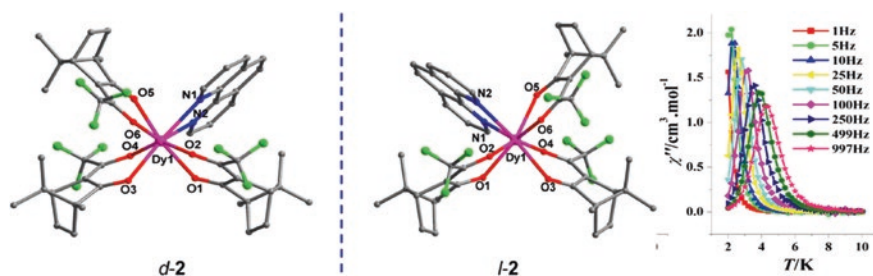


Fig. 2.30 The crystal structures and relaxation dynamics of the enantiomeric pair of Dy β -diketone complexes with chiral β -diketone ligands L2 and auxiliary ligand phen. Reprinted with the permission from Ref. [77]. Copyright 2013 American Chemical Society

switches [81, 82]. Therefore, the above materials provide the great potential applications in multifunctional materials combining the light, electronic, and magnetic properties. However, this kind of ligands is rarely explored in the synthesis of lanthanide SIMMs to date. Here, those ligands containing bipyridine-type ligands (Lcap5–Lcap7 in Fig. 2.21) are very suitable for the auxiliary ligands of the β -diketone Dy complexes, which provide a great platform for studying this kind of lanthanide SIMMs.

In 2012, the β -diketone Dy SIMM functionalized by a ruthenium carbon-rich moiety (Lcap7 in Fig. 2.21) was presented by Norel et al. [83]. The structure was shown in Fig. 2.31, where the classical SAP geometry is still kept around Dy ion in spite of the large volume of auxiliary ligands. The ac magnetic susceptibilities measurements at zero-dc field display the temperature-dependent χ'' maxima at the high-temperature region and a temperature-independent quantum tunneling region. Notably, as shown in Fig. 2.31b, the application of a dc field results in the occurrence of multiple relaxation processes, which is not observed in the conventional β -diketone examples. It is an important issue to be discussed for the reasons of the multiple relaxation processes, which may be related to the strong ligand-mediated electronic effects. Clearly, the external dc field of 480 and 1000 Oe can significantly reduce the efficiency of the underbarrier process, as indicated by the slowing quantum tunneling relaxation times (Fig. 2.31). Under the dc field of 1000 Oe, two effective barriers were extracted to be 11 and 33 K at the low- and high-temperature regions, respectively.

In 2013, E. Pointillart et al. reported the magnetic investigations of two mononuclear β -diketone Dy complexes which were built from the reaction of the auxiliary ligands Lcap5/Lcap6 and $\text{Dy}(\text{hfac})_3 \cdot 2\text{H}_2\text{O}$ [32]. Here, the strong π – π interactions and hydrogen bonds in the crystal structure lead to the formation of head-to-tail dimers. For the complex $[\text{Dy}(\text{hfac})_3(\text{Lcap5})]$, no any out-of-phase signals in zero-dc field were observed, while complex $[\text{Dy}(\text{hfac})_3(\text{Lcap6})]$ shows a clear out-of-phase ac signal below 8 K in zero-dc field. In particular, the diluted samples of $[\text{Dy}(\text{hfac})_3(\text{Lcap6})]$ demonstrate a quantum tunneling time nearly 30 times slower than in the pure compound. In addition, the multiple relaxation processes were

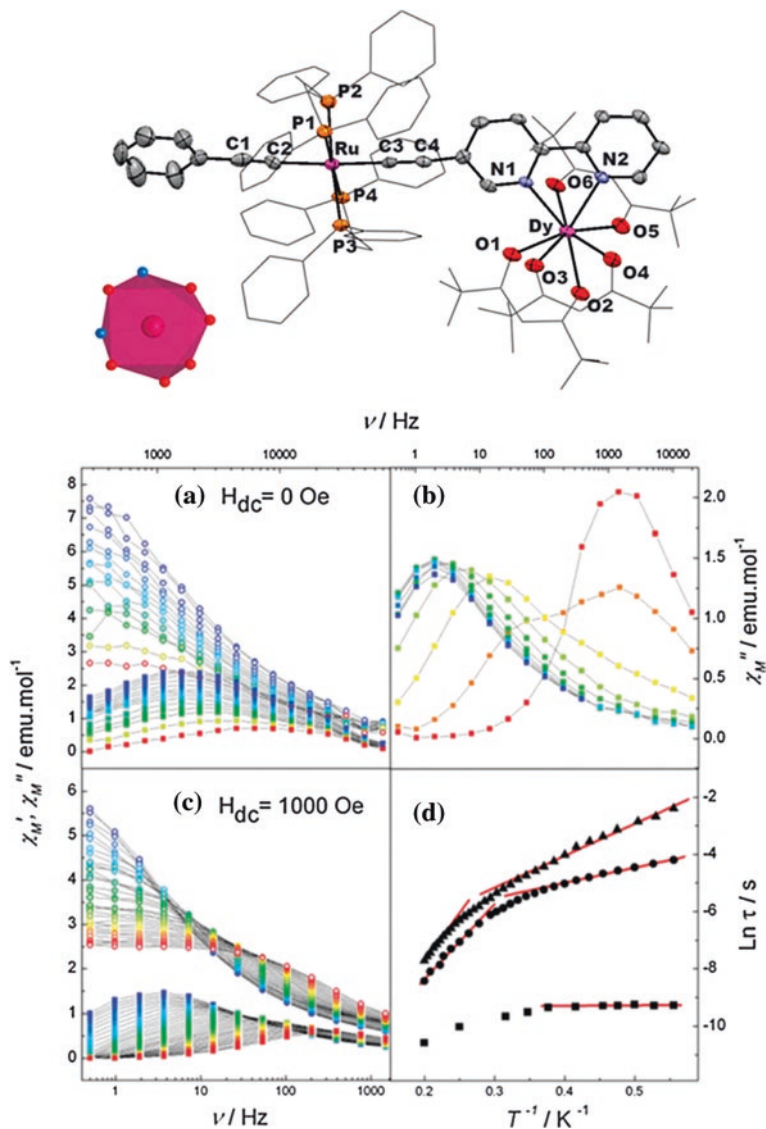


Fig. 2.31 The crystal structure and ac susceptibility data of Dy β -diketone system with capping ligand Lcap7 containing a ruthenium carbon-rich moiety. Reproduced from Ref. [83] by permission of The Royal Society of Chemistry

also observed through the application of an appropriate dc field. Further, the substitution of β -diketone ligand hfac by tta ligand leads to the formation of complex [Dy(tta)₃(Lcap6)], whose magnetic properties were investigated systematically by angular-resolved magnetometry and MCD measurement and ab initio calculations, as seen in Fig. 2.32. Here, the angular-resolved magnetometry measurement indicated

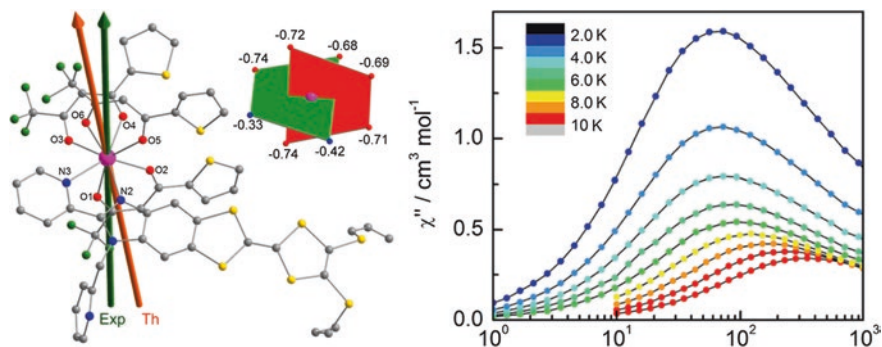


Fig. 2.32 The crystal structure, magnetic anisotropic axis and relaxation dynamics of $[\text{Dy}(\text{hfac})_3(\text{Lcap6})]$. Reprinted with the permission from Ref. [32]. Copyright 2013 American Chemical Society

that the strong Ising-type anisotropy axis is almost parallel to the red plane in Fig. 2.32 and passes through the two trans- β -diketonate ligands, which is consistent with the results of ab initio calculations with only a small deviation of 7.6° . The complex shows the similar relaxation dynamics properties to $[\text{Dy}(\text{hfac})_3(\text{Lcap6})]$ under zero- or nonzero-dc field with only a small increase of effective barriers. Notably, the hysteresis loops at 2 K can be recorded in the MCD spectrum on a solid solution, highlighting the molecular origin of magnetization dynamics.

2.3.5 The SIMMs with Radical Ligands

To date, the most widely investigated family of radical ligands in the field of lanthanide molecular magnets is the nitronyl nitroxide radical systems (NIT-R in Fig. 2.21), which show the high stability and the strong coordinate ability to lanthanide ions in the β -diketone lanthanide systems [84]. Nowadays, a great number of such lanthanide complexes have been reported, ranging from the mononuclear, binuclear and even to single-chain complexes bridged by the NIT radicals. As is well known, the first rare earth-radical-based coordination polymer exhibiting SCM behavior was reported in 2005 by Sessoli [65]. In the chain molecule, the radical NIT-C₆H₄Oph plays an important bridging role between the Dy ions, leading to a low ratio of interchain/intrachain interactions. In addition, several binuclear Tb complexes bridged by the NIT-R radical ligands show the strong SMM behavior, which will be discussed in next chapter. In contrast, the reported mononuclear Tb/Dy complexes with the NIT-R radical demonstrated the relatively weak SMM behavior and fast QTM [85–93]. Here, only two representative examples were exhibited. In addition, other types of radical systems were also explored recently with some examples showing the strong SMM behavior, which further expand this field in pursuit of the better lanthanide–radical SMM systems.

As shown in Fig. 2.33, the monodentate and bidentate chelate NIT-R radical ligands lead to the distinct structures in lanthanide coordination complexes due to their different coordinate modes. In the first example, $[\text{Tb}(\text{hfac})_3(\text{NIT-PhOEt})_2]$, two radical ligands are coordinating to the central Tb ion through the oxygen atom of one N-O group, leading to the novel mononuclear tri-spin lanthanide system, where the Tb ion is located in a distorted dodecahedron geometry [85]. The continuously increasing $\chi_m T$ values with the decreasing temperature are indicative of the strong ferromagnetic interactions between Tb ion and the radical ligands. Importantly, the clear blocking behavior of magnetization was observed in the complex, as indicated in the ac susceptibility signal under zero-dc applied field in Fig. 2.33. The effective barrier was given to be 29 K, which seems to be so small compared to the above lanthanide SMM. For the second example, the bidentate radical ligand provides a same coordinate mode to the common capping ligand, thus leading to the formation of the similar coordinate geometry to the seminal complex around Tb ion [86]. Similarly, the ferromagnetic interactions were observed between the Tb ion and radical ligand. Meanwhile, the complex also displays the temperature- and frequency-dependent χ'' signals below 6 K. However, a smaller effective barrier, $U_{\text{eff}} = 17$ K, was demonstrated under zero-dc applied

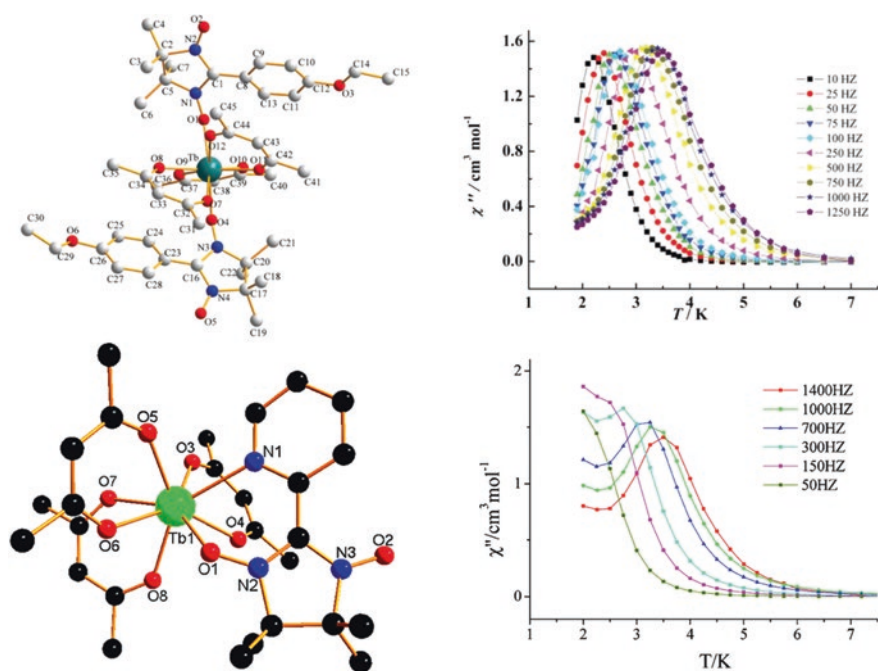


Fig. 2.33 The crystal structure and relaxation dynamics of two Tb β -diketone systems with NIT-R radical ligands. *Top* Reproduced from Ref. [85] by permission of The Royal Society of Chemistry. *Bottom* Reprinted with the permission from Ref. [86]. Copyright 2010 American Chemical Society

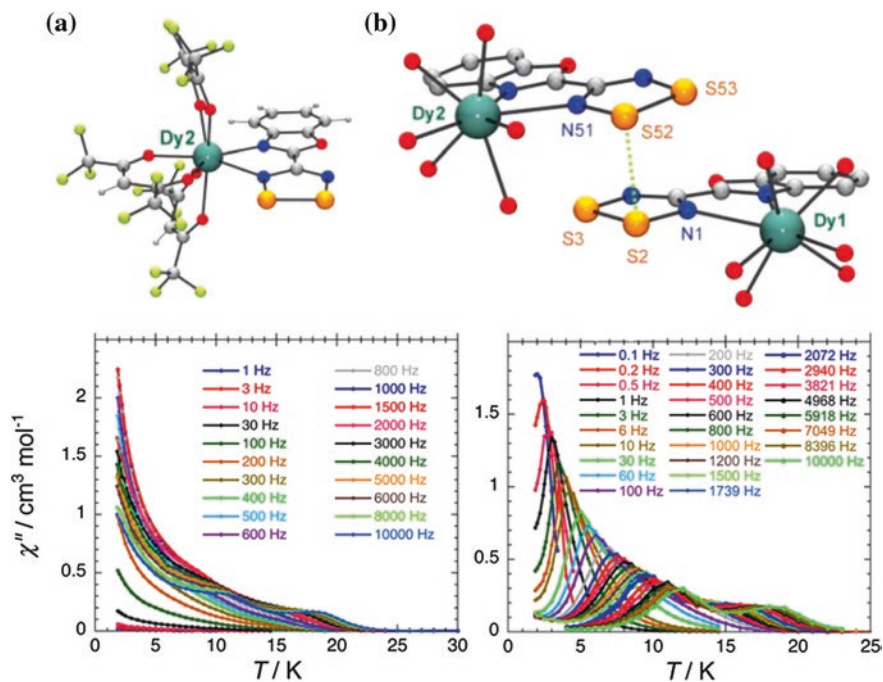


Fig. 2.34 The crystal structure and relaxation dynamics under zero- and nonzero-dc fields of Dy β -diketone systems with boADTDA radical ligand. Reprinted with the permission from Ref. [94]. Copyright 2013 American Chemical Society

field. Here although the SMM properties are not so fascinating, it is a helpful exploration for the novel lanthanide-radical coupling system.

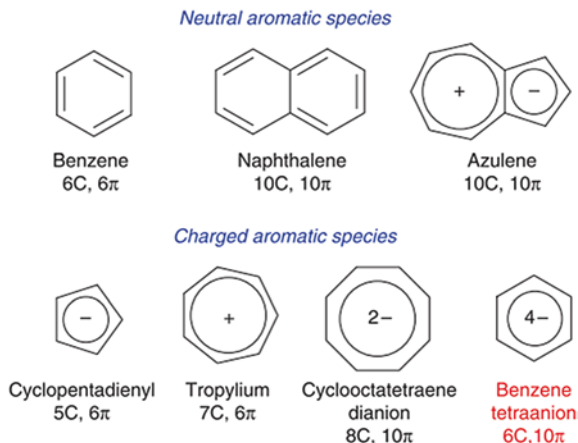
Furthermore, the new type of chelate radical ligand, 4-(benzoxazol-2'-yl)-1,2,3,5-dithiadiazolyl (boADTDA in Fig. 2.21) [94], was also explored to construct the lanthanide-radical SMM system. As a result, a supramolecular species composed of a pair of non-equivalent Dy^{III}-radical complexes was obtained, as seen in Fig. 2.34, where two Dy ions are located in the different coordinate geometries, one being the distorted SAP geometry and the other being the dodecahedral geometry. In the molecular pairs, the close S-S contact leads to a *twisted-cofacial* interaction between two radical ligands, which further results in strong antiferromagnetic coupling between the DTDA radical spins. Obviously, the Dy complex exhibits the out-of-phase signals of ac susceptibility under zero-dc applied field, but the rapidly increasing χ'' values at low temperature are indicative of the presence of fast QTM relaxation, which may be related to the above antiferromagnetic coupling within the molecule pairs. Further, the application of a dc applied field leads to the occurrence of two relaxation processes (Fig. 2.34), which should correspond to the presence of two different metal centers in the complex. In particular, the almost same effective barriers were extracted to be 100 K for the two relaxation processes, but showing the different pre-exponential factors.

2.4 Organometallic SIMMs

To date, the most significant achievements in the SIMM field were present in the organometallic lanthanide SMMs, which exhibit not only the large effective barriers but also the very high blocking temperature (T_B) close to the T_B record achieved in the N_2^{3-} -bridged Tb_2 SMMs. Compared with the common O- or N-based coordination complexes, the organometallic systems provide alternative special chemical environments due to the applications of air-sensitive reagents with the extremely strong basicity, which potentially results in the stronger and more axial crystal field around lanthanide ions as well as thus the improved SMM properties [95]. In fact, the exploration into this aspect can date back to 2010 when an organometallic Dy_2 complex shows typical SMM behavior [96], but the mononuclear organometallic lanthanide SMMs were developed later. Now in the field, the most widely investigated species are the lanthanide systems coordinated by the negative-charged aromatic ligands, mainly cyclopentadienide (Cp^-) and cyclooctatetraene dianion (COT^{2-}) [9, 14, 20, 33], which exhibits the similar aromaticity to the neutral naphthalene and benzenoid compounds (Fig. 2.35) with the π electron cloud created by the multiple sp^2 carbon atoms [97]. The first reported example was $[(\eta^5-Cp^*)Er(\eta^8-COT)]$ SIMM [9] exhibiting the high effective barriers and blocking temperature, which further stimulates the researching interests in the new type of lanthanide SMM system. To date, the system has been extended well with the several important examples showing the high SMM performance, which achieves its celebrity status in the developments of SIMMs.

The first system, $[(Cp^*)Ln(COT)]$ ($Ln = Tb^{III}, Dy^{III}, Ho^{III}, Er^{III}, Tm^{III}, Y^{III}$; $Cp^* = C_5Me_5^-$; $COT = C_8H_8^{2-}$), was reported by S. Gao and coworkers since 2011 [9, 98]. The complex features the single lanthanide ion sandwiched by two unparallel aromatic ligands with a slight tilt angle, an important factor in determining the quantum tunneling relaxation time. Further research demonstrates

Fig. 2.35 The neutral and charged aromatic systems with the π electron cloud created by the multiple sp^2 carbon atoms. Reprinted by permission from Macmillan Publishers Ltd. Ref. [97], copyright 2013



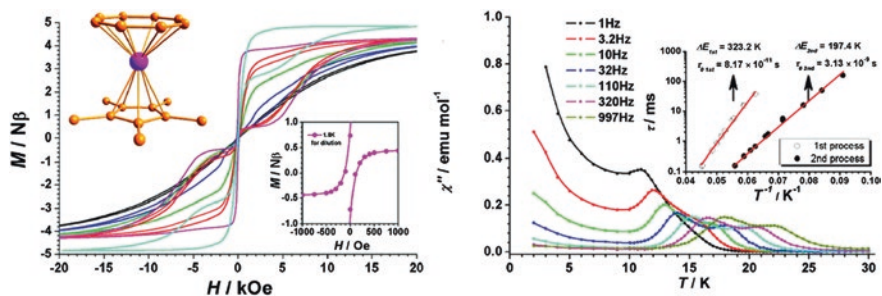


Fig. 2.36 The crystal structure and magnetic properties of $[(\text{Cp}^*)\text{Er}(\text{COT})]$. Reprinted with the permission from Ref. [9]. Copyright 2011 American Chemical Society

that the bending of the axis induced by asymmetric intermolecule interactions increases with the increment of ionic radius of lanthanide ions from Tm to Tb ions. Nevertheless, the sandwiched modes from two ligands with the high π -electron density are favorable to the strong axial anisotropy of lanthanide ions. Importantly, the ac susceptibility data reveal that the Er^{III} compound behaves as the better SIMM compared with other lanthanide complexes. Here, the out-of-phase signals in Fig. 2.36 demonstrate two clear maxima below 25 K indicating the two relaxation processes, as a possible result of the presence of two conformations in the crystal lattice. Therefore, two high effective barriers were given to be 323 and 197 K, which are among the highest effective barriers discovered to date. Further, the butterfly-shaped hysteresis loop with a coercive field was observed at 1.8 K, indicating the strongly blocking behavior for magnetic moments. Here, the strong SMM behavior mainly results from the strong single-ion anisotropy of Er ion, further leading to an Ising ground state well separated from other excited states, which has been confirmed by the recent angular-resolved magnetometry experiments and ab initio calculations [99]. Furthermore, both Dy^{III} and Ho^{III} compounds exhibit the field-induced SMM behavior.

Remarkably, two stronger Er-based SIMMs similar to above complex were obtained by J.R. Long group through applying the single aromatic ligand, COT^{2-} [33]. Here, both complexes contain the same part of $[\text{Er}(\text{COT})_2]^-$ with some slight differences and show the almost same static and dynamic magnetic properties. Therefore, only one example was described below, as shown in Fig. 2.37. Here, two almost coplanar COT^{2-} ligands lead to a higher symmetry close to D_{8h} in the $[\text{Er}(\text{COT})_2]^-$ part compared to the above $[(\text{Cp}^*)\text{Ln}(\text{COT})]$ complex. Dc magnetic susceptibility data reveal a precipitous drop of $\chi_m T$ values below 10 K indicating the strongly blocking of magnetization (Fig. 2.37). In order to further explore the magnetic blocking behavior, the ac magnetic susceptibility measurements were also performed, and therefore, the clear out-of-phase maxima are present below 27 K, which gives a effective barrier of 147 cm^{-1} (212 K). Most importantly, the hysteresis loops were observed below 10 K, which represents the highest blocking temperature yet observed for a mononuclear complex and the second highest for any single-molecule magnet. Nevertheless, as seen in most lanthanide SIMMs,

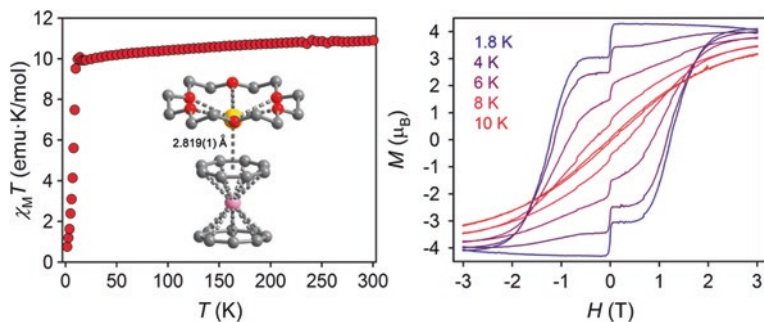


Fig. 2.37 The crystal structure and static magnetic properties of $[\text{Er}(\text{COT})_2]^-$. Reprinted with the permission from Ref. [33]. Copyright 2013 American Chemical Society

the magnetization in hysteresis loop still exhibits a sudden drop when approaching zero field, thus leading to the disappearance of coercive field. Further investigations indicate that such a drop mainly arise from the magnetic avalanche effects induced by intermolecular dipolar interactions. Therefore, the magnetic dilution for the above samples results in the obviously enhanced coercive field, and only a small drop of magnetization was observed at zero field, as seen in Fig. 2.37.

To further gain insight into the magnetic blocking mechanism in the molecule, L.F. Chibotaru et al. performed ab initio calculations for the Dy and Er complexes, as shown in Fig. 2.38 [20]. The results indicated that the local high symmetry for

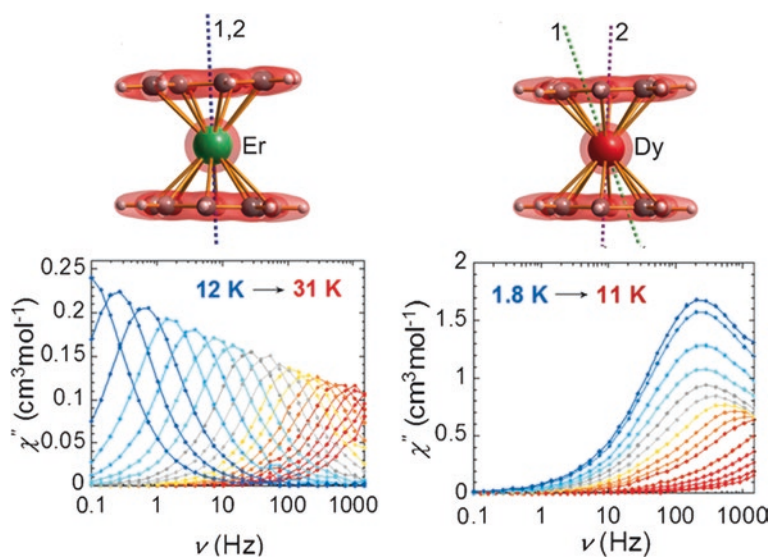


Fig. 2.38 The calculated anisotropic axes and relaxation dynamics of the Er and Dy complexes in $[\text{Er}(\text{COT})_2]^-$. Reproduced from Ref. [20] by permission of John Wiley & Sons Ltd.

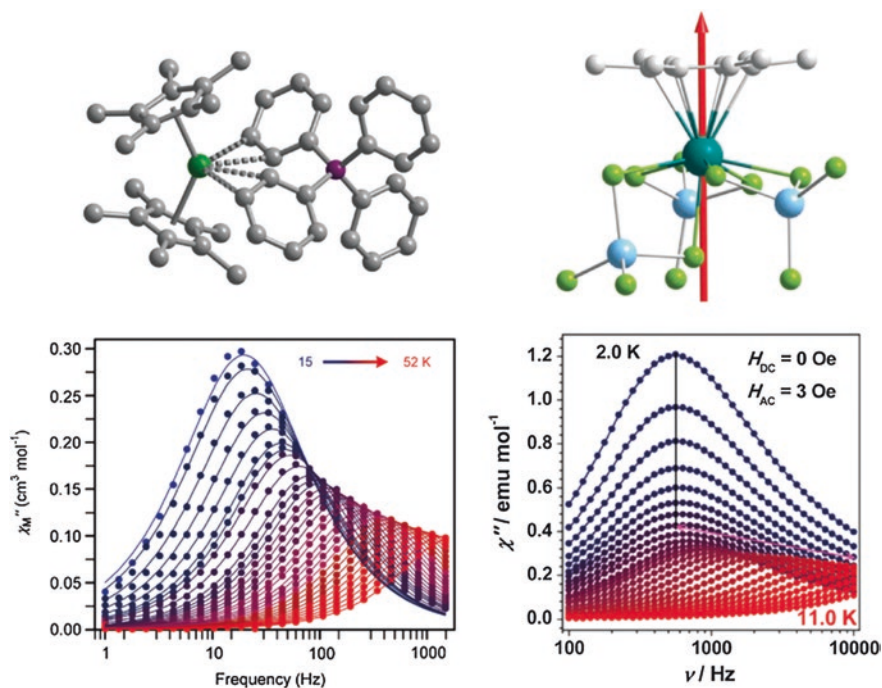


Fig. 2.39 The crystal structures and relaxation dynamics of [Cp*₂Ln(BPh₄)] from J.R. Long and [(C₆Me₆)Dy(AlCl₄)₃] from S. Gao. *Left* Reproduced from Ref. [101] by permission of John Wiley & Sons Ltd. *Right* Reproduced from Ref. [102] by permission of The Royal Society of Chemistry

the Er complex plays an extremely crucial role in promoting the magnetic relaxation and suppressing the QTM. In the Er complex, the ground state is well separated from the low-lying excited states and, importantly, the ground and first excited Kramers doublets exhibit the strong uniaxial anisotropy and almost collinear anisotropy axes, thus leading to the magnetic relaxation pathway via second excited state. By contrast, the corresponding Dy analogue exhibits the weak SMM behavior, which is mainly due to the low ground state and fast QTM arising from the large transversal components. Further, the determination of crystal parameters gives a reasonable explanation for such a large difference. The important negative crystal parameters B_2^0 and B_4^0 in the Er complex reveal the stronger equatorial component of the ligand field than the axial one, which supports the easy axis anisotropy and the large spin ground state for the Er ion, while the opposite case occurs in Dy complex. In addition, the trimethylsilyl substituted Dy and Er species reported by M. Murugesu exhibit similar SMM properties [100].

Recently, the J. R. Long and S. Gao groups explored the low-symmetric organometallic lanthanide systems, as shown in Fig. 2.39, both of which exhibit the typical SMM properties. In particular, for the first system, [Cp*₂Ln(BPh₄)] (Ln = Tb and Dy) [101], the Dy species shows the strongly magnetic blocking behavior, as

evidenced by the high blocking temperature up to 52 K characterized by the out-of-phase signals of ac susceptibility data in Fig. 2.39. Further, the effective barrier was extracted to be 331 cm^{-1} (477 K), which is of the highest known for the mononuclear Dy-based SMMs. Meanwhile, the Tb analogue also exhibits the robust field-induced SMM behavior with a large effective barrier of 216 cm^{-1} (311 K). Here, the authors attributed their large barriers to the bent ligand field presented to the Ln^{III} centers due to the weak interactions between the lanthanide ions and BPh_4^- anion. The second example, $[(\text{C}_6\text{Me}_6)\text{Dy}(\text{AlCl}_4)_3]$, reported by S. Gao et al. [102] demonstrates a half-sandwich structure with the coordination of a neutral π -bonded arene ligand to Dy ion. An effective barrier of 101 K was present in the complex under zero-dc applied field, which mainly arises from the strong single-ion anisotropy of Dy ion indicated by the ab initio calculations. Finally, it is noted that in spite of the high barriers the fast tunneling relaxation is clearly present in those complexes compared with the above double-decker organometallic complexes, which is as a main result of the internal low-symmetric factors of local crystal field.

2.5 Conclusion

The most important lanthanide SIMM systems including the lanthanide phthalocyanine, lanthanide β -diketone, and organometallic lanthanide systems have been reviewed in detail in this chapter. Here, we provide a clear guideline for designing the effective SMMs in each class through systematically discussing the corresponding lanthanide SIMMs discovered to date. In addition, some low-symmetric lanthanide complexes with the local axial coordination geometries around lanthanide ions which also behave as typical SMMs even with the very high effective barriers are not discussed here. Undoubtedly, the lanthanide SIMM is the most important class in the development of SMM to date; for that, they play an outstanding role not only in the assembly of lanthanide SMMs with high effective barriers and blocking temperature, but also in elucidating the correlation between the magnetic properties and the structural features. In particular, both the previous $[\text{LnPc}_2]$ complexes and the recently discovered lanthanide organometallic complexes demonstrate the great potential in further promoting the SMM properties and the future technological applications as quantum bits.

References

1. Miller JS (2011) Magnetically ordered molecule-based materials. *Chem Soc Rev* 40(6):3266–3296. doi:10.1039/c0cs00166j
2. Miller JS, Epstein AJ (2000) Molecule-based magnets-an overview. *MRS Bull* 25(11):21–30
3. Sun H-L, Wang Z-M, Gao S (2010) Strategies towards single-chain magnets. *Coord Chem Rev* 254(9–10):1081–1100. doi:10.1016/j.ccr.2010.02.010

- Miyasaka H, Julve M, Yamashita M et al (2009) Slow dynamics of the magnetization in one-dimensional coordination polymers: single-chain magnets. *Inorg Chem* 48(8):3420–3437. doi:[10.1021/ic802050j](https://doi.org/10.1021/ic802050j)
- Christou G, Gatteschi D, Hendrickson DN et al (2000) Single-molecule magnets. *MRS Bull* 25(11):66–71. doi:[10.1557/mrs2000.204](https://doi.org/10.1557/mrs2000.204)
- Bernot K, Luzon J, Bogani L et al (2009) Magnetic anisotropy of dysprosium(III) in a low-symmetry environment: a theoretical and experimental investigation. *J Am Chem Soc* 131(15):5573–5579. doi:[10.1021/ja8100038](https://doi.org/10.1021/ja8100038)
- Rinehart JD, Fang M, Evans WJ et al (2011) Strong exchange and magnetic blocking in N_2^{3-} -radical-bridged lanthanide complexes. *Nat Chem* 3(7):538–542. doi:[10.1038/nchem.1063](https://doi.org/10.1038/nchem.1063)
- Jiang SD, Wang BW, Su G et al (2010) A mononuclear dysprosium complex featuring single-molecule-magnet behavior. *Angew Chem Int Ed* 49(30):7448–7451. doi:[10.1002/anie.201004027](https://doi.org/10.1002/anie.201004027)
- Jiang S-D, Wang B-W, Sun H-L et al (2011) An organometallic single-ion magnet. *J Am Chem Soc* 133(13):4730–4733. doi:[10.1021/ja200198v](https://doi.org/10.1021/ja200198v)
- Feltham HLC, Brooker S (2014) Review of purely 4f and mixed-metal *nd-4f* single-molecule magnets containing only one lanthanide ion. *Coord Chem Rev* 276:1–33. doi:[10.1016/j.ccr.2014.05.011](https://doi.org/10.1016/j.ccr.2014.05.011)
- Ishikawa N, Sugita M, Ishikawa T et al (2003) Lanthanide double-decker complexes functioning as magnets at the single-molecular level. *J Am Chem Soc* 125(29):8694–8695. doi:[10.1021/ja029629n](https://doi.org/10.1021/ja029629n)
- AlDamen MA, Clemente-Juan JM, Coronado E et al (2008) Mononuclear lanthanide single-molecule magnets based on polyoxometalates. *J Am Chem Soc* 130(28):8874–8875. doi:[10.1021/ja801659m](https://doi.org/10.1021/ja801659m)
- Chen G-J, Guo Y-N, Tian J-L et al (2012) Enhancing anisotropy barriers of dysprosium(III) single-ion magnets. *Chem Eur J* 18(9):2484–2487. doi:[10.1002/chem.201103816](https://doi.org/10.1002/chem.201103816)
- Jeletic M, Lin P-H, Le Roy JJ et al (2011) An organometallic sandwich lanthanide single-ion magnet with an unusual multiple relaxation mechanism. *J Am Chem Soc* 133(48):19286–19289. doi:[10.1021/ja207891y](https://doi.org/10.1021/ja207891y)
- Freedman DE, Harman WH, Harris TD et al (2010) Slow magnetic relaxation in a high-spin iron(II) complex. *J Am Chem Soc* 132(4):1224–1225. doi:[10.1021/ja909560d](https://doi.org/10.1021/ja909560d)
- Zadrozny JM, Long JR (2011) Slow magnetic relaxation at zero field in the tetrahedral complex $[Co(SPh)_4]^{2-}$. *J Am Chem Soc* 133(51):20732–20734. doi:[10.1021/ja210014z](https://doi.org/10.1021/ja210014z)
- Zadrozny JM, Xiao DJ, Atanasov M et al (2013) Magnetic blocking in a linear iron(I) complex. *Nat Chem* 5(7):577–581. doi:[10.1038/nchem.1630](https://doi.org/10.1038/nchem.1630)
- Rinehart JD, Long JR (2009) Slow magnetic relaxation in a trigonal prismatic uranium(III) complex. *J Am Chem Soc* 131(35):12558–12559. doi:[10.1021/ja906012u](https://doi.org/10.1021/ja906012u)
- Magnani N, Apostolidis C, Morgenstern A et al (2011) Magnetic memory effect in a transuranic mononuclear complex. *Angew Chem Int Ed* 50(7):1696–1698. doi:[10.1002/anie.201006619](https://doi.org/10.1002/anie.201006619)
- Ungur L, Le Roy JJ, Korobkov I et al (2014) Fine-tuning the local symmetry to attain record blocking temperature and magnetic remanence in a single-ion magnet. *Angew Chem Int Ed* 53(17):4413–4417. doi:[10.1002/anie.201310451](https://doi.org/10.1002/anie.201310451)
- Zhang P, Zhang L, Wang C et al (2014) Equatorially coordinated lanthanide single ion magnets. *J Am Chem Soc* 136(12):4484–4487. doi:[10.1021/ja500793x](https://doi.org/10.1021/ja500793x)
- Watanabe A, Yamashita A, Nakano M et al (2011) Multi-path magnetic relaxation of mono-dysprosium(III) single-molecule magnet with extremely high barrier. *Chem Eur J* 17(27):7428–7432. doi:[10.1002/chem.201003538](https://doi.org/10.1002/chem.201003538)
- Rinehart JD, Long JR (2011) Exploiting single-ion anisotropy in the design of f-element single-molecule magnets. *Chem Sci* 2(11):2078–2085. doi:[10.1039/C1SC00513H](https://doi.org/10.1039/C1SC00513H)
- Cucinotta G, Perfetti M, Luzon J et al (2012) Magnetic anisotropy in a dysprosium/DOTA single-molecule magnet: beyond simple magneto-structural correlations. *Angew Chem Int Ed* 51(7):1606–1610. doi:[10.1002/anie.201107453](https://doi.org/10.1002/anie.201107453)

25. Boulon M-E, Cucinotta G, Luzon J et al (2013) Magnetic anisotropy and spin-parity effect along the series of lanthanide complexes with DOTA. *Angew Chem Int Ed* 52(1):350–354. doi:[10.1002/anie.201205938](https://doi.org/10.1002/anie.201205938)
26. Meihaus KR, Minasian SG, Lukens WW et al (2014) Influence of pyrazolate vs N-heterocyclic carbene ligands on the slow magnetic relaxation of homoleptic tris-chelate lanthanide(III) and uranium(III) complexes. *J Am Chem Soc* 136(16):6056–6068. doi:[10.1021/ja501569t](https://doi.org/10.1021/ja501569t)
27. Benelli C, Gatteschi D (2002) Magnetism of lanthanides in molecular materials with transition-metal ions and organic radicals. *Chem Rev* 102(6):2369–2388. doi:[10.1021/cr010303r](https://doi.org/10.1021/cr010303r)
28. Skomski R (2008) Simple models of magnetism. Oxford University Press, New York
29. Zhang P, Guo Y-N, Tang J (2013) Recent advances in dysprosium-based single molecule magnets: structural overview and synthetic strategies. *Coord Chem Rev* 257(11–12):1728–1763. doi:[10.1016/j.ccr.2013.01.012](https://doi.org/10.1016/j.ccr.2013.01.012)
30. Ungur L, Chibotaru LF (2011) Magnetic anisotropy in the excited states of low symmetry lanthanide complexes. *Phys Chem Chem Phys* 13(45):20086–20090. doi:[10.1039/C1CP22689D](https://doi.org/10.1039/C1CP22689D)
31. Ishikawa N, Sugita M, Wernsdorfer W (2005) Quantum tunneling of magnetization in lanthanide single-molecule magnets: bis(phthalocyaninato)terbium and bis(phthalocyaninato) dysprosium anions. *Angew Chem Int Ed* 44(19):2931–2935. doi:[10.1002/anie.200462638](https://doi.org/10.1002/anie.200462638)
32. da Cunha TT, Jung J, Boulon M-E et al (2013) Magnetic poles determinations and robustness of memory effect upon solubilization in a Dy^{III}-based single ion magnet. *J Am Chem Soc* 135(44):16332–16335. doi:[10.1021/ja4089956](https://doi.org/10.1021/ja4089956)
33. Meihaus KR, Long JR (2013) Magnetic blocking at 10 K and a dipolar-mediated avalanche in salts of the bis(η^8 -cyclooctatetraenide) complex [Er(COT)₂]⁻. *J Am Chem Soc* 135(47):17952–17957. doi:[10.1021/ja4094814](https://doi.org/10.1021/ja4094814)
34. Guo Y-N, Ungur L, Granroth GE et al (2014) An NCN-pincer ligand dysprosium single-ion magnet showing magnetic relaxation via the second excited state. *Sci Rep* 4:5471. doi:[10.1038/srep05471](https://doi.org/10.1038/srep05471)
35. Sorace L, Benelli C, Gatteschi D (2011) Lanthanides in molecular magnetism: old tools in a new field. *Chem Soc Rev* 40(6):3092–3104. doi:[10.1039/C0CS00185F](https://doi.org/10.1039/C0CS00185F)
36. Liu J-L, Chen Y-C, Zheng Y-Z et al (2013) Switching the anisotropy barrier of a single-ion magnet by symmetry change from quasi-D_{5h} to quasi-O_h. *Chem Sci* 4(8):3310–3316. doi:[10.1039/c3sc50843a](https://doi.org/10.1039/c3sc50843a)
37. Baldovı JJ, Cardona-Serra S, Clemente-Juan JM et al (2012) Rational design of single-ion magnets and spin qubits based on mononuclear lanthanoid complexes. *Inorg Chem* 51(22):12565–12574. doi:[10.1021/ic302068c](https://doi.org/10.1021/ic302068c)
38. Gorller-Walrand C, Binnemans K (1996) Rationalization of crystal-field parametrization Chap. 155. In: Gschneidner KA Jr, LeRoy E (eds) Handbook on the physics and chemistry of rare earths, vol 23. Elsevier, Amsterdam, pp 121–283. doi:[10.1016/S0168-1273\(96\)23006-5](https://doi.org/10.1016/S0168-1273(96)23006-5)
39. Dolbecq A, Dumas E, Mayer CR et al (2010) Hybrid organic–inorganic polyoxometalate compounds: from structural diversity to applications. *Chem Rev* 110(10):6009–6048. doi:[10.1021/cr1000578](https://doi.org/10.1021/cr1000578)
40. Huang C (2010) Rare earth coordination chemistry: fundamentals and applications. John Wiley & Sons (Asia) Pte Ltd. Singapore
41. Ishikawa N (2010) Phthalocyanine-based magnets. In: Jiang J (ed) Functional phthalocyanine molecular materials, vol 135. Structure and bonding. Springer, Berlin, pp 211–228. doi:[10.1007/978-3-642-04752-7_7](https://doi.org/10.1007/978-3-642-04752-7_7)
42. Takamatsu S, Ishikawa T, Koshihara S et al (2007) Significant increase of the barrier energy for magnetization reversal of a single-4f-ionic single-molecule magnet by a longitudinal contraction of the coordination space. *Inorg Chem* 46(18):7250–7252. doi:[10.1021/ic700954t](https://doi.org/10.1021/ic700954t)
43. De Cian A, Moussavi M, Fischer J et al (1985) Synthesis, structure, and spectroscopic and magnetic properties of lutetium(III) phthalocyanine derivatives: LuPc₂·CH₂Cl₂ and [LuPc(OAc)(H₂O)₂]·H₂O·2CH₃OH. *Inorg Chem* 24(20):3162–3167. doi:[10.1021/ic00214a016](https://doi.org/10.1021/ic00214a016)

44. Ishikawa N, Sugita M, Okubo T et al (2003) Determination of ligand-field parameters and f-electronic structures of double-decker bis(phthalocyaninato)lanthanide complexes. *Inorg Chem* 42(7):2440–2446. doi:[10.1021/ic026295u](https://doi.org/10.1021/ic026295u)
45. Thomas L, Lioni F, Ballou R et al (1996) Macroscopic quantum tunnelling of magnetization in a single crystal of nanomagnets. *Nature* 383(6596):145–147. doi:[10.1038/383145a0](https://doi.org/10.1038/383145a0)
46. Ishikawa N, Sugita M, Wernsdorfer W (2005) Nuclear spin driven quantum tunneling of magnetization in a new lanthanide single-molecule magnet: bis(phthalocyaninato)holmium anion. *J Am Chem Soc* 127(11):3650–3651. doi:[10.1021/ja0428661](https://doi.org/10.1021/ja0428661)
47. Ishikawa N, Ohno O, Kaizu Y (1993) Electronic states of bis(phthalocyaninato)lutetium radical and its related compounds: the application of localized orbital basis set to open-shell phthalocyanine dimers. *J Phys Chem* 97(5):1004–1010. doi:[10.1021/j100107a006](https://doi.org/10.1021/j100107a006)
48. Takamatsu S, Ishikawa N (2007) A theoretical study of a drastic structural change of bis(phthalocyaninato)lanthanide by ligand oxidation: towards control of ligand field strength and magnetism of single-lanthanide-ionic single molecule magnet. *Polyhedron* 26(9–11):1859–1862. doi:[10.1016/j.poly.2006.09.020](https://doi.org/10.1016/j.poly.2006.09.020)
49. Ishikawa N, Sugita M, Tanaka N et al (2004) Upward temperature shift of the intrinsic phase lag of the magnetization of bis(phthalocyaninato)terbium by ligand oxidation creating an $S = 1/2$ spin. *Inorg Chem* 43(18):5498–5500. doi:[10.1021/ic049348b](https://doi.org/10.1021/ic049348b)
50. Ishikawa N, Mizuno Y, Takamatsu S et al (2008) Effects of chemically induced contraction of a coordination polyhedron on the dynamical magnetism of bis(phthalocyaninato)disprosium, a single-4f-ionic single-molecule magnet with a Kramers ground state. *Inorg Chem* 47(22):10217–10219. doi:[10.1021/ic8014892](https://doi.org/10.1021/ic8014892)
51. Gonidec M, Davies ES, McMaster J et al (2010) Probing the magnetic properties of three interconvertible redox states of a single-molecule magnet with magnetic circular dichroism spectroscopy. *J Am Chem Soc* 132(6):1756–1757. doi:[10.1021/ja9095895](https://doi.org/10.1021/ja9095895)
52. McInnes EJJ, Pidcock E, Oganessian VS et al (2002) Optical detection of spin polarization in single-molecule magnets $[\text{Mn}_{12}\text{O}_{12}(\text{O}_2\text{CR})_{16}(\text{H}_2\text{O})_4]$. *J Am Chem Soc* 124(31):9219–9228. doi:[10.1021/ja020456b](https://doi.org/10.1021/ja020456b)
53. Gonidec M, Krivokapic I, Vidal-Gancedo J et al (2013) Highly reduced double-decker single-molecule magnets exhibiting slow magnetic relaxation. *Inorg Chem* 52(8):4464–4471. doi:[10.1021/ic3027418](https://doi.org/10.1021/ic3027418)
54. Ganivet CR, Ballesteros B, de la Torre G et al (2013) Influence of peripheral substitution on the magnetic behavior of single-ion magnets based on homo- and heteroleptic Tb^{III} bis(phthalocyaninate). *Chem Eur J* 19(4):1457–1465. doi:[10.1002/chem.201202600](https://doi.org/10.1002/chem.201202600)
55. Gonidec M, Luis F, Vilchez Á et al (2010) A liquid-crystalline single-molecule magnet with variable magnetic properties. *Angew Chem Int Ed* 49(9):1623–1626. doi:[10.1002/anie.200905007](https://doi.org/10.1002/anie.200905007)
56. Gonidec M, Amabilino DB, Veciana J (2012) Novel double-decker phthalocyaninato terbium(III) single molecule magnets with stabilised redox states. *Dalton Trans* 41(44):13632–13639. doi:[10.1039/c2dt31171b](https://doi.org/10.1039/c2dt31171b)
57. Katoh K, Isshiki H, Komeda T et al (2011) Multiple-decker phthalocyaninato $\text{Tb}(\text{III})$ single-molecule magnets and $\text{Y}(\text{III})$ complexes for next generation devices. *Coord Chem Rev* 255(17–18):2124–2148. doi:[10.1016/j.ccr.2011.02.024](https://doi.org/10.1016/j.ccr.2011.02.024)
58. Katoh K, Umetsu K, Breedlove Brian K et al (2012) Magnetic relaxation behavior of a spatially closed dysprosium(III) phthalocyaninato double-decker complex. *Sci China Chem* 55(6):918–925. doi:[10.1007/s11426-012-4615-9](https://doi.org/10.1007/s11426-012-4615-9)
59. Waters M, Moro F, Krivokapic I et al (2012) Synthesis, characterisation and magnetic study of a cyano-substituted dysprosium double decker single-molecule magnet. *Dalton Trans* 41(4):1128–1130. doi:[10.1039/c1dt11880c](https://doi.org/10.1039/c1dt11880c)
60. Tanaka D, Inose T, Tanaka H et al (2012) Proton-induced switching of the single molecule magnetic properties of a porphyrin based Tb^{III} double-decker complex. *Chem Commun* 48(63):7796–7798. doi:[10.1039/c2cc00086e](https://doi.org/10.1039/c2cc00086e)

61. Wang H, Wang K, Tao J et al (2012) Twist angle perturbation on mixed (phthalocyaninato) (porphyrinato) dysprosium(III) double-decker SMMs. *Chem Commun* 48(24):2973–2975. doi:[10.1039/c2cc16543k](https://doi.org/10.1039/c2cc16543k)
62. Williams UJ, Mahoney BD, DeGregorio PT et al (2012) A comparison of the effects of symmetry and magnetoanisotropy on paramagnetic relaxation in related dysprosium single ion magnets. *Chem Commun* 48(45):5593–5595. doi:[10.1039/c2cc31227a](https://doi.org/10.1039/c2cc31227a)
63. AlDamen MA, Cardona-Serra S, Clemente-Juan JM et al (2009) Mononuclear lanthanide single molecule magnets based on the polyoxometalates $[\text{Ln}(\text{W}_5\text{O}_{18})_2]^{9-}$ and $[\text{Ln}(\beta_2\text{-SiW}_{11}\text{O}_{39})_2]^{13-}$ ($\text{Ln}^{\text{III}} = \text{Tb}, \text{Dy}, \text{Ho}, \text{Er}, \text{Tm}, \text{and Yb}$). *Inorg Chem* 48(8):3467–3479. doi:[10.1021/ic801630z](https://doi.org/10.1021/ic801630z)
64. Cardona-Serra S, Clemente-Juan JM, Coronado E et al (2012) Lanthanoid single-ion magnets based on polyoxometalates with a 5-fold symmetry: the series $[\text{LnP}_5\text{W}_{30}\text{O}_{110}]^{12-}$ ($\text{Ln}^{3+} = \text{Tb}, \text{Dy}, \text{Ho}, \text{Er}, \text{Tm}, \text{and Yb}$). *J Am Chem Soc* 134(36):14982–14990. doi:[10.1021/ja305163t](https://doi.org/10.1021/ja305163t)
65. Bogani L, Sangregorio C, Sessoli R et al (2005) Molecular engineering for single-chain-magnet behavior in a one-dimensional dysprosium-nitronyl nitroxide compound. *Angew Chem Int Ed* 44(36):5817–5821. doi:[10.1002/anie.200500464](https://doi.org/10.1002/anie.200500464)
66. Aravena D, Ruiz E (2013) Shedding light on the single-molecule magnet behavior of mononuclear Dy^{III} complexes. *Inorg Chem* 52(23):13770–13778. doi:[10.1021/ic402367c](https://doi.org/10.1021/ic402367c)
67. Chilton NF, Collison D, McInnes EJJ et al (2013) An electrostatic model for the determination of magnetic anisotropy in dysprosium complexes. *Nat Commun* 4:2551. doi:[10.1038/ncomms3551](https://doi.org/10.1038/ncomms3551)
68. Bi Y, Guo Y-N, Zhao L et al (2011) Capping ligand perturbed slow magnetic relaxation in dysprosium single-ion magnets. *Chem Eur J* 17(44):12476–12481. doi:[10.1002/chem.201101838](https://doi.org/10.1002/chem.201101838)
69. Wang Y-L, Gu B, Ma Y et al (2014) A new D_{2d} -symmetry Dy^{III} mononuclear single-molecule magnet containing a monodentate N-heterocyclic donor ligand. *CrystEngComm* 16(11):2283–2289. doi:[10.1039/c3ce42212g](https://doi.org/10.1039/c3ce42212g)
70. Cao D-K, Gu Y-W, Feng J-Q et al (2013) Mononuclear lanthanide complexes incorporating an anthracene group: structural modification, slow magnetic relaxation and multicomponent fluorescence emissions in Dy compounds. *Dalton Trans* 42(32):11436–11444. doi:[10.1039/c3dt51176f](https://doi.org/10.1039/c3dt51176f)
71. Wang Y-L, Ma Y, Yang X et al (2013) Syntheses, structures, and magnetic and luminescence properties of a new Dy^{III} -based single-ion magnet. *Inorg Chem* 52(13):7380–7386. doi:[10.1021/ic400006n](https://doi.org/10.1021/ic400006n)
72. Silva MR, Martin-Ramos P, Coutinho JT et al (2014) Effect of the capping ligand on luminescent erbium(III) β -diketonate single-ion magnets. *Dalton Trans* 43(18):6752–6761. doi:[10.1039/c4dt00168k](https://doi.org/10.1039/c4dt00168k)
73. Li X-L, Chen C-L, Gao Y-L et al (2012) Modulation of homochiral Dy^{III} complexes: single-molecule magnets with ferroelectric properties. *Chem Eur J* 18(46):14632–14637. doi:[10.1002/chem.201201190](https://doi.org/10.1002/chem.201201190)
74. Li D-P, Zhang X-P, Wang T-W et al (2011) Distinct magnetic dynamic behavior for two polymorphs of the same $\text{Dy}(\text{III})$ complex. *Chem Commun* 47(24):6867–6869. doi:[10.1039/C1CC11659B](https://doi.org/10.1039/C1CC11659B)
75. Li D-P, Wang T-W, Li C-H et al (2010) Single-ion magnets based on mononuclear lanthanide complexes with chiral schiff base ligands $[\text{Ln}(\text{FTA})_3\text{L}]$ ($\text{Ln} = \text{Sm}, \text{Eu}, \text{Gd}, \text{Tb}$ and Dy). *Chem Commun* 46(17):2929–2931. doi:[10.1039/B924547B](https://doi.org/10.1039/B924547B)
76. Wang Y, Li X-L, Wang T-W et al (2009) Slow relaxation processes and single-ion magnetic behaviors in dysprosium-containing complexes. *Inorg Chem* 49(3):969–976. doi:[10.1021/ic901720a](https://doi.org/10.1021/ic901720a)
77. Liu C-M, Zhang D-Q, Zhu D-B (2013) Field-induced single-ion magnets based on enantiopure chiral β -diketonate ligands. *Inorg Chem* 52(15):8933–8940. doi:[10.1021/ic4011218](https://doi.org/10.1021/ic4011218)

78. Coronado E, Galan-Mascaros JR, Gomez-Garcia CJ et al (2000) Coexistence of ferromagnetism and metallic conductivity in a molecule-based layered compound. *Nature* 408(6811):447–449. doi:[10.1038/35044035](https://doi.org/10.1038/35044035)
79. Kubo K, Shiga T, Yamamoto T et al (2011) Electronic state of a conducting single molecule magnet based on Mn-salen type and Ni-dithiolene complexes. *Inorg Chem* 50(19): 9337–9344. doi:[10.1021/ic200863c](https://doi.org/10.1021/ic200863c)
80. Pointillart F, Le Gal Y, Golhen S et al (2011) Single-molecule magnet behaviour in a tetrathiafulvalene-based electroactive antiferromagnetically coupled dinuclear dysprosium(III) complex. *Chem Eur J* 17(37):10397–10404. doi:[10.1002/chem.201100869](https://doi.org/10.1002/chem.201100869)
81. Di Piazza E, Norel L, Costuas K et al (2011) *d-f* Heterobimetallic association between ytterbium and ruthenium carbon-rich complexes: redox commutation of near-IR luminescence. *J Am Chem Soc* 133(16):6174–6176. doi:[10.1021/ja2023515](https://doi.org/10.1021/ja2023515)
82. Norel L, Feng M, Bernot K et al (2014) Redox modulation of magnetic slow relaxation in a 4f-based single-molecule magnet with a 4d carbon-rich ligand. *Inorg Chem* 53(5):2361–2363. doi:[10.1021/ic403081y](https://doi.org/10.1021/ic403081y)
83. Norel L, Bernot K, Feng M et al (2012) A carbon-rich ruthenium decorated dysprosium single molecule magnet. *Chem Commun* 48(33):3948–3950. doi:[10.1039/c2cc30604b](https://doi.org/10.1039/c2cc30604b)
84. Woodruff DN, Winpenny REP, Layfield RA (2013) Lanthanide single-molecule magnets. *Chem Rev* 113:5110–5148. doi:[10.1021/cr400018q](https://doi.org/10.1021/cr400018q)
85. Zhou N, Ma Y, Wang C et al (2009) A monometallic tri-spin single-molecule magnet based on rare earth radicals. *Dalton Trans* 40:8489–8492. doi:[10.1039/b908639k](https://doi.org/10.1039/b908639k)
86. Wang X-L, Li L-C, Liao D-Z (2010) Slow magnetic relaxation in lanthanide complexes with chelating nitronyl nitroxide radical. *Inorg Chem* 49(11):4735–4737. doi:[10.1021/ic100008g](https://doi.org/10.1021/ic100008g)
87. Bernot K, Pointillart F, Rosa P et al (2010) Single molecule magnet behaviour in robust dysprosium-biradical complexes. *Chem Commun* 46(35):6458–6460. doi:[10.1039/c0cc00966k](https://doi.org/10.1039/c0cc00966k)
88. Wang X, Bao X, Xu P et al (2011) From discrete molecule to one-dimension chain: two new nitronyl nitroxide–lanthanide complexes exhibiting slow magnetic relaxation. *Eur J Inorg Chem* 2011(24):3586–3591. doi:[10.1002/ejic.201100296](https://doi.org/10.1002/ejic.201100296)
89. Mei X-L, Ma Y, Li L-C et al (2012) Ligand field-tuned single-molecule magnet behaviour of 2p-4f complexes. *Dalton Trans* 41:505–511. doi:[10.1039/C1DT11795E](https://doi.org/10.1039/C1DT11795E)
90. Wang X-L, Tian H-X, Ma Y et al (2011) Slow magnetic relaxation in lanthanide complexes with chelating imino nitroxide radicals. *Inorg Chem Commun* 14(11):1728–1731. doi:[10.1016/j.inoche.2011.07.016](https://doi.org/10.1016/j.inoche.2011.07.016)
91. Hu P, Zhu M, Mei X et al (2012) Single-molecule magnets based on rare earth complexes with chelating benzimidazole-substituted nitronyl nitroxide radicals. *Dalton Trans* 41(48):14651–14656. doi:[10.1039/c2dt31806g](https://doi.org/10.1039/c2dt31806g)
92. Tian L, Sun Y-Q, Na B et al (2013) A family of homologous heterospin complexes based on lanthanides and biradical ligands. *Eur J Inorg Chem* 2013(24):4329–4335. doi:[10.1002/ejic.201300524](https://doi.org/10.1002/ejic.201300524)
93. Coronado E, Giménez-Saiz C, Recueno A et al (2011) Single-molecule magnetic behavior in a neutral terbium(III) complex of a picolinate-based nitronyl nitroxide free radical. *Inorg Chem* 50(16):7370–7372. doi:[10.1021/ic2010425](https://doi.org/10.1021/ic2010425)
94. Fatila EM, Rouzières M, Jennings MC et al (2013) Fine-tuning the single-molecule magnet properties of a [Dy(III)-radical]₂ pair. *J Am Chem Soc* 135(26):9596–9599. doi:[10.1021/ja403794d](https://doi.org/10.1021/ja403794d)
95. Layfield RA (2014) Organometallic single-molecule magnets. *Organometallics* 33(5):1084–1099. doi:[10.1021/om401107f](https://doi.org/10.1021/om401107f)
96. Layfield RA, McDouall JJW, Sulway SA et al (2010) Influence of the N-bridging ligand on magnetic relaxation in an organometallic dysprosium single-molecule magnet. *Chem Eur J* 16(15):4442–4446. doi:[10.1002/chem.201000158](https://doi.org/10.1002/chem.201000158)
97. Huang W, Dulong F, Wu T et al (2013) A six-carbon 10π-electron aromatic system supported by group 3 metals. *Nat Commun* 4:1448. doi:[10.1038/ncomms2473](https://doi.org/10.1038/ncomms2473)

98. Jiang S-D, Liu S-S, Zhou L-N et al (2012) Series of lanthanide organometallic single-ion magnets. *Inorg Chem* 51(5):3079–3087. doi:[10.1021/ic202511n](https://doi.org/10.1021/ic202511n)
99. Boulon M-E, Cucinotta G, Liu S-S et al (2013) Angular-resolved magnetometry beyond triclinic crystals: out-of-equilibrium studies of Cp*ErCOT single-molecule magnet. *Chem Eur J* 19(41):13726–13731. doi:[10.1002/chem.201302600](https://doi.org/10.1002/chem.201302600)
100. Le Roy JJ, Korobkov I, Murugesu M (2014) A sandwich complex with axial symmetry for harnessing the anisotropy in a prolate erbium(III) ion. *Chem Commun* 50(13):1602–1604. doi:[10.1039/c3cc48557a](https://doi.org/10.1039/c3cc48557a)
101. Demir S, Zadrozny JM, Long JR (2014) Large spin-relaxation barriers for the low-symmetry organolanthanide complexes [Cp*₂Ln(BPh₄)] (Cp* = pentamethylcyclopentadienyl; Ln = Tb, Dy). *Chem Eur J* 20(31):9524–9529. doi:[10.1002/chem.201403751](https://doi.org/10.1002/chem.201403751)
102. Liu S-S, Ziller JW, Zhang Y-Q et al (2014) A half-sandwich organometallic single-ion magnet with hexamethylbenzene coordinated to the Dy(III) ion. *Chem Commun* 50(77):11418–11420. doi:[10.1039/c4cc04262j](https://doi.org/10.1039/c4cc04262j)

Chapter 3

Dinuclear Lanthanide Single-Molecule Magnets

Abstract In this chapter, the role of magnetic interactions between lanthanide centers is highlighted in the modulation of magnetic dynamics especially at low-temperature region. It consists of the elucidation of the relaxation mechanisms of typical dinuclear lanthanide SMMs such as N_2^{3-} -radical-bridged, asymmetric, and magnetically diluted Dy_2 systems. Furthermore, detailed investigations into the dinuclear lanthanide systems with different bridging ligands that link the lanthanide centers are presented, and the distinct SMM behaviors are discussed. Remarkably, the delocalized radical and aromatic bridging ligands proved very effective in promoting magnetic exchange between lanthanide centers.

Keywords Magnetic interactions · Bridging ligands · Quantum tunneling · Radical bridge · Relaxation dynamics

The previous chapter has exhibited the synthetic strategies and the great achievements of mononuclear lanthanide SMMs, i.e., lanthanide SIMMs, where the strong single-ion anisotropy arising from the high local symmetry or the suitable charge distribution around lanthanide ions plays an extremely key role in the occurrence of SMM behavior for a mononuclear lanthanide complex. Nevertheless, the fast QTM relaxation against the better performance of SMM is a prevalent feature for lanthanide SIMMs, as evidenced by the butterfly-shaped hysteresis with extremely reduced or even the disappearance of magnetization at zero-dc field. In particular, there is an increasing contribution from QTM to the overall relaxation with the decreasing of temperature, which is very unfavorable to a practical device application of SMMs as memory components. Therefore, how to reduce QTM relaxation at low temperature remains a key point of investigation in SMM research. Considering the effective suppression of QTM in the strongly coupled polynuclear transition metal complexes [1], similarly we are able to design and construct polynuclear lanthanide clusters to reduce QTM through increasing the magnetic interaction between lanthanide ions. In fact, some polynuclear SMMs have shown the great potential in the suppression of QTM with

two well-known examples, i.e., N_2^{3-} -radical-bridged Ln_2 complex [2] and the asymmetric Dy_2 with hydrazone ligands [3]. In addition, the construction of the systems with higher nuclearity is viewed as a way to enhance the effective barrier (U_{eff}) through increasing the total spin ground state of the molecule in the strongly coupled systems [4], which can be applied to polynuclear lanthanide SMM systems in spite of the huge difficulty arising from the strong single-ion anisotropy of lanthanide ions and the weak magnetic interactions between them. To date, considerable efforts of some researchers have been devoted to these aspects, and some groundbreaking results have been obtained including the observations of the ultrahigh blocking barriers [5–7] and some particular magnetic phenomenon [8, 9] occurring in polynuclear lanthanide SMMs. In this chapter, we mainly focus on the simplest polynuclear molecular units, Ln_2 SMMs, which allow the study of the effects of magnetic interactions between two spin carriers on SMM behavior. The detailed investigations on these systems are of critical importance for examining how the nature and strength of interactions between lanthanide ions as well as possible alignment of spin vectors and anisotropy axes influence the slow magnetic relaxation behavior, which are expected to be extended into the systems with higher nuclearity [10].

3.1 Magnetic Interactions

As the research center of magnetism, magnetic interactions have been always the key parameter in determining the magnetic performance in both the traditional permanent magnets and molecule-based magnets developed recently. Here, the molecule-based magnetic materials mainly include the three-dimensional (3D) magnetic ordering materials [11], 1D single-chain magnets (SCM) [12], and 0D SMMs. Generally, the strong interactions between magnetic centers in 3D magnetic systems lead to magnetic ordering below a critical or magnetic ordering temperature, T_c , which is determined by the strength of interactions. Especially, the occurrence of single-chain magnetic behavior in a 1D Ising magnetic system hinges on the high ratio of the interaction within the chain, J , and that between chains, J' [13]. Even in 0D magnetic systems, the magnetic interactions still play an irreplaceable role in creating the high-performance SMMs or the theoretical study of magnetism, as indicated by the discovered polynuclear lanthanide or transition metal SMMs [2]. In addition, although, as seen in the last chapter, some mononuclear complexes exhibit high effective barriers for spin reversal, the effective control of the magnetic coupling between different spin centers in a metal cluster still represents the most promising approach to breaking the present barrier and blocking temperature records and further achieving the dream of storing and processing magnetic information at the molecular level [10]. Thus, to obtain strongly coupled polynuclear lanthanide systems is a great challenge for future research in this field.

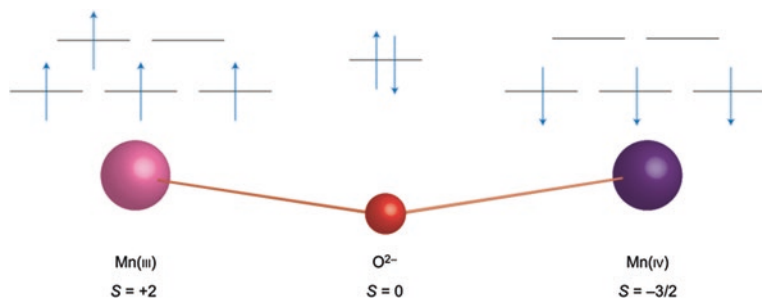


Fig. 3.1 A superexchange pathway via a diamagnetic O-bridge. Reprinted by permission from Macmillan Publishers Ltd.: Ref. [14], copyright 2010

In general, the paramagnetic metal ions are separated by one or more bridging atoms in the molecule-based magnetic materials, as shown in Fig. 3.1, and thus, a superexchange coupling mechanism is operative [14]. In order to discuss the exchange interactions between magnetic sites at the atomic level, the Hamiltonian can be written:

$$H = -2 \sum J_{ij} \mathbf{S}_i \cdot \mathbf{S}_j$$

where the sign of the exchange coupling constant J_{ij} indicates the type of interaction [ferro- ($J > 0$) or antiferromagnetic ($J < 0$)], while its magnitude describes the strength of interaction between pairs of spins, and the sum is run over all pairwise interactions of spins i and j in a lattice. Further, the Hamiltonian can be expanded into three directions [15]:

$$H = -2 \sum [J_{xy} (\mathbf{S}_{ix} \cdot \mathbf{S}_{jx} + \mathbf{S}_{iy} \cdot \mathbf{S}_{jy}) + J_z \mathbf{S}_{iz} \cdot \mathbf{S}_{jz}]$$

Therefore, three classical models can be introduced here. The isotropic model, referred to as the Heisenberg model, is obtained when $J_{xy} = J_z$, which is widely used to explain the “spin-only” magnetism for which orbital angular momentum is quenched, like in the Cu complexes. The second is the XY model which corresponds to $J_z = 0$. Finally, when $J_{xy} = 0$, the Ising model can be obtained, showing the magnetic exchange interactions between the strongly anisotropic metal ions. In this book, we are mainly concerned about the low-dimensional lanthanide SMMs, and thus, the Ising model seems to be exceedingly important in explaining their magnetic properties.

As is well known, the lanthanide complexes show the very weak magnetic interactions when compared with the transition metal complexes, which are determined by the internal nature of lanthanide ions, as seen in the first chapter. To date, the strongest magnetic interactions were observed in the N_2^{3-} -radical-bridged Ln_2 complex in Fig. 3.2 [2]. Even so, it has turned out to be a key factor in affecting the SMM performance, especially the magnetic behaviors at the low-temperature region. The effects are shown well in three most typical dinuclear lanthanide SMMs below.

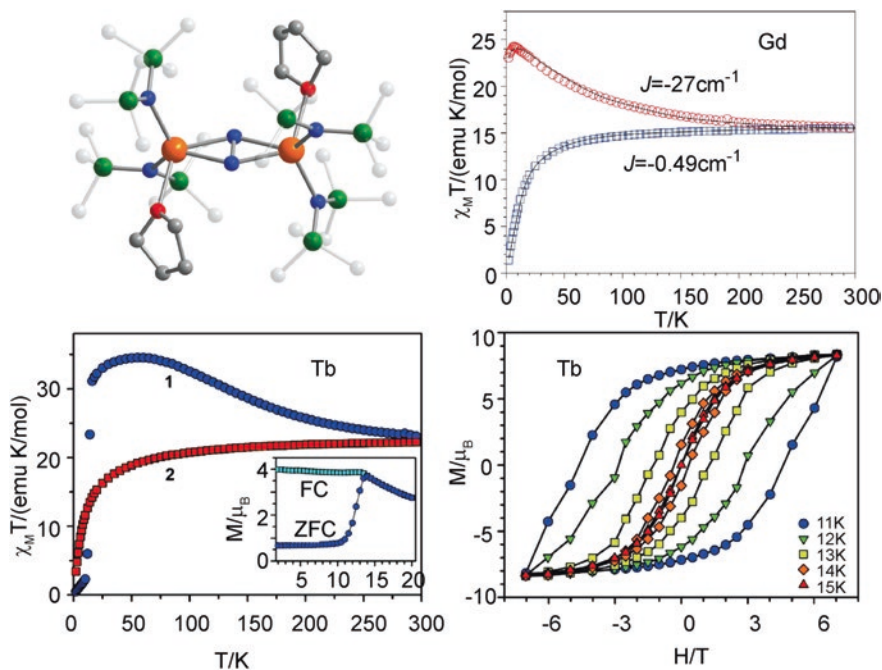


Fig. 3.2 The crystal structure and static magnetic properties of the N_2^{3-} -radical-bridged lanthanide family. Reprinted by permission from Macmillan Publishers Ltd.: Ref. [2], copyright 2011. Reprinted with the permission from Ref. [16]. Copyright 2011 American Chemical Society

In 2011, J.R. Long et al. reported the magnetism of the N_2^{3-} -radical-bridged dilanthanide complexes, $([(Me_3Si)_2N]_2(THF)Ln)_2(\mu-\eta^2:\eta^2-N_2)$ ($Ln = Gd, Dy,$ and Tb), generated through the reduction of the corresponding non-magnetic N_2^{2-} -bridged complex [2, 16]. The structures are exhibited in Fig. 3.2 with the five-coordinate lanthanide ions located in a pseudo-tetrahedral environment. The comparison of direct current (dc) magnetic susceptibility data between the radical- and non-radical-bridged complexes is clearly indicative of the presence of strong magnetic interactions in the radical-bridged complexes. To date, the strongest magnetic coupling of $J = -27 \text{ cm}^{-1}$ between a Gd^{III} center and a paramagnetic ligand observed for a gadolinium compound was revealed in the N_2^{3-} -bridged Gd_2 complexes. Notably, the sudden decrease of $\chi_m T$ value with the decreasing temperature at low temperature suggests the strongly blocking of magnetic moments as confirmed by the occurrence of SMM behavior in the Dy and Tb analogues. Such an unusual magnetic coupling is indicative of the effectiveness of the N_2^{3-} -radical in mediating strong magnetic exchange coupling between lanthanide ions. Further, the robust single-molecule magnetic behaviors were observed clearly in the Dy and Tb analogues through ac magnetic susceptibility measurements, and their effective barriers were given to be 123 cm^{-1} (177 K) and 227 cm^{-1} (327 K). Although the effective barriers seem not to be so high when compared with some SMMs showing the high

effective barriers, the perfect linear relationship in the $\ln(\tau)$ versus $1/T$ plots can be kept within the whole investigated temperature domain of ac magnetic susceptibility measurements, indicating the single dominant Orbach process. Rarely, the dc magnetization decay experiments indicated that the radical-bridged Tb_2 SMM can reach the blocking temperature where the magnetic relaxation time is 100 s. Here, the temperature was estimated to be 13.9 K, which is rather high when compared with the 6.7 K of the Dy congener and 3.2 K of $[\text{Mn}_6\text{O}_2(\text{sao})_6(\text{O}_2\text{CPh})_2(\text{EtOH})_4]$ [16]. More clearly, in Tb complex, the perfect magnetic hysteresis curve without steps was observed at the temperature as high as 14 K at an average sweep rate of 0.9 mT/s, as shown in Fig. 3.2. Here, the strongly blocking behavior of magnetization should be as a result of the effective coupling interactions between lanthanide ions mediated by the radical bridge with the diffuse spin orbitals.

The asymmetric Dy_2 SMM, $[\text{Dy}_2(\text{ovph})_2\text{Cl}_2(\text{MeOH})_3]\cdot\text{MeCN}$ (H_2ovph = pyridine-2-carboxylic acid [(2-hydroxy-3-methoxyphenyl)methylene] hydrazide), was published by our group in 2011 [3]. Its structure and ac magnetic susceptibility properties are shown in Fig. 3.3. The crystal structure reveals that two Dy ions are located in the distinct local coordination environments, one being the nearly perfect pentagonal bipyramidal geometry and the other being the eight-coordinate hula hooplike geometry. As a possible result of the structural features, its ac magnetic susceptibility data display the broad χ'' peak and significantly broadened Cole–Cole plots, indicating the closely spaced multiple relaxation process. Here, we mainly focus on the disappearing χ' and χ'' signals as the temperature approaches 2 K, which is different from the case in most lanthanide SMMs. Such a suddenly disappearing susceptibility signals at low temperature are indicative of the almost completely “freezing” of the magnetic moment by the anisotropy barriers and also as a signature of the effective suppression of QTM relaxation.

In order to explain such a phenomenon, *ab initio* calculations were performed with the calculated results shown in Figs. 3.3 and 3.4. Here, both Dy ions exhibit the strong local single-ion anisotropy, and two corresponding anisotropic axes are

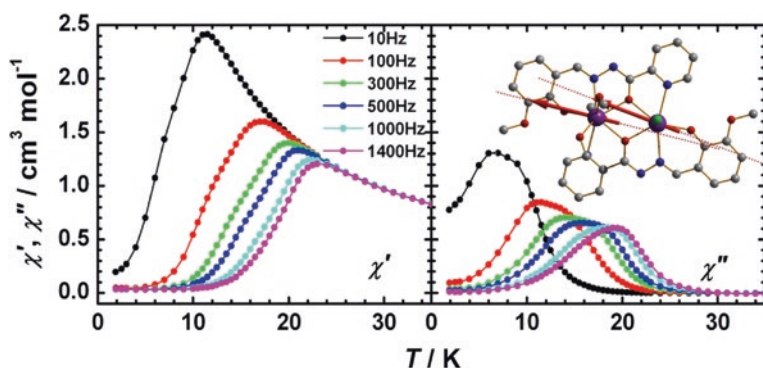


Fig. 3.3 The crystal structure, anisotropic axes and relaxation dynamics of asymmetric Dy_2 SMM, $[\text{Dy}_2\text{ovph}_2\text{Cl}_2(\text{MeOH})_3]\cdot\text{MeCN}$. Reprinted with the permission from Ref. [3]. Copyright 2011 American Chemical Society

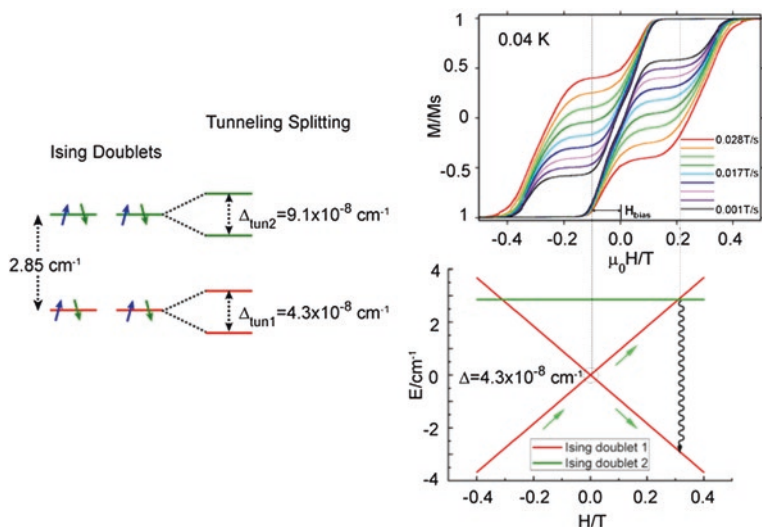


Fig. 3.4 The exchange spectrum of the Dy_2 molecule and plot of normalized magnetization (M/M_s) versus $\mu_0 H$. The loops are shown at different sweep rates at 0.04 K. Zeeman diagrams calculated for the field applied along the anisotropy axis of the ground exchange doublet. Reprinted with the permission from Ref. [3]. Copyright 2011 American Chemical Society

situated in the plane formed by the two dysprosium ions and one bridging oxygen atom in a near-parallel alignment, which results in the relatively strong ferromagnetic interactions between two Dy ions. Therefore, the magnetic interactions between the lowest Kramers doublets of two Dy ions further lead to two Ising exchange doublets separated by 2.85 cm^{-1} , as shown in Fig. 3.4. Importantly, each Ising doublet exhibits a very small tunneling splitting, about the order of 10^{-8} cm^{-1} , which is responsible for the weak QTM relaxation at low temperature.

In addition, the magnetic investigations for the diluted samples were performed with the purpose of elucidating the origin of the slow relaxation of the magnetization in the Dy_2 SMM, $[\text{Dy}_2(\text{valdien})_2(\text{NO}_3)_2]$ ($\text{H}_2\text{valdien} = \text{N}1, \text{N}3\text{-bis}(3\text{-methoxysalicylidene})\text{diethylenetriamine}$), as shown in Fig. 3.5 [17]. Ab initio calculations reveal obvious antiferromagnetic exchange coupling in the undiluted Dy_2 sample, which exhibits the typical SMM behavior as evidenced by the ac susceptibility data. Further, magnetism–structure relationships will be discussed below, and here, we focus on the diluted investigations for it. As shown in Fig. 3.5, the ac susceptibility investigations for the diluted and undiluted samples at 0 Oe show the clear χ'' signals with the peaks at the almost same position, but showing the distinct magnetic signals at low temperature. Further, the slightly increasing barriers with increasing percentage of Dy dilution suggest that the single-ion anisotropy has a dominant contribution to the effective barrier for spin reversal in the Dy_2 species. Nevertheless, importantly, the increasing tail of χ'' in the diluted samples is indicative of the presence of an important tunneling relaxation pathway

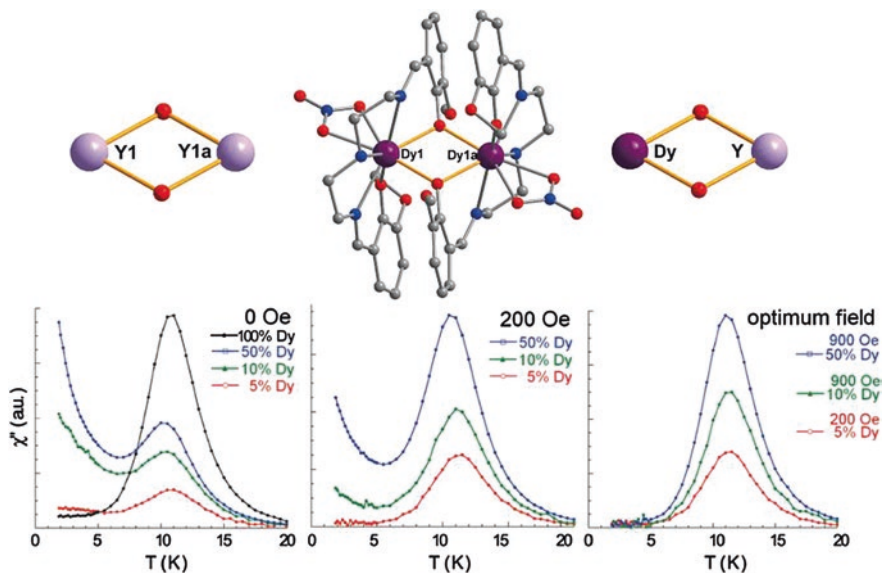


Fig. 3.5 The magnetic dilution studies of magnetic dynamics in $[\text{Dy}_2(\text{valdien})_2(\text{NO}_3)_2]$. Reprinted with permission from Ref. [17]. Copyright 2011 American Chemical Society

in $[\text{YDy}]$ species at low temperature, which were not observed in the undiluted Dy_2 sample. The above results demonstrated that the effective coupling between lanthanide magnetic centers can significantly reduce the QTM relaxation at zero dc applied field. At the same time, the applications of optimum dc field in different diluted samples can also suppress the QTM relaxation at low temperature, as indicated by the χ'' tail in Fig. 3.5.

Three above examples provide significant insight into the effect of magnetic interactions on the SMM behavior, where the ferro- or antiferromagnetic interactions are mediated via radical ligands or diamagnetic bridges. The suitable magnetic interactions between lanthanide centers support the occurrence of the robust “magnet-type” behavior with the effective suppression of QTM relaxation at low temperature, which are of critical importance for the envisaged technological applications of these molecules. As such, considerable effort for chemists is devoted to the investigation of different bridging moieties between lanthanide metal centers.

3.2 The Coupling of Two SIMMs

The previous chapter has presented that the strong SMM behavior can be observed in mononuclear lanthanide complexes, especially in lanthanide phthalocyanine complexes and organometallic complexes. Here, in order to further obtain the

dinuclear and even more multinuclear lanthanide SMMs, the most direct and effective method should be to extend mononuclear SMM species into the multinuclear systems while keeping, even advancing, their SMM properties via mediating the magnetic interactions between magnetic centers. In fact, a great number of dinuclear lanthanide SMMs arising from the coupling of two SIMMs have been constructed by some researchers through the aggregating of two mononuclear species or adding bridging ligands into reaction systems. Here, some typical examples were demonstrated below.

3.2.1 Triple-Decker Lanthanide Phthalocyanine System

For the double-decker lanthanide phthalocyanine complexes, the investigations of magnetic properties and the determination of ligand parameters performed by N. Ishikawa have been presented in previous chapter. Here, we focus on the analysis of magnetic interactions in the asymmetric triple-decker lanthanide phthalocyanine complexes, PcLnPcLnPc^* referred to as $[\text{Ln}, \text{Ln}]$ ($\text{Ln} = \text{Tb}, \text{Dy}, \text{Ho}, \text{Er}, \text{Tm}$ and Yb), where two metal sites are able to be distinguished through applying the substituted phthalocyanine ligand in the process of adding the third layer to the mononuclear lanthanide phthalocyanine complexes, as shown in Fig. 2.6 [18]. Therefore, the heterodinuclear lanthanide phthalocyaninato complexes, PcYPcLnPc^* as $[\text{Y}, \text{Ln}]$ and PcLnPcYPc^* as $[\text{Ln}, \text{Y}]$, were also prepared, which provide the important opportunity for studying the magnetic contributions of each metal center to the whole magnetic properties. In addition, the electronic structure of individual f -shells was able to be obtained using the multidimensional simplex minimization method [19]. Further, the magnetic interactions can be extracted by the definition:

$$\Delta\chi_m T = \chi_m([\text{Ln}, \text{Ln}])T - [\chi_m([\text{Ln}, \text{Y}])T + \chi_m([\text{Y}, \text{Ln}])T]$$

The resulting $\Delta\chi_m T$ versus T plots are given in Fig. 3.6, showing the distinct trend between the Tb_2 , Dy_2 , and Ho_2 complexes and the Er_2 , Tm_2 , and Yb_2 complexes. The theoretical values of $\Delta\chi_m T$ obtained from the Hamiltonian containing the Hamiltonian terms of every metal center and the magnetic dipolar interactions (\mathbf{V}_{12}) are well in agreement with the measured data in Fig. 3.6, thus indicating the main dipole nature of magnetic interactions. Clearly, the positive $\Delta\chi_m T$ values at low temperature indicate the existence of a ferromagnetic interaction between the lanthanide ions for Tb_2 , Dy_2 , and Ho_2 complexes, while the Er_2 and Tm_2 complexes show the negative $\Delta\chi_m T$ values suggesting the presence of antiferromagnetic interactions. In addition, the small magnitude of $\Delta\chi_m T$ value reveals the almost negligible magnetic interactions between metal centers in the Yb_2 complex.

In order to explain the differences of interactions, a simplified model with an “ensemble-averaged approximation” of the magnetic susceptibility tensor was supposed to compare with the anisotropic magnetic susceptibility tensors χ_ξ ($\xi = x, y, z$) of $[\text{Ln}, \text{Ln}]$, $[\text{Y}, \text{Ln}]$, and $[\text{Ln}, \text{Y}]$ at the local sites of paramagnetic

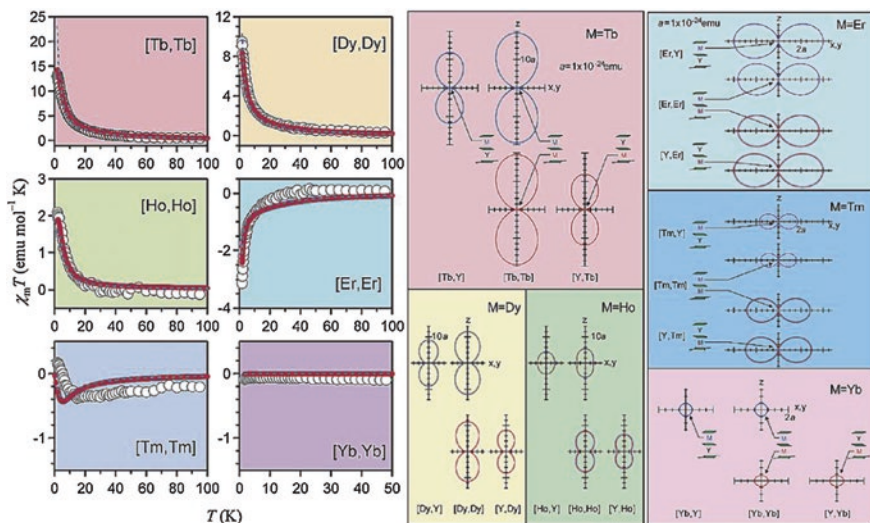


Fig. 3.6 The $\Delta\chi_m T$ versus T plots indicating the magnetic interactions of lanthanide ions, and xz cross sections of the closed surfaces representing anisotropic magnetic susceptibility tensors of [Y, Ln], [Ln, Ln], and [Ln, Y]. Reprinted with the permission from Ref. [18]. Copyright 2002 American Chemical Society

centers, which are shown in Fig. 3.6 [18]. For the Tb_2 , Dy_2 , and Ho_2 complexes, the dipole ferromagnetic interactions lead to the increasing height of the closed surfaces compared to that of the non-interacting systems at the z -direction and the resulting positive $\Delta\chi_m$ values. In particular, the maximum $\Delta\chi_m T$ value among three complexes was observed in Tb_2 complex as a result of the negligible $\Delta\chi_x$ and $\Delta\chi_y$. Similarly, χ_ξ at xy plane is larger than χ_z , thus $\Delta\chi_x$ and $\Delta\chi_y$ are dominant, leading to the negative $\Delta\chi_m$ values in the Er_2 complex. In contrast, the almost spherical closed surface in the Yb_2 complex leads to the negligible magnetic interactions. We believe that this is one of the most successful example combining the experimental analysis and theoretical explanation in the magnetic interactions. Further, the effect of the f - f interaction on the dynamic magnetism was investigated by the comparison between the [Tb, Tb] complex and its diluted samples, [Tb, Y] and [Y, Tb].

Figure 3.7 shows the temperature dependence of ac susceptibilities of three complexes under a zero- and non-zero-dc magnetic field, respectively [20]. It is obvious that the [Tb, Tb] complex exhibits two-step relaxation process as a result of two asymmetric metal centers in the complex. By contrast, the χ_M''/χ_M' peaks of the [Y, Tb] and [Tb, Y] complexes shift to higher temperatures upon applying a dc field, while the application of the dc field does not change the positions of the two χ_M''/χ_M' peaks in the [Tb, Tb] complex, suggesting that the QTM relaxation has been suppressed by the clear ferromagnetic f - f interactions between two Tb^{III} ions under zero-dc field. It is more important that the positions of the shifted

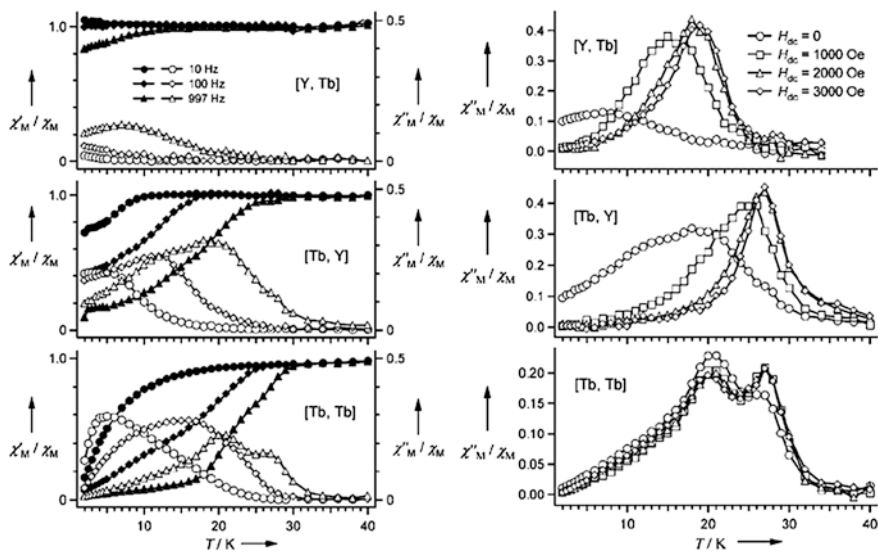


Fig. 3.7 The temperature dependence of ac susceptibilities of [Y, Tb], [Tb, Y], and [Tb, Tb] under a zero- and nonzero-dc magnetic field. Reproduced from Ref. [20] with permission from John Wiley & Sons Ltd.

peaks of both the mono-Tb complexes almost coincide with the two peaks of the Tb_2 complex, revealing that the two relaxation processes correspond to the Tb ions at two sites, respectively. To date, this is the only kind of multinuclear lanthanide examples where the different relaxation processes are able to be ascribed to the lanthanide ions at the certain sites.

In addition, triple-decker substituted Pc complex with symmetric Tb^{III} sites, $[Tb_2(obPc)_3]$ ($obPc =$ dianion of 2,3,9,10,16,17,23,24-octabutoxyphthalocyanine), has also been reported by Katoh at 2011 [21]. Similarly, the ferromagnetic interactions were also observed in the complex. The ac susceptibility data show only a single relaxation peak at 1488 Hz and 24 K under zero-dc field, as shown in Fig. 3.8. Here, an effective barrier of 230 cm^{-1} (331 K) was given through the

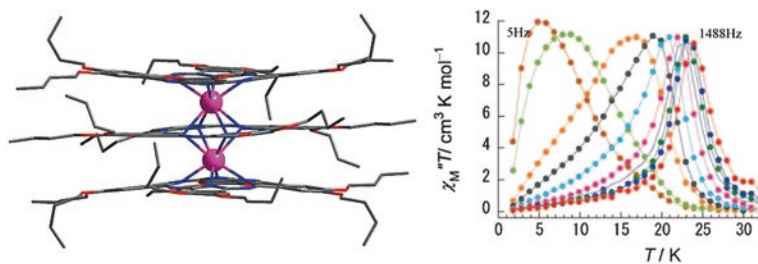


Fig. 3.8 The crystal structure and χ'' signals of ac susceptibility of $[Tb_2(obPc)_3]$. Reproduced from Ref. [21] with permission from John Wiley & Sons Ltd.

Arrhenius fitting. Nevertheless, the application of a dc magnetic field leads to the presence of two magnetic relaxation processes, as indicated by the Argand plots showing a transition from a one-component system to a two-component system with the increase in the strength of the dc field.

In 2012, N. Ishikawa et al. reported a similar triple-decker mixed-ligand bis-Tb^{III} complex, PcTbPcTb(T(*p*-OMe)PP) (T(*p*-OMe)PP = tetra-*p*-methoxyphenylporphyrinato), with not only a SAP coordination site but also a well-defined square-prismatic (SP) site, which was shown in Fig. 3.9 [22]. The dc susceptibility measurements reveal that the complex also shows the ferromagnetic interactions between two sharply different magnetic sites. The diluted complexes, [Tb, Y] and [Y, Tb], were also prepared by the same synthetic approach to the above complex. As shown in Fig. 3.9, [Tb, Tb] has much longer τ than [Tb, Y] and [Y, Tb] at $H_{dc} = 0$ Oe because of the strong hindrance of quantum tunneling path in SAP site by magnetic dipolar interaction between the two ions. Further, the application of a dc applied field in [Tb, Tb] leads to the shifts of relaxation peaks to lower frequency, and at the same time, the peaks display the weak shoulder at high-frequency region. Here, comparing the ac susceptibility data of the [Tb, Tb], [Tb, Y] and [Y, Tb] under 1000-Oe field, we can see that the peaks are associated with the Tb ion at SAP site.

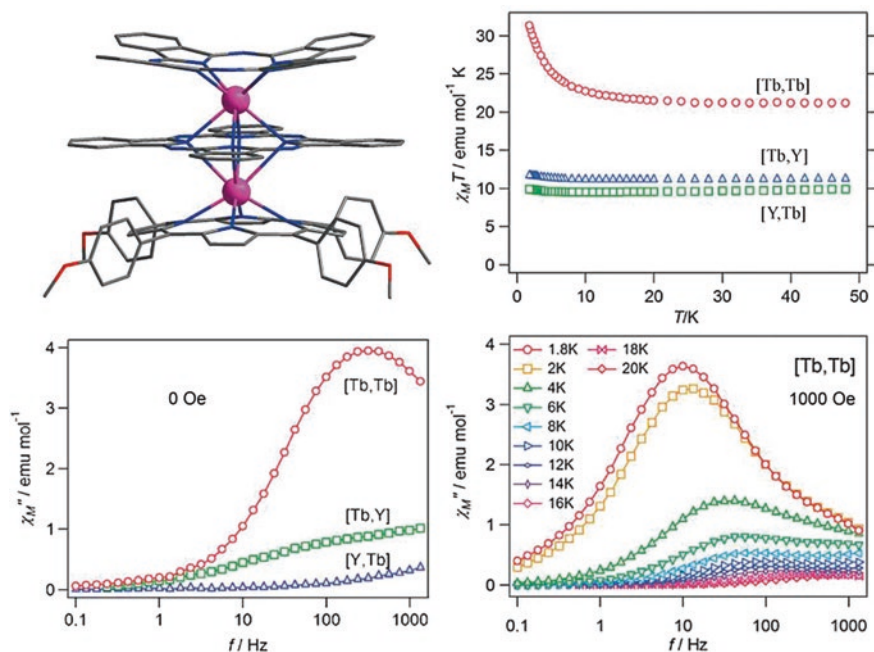


Fig. 3.9 The crystal structure and magnetic properties of the diluted and undiluted samples of PcTbPcTb(T(*p*-OMe)PP). Reproduced from Ref. [22] with permission from The Royal Society of Chemistry

The above examples give a clear presentation on the assembly of triple-decker lanthanide phthalocyanine SMMs arising from the coupling of two [TbPc₂] SIMMs. The obvious ferromagnetic interactions between two Tb ions were present in those complexes, and the interactions further play a positive influence on the suppression of QTM under zero-dc field.

3.2.2 Dinuclear β -Diketone SMMs

The mononuclear Dy β -diketone complexes have proved to be good candidates for designing typical SIMMs. Therefore, the coupling strategies based on the mononuclear building units are expected to be used to improve their SMM behavior, like in the above lanthanide phthalocyanine systems. To date, the most effective method is to add the bridging ligands to the reacting systems containing the lanthanide β -diketone salts, especially the lanthanide hfac salt. Figure 3.10 lists the reported typical bridging ligands, which are classified into three classes: the small monodentate ligands; the ligands incorporating two capping sites (L1 and L2); and the TTF-based pyridine-N-oxide ligands (L3–L6).

In 2010, we constructed the first pyrazine-bridged Dy₂ complex (Fig. 3.11), formulated as [Dy(hfac)₃(H₂O)₂]₂(μ -pz)·pz, through applying the hfac ligand with the strong electron-withdrawing effect, which facilitates the coordination

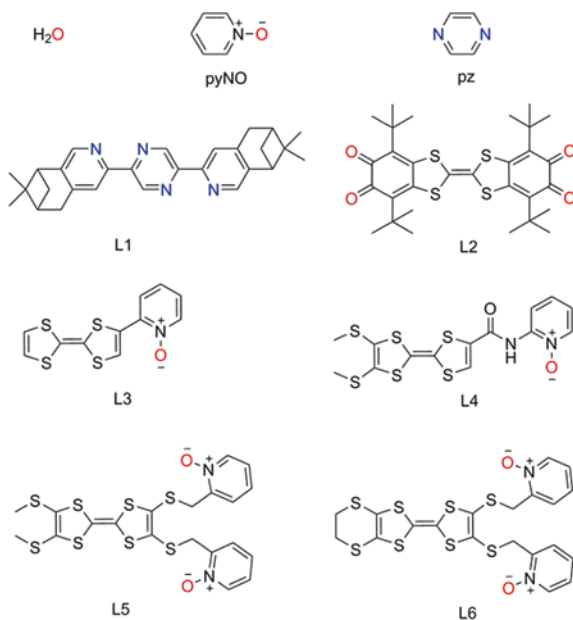


Fig. 3.10 Typical bridging ligands in lanthanide β -diketone systems

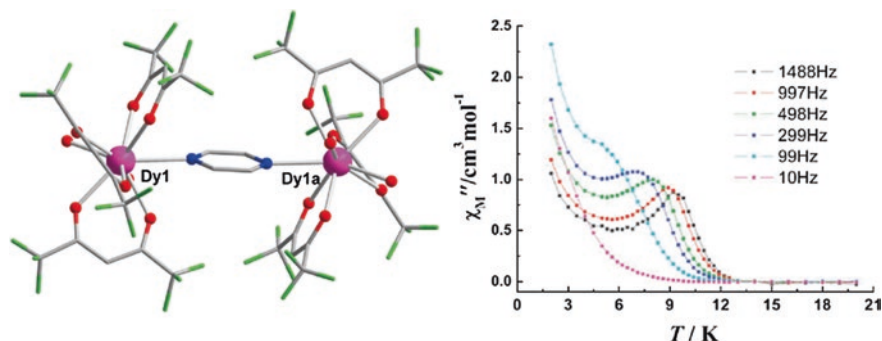


Fig. 3.11 The crystal structure and relaxation dynamics of $[\text{Dy}(\text{hfac})_3(\text{H}_2\text{O})_2]_2(\mu_2\text{-pz})\cdot\text{pz}$. Reproduced from Ref. [23] with permission from The Royal Society of Chemistry

of $4f$ metal ions to non-chelating nitrogen-containing donors [23]. Here, two $[\text{Dy}(\text{hfac})_3(\text{H}_2\text{O})_2]$ units are linked by a pyrazine ligand, leading to a centrosymmetric Dy_2 metal core with a Dy–Dy separation of 8.09 Å, and each Dy^{III} ion is characterized by a three-capped trigonal prismatic environment. The obvious magnetic interactions were not observed between metal centers, which should be as a result of the long distance between them. The ac susceptibility data exhibit that the relaxation follows a thermally activated mechanism above 9 K giving an effective barrier of 110 K with a pre-exponential factor (τ_0) of 8.4×10^{-10} s under zero-dc field. Although the barrier seems to be larger than that of $[\text{Dy}(\text{acac})_3(\text{H}_2\text{O})_2]$, the temperature-independent relaxation process is still present in the complex, as indicated by the increasing tail with the decreasing of temperature at low temperature (Fig. 3.11).

In 2012 and 2013, two Dy SMMs, $[\text{Dy}(\text{hfac})_3(\text{pyNO})]_2$ [24] and $[\text{Dy}(\text{hfac})_3(\text{H}_2\text{O})_2]$ [25], were reported by K. Bernot et al. Here, they display the similar structures, which can be viewed as the linking of two $\text{Dy}(\text{hfac})_3$ moieties via pyridine-N-oxide (pyNO) and H_2O molecules, as shown in Fig. 3.12. It is noteworthy that the original SAP coordination geometry is still kept around Dy ions for two complexes. Nevertheless, the dc susceptibility measurements reveal distinct magnetic interactions between two Dy centers in two complexes. In pyNO-bridged Dy_2 SMM, a parameter of $J = -2.46 \text{ cm}^{-1}$, clearly indicating the antiferromagnetic interactions, was obtained by fitting the dc susceptibility data, while obvious ferromagnetic interactions were observed in the H_2O -bridged system with an interaction parameter of $J = 2.26 \text{ cm}^{-1}$ for the effective spin $S_{\text{eff}} = 1/2$. The reasons for the differences have not been clear to date, but the triclinic space group for H_2O -bridged Dy_2 allows the direct detection of the magnetic anisotropy of Dy ions through the single-crystal magnetization measurements. The results reveal that the easy magnetization axes of Dy centers almost coincide with the pseudo- C_4 axis of the SAP coordination polyhedron, as shown in Fig. 3.12. Here, the ac susceptibility data of two Dy_2 complexes in Fig. 3.12 both exhibit clear χ'' signals indicative of the typical SMM behaviors. However, the

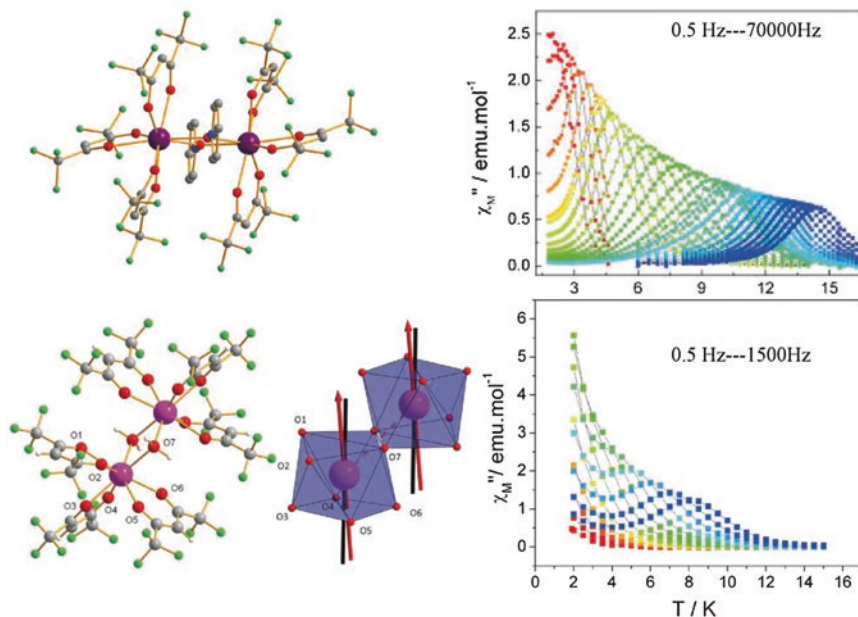


Fig. 3.12 The crystal structure and relaxation dynamics of $[\text{Dy}(\text{hfac})_3(\text{pyNO})]_2$ and $[\text{Dy}(\text{hfac})_3(\text{H}_2\text{O})]_2$. (Top) Reproduced from Ref. [24] with permission from John Wiley & Sons Ltd. (Bottom) Reproduced from Ref. [25] with permission from The Royal Society of Chemistry

pyNO-bridged Dy_2 displays a higher effective barrier ($U_{\text{eff}} = 167 \text{ K}$) than that in H_2O -bridged Dy_2 complexes ($U_{\text{eff}} = 92 \text{ K}$), and the slower tunneling relaxation times (τ_{QTM}) were observed in the pyNO-bridged complexes, as shown in the $\ln(\tau)$ versus $1/T$ plots. In addition, the magnetic dilution investigations in the H_2O -bridged Dy_2 complex reveal the slower QTM relaxation present in undiluted samples under zero-dc field, indicating the suppressing effects of magnetic interactions on the QTM.

In 2012, a chiral bridging ligand L1 (Fig. 3.10) incorporating two capping sites similar to the bipyridine was applied to construct the chiral dinuclear Dy_2 SMM, as shown in Fig. 3.13 [26]. In the complex, both Dy ions adopt the distorted square-antiprismatic coordination environments but showing different distortions, as indicated by the different creased angles of two approximate square planes for the two Dy ions. Here, there were no obvious magnetic interactions observed in the dc susceptibility characterization of the complex. However, its ac susceptibility signals reveal distinct slow relaxation behavior of magnetization from its corresponding mononuclear complex described in the last chapter. By contrast, the Dy_2 complex exhibits more complex relaxation processes, and its corresponding χ'' peaks occur at higher temperature, as shown in Fig. 3.13. In particular, the Argand plots are clearly indicative of the presence of two-step

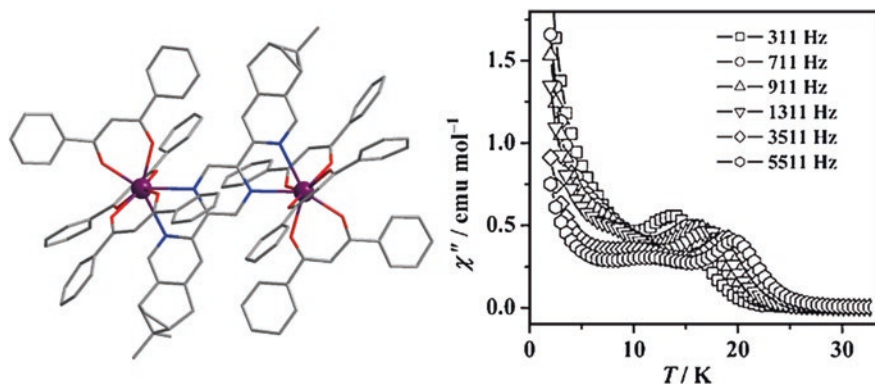


Fig. 3.13 The crystal structure and relaxation dynamics of the chiral dinuclear Dy₂ SMM. Reproduced from Ref. [26] with permission from John Wiley & Sons Ltd.

relaxation process, which are probably associated with the two different metal centers present in the molecules.

In addition, a new type of multidentate quinone–tetrathiafulvalene–quinone bridging ligands containing two capping sites, L2 in Fig. 3.10, was also synthesized by L. Ouahab, to construct novel Dy₂ complex in Fig. 3.14 showing the slow relaxation of magnetization [27]. The ligand L2 links two Dy(hfac)₃(H₂O) moieties, leading to the tricapped trigonal prismatic geometry around each Dy ion coordinated by nine oxygen atoms. Here, the large bridging ligand leads to a long intramolecular Dy–Dy distance equal to 17.497 Å, which is much longer than the shortest intermolecular distance of 5.963 Å due to the presence of intermolecular hydrogen bonds. Further, the slow relaxation behavior of magnetization was observed within a small temperature region, 1.9–3.8 K, under zero-dc field. The $\ln\tau$ versus $1/T$ plots exhibit an obvious deviation from the thermally activated process, as shown in Fig. 3.14, and a small effective barrier was given to be 15 K. Such a weak SMM behavior may be as a result of the local low-symmetry environments around Dy ions. In addition, the application of a moderate external dc field effectively enhances its SMM behavior.

For the third kind of bridging ligand, TTF-based pyridine-N-oxide ligands, a great number of Dy or Yb complexes showing slow relaxation behavior have been reported. Meanwhile, the electrochemical and luminescence properties were also widely investigated for them, potentially providing good candidates for the design of multifunctional materials. Some typical features of the TTF-based ligands have been described in previous chapter, and thus, we only choose two representative examples to elucidate their corresponding magnetic properties.

The Dy₂ complex bridged by ligand L3 in Fig. 3.15 was reported in 2011 by L. Ouahab group [28]. As shown in Fig. 3.10, the ligand L3 contains only one site capable of coordinating to lanthanide ions, i.e., the O atom in pyridine-N-oxide, and thus, it shows similar bridging mode to the above pyNO ligand. Similarly,

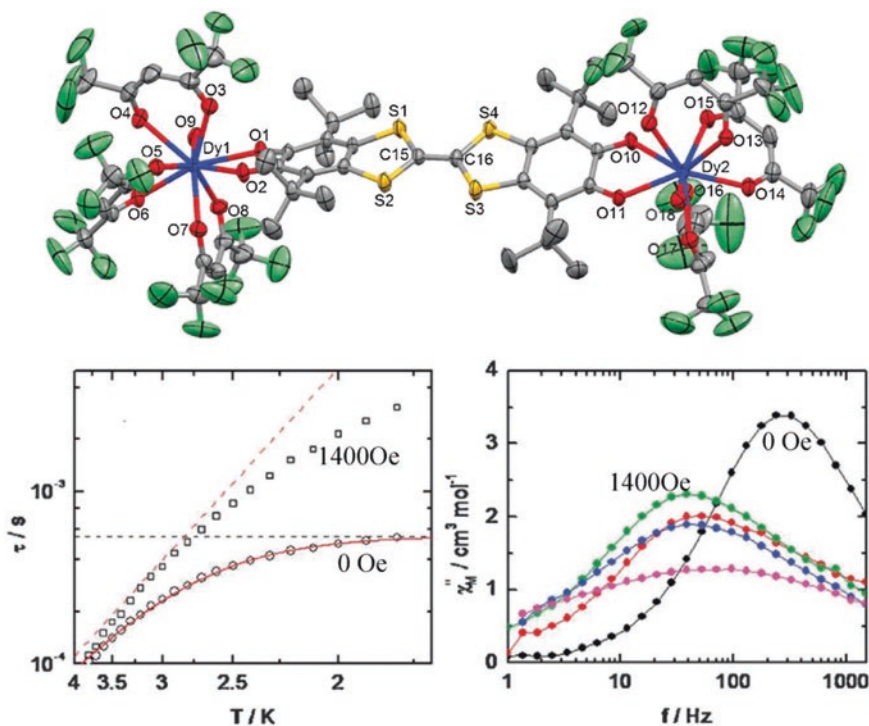


Fig. 3.14 The crystal structure and relaxation dynamics of Dy_2 β -diketone system bridged by quinone–tetrathiafulvalene–quinone. Reproduced from Ref. [27] with permission from The Royal Society of Chemistry

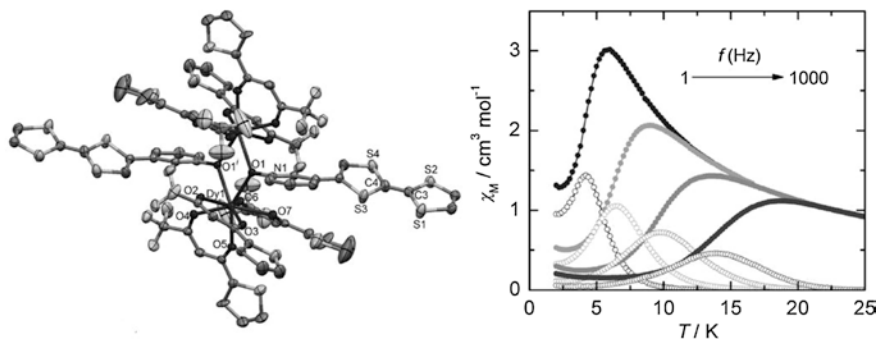


Fig. 3.15 The crystal structure and relaxation dynamics of Dy_2 β -diketone system bridged by TTF-based pyridine-N-oxide ligand L3. Reproduced from Ref. [28] with permission from John Wiley & Sons Ltd.

the complex is also able to be viewed as the linking of two $\text{Dy}(\text{tta})_3$ moieties via ligand L3, and the Dy ions exhibit distorted SAP coordination geometry. Further, clear antiferromagnetic interactions were present between two Dy centers through comparing the dc susceptibility data of the Dy_2 complex and its corresponding mononuclear complex. Importantly, the mononuclear complex does not show χ'' signals typical of SMM behavior, while obvious out-of-phase signals were observed below 20 K in the Dy_2 complex, as shown in Fig. 3.15. This clearly exhibits that the magnetic interactions between the metal centers play an important role in inducing slow relaxation of magnetization under the zero-dc applied field. In addition, the fitting based on the Arrhenius law at high temperature regime afforded an effective barrier of 87 K.

Finally, the TTF-based ligands L5 and L6 with two 2-pyridyl-N-oxidemethylthio arms were also explored to construct multinuclear lanthanide SMMs, as shown in Fig. 3.16 [29]. In the complexes, two $\text{Dy}(\text{hfac})_3$ moieties were linked by two L5 or L6 ligands, leading to the formation of dinuclear complexes with formula $[\text{Dy}(\text{hfac})_3(\text{L5/L6})]_2$. The ac susceptibility data reveal that the Dy_2 bridged by L5 shows the weak χ'' signals under zero-dc field, and the applications of the dc field result in the obvious SMM behavior, as indicated in Fig. 3.16. A small effective barrier of 8.7 cm^{-1} (12.5 K) was afforded at 1200 Oe. By contrast, the Dy_2 complex bridged by L6 does not exhibit any out-of-phase signals, the reasons for which may be as a result of the slight differences of local coordination geometries of Dy ions.

In conclusion, a great number of multidentate ligands can be used to bridge mononuclear lanthanide β -diketone SMMs through alternation of the auxiliary ligands, which provides a facile approach to construct lanthanide SMMs incorporating two SIMMs. Importantly, the magnetic interactions between two metal centers can be easily modified through altering the nature of bridging ligands.

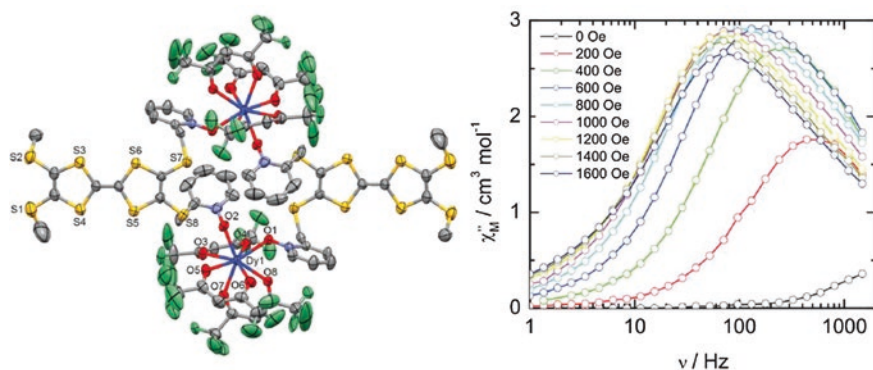


Fig. 3.16 The crystal structure and relaxation dynamics of Dy_2 β -diketone system bridged by TTF-based pyridine-N-oxide ligand L5. Reprinted with the permission from Ref. [29]. Copyright 2013 American Chemical Society

3.2.3 Dinuclear Lanthanide Radical SMMs

In the mononuclear lanthanide NIT-R radical systems introduced in last chapter, the R group usually has no site to coordinate to lanthanide ions or only one-coordinate site assisting the radical part to form the bidentate chelating coordinate sites. Here, in order to extend the nuclearity of this system without other auxiliary ligands, the R group should be modified to have more coordinate sites to link metal ions. The NIT-R bridging ligands with the functionalized R groups are shown in Fig. 3.17, where those radical ligands play a bridging role between two lanthanide ions, leading to the formation of dinuclear lanthanide radical systems.

In 2007, R. Sessoli et al. reported the first NIT-R bridged Dy₂ SMM, which resulted from the reaction of Dy(hfac)₃·2H₂O and NIT-4py in Fig. 3.17 [30]. As shown in Fig. 3.18, the molecular structure comprises two bridging NIT-4py radicals, each one coordinating two lanthanide ions via an oxygen atom and the nitrogen of the pyridine ring. In the $\chi_m T$ versus T plots, the increasing $\chi_m T$ values with the decreasing temperature and its corresponding fitting at low-temperature region reveal that the strong ferromagnetic interactions are present between the lanthanide ion and the radical ligands. The ac susceptibility data exhibit frequency and temperature dependent χ'' signals without maxima. Further, the application of a 2000-Oe static field leads to the occurrence of frequency-dependent χ'' peaks as a clear indication of SMM behavior. Here, the effective barrier was given to be 13 K, which is small when compared to some above examples. In addition, the magnetic dilution investigation in the isostructural diamagnetic Y complex suggests that the weak interaction between Dy ions has the effect of reducing the QTM rate.

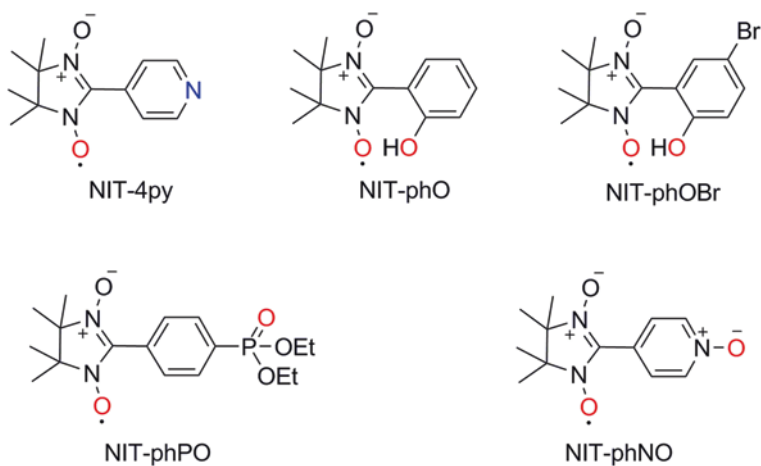


Fig. 3.17 The NIT-R bridging ligands used in Ln₂-radical systems

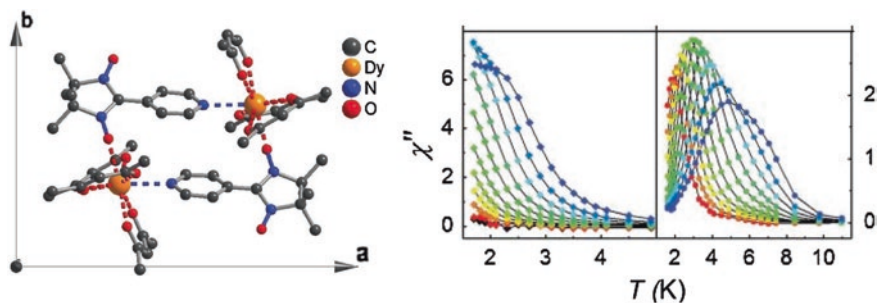


Fig. 3.18 The crystal structure and relaxation dynamics of Dy₂-radical system with NIT-4py. Reproduced from Ref. [30] with permission from The Royal Society of Chemistry

In addition, some other NIT-R radical-bridged dinuclear lanthanide complexes were also reported, as shown in Fig. 3.19, but they only exhibit weak slow magnetic relaxation behavior even under a nonzero-dc applied field [31–33]. Therefore, their crystal structure and magnetic properties are not described in detail here. However, as examples bridged by the NIT-R radical ligands, they still provide us some important information for the future researches in the radical-bridged multinuclear lanthanide systems.

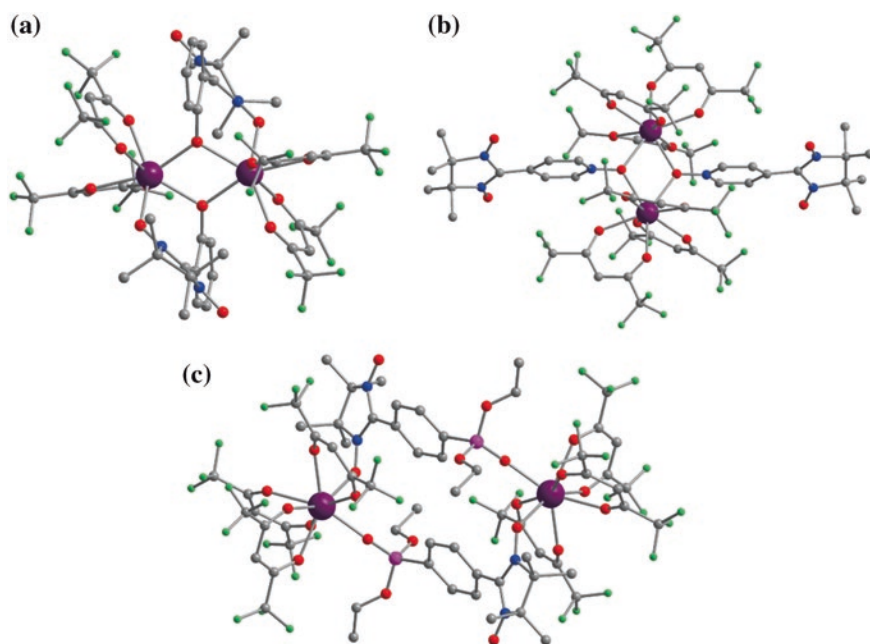


Fig. 3.19 The crystal structure of other Ln₂-radical systems. Figures generated from data first reported in Refs. [31–33]

3.2.4 Organometallic Multidecker Ln-COT SMMs

In the last chapter, we have seen the good SMM performance of mononuclear organometallic lanthanide complexes [34], and thus, their SMM properties are expected to be further improved through the coupling strategies. In fact, several SMM examples coupling two $[\text{Ln}(\text{COT})_2]^-$ SIMM units have been reported recently by M. Murugesu group. In particular, the coupling of two $[\text{Er}(\text{COT})_2]^-$ SIMMs directly results in the clearly enhanced SMM properties as revealed by the improved effective barriers.

At first, the three-layer dinuclear Dy complex, $[\text{Dy}_2(\text{COT}'')_3]$, was constructed through applying the silylated COT''^{2-} aromatic ligands. [35] As shown in Fig. 3.20, two Dy centers were bridged by a central COT''^{2-} aromatic ligand, which provides an ideal delocalized superexchange pathway. Here, three COT''^{2-} ligands exhibit a near-parallel arrangement with the angle of 177.4° between three COT''^{2-} centroids. In addition, the outer COT'' centroids keep a shorter distance from the Dy ions than the inner one. Importantly, further DFT calculations reveal a weak direct covalent interaction between Dy centers, indicating the effective modulation for the magnetic interactions via the central delocalized COT'' ligand. In addition, the isotropic $[\text{Gd}_2(\text{COT}'')_3]$ provided further evidence of the strength and nature of magnetic coupling interactions. Nevertheless, the ab initio calculations suggest a nonlinear arrangement for the anisotropic axes of two Dy ions, as shown in Fig. 3.20, which is unfavorable for the improvement of the SMM properties. Therefore, the complex relaxation processes were observed in the Dy_2 complex, as indicated by the broad out-of-phase peaks of the ac susceptibility data below 10 K (Fig. 3.20), and three small effective barriers were extracted to be 24, 14, and 9 K. Even so, the exploration for the Dy_2 complex gave an important clue for the fact that the Er analogue would behave as a better SMM.

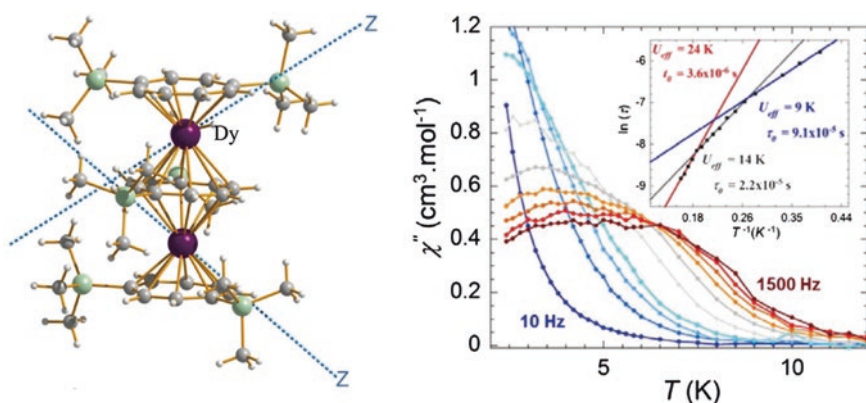


Fig. 3.20 The crystal structure and relaxation dynamics of three-layer dinuclear Dy complex, $[\text{Dy}_2(\text{COT}'')_3]$. Reprinted with the permission from Ref. [35]. Copyright 2013 American Chemical Society

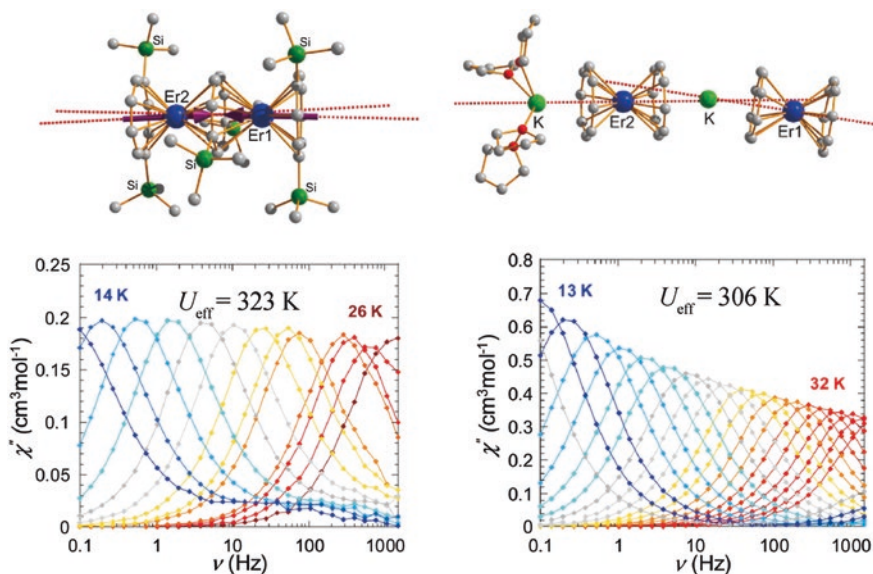


Fig. 3.21 The crystal structure, anisotropic axes, and relaxation dynamics of three- and tetralayer dinuclear Er complex. Reprinted with permission from Ref. [36]. Copyright 2014 American Chemical Society

Further, the triple-decker Er_2 complex was synthesized using the same approach to the above Dy_2 complex [36]. As expected, the more strongly magnetic blocking behavior was observed in the complex in contrast to the mononuclear Er species (Fig. 3.21), which are evidenced by the increasing effective barrier (323 K) and the higher blocking temperature up to 12 K. In order to explain the reason for the enhancement of SMM properties, ab initio calculations were performed, revealing that both Er ions keep the strictly axial anisotropy while showing a near-parallel arrangement with a small angle of 4.2° , and most importantly, an additional blocking mechanism is present in the complex due to the strong exchange interaction between the Er centers mediated by the delocalized aromatic bridge. In addition, a tetralayer sandwich Er_2K_2 complex was also constructed with the structure shown in Fig. 3.21. The complex contains two $[\text{Er}(\text{COT})_2]^-$ units bridged by a K^+ ion and an additional $\text{K}(\text{THF})_4$ counteranion. Similarly, two $[\text{Er}(\text{COT})_2]^-$ units display a near-linear arrangement with a Er-K-Er angle of 169.57° , but a long intramolecular distance of 8.82 \AA between Er centers is present, which greatly reduces the intramolecular magnetic coupling interactions. Even so, the SMM properties are still improved to a certain extent through the coupling compared with the mononuclear species, and thus, a large effective barrier is obtained to be 306 K. Notably, although the hysteresis loops were observed at a high temperature up to 12 K, the fast QTM relaxation at zero field leads to the disappearance of coercive field. Here, such a successful coupling strategy will stimulate further exploration for the larger molecular systems coupling more

$[\text{Er}(\text{COT})_2]^-$ units, presenting a unique approach for isolating SMMs/SCMs with large blocking temperatures for magnetization reversal.

3.3 The Choice of Bridging Ligands

The above examples have provided the powerful evidences for the positive effects of a suitable magnetic interaction on enhancing the magnetization blocking of the individual molecule. In order to promote the magnetic interactions, researchers examined a variety of different bridging ligands from the common diamagnetic oxygen-based groups to the recently discovered radical- and sulfur-based bridges, and some of them have been proved very successful, especially for the coupling via N_2^{3-} -radical leading to the strong magnetization blocking at a relatively high temperature, as discussed in Sect. 3.1. In order to further elucidate the critical role of magnetic interactions in mediating SMM properties, we take a series of dinuclear organometallic cyclopentadienide lanthanide SMMs as an example to show the changes of SMM behaviors with varying the bridging atoms from the Cl [37], N [38] to S [39] atoms and the final bipyramidal radical [40]. In particular, the S- and bipyramidal radical-bridged complexes were found to be among the strongest magnetization blocking systems.

The series of organometallic Dy_2 complexes **1–3** in Fig. 3.22 were reported subsequently by R.A. Layfield and coworkers since 2010. Except complex **1b** showing the 1D chain structure linked by Cl atoms, all other complexes exhibit the dinuclear structures with similar motif but linked by distinct bridging atoms, which create a good platform for getting insight into the correlation between the magnetic properties and the magnetic interactions modulated by the different types of bridging atoms.

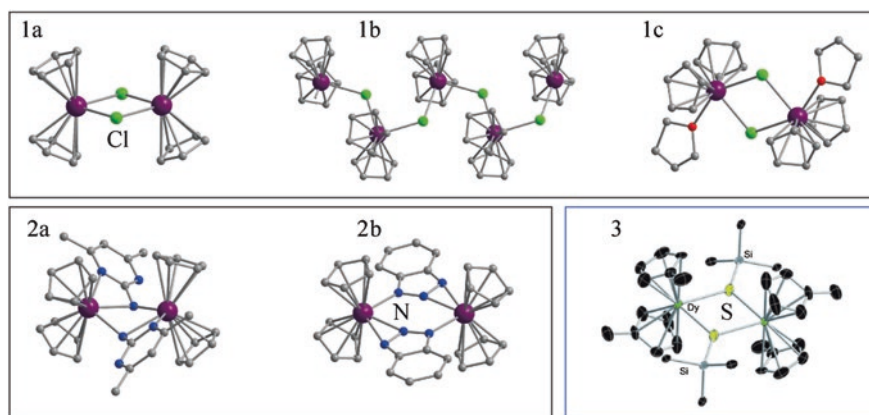


Fig. 3.22 The crystal structure of series of organometallic Dy_2 complexes **1–3** bridged by different types of bridging atoms. **3** Reproduced from Ref. [39] with permission from John Wiley & Sons Ltd.

For Cl-bridged complexes **1a** and **1b**, the centrosymmetric dimer **1a** contains eight-coordinate dysprosium coordinated by two η^5 -Cp ligands and two μ -chloro ligands with Dy-Cl-Dy angle of $96.62(5)^\circ$ and the Cl-Dy-Cl angle of $79.91(16)^\circ$, while polymer chain **1b** comprises $[\text{Cp}_2\text{Dy}]$ units bridged by μ -chloro ligands with much greater Dy(1)-Cl(1)-Dy(1A) and Cl(1)-Dy(1)-Dy(1A) angles of $123.15(7)^\circ$ and $89.82(4)^\circ$, respectively. [37] Notably, a powder X-ray diffraction experiment revealed that complexes **1a** and **1b** cocrystallize in a 3:1 ratio in the crystal. Therefore, the ac susceptibility data under zero-dc applied field reveal two independent relaxation processes involving ca. 3:1 ratio of χ for the low- and high-temperature relaxation, respectively, which is comparable to the proportion of **1a** and **1b** in the crystal. As a result, the low-temperature relaxation is related to the dinuclear Dy_2 complex **1a** with an effective barrier of 38 K, while the high-temperature relaxation arises from the Cl-bridged Dy chain **1b** showing a larger barrier of 98 K, as shown in Fig. 3.23. Further, the application of a dc applied field has no effects on the whole relaxation process of **1b** and the high-temperature relaxation of complex **1a**, but slows down the low-temperature QTM relaxation in **1a**. In addition, complex **1c** was well isolated through a Soxhlet extraction on the above complex in THF followed by slow cooling of the reaction. The main structural difference between **1c** and **1a** is the coordination of a THF molecule to the Dy ion in **1c** leading to the different local coordination geometry. Nevertheless, as shown in Fig. 3.23, although complex **1c** shows an increasing effective barrier (49 K) compared to that of **1a**, the crossover from the thermally activated relaxation to the QTM process was observed in the complex.

In addition, two organometallic Dy_2 complexes **2a** and **2b** in Fig. 3.22 are bridged by the different N-based bridging ligands, one being the N-heterocycle conjugate ligand and the other being the common deprotonated amido ligand [38]. It is notable that the Ln_2N_2 core in **2a** is not a planar structure, but showing a large dihedral angle between N-Dy-N planes. Here, the similar static magnetic properties were observed in two complexes. Nevertheless, ac susceptibility data reveal the distinct relaxation dynamics for them. Here, complex **2a** only shows a weak increase in χ'' below 4 K under zero-dc field, while obvious SMM behavior was observed in complex **2b** as evidenced by the well-resolved χ'' peaks. As shown in Fig. 3.23, the effective barrier of **2b** under zero-dc applied field was extracted to be 47 K, which is of the same order of magnitude as that of complexes **1a** and **1c**. In order to explain the difference of relaxation dynamics for **2a** and **2b**, the calculations including the DFT and Mulliken population analysis were performed. The results indicated that the magnetic interactions in complex **2b** were almost negligible due to the nature of the π orbital and thus the SMM behavior was as a main result of the local single-ion anisotropy of Dy ions. In contrast, the interactions in **2b** were still present due to the effective communications between Dy (d orbitals) and N (p orbitals). Here, although its strength was too weak to have a significant influence on the static magnetic behavior, it is enough to induce the magnetization reversal via a direct or QTM pathway without a barrier, similar to the effects of intermolecular interactions.

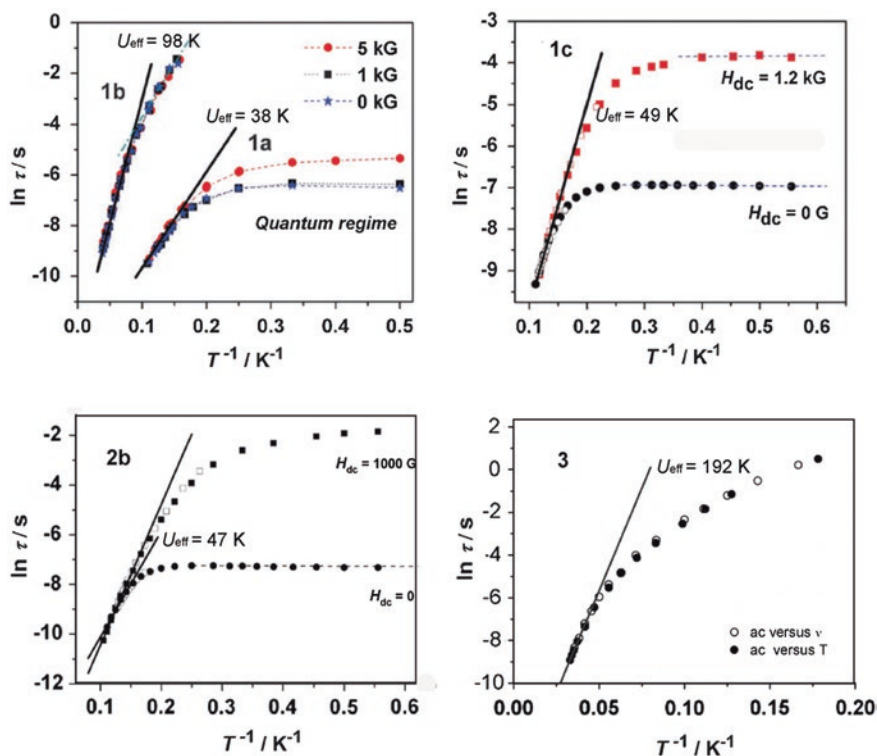


Fig. 3.23 The effective barriers of series of organometallic Dy₂ complexes 1–3 bridged by different types of bridging atoms. (Top) Reproduced from Ref. [37] with permission from The Royal Society of Chemistry. (Bottom) Reproduced from Refs. [38, 39] with permission from John Wiley & Sons Ltd.

Further, similar organometallic Dy₂ complex **3** bridged by soft donors S atoms in Fig. 3.22 was reported in 2012, showing the clearly enhanced SMM properties compared to the above complexes [39]. Here, the coordination of S atoms to Dy ions provides the very different crystal field around Dy ions and the different type of magnetic exchange interactions from the conventional hard oxygen or nitrogen donor-bridged complexes. It is expected that the magnetic exchange interactions between Dy ions could be promoted effectively through the application of soft donor S with more diffuse orbitals which increase orbital overlap between lanthanide ions and bridging atoms. Therefore, among those organometallic Dy₂ complexes, the strongest magnetization blocking behavior was observed here, which are indicated by the frequency dependence of ac out-of-phase signals at the temperature up to 40 K. Most importantly, the effective barrier was given to be 192 K, which is three times larger than that of several other complexes, as shown in Fig. 3.23.

In order to get a further deep insight into the above experimental results, ab initio calculations were performed by L.F. Chibotaru et al. The calculated results

Table 3.1 The anisotropic tensors and magnetic interactions between two Dy centers [39]

	1a	1b	1c	2b	3
g_x	0.0004	0.0009	0.0224	0.0073	0.0012
g_y	0.0009	0.0015	0.0479	0.0884	0.0019
g_z	19.4090	19.3590	18.9208	19.0530	19.3611
$J_{\text{exch}} (\text{cm}^{-1})$			0.08550		-2.19475
$J_{\text{dipolar}} (\text{cm}^{-1})$			-1.99075		-2.22550
$J (\text{cm}^{-1})$			-1.90525		-4.42025

in Table 3.1 reveal that all Dy₂ complexes show the strong Ising-type single-ion anisotropy for the local Dy ions, as indicated by the large g_z values in the ground doublets, but the transversal components are different for them. The complexes **1b** and **3** exhibit less transversal components characterized by g_x and g_y than complexes **1c** and **2b** and thus, the QTM and direct relaxations are much less prominent. Further, the magnetic interactions including the exchange interaction (J_{exch}) and the magnetic dipole–dipole interaction (J_{dipolar}) were also compared between complexes **1c** and **3** in Table 3.1. Here, while the dipolar couplings in **1c** and **3** are similar, the exchange interaction in **3** is twice as large as that in **1c**, indicating the successful strategies of promoting the magnetic interactions via the soft donors as the bridges. Such a relatively strong exchange interactions also play a critical role in the suppression of tunneling relaxation at low temperature like in the asymmetric Dy₂ system in Sect. 3.1.

Finally for the dinuclear organometallic cyclopentadienide lanthanide SMMs, the well-known example is the bipyramidal radical-bridged Tb₂ complex, [(Cp*₂Ln)₂(μ-bpym-)](BPh₄), in Fig. 3.24, which displays a high blocking temperature up to 6.5 K [40]. The lanthanide complexes with Gd, Tb, or Dy ions were prepared through mixing Cp*₂Ln(BPh₄) and bipyramid together in THF and subsequent reduction with KC₈. Here, the much stronger exchange coupling interactions were exhibited in the complexes compared to the above Dy₂ complexes, as indicated by the obvious increases in $\chi_m T$ at low temperatures similar to the case in the N₂³⁻-radical-bridged dilanthanide system. As expected, both Dy and Tb congeners exhibit typical SMM properties, but it is stronger in the Tb complex. The ac susceptibility data for the Tb complex are shown in Fig. 3.24, where the χ'' peaks were observed until 17.5 K. The effective barrier was fitted to be 126 K, which seems to be slightly smaller than that in the S-bridged Dy₂ complex, but the ln(τ) versus 1/T plots show the perfect linear relationship indicating the dominant Orbach process within the investigated temperature domain. Most importantly, the hysteresis loops were observed at a relatively high temperature (6.5 K), indicating the very strong blocking for its magnetic moments in the Tb₂ complex, which should be associated to the strong magnetic coupling between lanthanide ions and the bridged radical ligands.

The above series of the organometallic dinuclear lanthanide SMMs demonstrate a clear route to design effective SMMs through modulating the magnetic coupling interactions with varying the bridging moieties from the common

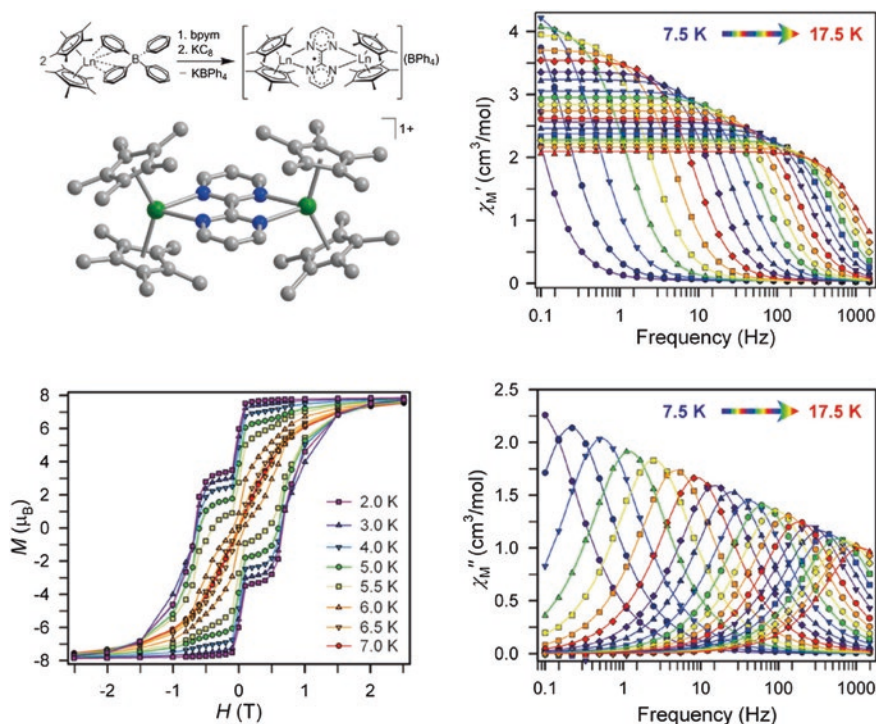


Fig. 3.24 The crystal structure and magnetic properties of radical-bridged Tb_2 complex, $[(\text{Cp}^*\text{Tb})_2(\mu\text{-bpym})](\text{BPh}_4)$. Reprinted with the permission from Ref. [40]. Copyright 2012 American Chemical Society

N-based ligands to the soft donor S, finally to the radical bridging group, strongly supporting the idea that the rational choice of bridging ligands can effectively promote the magnetic interactions between lanthanide ions and lead to the strongly blocked SMMs. In particular, the S- and radical bridges have proven highly successful in promoting magnetic interactions between lanthanide centers, which depends on the internal nature of $4f$ orbitals.

3.4 Dinuclear SMMs with O-Bridges

The outstanding SMM properties have made the organometallic complexes an eye-catching researching frontier, which mainly benefits from their special crystal field and magnetic interactions provided by the ligands with exceptionally high reactivity. However, from a synthetic point of view, it is easier to prepare the common oxygen-based lanthanide systems and expand them when compared with the air-sensitive lanthanide complexes. Therefore, it is still expected that the SMM

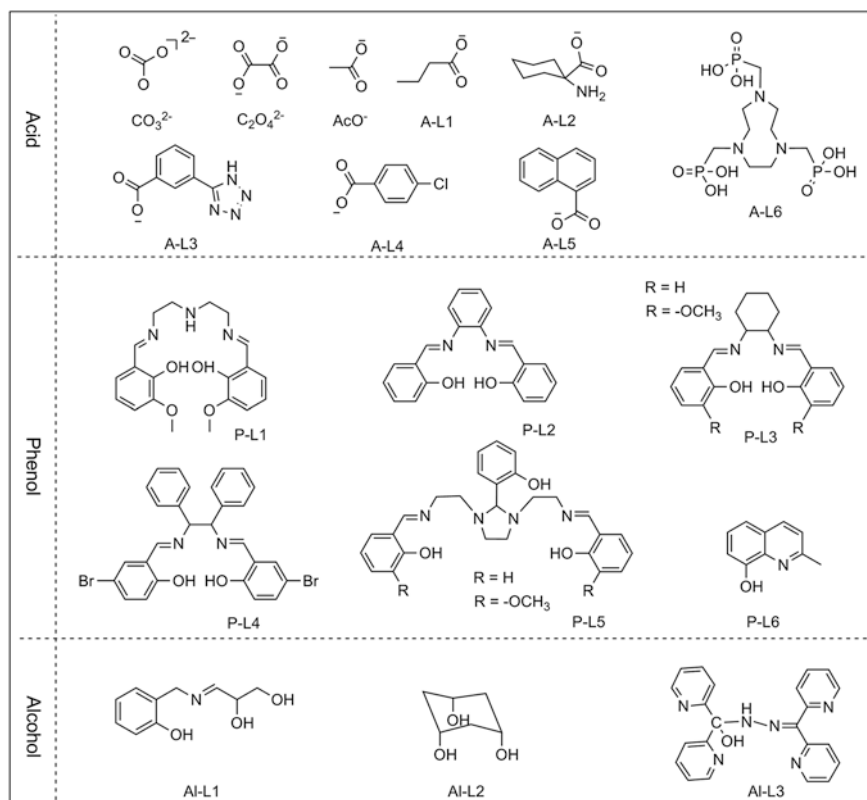


Fig. 3.25 The O-bridging ligands used in the common O-bridging systems

properties could be also enhanced efficiently for the common oxygen-based lanthanide complexes only through modulating the local coordination environments around lanthanide ions and the properties of O-bridge. In fact, early studies on polynuclear lanthanide SMMs were mainly concentrated on this aspect, and now, a great number of research groups are still devoted to exploring the new lanthanide systems aiming at obtaining lanthanide SMMs with high magnetic performance in the common O-bridging systems. Here, we review the O-bridging ligands used in the dinuclear lanthanide complexes showing slow relaxation of magnetization. Those ligands can be classified into four classes in Fig. 3.25: carboxylato-, phenoxido-, alkoxido-, and hydrazone-O ligands. Here, the hydrazone ligands are not listed, and it will be discussed in detail in the fifth chapter. For the first three classes of O-based ligands, their corresponding protonated species exhibit the decreasing acidity and reversely the increasing alkalinity for the deprotonated species, and thus, it is anticipated that usually alkoxido-O bridges should support the stronger magnetic coupling interactions between magnetic centers. Nevertheless, some other factors should be also considered in affecting the SMM performance

of the different lanthanide complexes, such as the coordinate mode of ligands, electronic effects of substituted groups, and the introduction of auxiliary ligands.

3.4.1 Carboxylato-Bridged Dy₂ SMMs

As an excellent linker, oxalate ligand is able to provide an efficient pathway for the superexchange interactions between the transition metal centers and demonstrates the great potential in the search for the molecule-based magnetic materials with chirality. Nevertheless, to date, only one oxalate-based Dy₂ SMM, [Dy₂(HBpz₃)₄(μ-ox)]·2CH₃CN·CH₂Cl₂, was successfully synthesized by some of us in 2009 [41]. As shown in Fig. 3.26, the oxalate anion links two Dy metal centers, and at the same time, the peripheral bulk capping ligands, hydrotris(pyrazolyl)-borate (Bpz³⁻), prevent the growth into 3D structures, minimizing the undesirable intermolecular magnetic interactions. Here, its dc magnetic susceptibility data at low temperature reveal that the bridging oxalate anion propagates a weak intramolecular ferromagnetic coupling between Dy ions. Further, the Dy₂ complex behaves as a typical SMM, which is evidenced by the presence of frequency-dependent χ'' maxima below 9 K in Fig. 3.26. An effective barrier about 40 K was obtained in ln(τ) versus 1/T plots. This work provides a promising strategy to design new lanthanide SMMs based on the versatile oxalate ligand.

To date, a lot Dy₂ complexes based on the common R-COO⁻ bridges were explored in the field of magnetism, as shown in Fig. 3.25, but their SMM properties are not so fascinating [42]. Here, only one typical example showing obvious SMM signals was demonstrated below. The complex in Fig. 3.27 was synthesized via an in situ hydrothermal reaction of 3-cyanobenzoic acid and the lanthanide metal salts in the presence of azide [43]. The two Dy ions are bridged by two carboxy groups in a μ-η¹:η¹ fashion, and each Dy ion is surrounded by the bicapped trigonal prismatic coordination geometry. As shown in most lanthanide SMMs, the

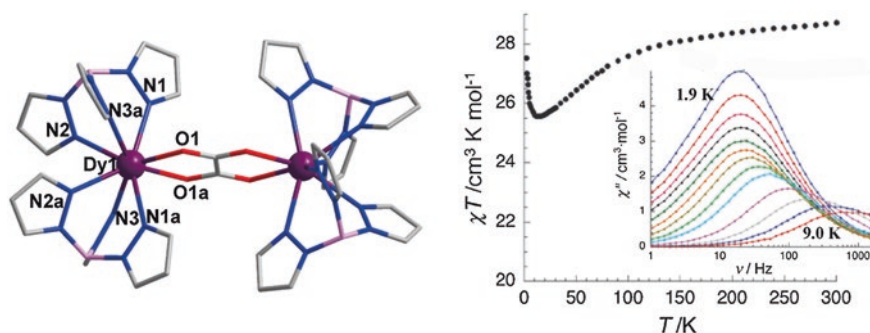


Fig. 3.26 The crystal structure and magnetic properties of oxalate-based Dy₂ SMM, [Dy₂(HBpz₃)₄(μ-ox)]·2CH₃CN·CH₂Cl₂. Reproduced from Ref. [41] with permission from The Royal Society of Chemistry

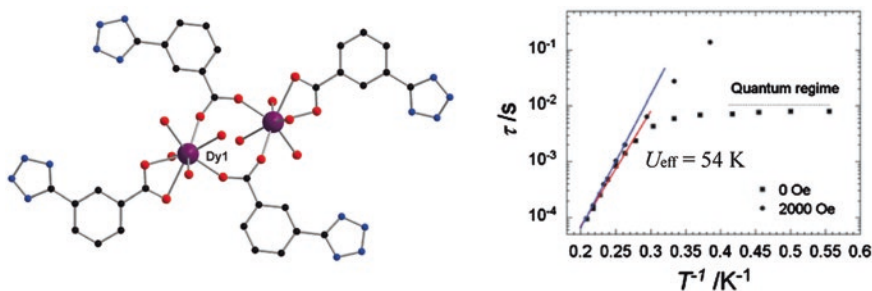


Fig. 3.27 The crystal structure and effective barrier of R-COO⁻ bridging Dy₂ SMM. Reproduced from Ref. [43] with permission from The Royal Society of Chemistry

SMM behavior with a crossover from a thermally activated process to the quantum tunneling relaxation was also observed under zero-dc applied field in the Dy₂ complex in Fig. 3.27. The effective barrier of 54 K seems to be high in the carboxylato-based Dy₂ SMM.

In particular, the magnetism of lanthanide metal phosphonate, [Dy(A-L6)(NO₃)(H₂O)]₂·8H₂O, was explored in 2013 by L-M Zheng and coworkers [44]. Here, the phosphonate ligand shown in Fig. 3.25 possesses three arms with the phosphonate groups capable of coordinating to the lanthanide ions. The structure in Fig. 3.28 reveals that two Dy centers are bridged by four phosphonate groups in two different coordinate modes. Furthermore, the presence of lattice water molecules in the crystal lead to the formation of a 3D extensive hydrogen bond network. The $\chi_m T$ versus T plots at low temperature reveal a weak ferromagnetic interaction between two Dy^{III} ions mediated through the μ_3 -O(P) and O-P-O bridges. Importantly, ac susceptibility data reveal enhanced SMM properties with the loss of lattice water, as indicated by the out-of-phase signals occurring at a higher temperature. For the species containing H₂O molecules, the χ'' peaks appear when applying a

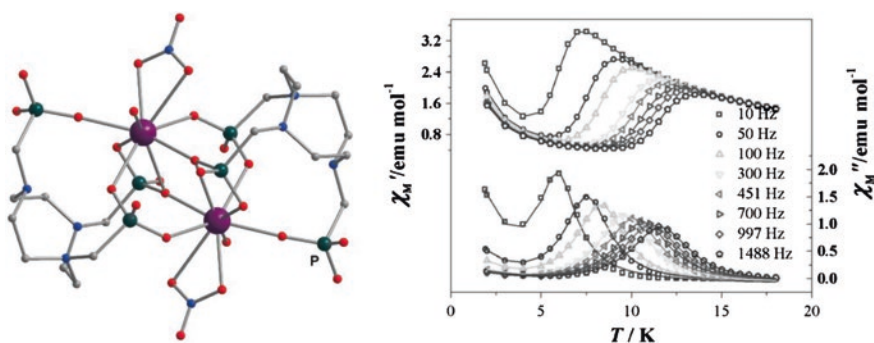


Fig. 3.28 The crystal structure and relaxation dynamics of the Dy₂ SMM bridged by phosphonate groups. Reproduced from Ref. [44] with permission from John Wiley & Sons Ltd.

dc field of 2000 Oe, and the effective barrier was given to be 46 K. In contrast, the dehydrated Dy_2 species exhibits stronger SMM behavior under zero-dc applied field and the effective barrier was 82 K, almost two times as large as that in the species containing H_2O . Further, the reversible modulations of their magnetic dynamics are achieved by desorption and absorption cycles of lattice water. This provides a promising approach to design the responsive lanthanide-based functional materials.

3.4.2 Phenoxido-Bridged Dy_2 SMMs

As shown in Fig. 3.25, the salen-type ligands play a dominant role in synthesizing this kind of Dy_2 SMMs, mainly because such ligands possess a coordinate pocket with the suitable size capable of incorporating a lanthanide ion and meanwhile the phenoxido groups play a role in bridging two lanthanide ions [42]. Here, we take two phenoxido-bridged complexes as examples to elucidate the magnetic performance of this kind of complexes. In particular, in the first examples based on the

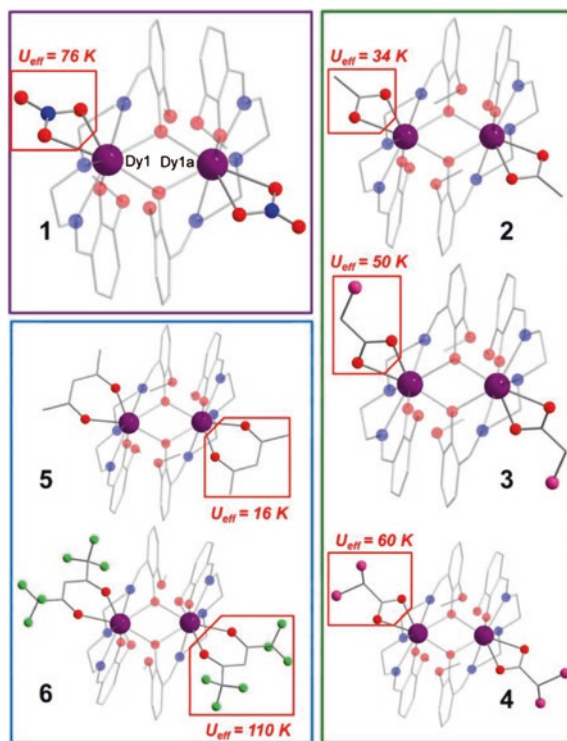


Fig. 3.29 The series of phenoxido-bridged Dy_2 SMMs with different coordinate anions. Reprinted with the permission from Ref. [46]. Copyright 2013 American Chemical Society

phenoxido-bridge, the barrier was enhanced greatly by fine-tuning the electronic effects in coordinate anions.

The magnetic dilution effects for the complex **1** in Fig. 3.29 have been described in detail in Sect. 3.1, revealing that the thermally activated barrier mainly arises from the local single-ion anisotropy of Dy ion, while the low-temperature QTM relaxation is suppressed effectively by the antiferromagnetic interactions between two Dy centers. The centrosymmetric dinuclear complex is composed of two eight-coordinate Dy^{III} ions in an intermediate coordination polyhedron between square antiprism (D_{4d}) and dodecahedron (D_{2d}). Ab initio calculations reveal the strongly anisotropic ($g_z = 19.547$) axis at each Dy ion and the strictly antiparallel orientations indicating the antiferromagnetic exchange interactions for two Dy ions. The effective barrier was extracted to be 76 K via the ac susceptibility data of complex **1** [45]. Further, they systematically investigated two different systems of Dy₂ complexes, showing the significant increase of effective barriers by adding electron-withdrawing substituents on the terminal coordinate anions, as shown in Fig. 3.29 [46]. The two kinds of Dy₂ complexes keep the same dinuclear core structure as to complex **1**, but with different terminal coordinate anions. In particular, for complex **5** and **6**, the introduction of strong electron-withdrawing F atoms at acac ligands results in a sevenfold increase in the effective barrier. Importantly, the series of Dy₂ SMM examples give a great evidence for the fact that the SMM properties are able to be enhanced greatly by fine-tuning the crystal field effects based on the O-bridged lanthanide complexes.

Another Dy₂ compound based on salen-type ligand P-L2 in Fig. 3.25 shows the unsymmetrical crystal structure with two Dy ions (Dy1, Dy2) located in two different coordination environments, as shown in Fig. 3.30 [47]. The eight-coordinate Dy1 adopts a distorted square-antiprismatic geometry, while a distorted capped trigonal prism is found for the seven-coordinated Dy2 ion. The slight increase of $\chi_m T$ values at low temperature reveals the weak intramolecular ferromagnetic interactions between the Dy^{III} centers. Importantly, the temperature

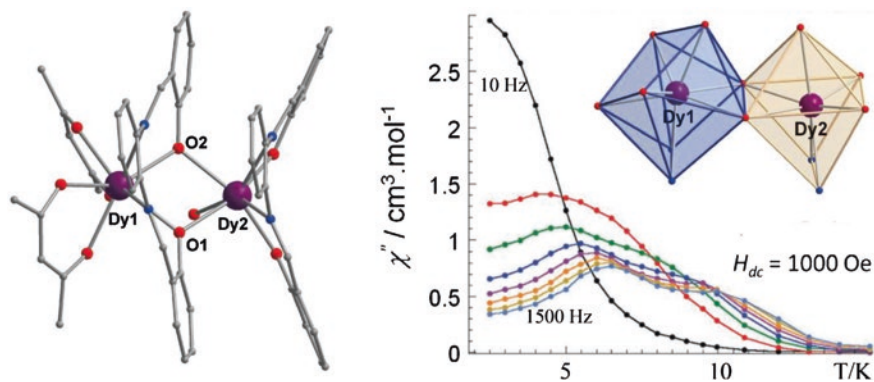


Fig. 3.30 The crystal structure and relaxation dynamics of the unsymmetrical Dy₂ SMM. Reproduced from Ref. [47] with permission from The Royal Society of Chemistry

dependence of ac susceptibility data demonstrates the full broad peaks indicating the multiple relaxation process under zero-dc applied field. Further, the application of an optimum field of 1000 Oe leads to the presence of two clear peaks (Fig. 3.30), which are related to two relaxation processes arising from two asymmetric lanthanide centers in the molecule. By fitting the relaxation times at different temperature regions, two energy barriers were obtained, i.e., $U_{\text{eff}} = 80$ K ($\tau_0 = 8.3 \times 10^{-8}$ s) and 36 K ($\tau_0 = 4.2 \times 10^{-7}$ s). Remarkably, its Yb₂ analogue also displays the SMM behavior with an effective barrier of 24.5 K upon applying a dc applied field of 1600 Oe. The complex represents the first example of a polynuclear Yb^{III} SMM reported.

3.4.3 Alkoxido-Bridged Dy₂ SMMs

To date, alkoxido-bridged dinuclear lanthanide SMMs are still rare due to the weak ability of deprotonation for alcoholic hydroxyl group. However, they show the relatively better SMM properties than the above O-bridged Dy₂ complexes. Two typical examples with alkoxido-bridges were presented below.

The first Dy₂ example was assembled by our group through applying a Schiff base ligand with two coordination pockets [48]. The complex demonstrates a centrosymmetric structure with two Dy ions located in the hula hooplike coordinate geometry. The sharp increase of $\chi_M T$ values at low temperature is indicative of the presence of ferromagnetic exchange interactions between two Dy ions. The obvious ac susceptibility signals are observed with the frequency-dependent maxima below 25 K in Fig. 3.31, indicating the strong SMM properties, which should arise from the strong axiality of Dy^{III} ion due to the hula hooplike coordination geometry. Importantly, the disappearance of χ'' signals at low temperature provides a powerful evidence of the suppression of QTM relaxation, mainly due to the strong

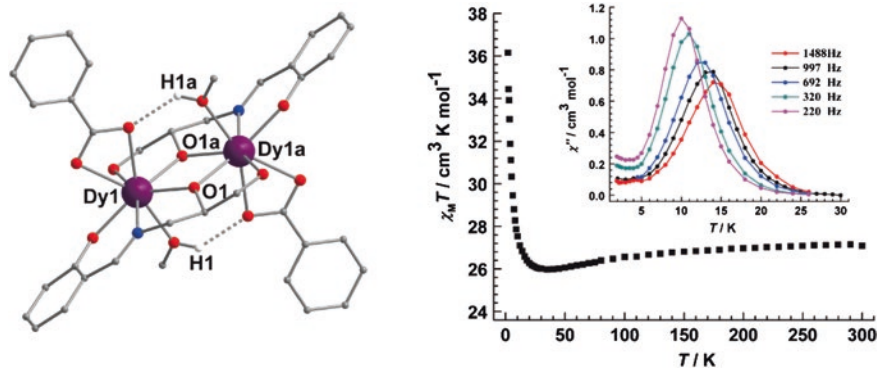


Fig. 3.31 The crystal structure and relaxation dynamics of the O-bridged Dy₂ SMM. Reprinted with the permission from Ref. [48]. Copyright 2013 American Chemical Society

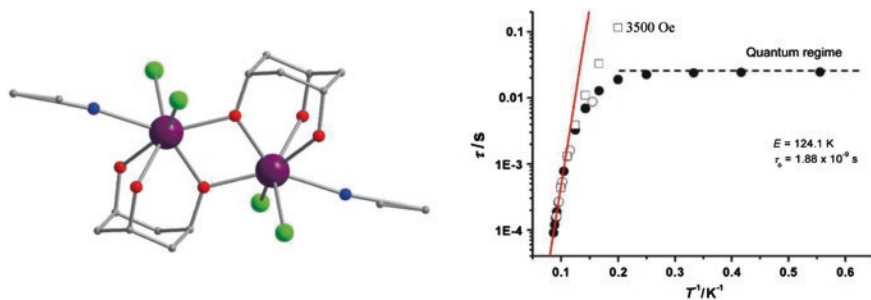


Fig. 3.32 The crystal structure and relaxation dynamics of the O-bridged Dy₂ SMM from Y–Z. Zheng et al. Reproduced from Ref. [49] with permission from The Royal Society of Chemistry

intramolecular ferromagnetic interactions as observed in the asymmetric Dy₂ in Sect. 3.1. The effective barrier for magnetization reversal is given to be 94 K, which is among the highest barrier for the O-bridged Dy₂ SMMs.

In addition, another alkoxido-bridged Dy₂ SMM was reported in 2013 by Zheng et al. [49]. The complex was synthesized through the solvothermal reaction of LnCl₃·6H₂O and the corresponding ligand A-L2 in Fig. 3.25, and its structure is shown in Fig. 3.32 with two Dy ions in the seven-coordinate environments. Under zero-dc applied field, the complex displays the clear SMM behavior with a crossover from the thermally activated process to QTM relaxation. Further, the application of a 3500-Oe dc field slows down the tunneling relaxation at low temperature, and an effective barrier of 124 K was obtained through the Arrhenius fitting, as shown in Fig. 3.32. In addition, the isostructural Yb₂ complex also shows the field-induced SMM behavior with an effective barrier of 19.5 K. Interestingly, the heterospin dinuclear SMM containing Dy and Yb centers were also investigated, showing the field-induced two-step relaxation process which corresponds to the Dy and Yb ions, respectively.

The above examples have shown the great potential of the common O-bridged lanthanide complexes in designing the strongly blocked SMMs. In particular, the series of phenoxido-bridged Dy₂ SMMs indicate that the effective barriers are able to be greatly enhanced through modulating some other critical factors based on the O-bridged core structure. Therefore, this is still a promising approach to obtain the ideal and stable lanthanide SMMs at common conditions for the easier technological applications as classical or quantum bits in the future.

3.5 Conclusion

In this chapter, the role of magnetic coupling interactions between lanthanide centers are highlighted in modulations of magnetic dynamics especially at the low-temperature region via elucidating the relaxation mechanisms in the simplest

multinuclear model systems, i.e., dinuclear lanthanide SMMs. Nevertheless, it should be noted that, in most lanthanide SMMs, the local crystal field effects around lanthanide ions are still the most critical parameter in obtaining the SMMs with high blocking barriers due to the internal strong single-ion anisotropy of lanthanide ions. Since the symmetry, electrostatic repulsion effects and some other factors in controlling the relaxation dynamics have been discussed in Chap. 2 and thus we mainly discussed the magnetic interactions in this chapter. As a step further, we will present a critical discussion in the assembly of lanthanide SMMs with higher nuclearities applying the above knowledge.

References

1. Gatteschi D, Sessoli R (2003) Quantum tunneling of magnetization and related phenomena in molecular materials. *Angew Chem Int Ed* 42(3):268–297. doi:10.1002/anie.200390099
2. Rinehart JD, Fang M, Evans WJ et al (2011) Strong exchange and magnetic blocking in N_2^{3-} -radical-bridged lanthanide complexes. *Nat Chem* 3(7):538–542. doi:10.1038/nchem.1063
3. Guo Y-N, Xu G-F, Wernsdorfer W et al (2011) Strong axiality and Ising exchange interaction suppress zero-field tunneling of magnetization of an asymmetric Dy_2 single-molecule magnet. *J Am Chem Soc* 133(31):11948–11951. doi:10.1021/ja205035g
4. Milios CJ, Vinslava A, Wernsdorfer W et al (2007) A record anisotropy barrier for a single-molecule magnet. *J Am Chem Soc* 129(10):2754–2755. doi:10.1021/ja068961m
5. Blagg RJ, Ungur L, Tuna F et al (2013) Magnetic relaxation pathways in lanthanide single-molecule magnets. *Nat Chem* 5(8):673–678. doi:10.1038/nchem.1707
6. Blagg RJ, Muryn CA, McInnes EJJ et al (2011) Single pyramid magnets: Dy_5 pyramids with slow magnetic relaxation to 40 K. *Angew Chem Int Ed* 50(29):6530–6533. doi:10.1002/anie.201101932
7. Guo Y-N, Xu G-F, Gamez P et al (2010) Two-step relaxation in a linear tetranuclear dysprosium(III) aggregate showing single-molecule magnet behavior. *J Am Chem Soc* 132(25):8538–8539. doi:10.1021/ja103018m
8. Tang J, Hewitt I, Madhu NT et al (2006) Dysprosium triangles showing single-molecule magnet behavior of thermally excited spin states. *Angew Chem Int Ed* 45(11):1729–1733. doi:10.1002/anie.200503564
9. Hewitt IJ, Tang J, Madhu NT et al (2010) Coupling Dy_3 triangles enhances their slow magnetic relaxation. *Angew Chem Int Ed* 49(36):6352–6356. doi:10.1002/anie.201002691
10. Habib F, Murugesu M (2013) Lessons learned from dinuclear lanthanide nano-magnets. *Chem Soc Rev* 42:3278–3288. doi:10.1039/C2CS35361J
11. Miller JS (2011) Magnetically ordered molecule-based materials. *Chem Soc Rev* 40(6):3266–3296. doi:10.1039/c0cs00166j
12. Bogani L, Sangregorio C, Sessoli R et al (2005) Molecular engineering for single-chain-magnet behavior in a one-dimensional dysprosium-nitronyl nitroxide compound. *Angew Chem Int Ed* 44(36):5817–5821. doi:10.1002/anie.200500464
13. Glauber RJ (1963) Time-dependent statistics of the Ising model. *J Math Phys* 4:294–307. doi:10.1063/1.1703954
14. Powell AK (2010) Molecular magnetism: a bridge to higher ground. *Nat Chem* 2(5):351–352. doi:10.1038/nchem.637
15. Carlin RL (1986) *Magnetochemistry*. Springer, Berlin
16. Rinehart JD, Fang M, Evans WJ et al (2011) A N_2^{3-} radical-bridged terbium complex exhibiting magnetic hysteresis at 14 K. *J Am Chem Soc* 133(36):14236–14239. doi:10.1021/ja206286h

17. Habib F, Lin P-H, Long J et al (2011) The use of magnetic dilution to elucidate the slow magnetic relaxation effects of a Dy₂ single-molecule magnet. *J Am Chem Soc* 133(23):8830–8833. doi:[10.1021/ja2017009](https://doi.org/10.1021/ja2017009)
18. Ishikawa N, Iino T, Kaizu Y (2002) Interaction between *f*-electronic systems in dinuclear lanthanide complexes with phthalocyanines. *J Am Chem Soc* 124(38):11440–11447. doi:[10.1021/ja027119n](https://doi.org/10.1021/ja027119n)
19. Nelder JA, Mead R (1965) A simplex method for function minimization. *Comput J* 7(4):308–313. doi:[10.1093/comjnl/7.4.308](https://doi.org/10.1093/comjnl/7.4.308)
20. Ishikawa N, Otsuka S, Kaizu Y (2005) The effect of the *f*–*f* interaction on the dynamic magnetism of a coupled 4^f system in a dinuclear terbium complex with phthalocyanines. *Angew Chem Int Ed* 44(5):731–733. doi:[10.1002/anie.200461546](https://doi.org/10.1002/anie.200461546)
21. Katoh K, Kajiwara T, Nakano M et al (2011) Magnetic relaxation of single-molecule magnets in an external magnetic field: an Ising dimer of a terbium(III)–phthalocyaninate triple-decker complex. *Chem Eur J* 17(1):117–122. doi:[10.1002/chem.201002026](https://doi.org/10.1002/chem.201002026)
22. Sakae S, Fuyuhiko A, Fukuda T et al (2012) Dinuclear single-molecule magnets with porphyrin-phthalocyanine mixed triple-decker ligand systems giving SAP and SP coordination polyhedra. *Chem Commun* 48(43):5337–5339. doi:[10.1039/C2CC31125A](https://doi.org/10.1039/C2CC31125A)
23. Ma Y, Xu G-F, Yang X et al (2010) Pyrazine-bridged Dy₂ single-molecule magnet with a large anisotropic barrier. *Chem Commun* 46:8264–8266. doi:[10.1039/C0CC01423K](https://doi.org/10.1039/C0CC01423K)
24. Yi X, Bernot K, Pointillart F et al (2012) A luminescent and sublimable Dy^{III}-based single-molecule magnet. *Chem Eur J* 18(36):11379–11387. doi:[10.1002/chem.201201167](https://doi.org/10.1002/chem.201201167)
25. Yi X, Bernot K, Cador O et al (2013) Influence of ferromagnetic connection of Ising-type Dy^{III}-based single ion magnets on their magnetic slow relaxation. *Dalton Trans* 42(19):6728–6731. doi:[10.1039/c3dt50762a](https://doi.org/10.1039/c3dt50762a)
26. Li X-L, Chen C-L, Gao Y-L et al (2012) Modulation of homochiral Dy^{III} complexes: single-molecule magnets with ferroelectric properties. *Chem Eur J* 18(46):14632–14637. doi:[10.1002/chem.201201190](https://doi.org/10.1002/chem.201201190)
27. Pointillart F, Klementieva S, Kuropatov V et al (2012) A single molecule magnet behaviour in a D_{3h} symmetry Dy(III) complex involving a quinone-tetrathiafulvalene-quinone bridge. *Chem Commun* 48(5):714–716. doi:[10.1039/c1cc16314k](https://doi.org/10.1039/c1cc16314k)
28. Pointillart F, Le Gal Y, Golhen S et al (2011) Single-molecule magnet behaviour in a tetrathiafulvalene-based electroactive antiferromagnetically coupled dinuclear dysprosium(III) complex. *Chem Eur J* 17(37):10397–10404. doi:[10.1002/chem.201100869](https://doi.org/10.1002/chem.201100869)
29. Pointillart F, Le Guennic B, Cauchy T et al (2013) A series of tetrathiafulvalene-based lanthanide complexes displaying either single molecule magnet or luminescence-direct magnetic and photo-physical correlations in the ytterbium analogue. *Inorg Chem* 52(10):5978–5990. doi:[10.1021/ic400253m](https://doi.org/10.1021/ic400253m)
30. Poneti G, Bernot K, Bogani L et al (2007) A rational approach to the modulation of the dynamics of the magnetisation in a dysprosium-nitronyl-nitroxide radical complex. *Chem Commun* 18:1807–1809. doi:[10.1039/b617898g](https://doi.org/10.1039/b617898g)
31. Liu R, Zhang C, Li L et al (2012) Ligand substitution effect on single-molecule magnet behavior in dinuclear dysprosium complexes with radical functionalized phenol as bridging ligands. *Dalton Trans* 41(39):12139–12144. doi:[10.1039/c2dt31310c](https://doi.org/10.1039/c2dt31310c)
32. Han T, Shi W, Zhang X-P et al (2012) A family of binuclear dysprosium(III) radical compounds with magnetic relaxation in ON and OFF states. *Inorg Chem* 51(23):13009–13016. doi:[10.1021/ic3021244](https://doi.org/10.1021/ic3021244)
33. Pointillart F, Bernot K, Poneti G et al (2012) Crystal packing effects on the magnetic slow relaxation of Tb(III)-nitronyl nitroxide radical cyclic dinuclear clusters. *Inorg Chem* 51(22):12218–12229. doi:[10.1021/ic301394x](https://doi.org/10.1021/ic301394x)
34. Layfield RA (2014) Organometallic single-molecule magnets. *Organometallics*. doi:[10.1021/om401107f](https://doi.org/10.1021/om401107f)
35. Le Roy JJ, Jeletic M, Gorelsky SI et al (2013) An organometallic building block approach to produce a multidecker 4f single-molecule magnet. *J Am Chem Soc* 135(9):3502–3510. doi:[10.1021/ja310642h](https://doi.org/10.1021/ja310642h)

36. Le Roy JJ, Ungur L, Korobkov I et al (2014) Coupling strategies to enhance single-molecule magnet properties of erbium-cyclooctatetraenyl complexes. *J Am Chem Soc* 136(22):8003–8010. doi:[10.1021/ja5022552](https://doi.org/10.1021/ja5022552)
37. Sulway SA, Layfield RA, Tuna F et al (2012) Single-molecule magnetism in cyclopentadienyl-dysprosium chlorides. *Chem Commun* 48:1508–1510. doi:[10.1039/C1CC14643B](https://doi.org/10.1039/C1CC14643B)
38. Layfield RA, McDouall JJW, Sulway SA et al (2010) Influence of the N-bridging ligand on magnetic relaxation in an organometallic dysprosium single-molecule magnet. *Chem Eur J* 16(15):4442–4446. doi:[10.1002/chem.201000158](https://doi.org/10.1002/chem.201000158)
39. Tuna F, Smith CA, Bodensteiner M et al (2012) A high anisotropy barrier in a sulfur-bridged organodysprosium single-molecule magnet. *Angew Chem Int Ed* 51(28):6976–6980. doi:[10.1002/anie.201202497](https://doi.org/10.1002/anie.201202497)
40. Demir S, Zadrozny JM, Nippe M et al (2012) Exchange coupling and magnetic blocking in bipyrimidyl radical-bridged dilanthanide complexes. *J Am Chem Soc* 134(45):18546–18549. doi:[10.1021/ja308945d](https://doi.org/10.1021/ja308945d)
41. Xu GF, Wang QL, Gamez P et al (2010) A promising new route towards single-molecule magnets based on the oxalate ligand. *Chem Commun* 46:1506–1508. doi:[10.1039/b920215c](https://doi.org/10.1039/b920215c)
42. Zhang P, Guo Y-N, Tang J (2013) Recent advances in dysprosium-based single molecule magnets: structural overview and synthetic strategies. *Coord Chem Rev* 257(11–12):1728–1763. doi:[10.1016/j.ccr.2013.01.012](https://doi.org/10.1016/j.ccr.2013.01.012)
43. Liang L, Peng G, Li G et al (2012) In situ hydrothermal synthesis of dysprosium(III) single-molecule magnet with lanthanide salt as catalyst. *Dalton Trans* 41(19):5816–5823
44. Ren M, Bao S-S, Hoshino N et al (2013) Solvent responsive magnetic dynamics of a dinuclear dysprosium single-molecule magnet. *Chem Eur J* 19(29):9619–9628. doi:[10.1002/chem.201300497](https://doi.org/10.1002/chem.201300497)
45. Long J, Habib F, Lin P-H et al (2011) Single-molecule magnet behavior for an antiferromagnetically superexchange-coupled dinuclear dysprosium(III) complex. *J Am Chem Soc* 133(14):5319–5328. doi:[10.1021/ja109706y](https://doi.org/10.1021/ja109706y)
46. Habib F, Brunet G, Vieru V et al (2013) Significant enhancement of energy barriers in dinuclear dysprosium single-molecule magnets through electron-withdrawing effects. *J Am Chem Soc* 135(36):13242–13245. doi:[10.1021/ja404846s](https://doi.org/10.1021/ja404846s)
47. Lin P-H, Sun W-B, Yu M-F et al (2011) An unsymmetrical coordination environment leading to two slow relaxation modes in a Dy₂ single-molecule magnet. *Chem Commun* 47(39):10993–10995. doi:[10.1039/C1CC14223B](https://doi.org/10.1039/C1CC14223B)
48. Zhang P, Zhang L, Lin S-Y et al (2013) Modulating magnetic dynamics of Dy₂ system through the coordination geometry and magnetic interaction. *Inorg Chem* 52(8):4587–4592. doi:[10.1021/ic400150f](https://doi.org/10.1021/ic400150f)
49. Leng J-D, Liu J-L, Zheng Y-Z et al (2013) Relaxations in heterolanthanide dinuclear single-molecule magnets. *Chem Commun* 49(2):158–160. doi:[10.1039/C2CC37036K](https://doi.org/10.1039/C2CC37036K)

Chapter 4

Single-Molecule Toroids and Multinuclear Lanthanide Single-Molecule Magnets

Abstract In this chapter, we first give a clear definition for single-molecule toroidic (SMT) on the basis of the toroidal magnetic moments of ground doublets present in triangular Dy₃ SMMs, which is further exemplified via several typical Dy-based single-molecular magnets (SMMs) showing toroidal magnetic moments. Secondly, we examine the typical polynuclear lanthanide complexes showing SMM behavior, and three main synthetic strategies are given as follows: building block approach, organometallic approach, and multidentate ligand approach. The information extracted from such investigation is expected to enhance our understanding to SMM performances of polynuclear lanthanide complexes and facilitate their future applications.

Keywords Single-molecule toroidic · Toroidal magnetic moments · Building block · Organometallic approach · Multidentate ligand


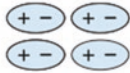

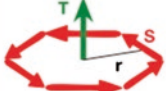
As mentioned in last two chapters, although the mono- and dinuclear lanthanide complexes have exhibited great achievements in obtaining strongly blocked SMMs due to the strong magnetic anisotropy of lanthanide ions, the limited spin centers in the complexes appear still to prevent the further enhancement of their single-molecular magnet (SMM) properties due to the limited number of unpaired electrons [1]. Theoretically speaking, the more the spin centers in one metal cluster, the larger spin ground state can be achieved when the ferromagnetic coupling interactions are present in the cluster. Nevertheless, it needs an accurate control for the magnetic anisotropy of each metal center and the magnetic exchange interactions between the metal ions, which seems to be a very challenging task. In particular, it turns to be more difficult for multinuclear lanthanide complexes because the core 4*f* orbital shielded by the external electrons usually leads to extremely strong magnetic anisotropy of lanthanide ions but poor communication with other metal ions. However, considerable effort of researchers has been devoted to this field, and some groundbreaking results were achieved in this respect. Importantly, the Dy₄K₂ SMM reported by Winpenny et al. created an effective barrier record of multinuclear lanthanide SMMs, 692 K [2], next to the highest barrier of 939 K in

SMMs [3], which suggests the great potential of multinuclear lanthanide clusters in obtaining strongly blocked SMMs. Furthermore, besides their SMM performance, the most important contributions to the SMM field are the discovery of some new magnetic phenomena such as spin chirality in Dy_3 triangle [4, 5], and the deepening comprehension of the complex relaxation mechanism arising from the different strongly anisotropic centers presents in one molecule [6]. The most typical example is the triangular Dy_3 SMM reported in 2006, showing the non-magnetic ground state due to the toroidal arrangement of anisotropic axes, which opens up the research field of multinuclear lanthanide SMMs [4]. Significantly, a new concept of single-molecule toroic (SMT) was put forward on the basis of the toroidal magnetic moments of ground doublets present in the cyclic lanthanide SMMs [7, 8]. In this chapter, we will firstly give a clear definition for SMT phenomena, which is exemplified via several typical Dy-based SMMs showing toroidal magnetic moments. Subsequently, we examine the typical polynuclear lanthanide complexes showing SMM behavior and classify them in the hope of drawing some lessons in synthesizing polynuclear lanthanide SMMs with high barriers for readers.

4.1 Single-Molecule Toroic

Ferrotoroidicity is viewed as the fourth form of ferroic order different from the three well-known forms: ferromagnetism, a spontaneous magnetization; ferroelectricity, a spontaneous polarization; and ferroelasticity, a spontaneous strain [9–12]. As shown in Fig. 4.1, in contrast to ferroelectric and ferromagnetic orders—one violating space-reversal symmetry and the other violating time-reversal symmetry, the existence of ferrotoroidicity violates both space- and time-inversion symmetry, which could be thus related to the coexistence of two order parameters (ferroelectric and ferromagnetic) in single phase materials. Therefore, such materials exhibit pronounced magnetoelectric correlations, and it is possible to induce a magnetization \mathbf{M} by an electric field \mathbf{E} and a polarization \mathbf{P} by a magnetic field \mathbf{H} , which in

Fig. 4.1 All forms of ferroic order under the parity operations of space and time. Reprinted by permission from Macmillan Publishers Ltd.: Ref. [9], copyright 2007

	Space	Invariant	Change
Time		Invariant	Change
Invariant		Ferroelastic 	Ferroelectric 
Change		Ferromagnetic 	Ferrotoroidic 

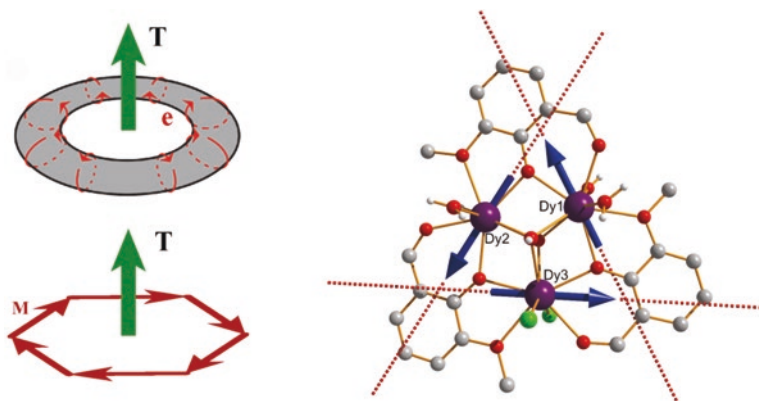


Fig. 4.2 The comparison of a *ring-shaped* torus and Dy_3 toroidal moment. *Left* reprinted by permission from Macmillan Publishers Ltd.: Ref. [9], copyright 2007. *Right* reproduced from Ref. [8] by permission of the Royal Society of Chemistry

principle allows the applications in transducers, magnetic field sensors, and especially the information storage where data can be written electrically and read magnetically [9, 10]. Here it should be stressed that the ferrotoroidic materials are based on the presence of toroidal moments generated by a vortex of magnetic moments, such as atomic spins or orbital currents, as shown in Fig. 4.1, and such a toroidal-like moment can be described by a vector, $\mathbf{T} = \sum_n \mathbf{r}_n \times \mathbf{s}_n$. Macroscopically, a classical example is a ring-shaped torus with an even number of current windings, where the current induces a circular magnetic field inside the solenoid, resulting in a toroidal moment perpendicular to the magnetic field (Fig. 4.2 left) [9].

Nevertheless, such research for the toroidal moment mainly focuses on atom-based magnetic materials in solid-state chemistry and physics, such as $Co_3B_7O_{13}Br$, Cr_2O_3 and the recent $LiCoPO_4$, which show a collective property due to the exchange interactions between magnetic moments in extended 3D structures [11, 12]. Contrary to them, magnetic molecular clusters possess a well-defined structure and are regularly arranged in large crystals, and thus macroscopic measurements can give a direct access to single-molecule properties. This allows us to design a target molecule-based system with specific properties and functions, including the one with desired non-collinear arrangement of magnetic moments corresponding to toroidal magnetization. In fact, such molecules have been reported in SMM field with several typical examples of Dy_3 triangles [5, 13], planar Dy_4 [14] and cyclic Dy_6 [15] showing the toroidal moment at ground state, as revealed by *ab initio* calculations. In particular, the non-magnetic ground state in the seminal Dy_3 SMMs reported by A.K. Powell et al. are well explained by the model with an almost toroidal arrangement of magnetic moments on Dy sites, as shown in Fig. 4.2 [5]. Further investigations of the magnetolectric properties revealed specific magnetoelectric and magneto-current effects of this compound related to its toroidal moment [7]. Therefore, by analogy with SMMs, we can call those molecular clusters as single-molecule toroids (SMTs) [8].

Table 4.1 Classification of SMTs based on toroidal magnetization and traditional magnetization

Compounds	Net toroidal moment		Mixed moment			Zero toroidal moment	Enhanced toroidal moment
	Dy ₄	Dy ₆ wheel	Dy ₃ -1	Dy ₃ -2	Dy ₆ -1	CuDy ₃	Dy ₆ -2
T_z	$\neq 0$	$\neq 0$	$\neq 0$	$\neq 0$	$\neq 0$	$= 0$	$T_{z1} + T_{z2}$
M/μ_B	$= 0$	$= 0$	$= 0.56$	$= 11.5$	$\neq 0$	$= 0.8$	$= 13.1$

In our recent tutorial review, four types of SMTs can be identified based on different toroidal magnetization and traditional magnetization in nine typical Dy-based SMTs discovered to date, i.e., net toroidal moment compounds, mixed-moment compounds, zero toroidal moment compounds, and enhanced toroidal moment compounds, as shown in Table 4.1 [8]. The detailed ab initio calculations for some of them reveal the different roles of the molecular symmetry, the coordination environment, and/or suitable exchange/dipolar interactions in defining the toroidal moments arising from the toroidal arrangements of Ising-like anisotropic axes of Dy ion. Here, we will give a further discussion for those SMT examples from a viewpoint of chemical synthesis, which undoubtedly serve as a valuable reference for synthetic chemists and will stimulate the increasing interest in the explorations of new magnetic systems with toroidal moments.

4.1.1 The Seminal Dy₃ SMT

In 2006, Powell and coworkers firstly reported the unusual magnetic properties of the triangular [Dy₃(μ_3 -OH)₂L₃Cl(H₂O)₅]Cl₃ (L = *o*-vanillin) complex, i.e., the coexistence of the slow magnetic relaxation and an almost diamagnetic ground state (Figs. 4.2 and 4.3), which thus initiates the great interest in the study of Dy₃ triangles and subsequent polynuclear lanthanide complexes [4]. The structure (Fig. 4.2) shows an almost C_{3h} symmetry of the triangular molecule bridged by two μ_3 -hydroxo and three μ_2 -phenoxide, and each of the eight-coordinated dysprosium centers is located in a trigonal dodecahedron showing a D_{2d} symmetric axis directing radially outward the triangle. Nevertheless, the calculated anisotropic axes of Dy ions are not along the symmetric axes, but points to the tangential direction to the vertices of the triangle, as shown in Fig. 4.2, which is greatly associated with the higher effective negative charge in phenoxide group [16]. The static magnetic behavior of both polycrystalline and single-crystal samples at low temperature reveals the existence of an almost non-magnetic ground state (Fig. 4.3) [5]. Nevertheless, the strong frequency dependence below 20 K, a signature of SMM behavior, was still observed with an effective barrier of 61.7 K, as shown in Fig. 4.3c, which should be associated with the thermally excited spin states of the Dy₃ molecule.

An effective explanation of the static magnetic behavior at low temperature is the model of toroidal magnetic moment based on the almost C_{3h} symmetry of the molecule and the large magnetic anisotropy of the Dy^{III} ions. The detailed

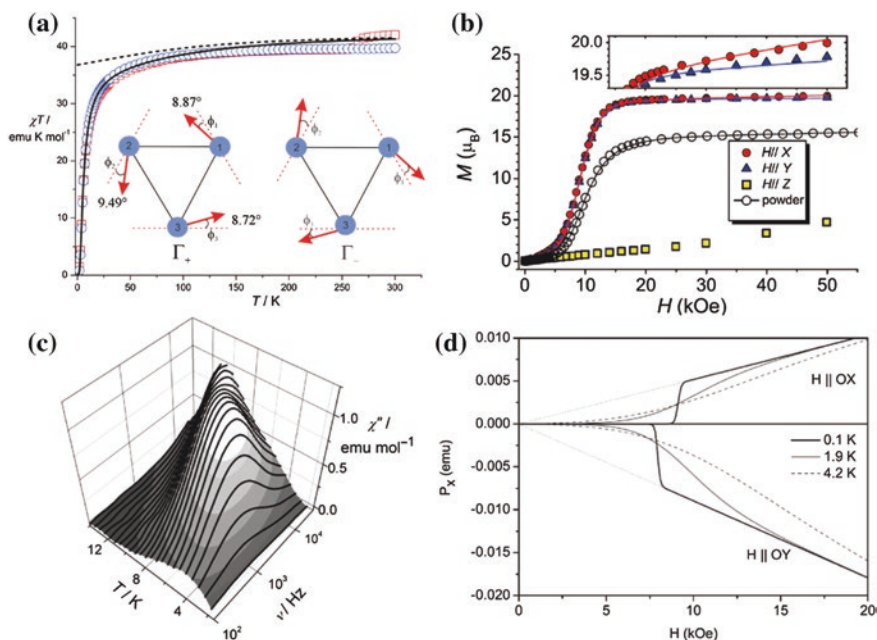


Fig. 4.3 The static magnetic properties (**a** powder sample; **b** single-crystal sample), dynamic magnetic susceptibility **c**, and the magnetolectric properties of Dy₃ SMM **d**. **a** Reproduced from Ref. [13] by permission of John Wiley & Sons Ltd. **b, d** Reprinted with permission from Refs. [5, 7]. Copyright 2008 and 2011 by American Physical Society. **c** Reproduced from ref. [4] by permission of John Wiley & Sons Ltd.

investigations combining single-crystal magnetic measurements, Hamiltonian models, and ab initio calculations confirm a reliable picture of the electronic structure of the Dy₃ system, revealing the non-collinear linkage of the single-ion easy axes of magnetization of the Dy ions that lie in the plane of the triangle at approximate 120° one from each other (Fig. 4.2) [5, 13, 16]. Remarkably, the complex ab initio calculations by L.F. Chibotaru et al. have given an accurate determination of magnetic anisotropic vector of each Dy site, and the coupling interactions between different Dy centers are responsible for the toroidal arrangement [13, 16]. As shown in Figs. 4.2 and 4.3a, the local large anisotropy axes with $g_z > 19.7$ are found to lie almost in the Dy₃ plane with an out-of-plane angle in the range of 2.4–8.81° and close to the tangential direction (the φ angles of anisotropy axis with tangential direction are 8.72–9.491°). It is the small out-of-plane deviations of magnetic axes from the Dy₃ plane that leads to a small total momentum of ca. 0.56 μ_B pointing perpendicularly to the plane in the ground state and the further increasing magnetization with field at a low-field limit in Fig. 4.3b, which is mainly as a result of the small deviations from an exact C_{3h} symmetry. Furthermore, the magnetic exchange interactions between Dy centers were also explored within the Lines model based on the obtained Kramers

doublets of each Dy center, where due to the strong single-ion anisotropy and weak magnetic interactions between them the effective Heisenberg Hamiltonian $H = -\sum_{i=1}^3 J_i \mathbf{S}_i \cdot \mathbf{S}_{i+1}$ with the real spin of Dy ion is able to be transferred into the non-collinear Ising model $H = -\sum_{i=1}^3 \tilde{J}_i \tilde{s}_{iz} \cdot \tilde{s}_{i+1z}$ with \tilde{s}_{iz} corresponding to the projection of the pseudo-spin $\tilde{s}_{iz} = 1/2$ on the anisotropy axis of site i [13]. The simulation for static powder magnetic data gave $J = -0.6 \text{ cm}^{-1}$, which corresponds to $\tilde{J} = 7.5 \text{ cm}^{-1}$ according to the relationship, $\tilde{J}_i = (25 \cos \varphi_{i,i+1}) J_i = -12.5 J_i$, ($\varphi_{i,i+1}$ is the angle between the anisotropy axes on sites i and $i + 1$, about 120°). Therefore, the positive \tilde{J} value reveals a ferromagnetic alignment of the local magnetization vectors along the anisotropy axes, thus leading to the toroidal magnetic moment. In fact, a total magnetic interaction containing the exchange and dipolar interactions was considered here, but more detailed studies latter separate the contributions from the exchange and dipolar interactions between magnetic moments suggesting that the dipolar interactions should play a key role in stabilizing the toroidal magnetic moment, which will be elucidated in the following examples. In addition, the above-revealed magnetic ground state is well corroborated by single-crystal magnetic studies presented by Sessoli et al. [5]. The best simulation for the static single-crystal magnetic data revealed the directions of these moments with respect to the tangential directions at the corresponding centers along $\varphi = 13^\circ + n60^\circ$ ($n = 0, 1, 2, \dots$), which is well agreement with the angles from ab initio calculations when $n = 1$.

The above theoretical and experimental investigations confirm the toroidal magnetic moment present in the triangular Dy₃ molecule, which offer an appealing route toward SMTs and ultimately multiferroic compounds. Such a fascinating magnetic behavior stimulates the increasing interest in new systems behaving as SMTs. Finally, as a significant step to final applications, the magnetoelectric properties for the above Dy₃ molecule were also explored, suggesting that an external magnetic field is able to induce the electric polarization in the crystal (Fig. 4.3) [7]. Therefore, lanthanide coordination complexes with toroidal magnetic moment might be good candidates to observe the macroscopic quantum magnetoelectric effects and other peculiar spin-electric effects.

4.1.2 New Dy₃-SMTs Systems

Two triangular Dy₃ compounds have been constructed by some of us through grafting bulky hydrazine onto the vanillin group, which keeps the main structure of *o*-vanillin in Fig. 4.4 [17]. Here, the almost same structural features to Dy₃ archetype were observed for them. Importantly, the static susceptibility data reveal the same trend to that of the seminal Dy₃ triangle (Fig. 4.4), which confirms the peculiar vortex-spin electronic structure, leading to the presence of toroidal magnetic moment. For the first Dy₃ complex in Fig. 4.4, ac susceptibility signals display the almost identical features to Dy₃ archetype, evidencing the similar SMM behavior for them, which should be as a result of the very close coordinate

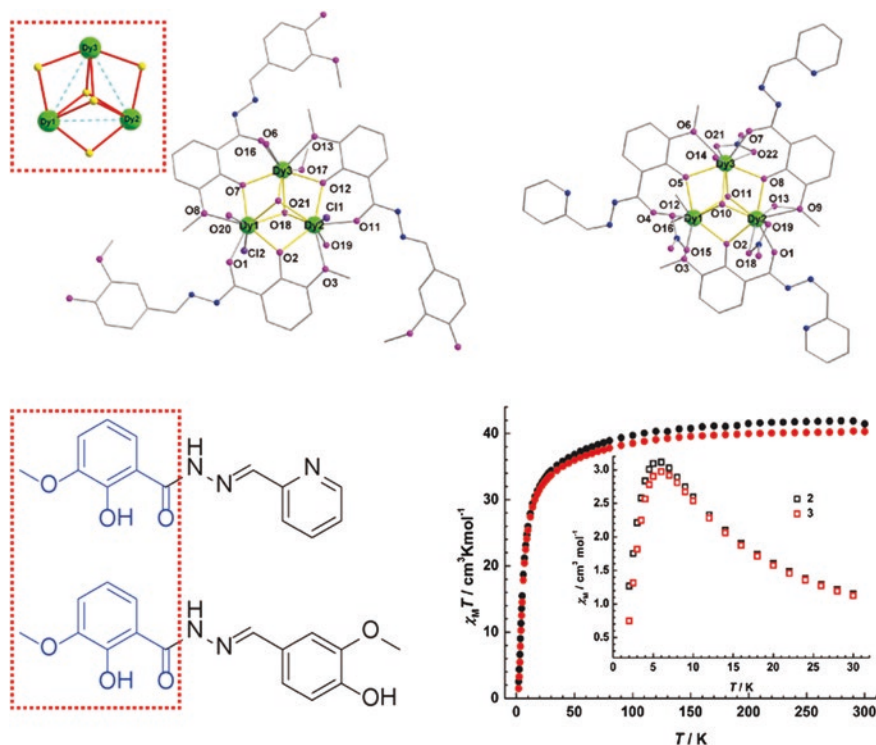


Fig. 4.4 The crystal structures and static magnetic properties of two triangular Dy_3 compounds with hydrazone ligands. Reprinted with the permission from Ref. [17]. Copyright 2012 American Chemical Society

environments of Dy ions including the coordinate geometries and coordinating anions. However, distinct dynamic magnetic behavior was revealed by ac susceptibility signals under zero-/nonzero-dc field for the second Dy_3 complex due to the crucial structural differences from the above complex. As shown in Fig. 4.4, the compound exhibits different coordinate geometry at the individual Dy sites due to the terminal $\eta^2\text{-NO}_3^-$ replacing the monodentate Cl^- ions or a solvent molecule. As a result, the out-of-phase ac susceptibility (χ'') curves in zero-dc field show the absence of frequency-dependent peaks. Their distinctive relaxation dynamics of two Dy_3 complexes mainly results from the different chemical environments of metal centers, which may have a great impact on the transversal component of anisotropy but do not change the directions of main axes of Dy ions and the whole toroidal magnetic moment.

In 2012, W. Shi and coworkers presented a novel triangular Dy_3 compound different from the above classical Dy_3 triangle through applying an amino-polyalcohol ligand with four $-\text{OH}$ arms [18]. Here, the three Dy^{III} ions are doubly bridged by two $\mu_3\text{-O}$ atoms from deprotonated $-\text{OH}$ arms of the ligands, leading to a Dy_3 triangle. However, the different structural features from the above Dy_3 motif are

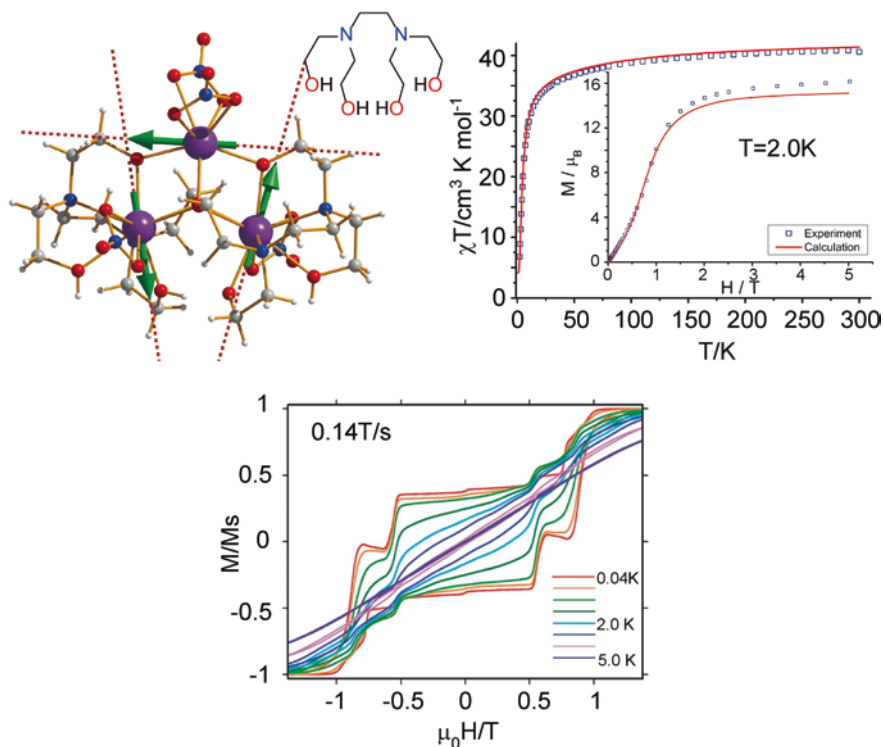


Fig. 4.5 The crystal structure, static magnetic, and electronic properties of Dy_3 triangle from W. Shi and coworkers. The calculated anisotropic axes show a toroidal alignment. Reproduced from Ref. [18] by permission of The Royal Society of Chemistry

observed; that is, one pair of Dy ions is not bridged by $\mu_2\text{-O}$ atom, thus resulting in a pseudo-isosceles triangle rather than an equilateral triangle. Even so, the static susceptibility measurements still display an antiferromagnetic interaction at low temperature, as indicated by an S-shaped M-H curve similar to that of the seminal Dy_3 complex, and the results of *ab initio* calculations also favor a toroidal alignment of local magnetic moments of the Dy_3 at the same time (Fig. 4.5). However, the anisotropic axes of Dy ions display a larger deviation from the Dy_3 plane with an angular range of $0.5\text{--}10.5^\circ$, which thus lead to an obvious nonvanishing magnetic moment in the Kramers doublet of the Dy_3 , as indicated by the different trend of χT versus T plots at low temperature from that of the seminal complex in Fig. 4.5. Remarkably, the magnetic interactions including exchange and dipolar interactions between Dy centers were also calculated based on the pseudo-spin Hamiltonian. The results reveal that the exchange interactions have the same features to that of the seminal Dy_3 triangle, which stabilize the toroidal magnetic moments. Nevertheless, the further calculated results suggest that the dipolar interactions show a larger magnitude than exchange interactions and the same sign, and thus the dipolar interactions should play a more crucial role in stabilizing the toroidal magnetic moments. Furthermore, the ac susceptibility

data demonstrate clear temperature-dependent out-of-phase signals (χ'') with two distinct peaks within the temperature range of 3–22 K, indicating the occurrence of multiple relaxation processes. Two effective barriers were given to be 43 and 91 K through the Arrhenius fitting. The open magnetic hysteresis curves (Fig. 4.5) of a single-crystal sample show the increasing coercive field with decreasing temperature below 5 K, further confirming its SMM properties. Here, the multiple magnetic steps in hysteresis loops correspond to the level crossings in the ground state of the four differently oriented Dy₃ molecules in cell units, which is revealed by ab initio calculations. Notably, the complex crystallized in a polar point space group *Pna*2₁ and thus the dielectric study was performed, revealing a paraelectric–ferroelectric phase transition at 470 K for this Dy₃ compound (Fig. 4.5). This is the first reported SMM that demonstrates a dielectric transition between a paraelectric phase and a ferroelectric phase.

4.1.3 Cyclic Dy₄ and Dy₆ SMT Systems

In 2012, M.-L. Tong et al. reported the first Dy₄ SMM showing a toroidal magnetic moment in the ground state similar to the above Dy₃ triangle in a planar Dy₄ complex, [Dy₄(μ₃-OH)₂(μ-OH)₂(2,2-bpt)₄(NO₃)₄(EtOH)₂] [2,2-bptH = 3,5-bis-(pyridin-2-yl)-1,2,4-triazole] [14]. Notably, the compound was assembled from a rigid multiple nitrogen-ligand with two bidentate chelating sites (Fig. 4.6), which is firstly used to construct polynuclear lanthanide complexes. Here, each Dy ion is surrounded by a distorted SAP geometry, and four Dy ions form a centrosymmetric parallelogram core (Fig. 4.6). The static magnetic measurements revealed an obvious decrease of $\chi_m T$ values at low temperature, indicating the possible antiferromagnetic interactions in the molecule. As a result, ab initio calculations are indicative of a non-magnetic ground state in the Dy₄ molecule, which mainly arises from the toroidal arrangement of four strong anisotropic axes of Dy ions. Here it should be noted that the local magnetic moments on four Dy centers completely compensate each other in the ground exchange state, leading to a net toroidal moment as a main result of its centrosymmetric structure, which is different from that in the above Dy₃ triangles. Further calculated results for magnetic interactions suggest the weak exchange interactions between Dy centers via the non-magnetic superexchange pathway, but larger dipolar magnetic interactions between them which further stabilize the toroidal moments. Furthermore, ac susceptibility signals with temperature- and frequency-dependent maxima provide the direct evidence of its SMM behavior, as shown in Fig. 4.6, showing an effective barrier of 80 K ($\tau_0 = 5.75 \times 10^{-6}$ s).

The first Dy₆ wheel compound can date back to 2010, when the group of Murray [19] reported the *S*₆-symmetric Dy₆ complex, [Dy(teaH)(NO₃)]₆·8MeOH, constructed using a amino-polyalcohol ligand (triethanolamine, teaH₃). The whole molecule shows a high symmetry with the asymmetric unit containing only one unique dysprosium ion located in distorted SAP geometry. Here ac susceptibility investigation was performed, and thus the χ'' versus *T* plots display

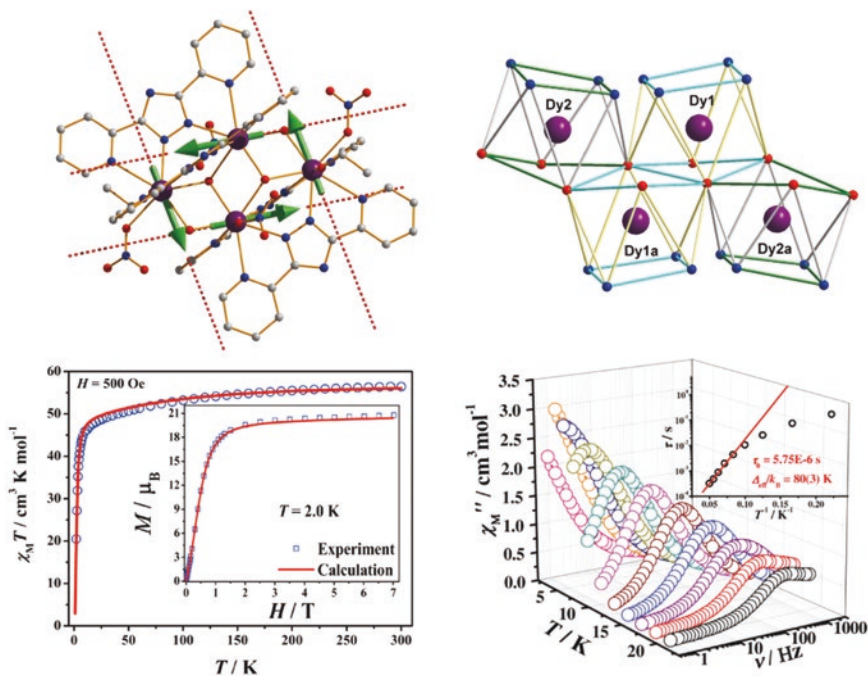


Fig. 4.6 The crystal structure, static, and dynamic magnetic properties of the first Dy_4 SMT reported M.-L. Tong et al. The calculated anisotropic axes show a toroidal alignment. Reprinted with permission from Ref. [14]. Copyright 2012 American Chemical Society

temperature-dependent signals but without peaks, revealing the onset of slow relaxation of magnetization. In order to further gain insight into magnetic properties of this rare highly symmetric Dy_6 wheel, complex but accurate ab initio calculations were demonstrated by Ungur et al. [15]. At first, only one single Dy center was considered due to the equivalent electronic structures for all Dy ions as a result of the S_6 symmetry. As a consequence, although the Dy center shows a strong anisotropic axis with $g_z = 19.26$, the relatively large transversal components ($g_x = 0.18$ and $g_y = 0.53$) were still revealed, which explain the weak SMM behavior present in the complex. Furthermore, the dipolar magnetic interactions were calculated in the highest approximation and the values all show the negative sign (Fig. 4.7 inset) indicating the antiferromagnetic interactions between magnetic moments of Dy centers. Here the strongest dipolar interaction is present between the nearest pairs of Dy ions, and the dipolar interaction between opposite Dy centers is stronger than the interaction between next-nearest neighbors mainly due to the parallel magnetic anisotropic axes between the opposite Dy sites. Importantly, good agreement was found between the experimental and theoretical static magnetic data when only considering the dipolar interactions, which thus suggest the very weak exchange interactions between Dy centers. We should notice that the anisotropic axis of each Dy center displays a great deviation

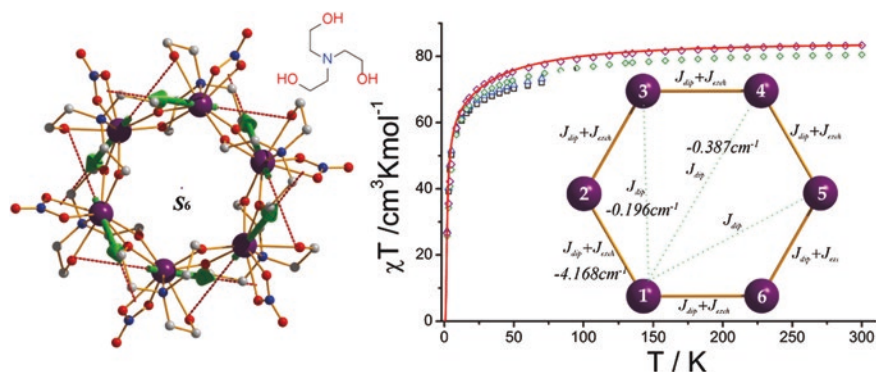


Fig. 4.7 The crystal structure, static magnetic properties of the S_6 -symmetric Dy_6 complex. The calculated anisotropic axes show a toroidal alignment. Reprinted with permission from Ref. [15]. Copyright 2012 American Chemical Society

from the Dy_6 plane, but the high symmetry of the molecule and antiferromagnetic interactions between Dy centers still result in a non-magnetic ground state for the whole molecule, since local magnetic moments on Dy centers completely compensate each other, which lead to the net toroidal moments for the Dy_6 molecule when their local magnetic moments are projected onto the plane of the wheel.

Although *ab initio* calculations revealed the presence of net toroidal moments in both Dy_4 and Dy_6 molecules, different feature is found between them. The almost coplanar property for magnetic moments of Dy ions has maximized its net toroidal moments in the planar Dy_4 molecule, whereas, theoretically speaking, the net toroidal moments for the Dy_6 molecule could be further improved by forcing the local anisotropy axes of the Dy ions to lie in the plane of the molecule [8].

4.1.4 Coupled Dy_3 -SMTs Systems

In Sects. 4.1.2 and 4.1.3, we have given an outline about the successful explorations of new magnetic systems with individual toroidal moments. In this section, the coupling interactions between Dy_3 SMTs will be highlighted to get insight into the coupling effects of toroidal moments, regarding how to stabilize the toroidal moments in a coupled system and in turn to enhance the toroidal moments by the linkage of two and even more SMT molecules. More importantly, it is expected that the magnet-like behavior is able to be improved through the coupling of Dy_3 units while grasping the unique properties of such systems, which seems to be very appealing for obtaining molecule-based materials with multiferroic properties. To date, such compounds are still rare, and here we give only three examples showing the coupling effects between Dy_3 units in different fashions, which were investigated carefully via detailed *ab initio* calculations or angle-resolved magnetometry.

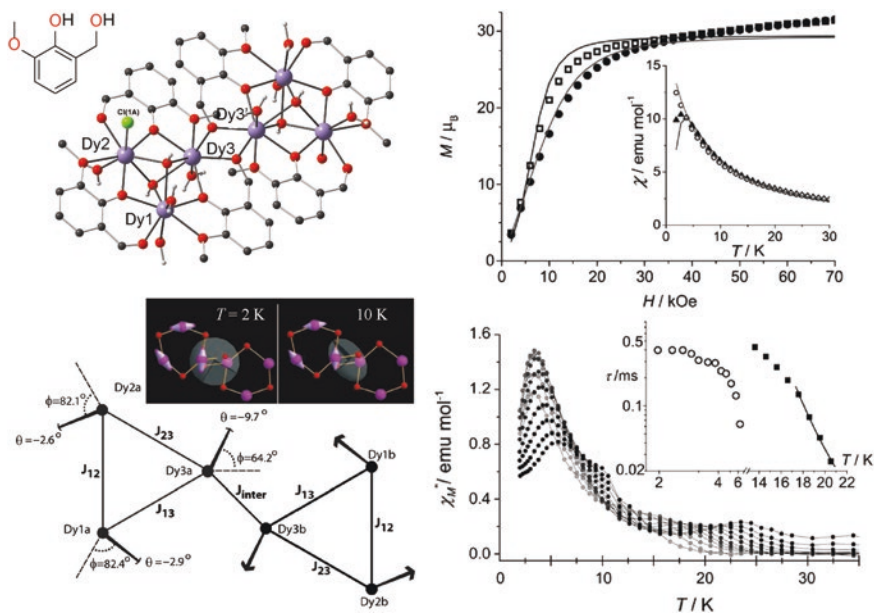


Fig. 4.8 The crystal structure, static, and dynamic magnetic properties of the coupled Dy₃-SMTs reported by A.K. Powell. The calculated anisotropic axes show the linkage of two Dy₃ toroidal alignments. Reproduced from Ref. [20] by permission of John Wiley & Sons Ltd.

As a continuing study on the seminal Dy₃ triangle, in 2010, A.K. Powell and coworkers reported the Dy₆ molecule incorporating two Dy₃ triangles in a vertex-to-vertex fashion, as shown in Fig. 4.8 [20]. In the molecule, two alcohol ligands resulting from the reduction of *o*-vanillin offer alkoxide bridges for the linkage of two Dy₃ units. Therefore, the planes of the two triangles in the Dy₆ molecule are strictly co-parallel, but not coplanar, and the perpendicular distance between them is 2.4757(6) Å. Here two Dy₃ units seem to possess the almost same motifs to the seminal Dy₃ complex, but a closer observation reveals the important difference in two central Dy ions of the Dy₆ molecule, where the original coordinate geometries are distorted to some extent, thus leading to the changes of magnetic properties. Ab initio calculations further reveal the important differences in the central Dy ions, i.e., their anisotropic axes showing a relatively large deviation from the corresponding Dy₃ plane by about 10° in contrast to that of the peripheral Dy ions (<3°). Experimentally, single-crystal magnetic characterization was also performed with the results shown in Fig. 4.8 inset. We see that an easy plane anisotropy occurs in the Dy₆ molecule at low temperature $T = 2$ K, but upon increasing temperature to 10 K, the anisotropy is transformed into an easy-axis type, which suggests the significant change of electronic populations from ground state to excited states. Furthermore, the magnetic interactions marked in Fig. 4.8 were obtained through fitting the angle-resolved magnetic susceptibility data. The results are indicative of the similar magnetic interactions within the Dy₃ units to that of the seminal Dy₃ triangle,

but a relatively weak interaction about 1.2 K was found between two Dy₃ units, which thus results in the small energy separation about 0.6 K between the ground and the first excited states. Therefore, the step at low field in the M - H curve was disappeared. Strikingly, in contrast to the seminal Dy₃ complex, ac susceptibility signals reveal the obviously enhanced SMM property with a high-effective barrier of 200 K, as shown in Fig. 4.8, which may be related to the unprecedented change in the nature of the magnetic anisotropy from an easy plane to easy-axis type on increasing the temperature.

In fact, before this, the first Dy₆ example coupling two Dy₃ triangles in a vertex-to-vertex fashion was constructed through an in situ aldol condensation reaction between some of the *o*-vanillin molecules and acetone by M. Murugesu and coworkers [21]. We can see in Fig. 4.9 that the in situ formed ligands offer a critical bridging role between two Dy centers, which is similar to the above Dy₆ molecule. However, the whole intramolecular ferromagnetic interactions are present in the molecule, as evidenced by the increase of the $\chi_m T$ product upon decreasing temperature above 40 K (Fig. 4.9). Unfortunately, here ab initio calculations were not performed. Consequently, the origin of magnetic interaction is not able to be determined and the evidences of toroidal moments have not been given. Nevertheless, a two-step-shaped hysteresis was observed with an opening of the loop below 1 K

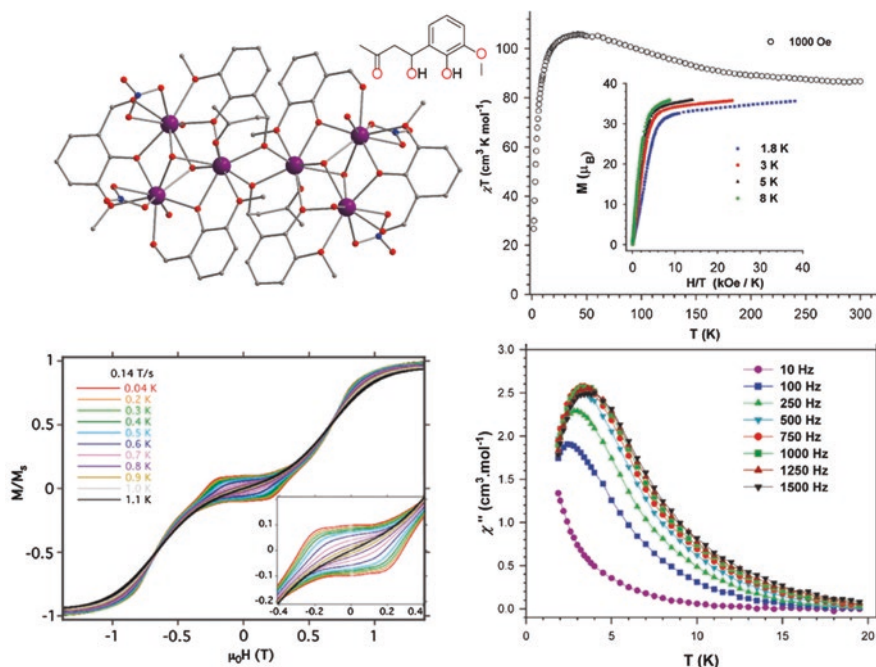


Fig. 4.9 The crystal structure, static, and dynamic magnetic properties of the coupled Dy₃-SMTs reported by M. Murugesu and coworkers. Reproduced from Ref. [21] by permission of The Royal Society of Chemistry

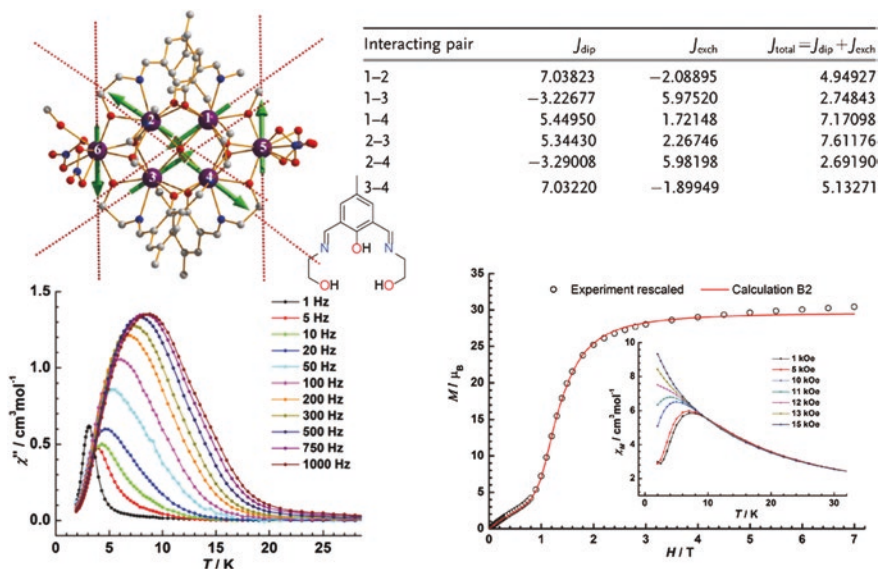


Fig. 4.10 The crystal structure, static, and dynamic magnetic properties of the coupled Dy₃-SMTs reported by J. Tang et al. The calculated anisotropic axes show the linkage of two Dy₃ toroidal alignments. Reproduced from Ref. [22] by permission of John Wiley & Sons Ltd.

(Fig. 4.9), which resembles the case occurring in the seminal Dy₃ molecule. Such hysteresis loops presumably arise from the toroidal arrangement of the magnetic moments on the Dy centers in the triangular units, with the Dy₃ plane being the easy plane of magnetization. In addition, ac susceptibility data under zero-dc field display obvious temperature-dependent out-of-phase (χ'') signals below 18 K, indicating its SMM behavior, affording an effective barrier about 10 K.

In contrast to the above Dy₆ SMMs, our group constructed a novel Dy₆ molecule coupling two Dy₃ units in an edge-to-edge fashion through a Schiff base ligand with two -OH arms, which provide alkoxide bridges between Dy centers [22]. As shown in Fig. 4.10, each Dy center from Dy1 to Dy5 sites is located in distorted SAP environments, while the Dy6 ion shows the monocapped SAP geometry due to the coordination of an additional methanol molecule. Remarkably, the presence of central μ_4 -O atom provides an important superexchange pathway for the communication among four central Dy sites. As a result, the edge-to-edge arrangement fixed by a μ_4 -O bridge effectively improves magnetic coupling interactions between two Dy₃ triangles and further enhances the toroidal magnetic moment of the molecule, which has been proved by ab initio calculations. The calculated anisotropic axes of Dy centers are present in Fig. 4.10. We can see that the toroidal arrangement is kept in each Dy₃ unit and they show similar anticlockwise arrangements of toroidal moments, but the important deviation out of the corresponding Dy₃ plane still occurs for anisotropic axis of each Dy center, which thus leads to a small nonzero magnetic ground state under the low-symmetry Dy₆ molecule. This

gives a reasonable explanation for the obviously increasing magnetization under a low field in Fig. 4.10. The exchange and dipolar interactions of each pair of Dy centers were further calculated, and the interaction parameters among four central Dy sites evidencing the coupling strength between two Dy units were listed in Fig. 4.10. In contrast to the above vertex-to-vertex Dy₆ molecule, the coupling interactions between two Dy₃ units were obviously enhanced, especially for the pairs of sites 1, 2 and 3, 4, where J_{total} is about 5 cm⁻¹. In addition, although the pairs of sites 1, 3 and 2, 4 display small J_{total} which is only due to the opposite sign for the exchange and coupling interactions, their J_{exch} are the largest among all pairs, which suggests the central $\mu_4\text{-O}$ atom provides an effective superexchange pathway for the coupling of two Dy₃ units. As a result, the exchange spectrum reveals a relatively large energy gap between the ground state and the first excited state about 7.6 cm⁻¹, which is comparable to that in the seminal Dy₃ molecule. Therefore, the clear S-shaped curve was observed in its $M\text{-}H$ plots, which indicates the effective enhancement of toroidal moments in the molecule via such linkage. Importantly, the typical SMM behavior is still observed in the molecule, as evidenced by the out-of-phase signals with frequency-dependent maxima in Fig. 4.10. Two effective barriers were extracted to be 34 and 41 K.

Except above Dy₆ examples, the enantiopure heterometallic 3d-4f 1D coordination polymers from D. Luneau and coworkers also demonstrate the coupling of Dy₃ units via a chiral Cu^{II} bis-valinate complex [23]. As shown in Fig. 4.11, the alternating structure between Dy₃ triangular building blocks and chiral mononuclear Cu complexes was observed in 1D molecular chain. Ab initio calculations reveal that the toroidal moments are still kept in those Dy₃ units, but the toroidal

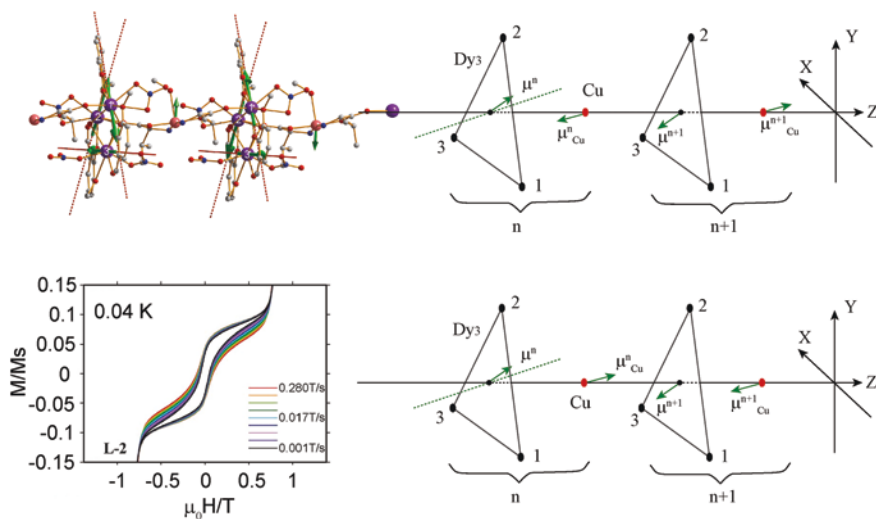


Fig. 4.11 The crystal structure, static magnetic properties of the 3d-4f 1D coordination polymers coupling Dy₃ units and a chiral Cu^{II} bis-valinate complex. Reproduced from Ref. [23] by permission of The Royal Society of Chemistry

moments in the neighboring Dy₃ units are opposite in sign and compensate each other, thus leading to a zero toroidal moment. In addition, as shown in Fig. 4.11 right, the sign of the magnetic interaction between Cu and Dy will not change the antiferromagnetic arrangement of the toroidal moments in the ground state of Dy₃ units, which mainly arises from the involvement of different types of Dy ion in the exchange pathway, that is, the coupling of (Dy1)ⁿ-(Cu)ⁿ-(Dy2)ⁿ⁺¹ in the molecule. Nevertheless, the application of a homogeneous magnetic field to its single-crystal sample is able to induce the inversion of one toroidal moment, which leads to the ferromagnetic coupling between toroidal moments and thus a strong toroidal magnetization. Finally, the hysteresis loops of single-crystal sample reveal the similar features to the seminal Dy₃ triangle, indicating its SMM properties.

As shown above, the toroidal states in the ground state of above coupled Dy₃ examples are quite robust since the anisotropic axis of individual Dy center is very difficult to be changed by the relatively weak coupling interactions between Dy₃ units. Even so, the magnetic coupling still has a great impact on the expression of toroidal moments, as seen in the above two Dy₆ molecules. The nature of magnetic coupling between Dy₃ units including its sign and strength directly affects the exchange coupling states of whole molecule, such as the separation between ground and excited states. Therefore, a suitable coupling interaction between toroidal units will enhance the toroidal moments in ground state. Such a systemic exploration seems to be very appealing for developing future molecule-based multiferroic materials.

4.1.5 Other Dy₃ Examples

In contrast, two Dy-based complexes, [Dy₃(L)(μ₃-OMe)₂(NO₃)₃](BPh₄) and [Dy₃(L)(μ₃-OMe)₂(NO₃)₃]·0.33[Dy(NO₃)₆], having the C₃-symmetric Dy₃ unit in Fig. 4.12 were reported by Colacio et al. in 2014 [24]. Although the Dy₃ unit demonstrates similar triangular core structure to the above Dy₃ complexes, the obvious asymmetry relative to the Dy₃ plane is present in the molecule due to the lack of mirror symmetry, as shown in Fig. 4.12. Here the individual Dy center is surrounded by a very distorted coordination geometry, but notably the shortest Dy–O bond about 2.182 Å is discovered between Dy center and the phenoxide-O atom below Dy₃ plane as in Fig. 4.12, which is proved to dominate the direction of anisotropic axis of Dy center. Ab initio calculations and electrostatic repulsion model reveal the consistent directions of local anisotropic axes almost perpendicular to the Dy₃ plane, which are presented in Fig. 4.12. Therefore, the toroidal moments in ground state cannot occur within the molecule. Furthermore, ab initio calculations also reveal the different properties of magnetic interactions from the seminal Dy₃ molecule. Finally, the clear out-of-phase signals in ac susceptibility data are indicative of their SMM behavior, which will not be described in detail here.

Similarly, in 2013, our group reported the Dy₃ compound in Fig. 4.13, which was assembled by using an in situ formed Schiff base ligand showing various

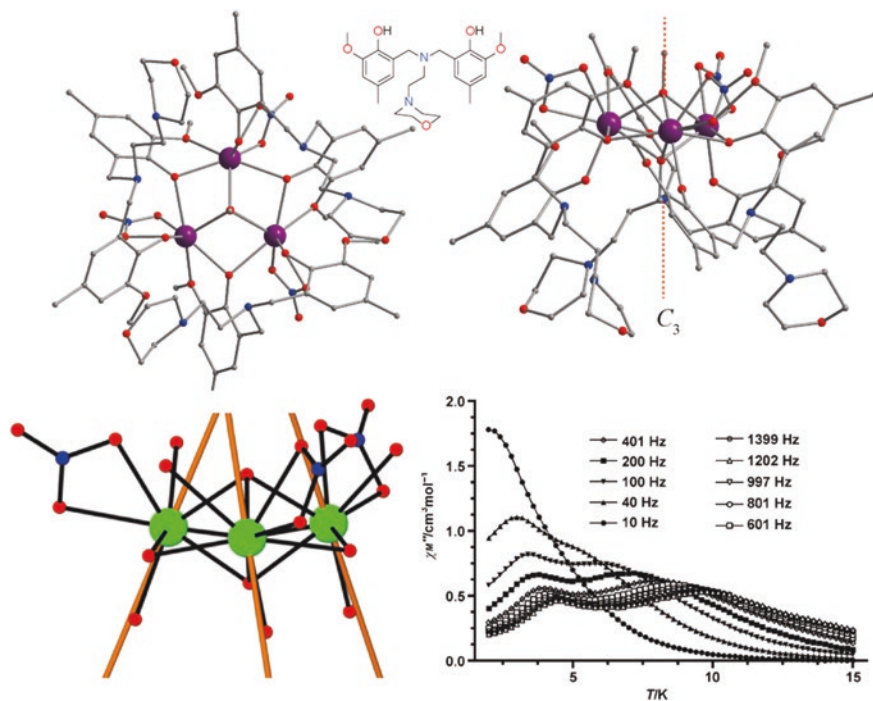


Fig. 4.12 The crystal structure, dynamic magnetic properties of the C_3 -symmetric Dy_3 complex reported by E. Colacio et al. The calculated anisotropic axes do not show the toroidal alignment. Reproduced from Ref. [24] by permission of John Wiley & Sons Ltd.

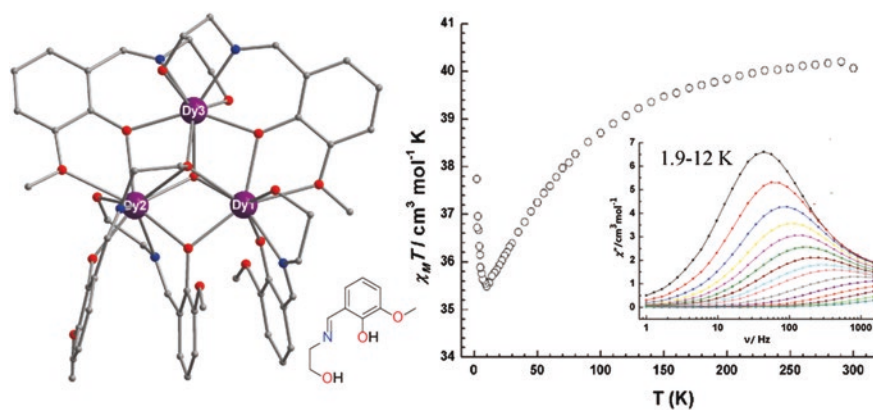


Fig. 4.13 The crystal structure, static, and dynamic magnetic properties of the ferromagnetic Dy_3 compound reported by J. Tang et al. Reproduced from Ref. [25] by permission of The Royal Society of Chemistry

coordinate modes [25]. Here the triangular core structure is still kept, but obviously the approximate C_{3h} symmetry is destroyed completely for the molecule. Furthermore, every Dy center demonstrates the different coordination environments. As a direct result, its dc magnetic susceptibility data at low temperature reveal the presence of ferromagnetic interactions in the molecule, suggesting the lack of toroidal moments. In addition, its SMM properties were indicated by the frequency-dependent out-of-phase signals below 12 K, giving an effective barrier of 13 K.

Comparing all above examples, we can see that the structural unit with cyclic arrangement of lanthanide ions is an underlying imperative in designing SMT molecules, but the local single-ion anisotropy of Dy sites and their arrangement in the whole molecule should be the most key parameters in determining the occurrence of toroidal moments, and further, the magnetic interactions including the exchange and coupling interactions between Dy centers play an assistant role in stabilizing the toroidal moments. In particular, the explorations into coupled Dy_3 toroidal moments provide a good understanding of the correlation between the moments and coupling interaction of them and prove that it is possible to enhance the toroidal moments using a coupling strategy. We believe that the above systematic review on toroidal moments in SMM field from a chemical viewpoint would offer a significant reference for scientists focusing on magnetoelectric and related multiferroic materials, which should be very helpful for developing multifunctional molecule-based materials and achieving their final applications.

4.2 High-Performance Multinuclear Lanthanide SMMs

In the first part of this chapter, we gave a detailed investigation on lanthanide SMT molecules showing toroidal moments, which can be viewed as an important product in the process of studying multinuclear lanthanide SMMs showing the nonlinear linkage of anisotropic magnetic moments. The following part will focus on how to design multinuclear lanthanide SMMs with more than three magnetic centers and to further improve their magnetic blocking properties. As seen in dinuclear lanthanide systems, the SMM behaviors of multinuclear lanthanide systems are still attributed to single-ion anisotropy of individual lanthanide center. As a result, improving single-ion anisotropy in those complexes is the overriding factor in enhancing their SMM behaviors. In addition, the magnetic coupling between metal centers plays a critical role in arranging the anisotropic magnetic axes at different magnetic sites, where a suitable arrangement is able to support the enhancement of SMM properties. Nevertheless, such a control for magnetic anisotropy in multinuclear lanthanide SMMs appears to be more difficult than in dinuclear lanthanide systems. To date, considerable effort of some researchers has been devoted to this aspect with a great number of multinuclear lanthanide SMMs discovered. Here we examine those polynuclear lanthanide complexes showing slow relaxation of magnetization, and, therefore, three main synthetic strategies

are drawn: building block approach, organometallic approach, and multidentate ligand approach. It is noted that the third strategy, a serendipitous approach, predominate in those approaches, is less efficient in isolating multinuclear lanthanide SMMs with high barriers due to the difficulty in controlling magnetic anisotropy and their arrangements, while the first two strategies seem to be more efficient in achieving strongly blocking lanthanide SMMs but with rare successful examples reported to date.

4.2.1 Building Block Approach

As mentioned in the assembly of dinuclear lanthanide SMMs in Chap. 3, it is still an ideal approach to build larger lanthanide SMMs through the linkage of high-performance magnetic blocking units, since magnetic anisotropy and coupling interactions within the building units have proved to be favorable for high SMM performance. In addition, the first part of this chapter has shown that the special magnetic properties of Dy₃ triangle are able to be well retained in their coupled systems and even can be effectively enhanced. Importantly, although such SMM examples still remain scarce to date, two clear examples comprising Dy₂ units present the great potential in achieving strongly blocked lanthanide SMMs.

In 2013, K. Katoh and coworkers reported the Tb₄ SMM, [Tb(obPc)₂]₂Tb(Fused-Pc)Tb[Tb(obPc)₂], displaying a coupling of two three-decker Tb₂ SMM units using a fused phthalocyaninato ligand, as shown in Fig. 4.14 [26]. In its molecular structure, Tb₂ units display the almost same structural motifs to the Tb₂ SMM (Tb₂(obPc)₃) in Chap. 3, and they are linked in a *syn* arrangement via the fused-Pc ligand. Therefore, the obvious ferromagnetic interactions still occur in the Tb₄ complex similar to that in Tb₂(obPc)₃. Remarkably, although the shortest distance about 1.16 nm of Tb sites between two Tb₂ units seem to be relatively long, dc magnetic measurements reveal an obvious ferromagnetic interaction between two Tb₂ units evidenced by the increasing $\Delta\chi_m T$ values with the decrease of temperature (Fig. 4.14). Importantly, the almost same SMM behavior to Tb₂(obPc)₃ SMM was also observed here, as evidenced by the similar ac susceptibility signals with a single out-of-phase peak at 25 K for the frequency of 1488 Hz under zero-dc field (Fig. 4.14). The effective barrier was estimated to be 149 cm⁻¹, comparable to 230 cm⁻¹ of Tb₂(obPc)₃ SMM. Furthermore, the relaxation dynamics of the Tb₄ demonstrates the similar magnetic field dependence to Tb₂(obPc)₃ SMM, where the application of a dc field leads to the appearance of two-step relaxation of magnetization. Therefore, the Tb₂(obPc)₃ units seem to be dominate the magnetic dynamics of the Tb₄ complex within the investigated temperature domain, while the weak magnetic interactions between two units have a negligible effect on its dynamic behavior.

In the next chapter, we will give a discussion on Dy-based SMMs based on rigid hydrazone ligands, where the Dy₂ complexes with Dy centers located in a hula hoop-like geometry show a relatively strong blocking behavior, and thus

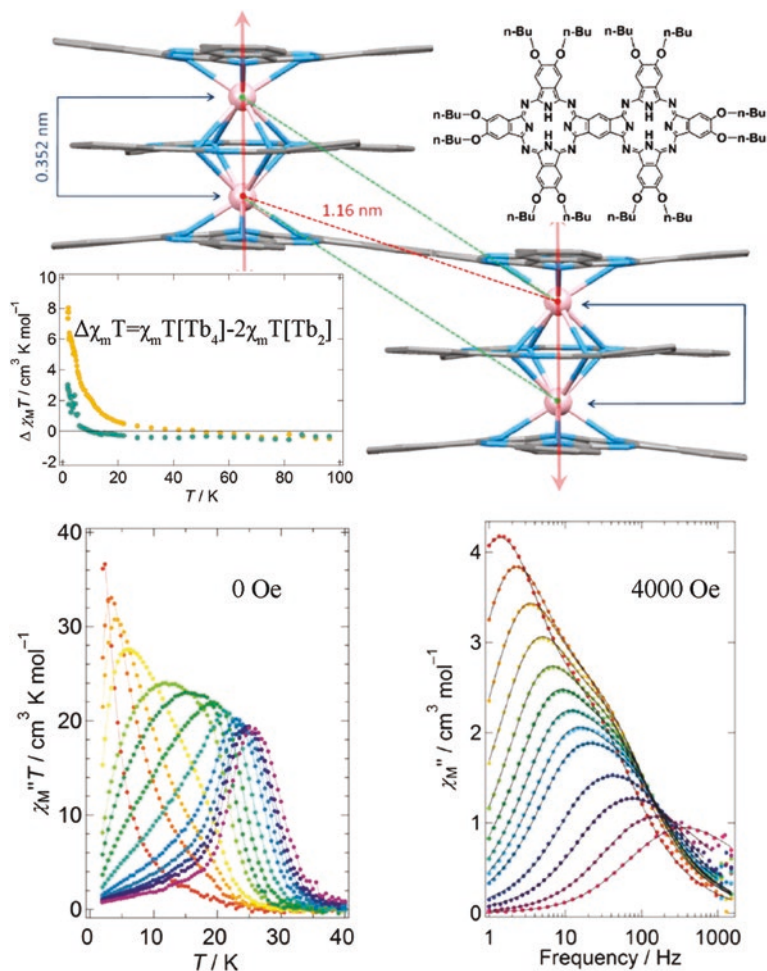


Fig. 4.14 The crystal structure, static, and dynamic magnetic properties of the Tb₄ SMM coupling two three-decker Tb₂ complexes. Reprinted with the permission from Ref. [26]. Copyright 2013 American Chemical Society

such Dy₂ units could be viewed as effective building blocks for larger strongly blocked SMMs [27]. Here our group has made some important contribution to this aspect. Typically, the Dy₆ complex in Fig. 4.15 was constructed by our group on the basis of two CO₃²⁻ bridges [28]. The structure can be considered as resulting from the formal linkage by two carbonato ligands of three petals of the Dy₂ units with the concomitant formal loss of the terminal ligands. Furthermore, similar bond distances and bond angles are observed between the Dy₂ units of Dy₆ and other Dy₂ complexes. Most importantly, the local hula hoop-like geometry is still present at each Dy site, which is mainly responsible for the maintenance of effective SMM behavior. The increasing $\chi_m T$ values with decreasing temperature at low

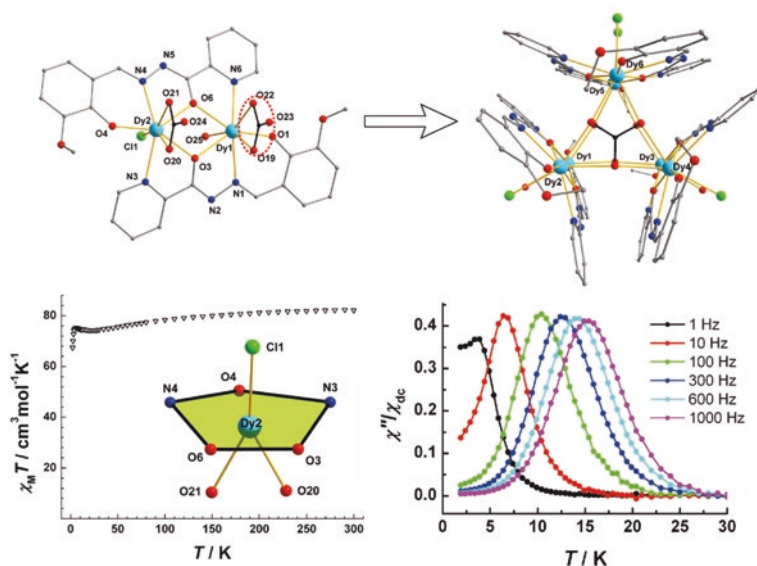


Fig. 4.15 The crystal structure, static, and dynamic magnetic properties of the Dy₆ complex containing three Dy₂ units reported by J. Tang et al. Reprinted with the permission from Ref. [27]. Copyright 2011 American Chemical Society

temperature suggest the presence of intramolecular ferromagnetic interactions, which also occurs in the Dy₂ complexes. Remarkably, the χ''/χ_{dc} versus T plots display a series of perfectly symmetric out-of-phase peaks at different frequency, indicating the dominance of a single relaxation process well in agreement with the presence of a unique coordination sphere in the Dy₆ complex. An effective barrier of 76 K was given with $\tau_0 = 1.2 \times 10^{-6}$ s.

The above two examples illustrate that the linkage of high-performance magnetic units is a highly effective avenue for exploring larger lanthanide SMMs. However, this strategy depends on the elaborate design of bridging ligands and/or reaction conditions.

4.2.2 Organometallic Approach

As seen in the assembly of mono- and dinuclear lanthanide SMMs, organometallic chemistry has achieved celebrity status in the design of strongly blocked lanthanide SMMs, since it can provide stronger crystal field and magnetic interactions or some special chemical environments such as the coordination of soft donors. Nevertheless, the examples of organometallic lanthanide SMMs with more metal centers have been reported rarely to date. Here we give three examples developed by R.E.P. Winpenny and coworkers, especially the first two examples show

the highest effective barriers in multinuclear lanthanide SMMs. It is noted that although the first two complexes appear to be the same to the common Werner-type lanthanide complexes based on hard O donors, the low coordination number around lanthanide ions and deprotonation of all coordinating alcohol are very difficult to be achieved under a common reacting condition, and thus the two complexes were assembled through an organometallic synthetic approach, that is, the standard Schlenk and glove box techniques under inert gas environment.

At first, the pyramid-like Dy₅ complex was reported in 2011, when the effective barrier reached up to 528 K, surpassing the barrier record of previously reported multinuclear lanthanide SMMs [29]. As shown in Fig. 4.16, the complex, [Dy₅O(OiPr)₁₃] (referred to as [Dy₅]), is bridged by one central μ₅-O, four μ₂-, and four μ₃-alkoxide ligands. Each six-coordinate Dy ion is located in an octahedral geometry, but with the Dy shifted to the terminal alkoxide and away from the central μ₅-oxide. A closer observation reveals the shortest bond distance about 2.04 Å between Dy center and the O atom of terminal alkoxide in contrast to other Dy–O bond, which proves to be very critical in defining the anisotropic axis of each Dy

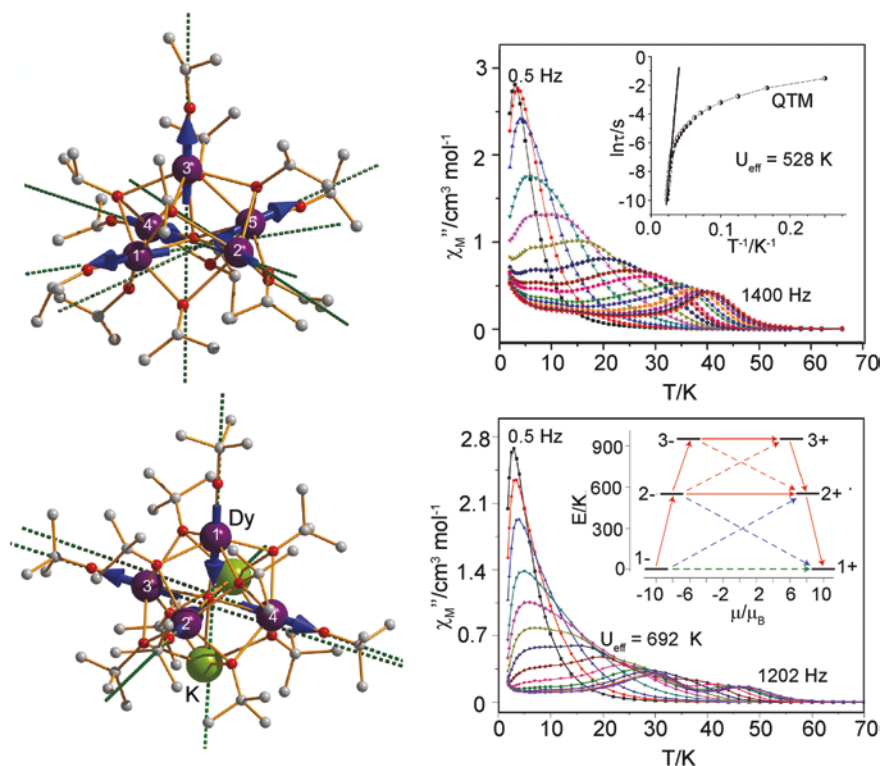


Fig. 4.16 The crystal structures, calculated anisotropic axes, and dynamic magnetic properties of [Dy₅O(OiPr)₁₃] and [Dy₄K₂O(OtBu)₁₂] C₆H₁₄. Reprinted by permission from Macmillan Publishers Ltd.: Ref. [2], copyright 2013. Reproduced from Ref. [29] by permission of John Wiley & Sons Ltd.

site. Importantly, ac susceptibility data demonstrate a highly blocking temperature about 41 K at the frequency of 1400 Hz (Fig. 4.16), indicating that the moments of $[\text{Dy}_5]$ molecule are blocked effectively. In order to detect the origin of strong SMM behavior of $[\text{Dy}_5]$, ab initio calculations were performed and thus reveal the large energy separation between ground and first excited doublets and the effective g values of $g_z \approx 20$ and $g_{x,y} \approx 0$ indicating the strong Ising-type anisotropy [2]. Remarkably, the directions of anisotropic axes are consistent with Dy-terminal alkoxide axis for all Dy sites. Furthermore, the calculations based on electrostatic model gave a clear correlation between the structural features and anisotropic directions of Dy centers. Mainly, the axis of ($\mu_5\text{-O}$)-Dy-(terminal alkoxide) presents a strong repulsive axial potential due to the shortest distance of Dy-terminal alkoxide bond and double negative charge of central $\mu_5\text{-O}$, and, therefore, the energy is minimized when the quantization axis is coincident with this direction.

Subsequently, the Dy-based complex, $[\text{Dy}_4\text{K}_2\text{O}(\text{OtBu})_{12}]\cdot\text{C}_6\text{H}_{14}$ (referred to as $[\text{Dy}_4\text{K}_2]$), was reported, giving a further increasing of effective barrier up to 692 K [2]. Here the molecular structure was exhibited in Fig. 4.16, displaying an oxo-centered octahedron comprising of four Dy and two *cis* arranged K ions. Importantly, the almost same geometry features to $[\text{Dy}_5]$ are observed at each Dy site, i.e., a short terminal alkoxide *trans* to the central oxide, which seems to greatly important to keep the high blocking barrier. Therefore, the results of ab initio calculations are indicative of the same nature of anisotropic axes of Dy centers compared with that in $[\text{Dy}_5]$ SMM. In addition, its ac susceptibility data give the different SMM features from $[\text{Dy}_5]$ complex, as shown at the bottom of Fig. 4.16 where two out-of-phase peaks are observed at 30 and 47 K for the frequency of 1202 Hz.

More importantly, the dilution for two above complexes leads to the further increase of their corresponding effective barriers, diluted $[\text{Dy}_5]$ reaching up to 804 K while diluted $[\text{Dy}_4\text{K}_2]$ to 842 K [2]. Notably, the effective barriers as high as ca. 800 K have far surpassed their energy gaps between the ground and the first excited states (576 K for $[\text{Dy}_5]$ and 536 K for $[\text{Dy}_4\text{K}_2]$). Consequently, the relaxation pathway via the first excited should be also blocked efficiently, which is compatible with the strongly axial anisotropy of first excited doublets ($g_z \approx 17$ and $g_{z,y} < 0.5$) and its parallel direction to that of ground doublets. Ab initio calculations presented the energy gaps between the ground and the second excited states about 986 and 888 K for $[\text{Dy}_5]$ and $[\text{Dy}_4\text{K}_2]$, consistent with the effective barriers of diluted samples (Fig. 4.16 inset). Further examining the effective barriers of undiluted samples, we can find that the barrier of 528 K for $[\text{Dy}_5]$ is comparable to the energy gap between the ground and the first excited states indicating the relaxation pathway via the first excited state, whereas the barrier of 692 K in $[\text{Dy}_4\text{K}_2]$ is still larger than the energy separation of the first excited state from the ground state suggesting the existence of competitive relaxation process via the second excited state. The reason may be due to the asymmetric arrangement of magnetic anisotropy axes of Dy ions leading to the weak internal transverse fields at Dy3 and Dy4 sites in $[\text{Dy}_4\text{K}_2]$. In addition, the typical SMM features were also observed in their corresponding isostructural Ho complexes, and in particular the effective barrier is as high as 400 K under a dc-applied field.

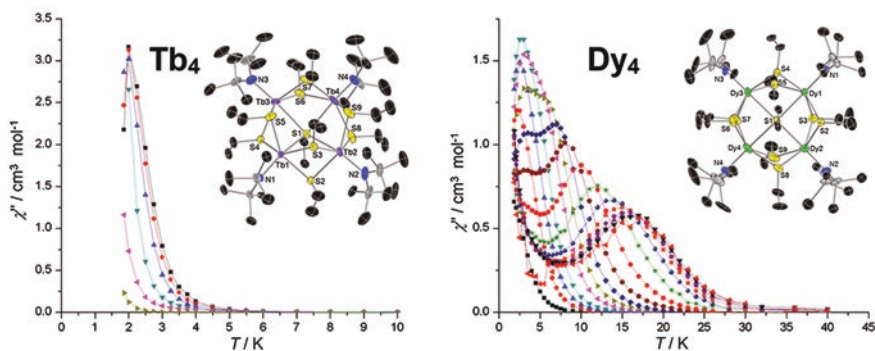


Fig. 4.17 The crystal structures and dynamic magnetic properties of the thiolate-bridged tetranuclear lanthanide compounds. Reprinted with the permission from Ref. [30]. Copyright 2013 American Chemical Society

Another typical example is the thiolate-bridged tetranuclear lanthanide compounds reported in 2013, $[\text{Li}(\text{THF})_4][\text{Ln}_4(\text{N}(\text{SiMe}_3)_2)_4(\mu\text{-SEt})_8(\mu_4\text{-SEt})]$, where $\text{Ln} = \text{Dy}$ and Tb [30]. In the third chapter, we have seen that such thiolate-bridged Dy_2 compound displays special soft ligand environments, strong magnetic interactions, and consequent high magnetization reversal barrier, which stimulates further magnetic investigations for such complexes. As demonstrated in Fig. 4.17, four lanthanide ions are assembled in the grid-like metal core by a central $\mu_4\text{-S}$ and eight peripheral $\mu_2\text{-S}$ atoms from ethanethiol ligands. The lanthanide centers are surrounded by distorted six-coordinate octahedral coordination environments similar to that in above $[\text{Dy}_4\text{K}_2]$ and $[\text{Dy}_5]$. The typical magnetic blocking behavior in the Dy_4 complex is evidenced by the clear temperature-dependent out-of-phase signals with the maxima below 20 K (Fig. 4.17 right). Consequently, an effective barrier for magnetization reversal can be obtained to be 46 cm^{-1} (66 K) with $\tau_0 = 4.3 \times 10^{-6} \text{ s}$. It is noteworthy that the obvious SMM behavior was also observed in the Tb_4 complex despite a small barrier of 4.6 cm^{-1} under a zero-applied field, which is rare in polynuclear lanthanide complexes due to the non-Kramers properties of Tb ion.

These examples illustrate the great potential of organometallic chemistry in synthesizing strongly blocked lanthanide SMMs, where it provides stronger crystal field and magnetic interactions or some special coordination environments. Furthermore, the exploration of magnetic properties under new chemical environments is also very crucial to better understand the complex magnetic behavior.

4.2.3 Multidentate Ligand Approach

Although the appealing potential in obtaining strongly blocked SMMs is present in above approaches, the main effort of most researchers in the assembly of multinuclear lanthanide SMMs is still devoted to the third approach, that is, the

common self-assembly method highlighting the design of multidentate ligands containing hard N and O donors. Since the discovery of the first multinuclear lanthanide SMM in 2006, the synthetic approach has greatly advanced the field of SMMs, especially in the aspects of the fundamental understanding of relaxation mechanism in weakly coupled SMM systems, because a great number of lanthanide SMMs were discovered here showing various magnetic phenomena, thus greatly enlarging the available database and improving the current knowledge of the structure–property relationship [31, 32]. This lays the significant foundation for discovering the stronger blocked lanthanide SMMs and achieving their future applications. Importantly, some of them also exhibit excellent SMM behavior, a typical example being the defect-dicubane Dy_4 SMM with a high barrier of 170 K and blocking temperature of 7 K [33].

We have examined the lanthanide SMMs with metal centers from three to six and here we will give a clear outline for ligands used, which all contain hard N and O donors due to their strong affinity for hard lanthanide ions, as shown in Figs. 4.18 and 4.19. We can see that the most important class among them is the Schiff base-type ligands derived from the reactions of an aromatic aldehyde and multidentate amine reagent as shown in Fig. 4.18. Typically, a universal but critical feature for those Schiff base ligands is the linkage of multiple coordinate pockets, which allow them to aggregate more lanthanide centers. In particular, the versatile *o*-vanillin-based Schiff base ligands exhibit the strong ability of

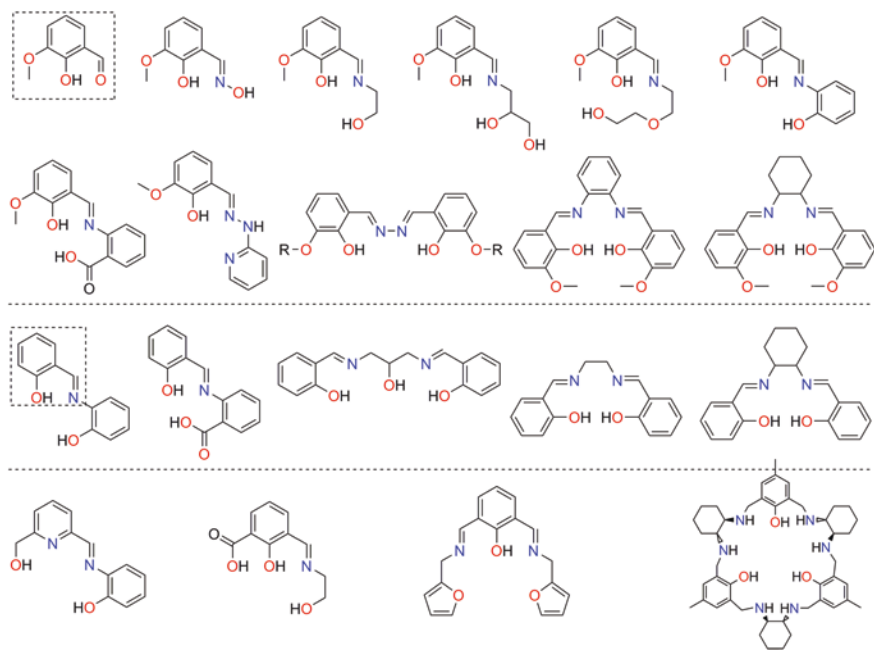


Fig. 4.18 The Schiff base-type ligands derived from the reactions of an aromatic aldehyde and multidentate amine reagent

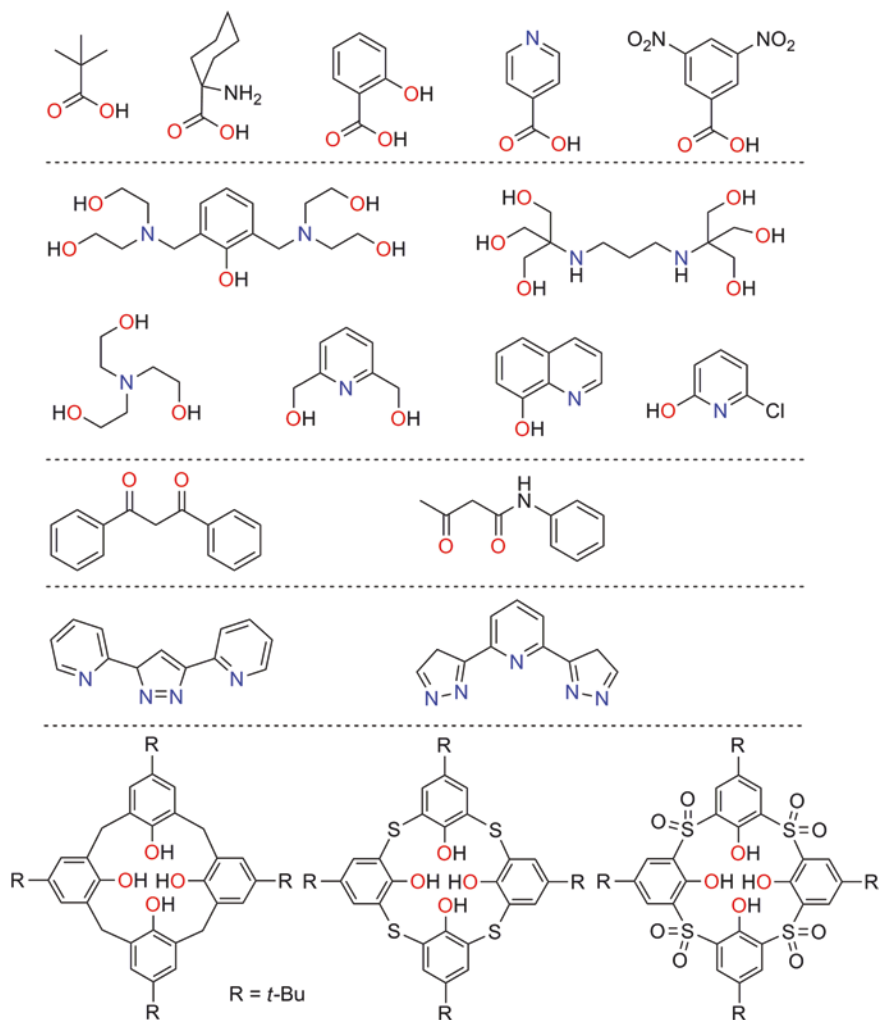


Fig. 4.19 The carboxylate, hydroxyl, N-based, and calixarene ligands used in the assembly of polynuclear lanthanide SMMs

chelating coordinate to lanthanide ions. Furthermore, an important class should be highlighted, i.e., the hydrazone-type ligands [34] showing the rigid planar structure and the facile keto-enol tautomerism, thus leading to the discoveries of some typical lanthanide SMMs, which will be systematically discussed in the next chapter.

In addition, some other types of ligands are also listed in Fig. 4.19, where the most important two classes are the carboxylate and hydroxyl ligands. It is noticed that although the carboxylate ligands demonstrate a strong bridging ability, leading to the formation of some larger lanthanide clusters, most of them do not show

good slow relaxation behavior, as mentioned in the third chapter. By contrast, the multidentate ligands with some hydroxyl arms also exhibit strong coordinate ability to lanthanide ions, yielding several excellent lanthanide SMMs. Notably, the multidentate ligands containing only nitrogen atoms were recently used to construct the lanthanide SMMs with one typical example being the above Dy₄ SMT. In the following sections, we will give a presentation for those multinuclear lanthanide SMMs highlighting the examples with relatively high-effective barriers.

4.2.3.1 Dy₃ SMMs

In the first part of this chapter, the typical Dy₃ triangular SMMs have been systematically described and thus only two examples with macrocyclic ligand are emphasized here. Due to the limited internal size of some rigid macrocyclic ligands, only mixed 3*d*-4*f* complexes have been isolated for them [35]. Here we were able to encapsulate three Dy ions inside the cavity of a macrocycle ligand by increasing the flexibility of the ligand through simply reducing the C=N double bonds of the Schiff base in Fig. 4.18 [36]. This modification leads to the successful assembly of two novel triangular Dy₃ complexes, as shown in Fig. 4.20. The almost identical Dy₃ core structure was observed in the two Dy₃ complexes with each eight-coordinate Dy^{III} ion located in distorted dodecahedral geometry. The slight differences are present in the different coordinating atoms: In the first compound, Dy1 and Dy2 are coordinated by one monodentate nitrate anion and one H₂O molecule in axial positions on opposite sides of the macrocycle, while Dy3 is completed by two H₂O molecules; but in the second complex, one SCN⁻ anion and one H₂O molecule coordinate to Dy1 and Dy2 on opposite sides of the macrocycle in axial positions, and two SCN⁻ anions complete the coordinate sphere of Dy3 center. Nevertheless, the distinct dynamic behaviors were observed in the two compounds. The obvious temperature- and frequency-dependent ac signals below 7 K without maxima occur in the first Dy₃ molecule under zero-dc field, and an further application of dc field has no influence on its SMM behavior. In contrast, the second complex shows no obvious out-of-phase ac signal under zero-dc field. However, an application of dc field leads to the occurrence of multiple relaxation behavior, as shown in Fig. 4.20. This work represents a successful rational design of Dy₃ triangles trapped in a macrocyclic ligand showing slow magnetic relaxation perturbed by axial ligands.

The first linear Dy₃ SMM in Fig. 4.21 was assembled through the modifications of *o*-vanillin ligand used in the seminal Dy₃ triangle [37]. The almost linear molecule structure with a Dy–Dy–Dy angle of 166.29° can be viewed as the opening of Dy₃ triangle, as shown in Fig. 4.21. Two peripheral Dy ions exhibit a geometry between dodecahedral and square antiprismatic, while a nearly perfect dodecahedral environment is observed at the central Dy site. The sharply increasing $\chi_m T$ value with decreasing temperature below 20 K is indicative of intramolecular ferromagnetic magnetic interactions between Dy centers. Ab initio calculations reveal the ground doublet of $m_J = \pm 15/2$ with $g_{x,y} \approx 0$ favorable to

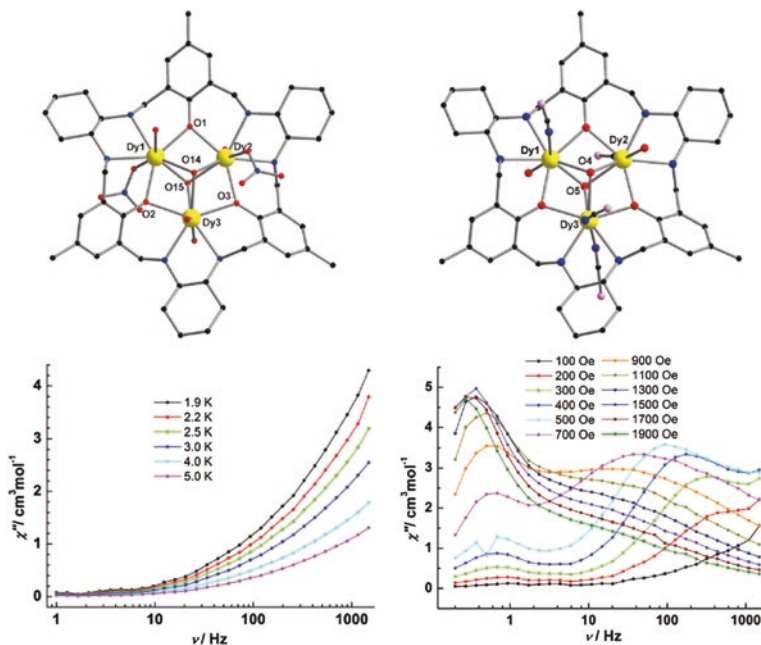


Fig. 4.20 The crystal structures and dynamic magnetic properties of the Dy_3 triangular SMMs with macrocyclic ligands. Reproduced from Ref. [36] by permission of The Royal Society of Chemistry

its SMM behavior. Importantly, the nearly collinear arrangement of the easy axes is shown in the linear Dy_3 with the small angles between their anisotropic axes, well in agreement with the structural transition from Dy_3 triangle to linear Dy_3 (Fig. 4.21) and the resulting intramolecular ferromagnetic magnetic interactions. The occurrence of a multiple relaxation process is evident in this compound due to the observations of the broaden peaks in the out-of-phase signals (Fig. 4.21), giving two effective barriers of 29 and 69 K with $\tau_0 = 6.3 \times 10^{-5}$ and 5.9×10^{-8} s, respectively. In addition, a family of linear Dy_3 and Tb_3 clusters with almost identical motif to above Dy_3 was assembled using the same type of ligands by Tong and coworkers in 2011 [38]. The Dy compounds demonstrate the similar static and dynamic magnetic behavior and thus expanded the family of linear Dy_3 SMMs based on oxime-type ligands.

Subsequently, two additional linear Dy_3 compounds were constructed through applying salicylic acid and 8-quinolinolate ligands, respectively, as shown in Fig. 4.21. Here both Dy_3 molecules exhibit obvious SMM behaviors, as evidenced by well-resolved out-of-phase maxima at different frequency. The second complex exhibits a single relaxation process with the obvious QTM relaxation and gives a near effective barrier to the first Dy_3 , about 65 K [39]. In contrast, the out-of-phase signals with two clear peaks are observed in the third complex, leading to two corresponding increased effective barriers of 48 and 92 K [40].

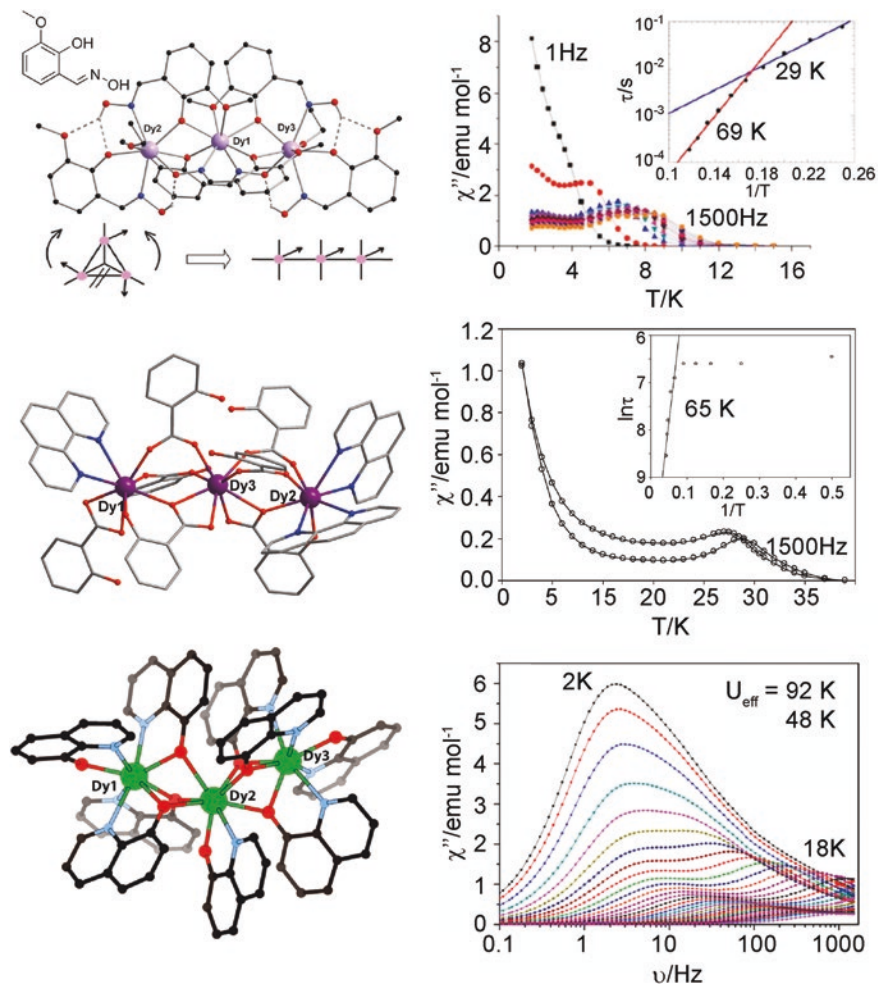


Fig. 4.21 The crystal structures and dynamic magnetic properties of the linear Dy₃ SMMs reported to date. *Top, Middle* Reproduced from Refs. [37, 39] by permission of The Royal Society of Chemistry. *Below* Reprinted with the permission from Ref. [40]. Copyright 2014 American Chemical Society

4.2.3.2 Dy₄ SMMs

Planar Dy₄

In 2009, the group of M. Murugesu reported a defect-dicubane Dy₄ SMM, [Dy₄(μ₃-OH)₂(bmh)₂(msh)₄Cl₂], showing a high magnetic blocking temperature about 7 K (Fig. 4.22), which seems to be the highest before the discovery of N₂³⁻-bridged Ln₂ SMMs [33]. The molecule contains four coplanar Dy^{III} centers bridged by two μ₃-OH ligands, four μ₂ phenoxide oxygen atoms, and two diaza bridging groups. The

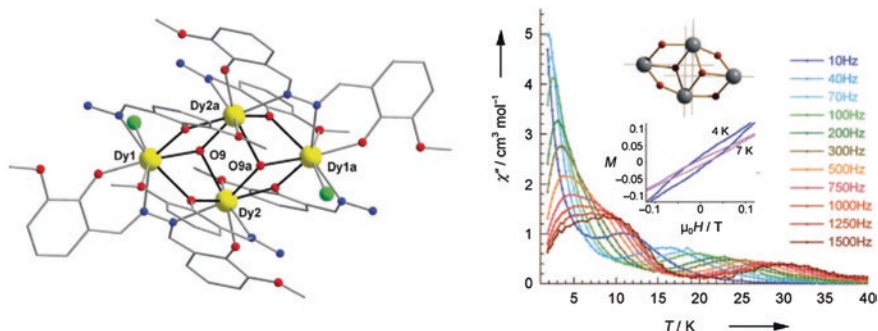


Fig. 4.22 The crystal structures and dynamic magnetic properties of the planar Dy_4 SMMs reported by M. Murugesu. Reproduced from Ref. [33] by permission of John Wiley & Sons Ltd.

out-of-phase ac signals were observed with two peaks at 30 and 9 K for 1500 Hz, indicating the occurrence of two-step relaxation process corresponding to two types of dysprosium ions. As a result, two effective barriers were given to be 9.7 and 170 K corresponding to the low- and high-temperature relaxation processes, respectively. To gain insight into the relaxation mechanism, ab initio calculations were performed, revealing the important uniaxial anisotropy at each Dy site, $g_z = 19.5$ for Dy1 and $g_z = 19.2$ for Dy2. The anisotropic axes on Dy1 and Dy2 sites are almost orthogonal to each other, making an angle of 28.78° and 3.18° with the Dy_4 plane, respectively. Furthermore, the anisotropic axes are parallel to each other for the Dy ions at opposite sites and point almost radially to each Dy site, as shown in Fig. 4.22 inset. The energy separations between the ground and the first excited states were calculated to be 83 and 199 K for Dy1 and Dy2 centers, respectively, which are comparable to the large effective barrier of 170 K, indicating that the main contribution to the blocking barriers of magnetization in this compound arises from the blocking behavior of magnetizations of individual dysprosium ions. It is noteworthy that the directions of anisotropic axes in the planar Dy_4 SMM are distinct from the Dy_4 SMT in the first part, where the anisotropic axes are arranged in a toroidal fashion. The main reason for this may be due to the different charge distribution around each Dy center.

In addition, some other planar Dy_4 complexes showing the similar core structure were also constructed by applying different types of ligands, as shown in Fig. 4.23, but their SMM properties are not so fascinating [41–44]. Therefore, they will not be described in detail here.

Finally, another interesting planar Dy_4 compound was also constructed using an amino-polyalcohol ligand, which provides the important alkoxide bridges, as shown in Fig. 4.24 [45]. Here a critical difference from the above Dy_4 complexes is observed in the core structure, where four Dy centers are aggregated by four $\mu_3\text{-O}$ from $-\text{OH}$ arms of the ligands. Therefore, the Dy_4 core can be viewed as the linkage of two edge-sharing Dy_3 triangles. Unfortunately, ab initio calculations were not performed in this example. The out-of-phase ac signals in Fig. 4.24 reveal two obvious relaxation peaks above 10 Hz, indicating the occurrence of two relaxation processes, which give two effective barriers of 44 and 107 K.

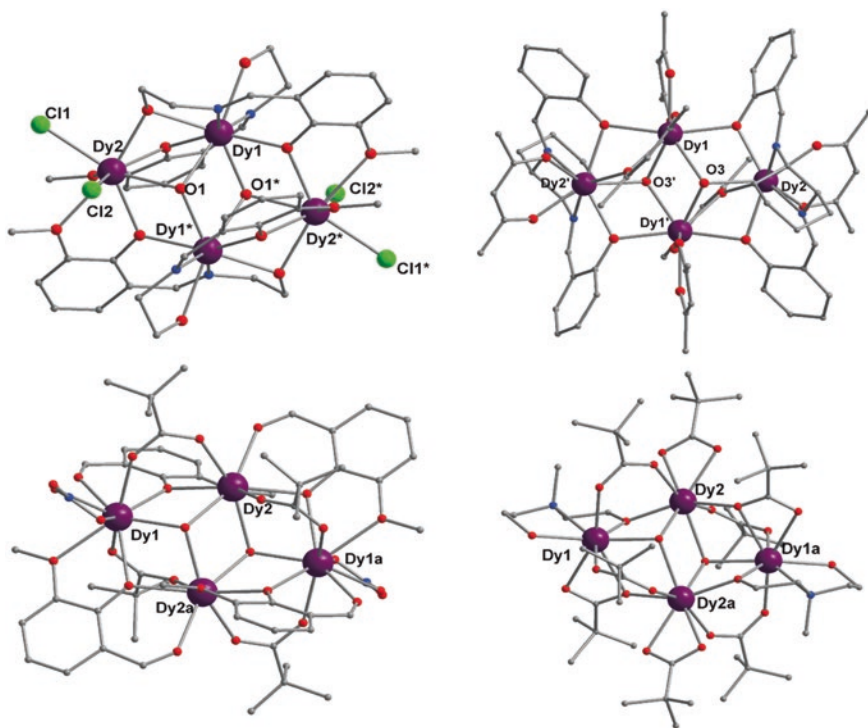


Fig. 4.23 The crystal structures of the planar Dy₄ SMMs reported to date. Figures generated from data first reported in Refs. [41–44]

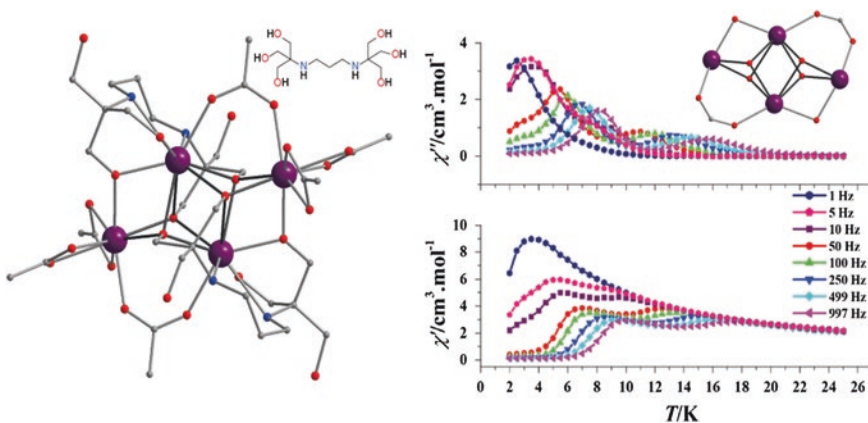


Fig. 4.24 The crystal structures and dynamic magnetic properties of the planar Dy₄ SMMs bridged by four μ_3 -O. Reproduced from Ref. [45] by permission of The Royal Society of Chemistry

Dy₄ Cubane

In 2014, E. Colacio reported the hydroxide-free cubane-shaped Dy₄ complex assembled by using compartmental Schiff base ligand and pivalic acid [46]. As shown in Fig. 4.25, the Dy₄ molecule contains a distorted cubane-like [Dy₄(μ₃-OR)₄]⁺⁸ core, in which adjacent Dy ions are further held together by pivalate anions in μ₂-η¹:η¹ form with Dy–O–Dy angles in range of 99.20(2)–115.10(2)°. The frequency- and temperature-dependent out-of-phase signals are present in Fig. 4.25 under zero-dc field, which is typical of multiple relaxation SMM behavior. Analysis of the dynamic magnetic data under an applied dc field of 1000 Oe gives two anisotropic effective barriers, $U_{\text{eff}} = 73$ K ($\tau_0 = 4.4 \times 10^{-8}$ s) and 47 K ($\tau_0 = 5.0 \times 10^{-7}$ s), for the slow and fast relaxations, respectively. In fact, several μ₃-OH-bridged Dy₄ complexes derived from carboxylate ligands showing the similar core structure were reported before, as shown in Fig. 4.26, but these complexes do not exhibit good SMM behavior [47–49].

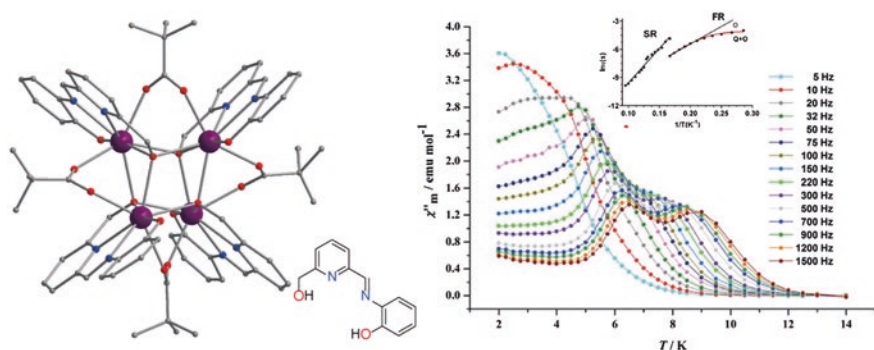


Fig. 4.25 The crystal structures and dynamic magnetic properties of the hydroxide-free cubane-shaped Dy₄ SMMs. Reprinted with the permission from Ref. [46]. Copyright 2014 American Chemical Society

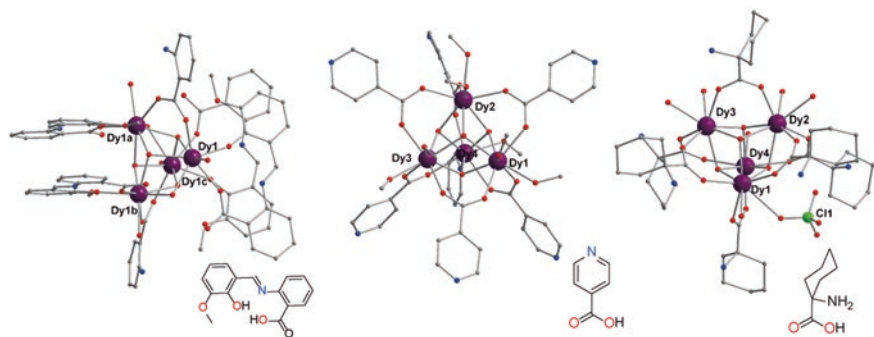


Fig. 4.26 The crystal structures of the hydroxide-bridged cubane-shaped Dy₄ complexes. Figures generated from data first reported in Refs. [47–49]

Dy₄ Tetrahedron

In 2011, the first μ_4 -O fixed Dy₄ SMM displaying tetrahedral core structure was constructed through applying the in situ formed hydrazone ligands [50]. Here two stereoisomers exist as a racemic mixture of enantiomers in the crystal structure with the central O atom as a chiral center. Such local chirality is induced by the coordination of the twisted diazine bridge from Schiff base ligands. Importantly, four Dy ions are located in different coordinated environments and are arranged in a distorted tetrahedral fashion. Therefore, ab initio calculations reveal strong single-ion anisotropy at each Dy site, and they all point to different directions, as shown in Fig. 4.27 top. Furthermore, the corresponding calculations gave an exchange interaction parameter of $J = -0.3 \text{ cm}^{-1}$, indicating the overall antiferromagnetic exchange coupling present within each Dy pair. The temperature-dependent ac signals with maxima are indicative of its typical SMM behavior and give an effective barrier of 23 K. In addition, the other μ_4 -O fixed Dy₄ tetrahedron showing slow relaxation of the magnetization was reported by our group (Fig. 4.27 bottom) [51].

Linear Dy₄ SMMs

Our group has reported two discrete linear Dy₄ SMMs through employing two different Schiff base ligands, as shown in Fig. 4.28 [52, 53]. Typically, the Dy centers

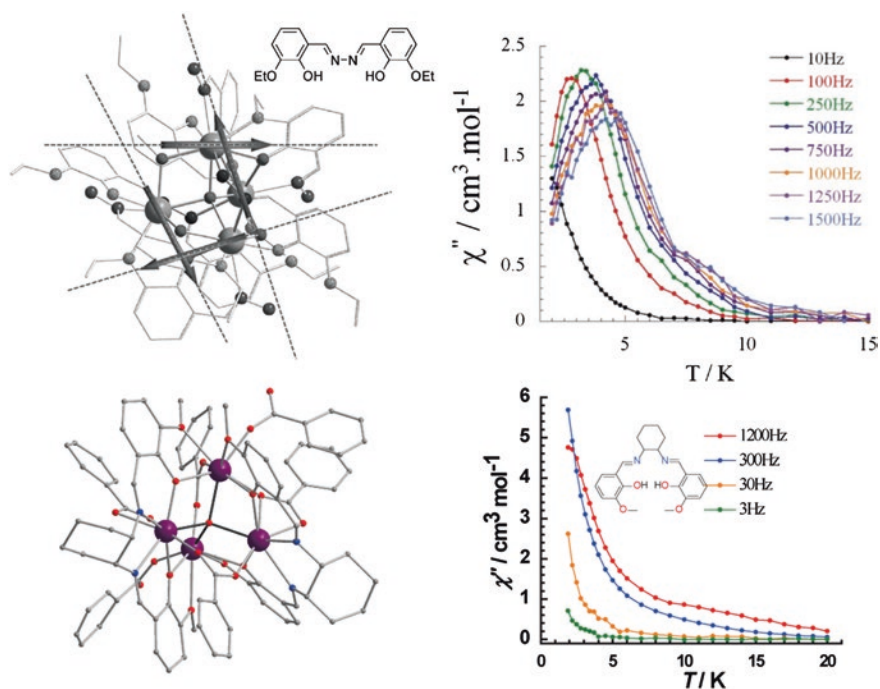


Fig. 4.27 The crystal structures and dynamic magnetic properties of two μ_4 -O fixed Dy₄ SMMs displaying tetrahedral core structure. Reproduced from Refs. [50, 51] by permission of John Wiley & Sons Ltd.

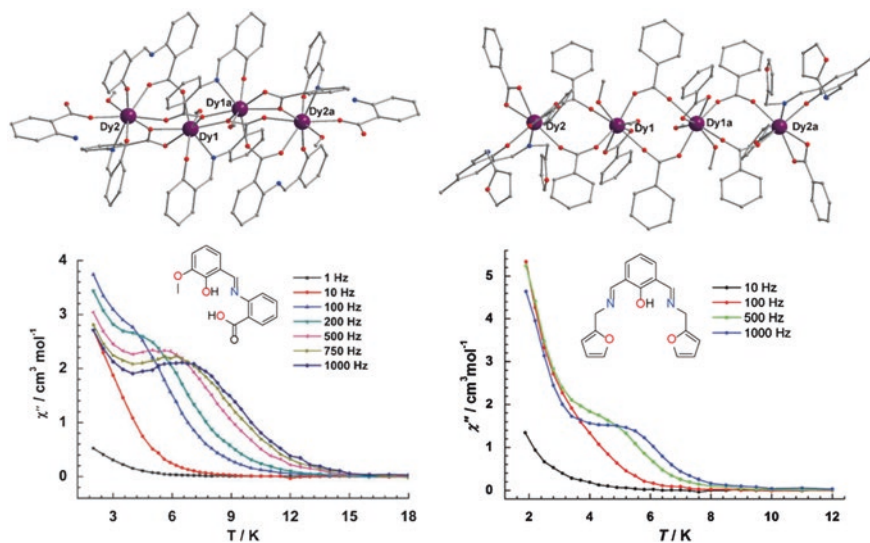


Fig. 4.28 The crystal structures and dynamic magnetic properties of two linear Dy_4 SMMs reported by our group. Reproduced from Refs. [52, 53] by permission of The Royal Society of Chemistry

are bridged by carboxylate bridges, but the bridges exhibit distinct bridging fashions in the two complexes. In the first complex of Fig. 4.28, three different binding modes can be discovered for the polydentate Schiff base ligand in its zwitterionic and di-deprotonated forms, which result in the formation of a linear core structure. Two asymmetric Dy^{III} centers are discovered with the distinct coordination geometries. In contrast, the presence of Schiff base ligand in the second complex provides effective hindrances to prevent the formation of extended structures (1D chain) bridged by the PhCOO^- , thus leading to the isolation of the linear Dy_4 complex with Dy-Dy-Dy angle of $175.673(2)^\circ$ [53]. Furthermore, the similar distorted bicapped trigonal-prismatic geometry is observed for two unique crystallographic Dy^{III} centers. Despite the different coordination geometries for two linear complexes, their out-of-phase ac signals in Fig. 4.28 reveal the similar magnetic blocking behaviors in them, thus giving almost equivalent energy barriers $U_{\text{eff}} = 20$ K and 17 K, respectively. Besides the two examples, some other linear Dy_4 complexes were also assembled by other groups using the different polydentate ligands, which are presented in Fig. 4.29 [54–56].

Seesaw-like Dy_4

In 2014, two unique *seesaw*-like Dy_4 complexes were reported by V. Chandrasekhar [57] and F.-P. Liang [58] groups, respectively. They are both constructed by applying *o*-vanillin-based Schiff base ligands which display various coordination modes. As shown in Fig. 4.30, four Dy centers are held together by an important $\mu_4\text{-O}$ atom, leading to the linkage of two edge-sharing Dy_3 units with an obvious dihedral angle. Importantly, all Dy centers are nine coordinate in them, but show the different coordinate geometries, which seem to be important to the occurrence of their different

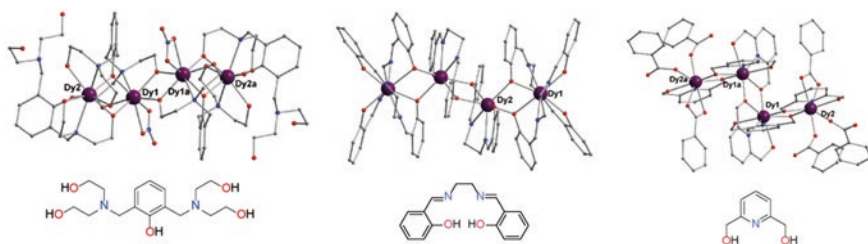
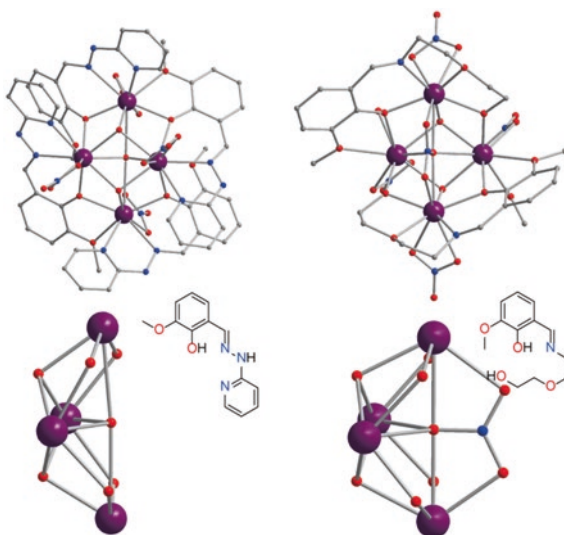


Fig. 4.29 The crystal structures of other linear Dy₄ SMMs reported so far. Figures generated from data first reported in Refs. [54–56]

Fig. 4.30 The crystal structures of two unique *seesaw*-like Dy₄ complexes. Figures generated from data first reported in Refs. [57, 58]



SMM behaviors. For the first complex, only the slow relaxation signals without out-of-phase maxima were observed, and thus the effective barrier cannot be extracted [57]. In contrast, the second complex shows the clear out-of-phase ac signals with maxima, affording a small effective barrier about 28 K [58].

In addition, some other Dy₄ SMMs showing different structural motifs or relatively high-effective barriers were also assembled using the hydrazone ligands, such as Dy₄ grid and Y-type Dy₄ SMMs, which will be investigated in detail in the next chapter.

4.2.3.3 Larger Lanthanide SMMs

Except Dy-based complexes with hydrazone ligands, most of the larger lanthanide clusters with common ligands do not show excellent SMM properties, which may

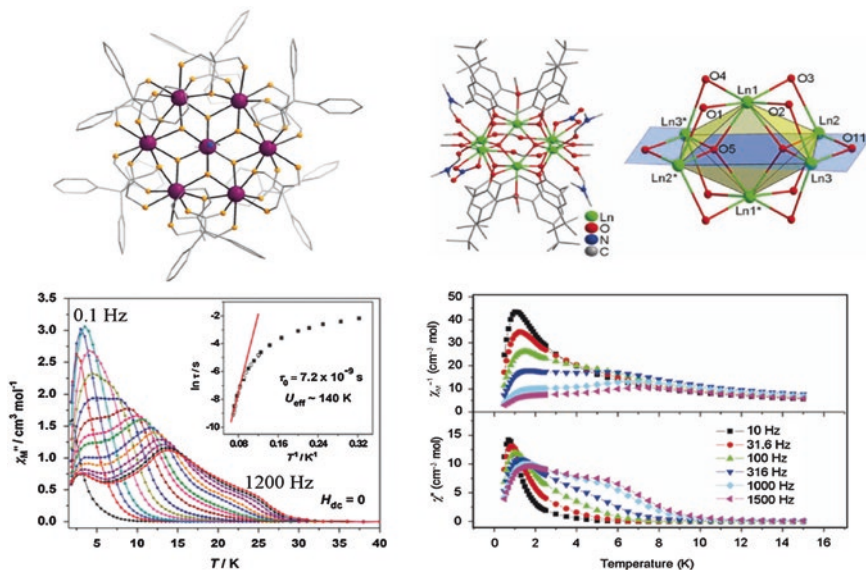


Fig. 4.31 The crystal structures and dynamic magnetic properties of the centered-hexagonal Dy_7 and octahedral Dy_6 clusters. *Left* Reproduced from Ref. [59] by permission of The Royal Society of Chemistry. *Right* Reprinted from Ref. [60], with kind permission from Springer Science+Business Media

be due to the difficult control for the local anisotropy of each lanthanide center. Here only two Dy-based examples exhibiting relatively good SMM behavior are presented to highlight the assembly of lanthanide SMMs with more magnetic centers to improve their SMM properties.

The first complex in Fig. 4.31 was constructed using the mixed ligands of a tripodal alcohol and triphenylacetic acid by D. Collison group [59]. The cluster processes a centered-hexagonal Dy_7 cores resembling a disk, where the peripheral and central Dy ions are held together by six $\mu_3\text{-OH}$ groups alternating above and below the metal plane. In contrast to the cyclic Dy_6 SMT in the first part, it seems to be fixed by the central $[\text{Dy}(\mu_3\text{-O})_6]$ group in the complex. Importantly, the strongly magnetic blocking behavior was observed in the complex, as evidenced by the well-resolved frequency-dependent out-of-phase susceptibility signals with maxima in Fig. 4.31. Consequently, a high-effective barrier was given to be about 140 K, which even surpasses the barriers in some lanthanide SMMs in the second and third chapters.

In 2012, W.P. Liao and coworkers reported the octahedral Dy_6 cluster, which was constructed by two tail-to-tail calixarene ligands, as shown in Fig. 4.31 right [60]. Here the Dy_6 core can be viewed as the coupling of two $\mu_4\text{-O}$ -bridged Dy_4 tetrahedrons in an edge-sharing fashion. The ac susceptibility data show obvious temperature-dependent out-of-phase (χ'') signals with the broaden peaks under a zero-dc field, indicating the possible multiple relaxation SMM behavior. Therefore, a small effective barrier was afforded to be about 8 K.

In conclusion, a brief summarization on multinuclear lanthanide SMMs has been given by us in the second part of this chapter. Three main synthetic approaches are extracted through examining the multinuclear lanthanide SMMs discovered to date. In particular, the first two approaches hold great potential in obtaining strongly blocked SMMs. The information extracted from such investigation will enhance our understanding to improve the SMM performances of polynuclear lanthanide complexes and facilitate their future applications.

References

1. Le Roy JJ, Jeletic M, Gorelsky SI et al (2013) An organometallic building block approach to produce a multidecker 4f single-molecule magnet. *J Am Chem Soc* 135(9):3502–3510. doi:[10.1021/ja310642h](https://doi.org/10.1021/ja310642h)
2. Blagg RJ, Ungur L, Tuna F et al (2013) Magnetic relaxation pathways in lanthanide single-molecule magnets. *Nat Chem* 5(8):673–678. doi:[10.1038/nchem.1707](https://doi.org/10.1038/nchem.1707)
3. Ganivet CR, Ballesteros B, de la Torre G et al (2013) Influence of peripheral substitution on the magnetic behavior of single-ion magnets based on homo- and heteroleptic Tb^{III} bis(phthalocyaninate). *Chem Eur J* 19(4):1457–1465. doi:[10.1002/chem.201202600](https://doi.org/10.1002/chem.201202600)
4. Tang J, Hewitt I, Madhu NT et al (2006) Dysprosium triangles showing single-molecule magnet behavior of thermally excited spin states. *Angew Chem Int Ed* 45(11):1729–1733. doi:[10.1002/anie.200503564](https://doi.org/10.1002/anie.200503564)
5. Luzon J, Bernot K, Hewitt IJ et al (2008) Spin chirality in a molecular dysprosium triangle: the archetype of the noncollinear ising model. *Phys Rev Lett* 100(24):247205. doi:[10.1103/PhysRevLett.100.247205](https://doi.org/10.1103/PhysRevLett.100.247205)
6. Guo Y-N, Xu G-F, Guo Y et al (2011) Relaxation dynamics of dysprosium(III) single molecule magnets. *Dalton Trans* 40(39):9953–9963. doi:[10.1039/C1DT10474H](https://doi.org/10.1039/C1DT10474H)
7. Plokhov DI, Popov AI, Zvezdin AK (2011) Quantum magnetoelectric effect in the molecular crystal Dy₃. *Phys Rev B* 84(22):224436. doi:[10.1103/PhysRevB.84.224436](https://doi.org/10.1103/PhysRevB.84.224436)
8. Ungur L, Lin S-Y, Tang J et al (2014) Single-molecule toroids in Ising-type lanthanide molecular clusters. *Chem Soc Rev* 43(20):6894–6905. doi:[10.1039/c4cs00095a](https://doi.org/10.1039/c4cs00095a)
9. Van Aken BB, Rivera J-P, Schmid H et al (2007) Observation of ferrotoroidic domains. *Nature* 449(7163):702–705. doi:[10.1038/nature06139](https://doi.org/10.1038/nature06139)
10. Eerenstein W, Mathur ND, Scott JF (2006) Multiferroic and magnetoelectric materials. *Nature* 442(7104):759–765. doi:[10.1038/nature05023](https://doi.org/10.1038/nature05023)
11. Spaldin NA, Fiebig M, Mostovoy M (2008) The toroidal moment in condensed-matter physics and its relation to the magnetoelectric effect. *J Phys Condens Matter* 20:434203. doi:[10.1088/0953-8984/20/43/434203](https://doi.org/10.1088/0953-8984/20/43/434203)
12. Zimmermann AS, Meier D, Fiebig M (2014) Ferroic nature of magnetic toroidal order. *Nat Commun* 5. doi:[10.1038/ncomms5796](https://doi.org/10.1038/ncomms5796)
13. Chibotaru LF, Ungur L, Soncini A (2008) The origin of nonmagnetic kramers doublets in the ground state of dysprosium triangles: evidence for a toroidal magnetic moment. *Angew Chem Int Ed* 47(22):4126–4129. doi:[10.1002/anie.200800283](https://doi.org/10.1002/anie.200800283)
14. Guo P-H, Liu J-L, Zhang Z-M et al (2012) The first Dy₄ single-molecule magnet with a toroidal magnetic moment in the ground state. *Inorg Chem* 51(3):1233–1235. doi:[10.1021/ic202650f](https://doi.org/10.1021/ic202650f)
15. Ungur L, Langley SK, Hooper TN et al (2012) Net toroidal magnetic moment in the ground state of a {Dy₆}-triethanolamine ring. *J Am Chem Soc* 134(45):18554–18557. doi:[10.1021/ja309211d](https://doi.org/10.1021/ja309211d)
16. Ungur L, Van den Heuvel W, Chibotaru LF (2009) Ab initio investigation of the non-collinear magnetic structure and the lowest magnetic excitations in dysprosium triangles. *New J Chem* 33(6):1224–1230. doi:[10.1039/B903126J](https://doi.org/10.1039/B903126J)

17. Xue S, Chen X-H, Zhao L et al (2012) Two bulky-decorated triangular dysprosium aggregates conserving vortex-spin structure. *Inorg Chem* 51(24):13264–13270. doi:[10.1021/ic301785v](https://doi.org/10.1021/ic301785v)
18. Wang Y-X, Shi W, Li H et al (2012) A single-molecule magnet assembly exhibiting a dielectric transition at 470 K. *Chem Sci* 3(12):3366–3370. doi:[10.1039/C2SC21023A](https://doi.org/10.1039/C2SC21023A)
19. Langley SK, Mobaraki B, Forsyth CM et al (2010) Structure and magnetism of new lanthanide 6-wheel compounds utilizing triethanolamine as a stabilizing ligand. *Dalton Trans* 39(7):1705–1708. doi:[10.1039/B921843B](https://doi.org/10.1039/B921843B)
20. Hewitt IJ, Tang J, Madhu NT et al (2010) Coupling Dy₃ Triangles Enhances Their Slow Magnetic Relaxation. *Angew Chem Int Ed* 49(36):6352–6356. doi:[10.1002/anie.201002691](https://doi.org/10.1002/anie.201002691)
21. Hussain B, Savard D, Burchell TJ et al (2009) Linking high anisotropy Dy₃ triangles to create a Dy₆ single-molecule magnet. *Chem Commun* 9:1100–1102. doi:[10.1039/B818295G](https://doi.org/10.1039/B818295G)
22. Lin S-Y, Wernsdorfer W, Ungur L et al (2012) Coupling Dy₃ Triangles to Maximize the Toroidal Moment. *Angew Chem Int Ed* 51:12767–12771. doi:[10.1002/anie.201206602](https://doi.org/10.1002/anie.201206602)
23. Novitchi G, Pilet G, Ungur L et al (2012) Heterometallic Cu^{II}/Dy^{III} 1D chiral polymers: chirogenesis and exchange coupling of toroidal moments in trinuclear Dy₃ single molecule magnets. *Chem Sci* 3(4):1169–1176. doi:[10.1039/c2sc00728b](https://doi.org/10.1039/c2sc00728b)
24. Hänninen MM, Mota AJ, Aravena D et al. (2014) Two C₃-Symmetric Dy₃^{III} complexes with triple di-μ-methoxy-μ-phenoxo bridges, magnetic ground state, and single-molecule magnetic behavior. *Chem Eur J* 20(27):8410–8420. doi:[10.1002/chem.201402392](https://doi.org/10.1002/chem.201402392)
25. Shen S, Xue S, Lin S-Y et al (2013) A triangular dysprosium with asymmetric central caps featuring ferromagnetic coupling and single-molecule magnet behaviour. *Dalton Trans* 42(29):10413–10416. doi:[10.1039/c3dt51235e](https://doi.org/10.1039/c3dt51235e)
26. Morita T, Katoh K, Breedlove BK et al (2013) Controlling the dipole-dipole interactions between Terbium(III) phthalocyaninato triple-decker moieties through spatial control using a fused Phthalocyaninato ligand. *Inorg Chem* 52(23):13555–13561. doi:[10.1021/ic4020459](https://doi.org/10.1021/ic4020459)
27. Guo Y-N, Xu G-F, Wernsdorfer W et al (2011) Strong axiality and ising exchange interaction suppress zero-field tunneling of magnetization of an asymmetric Dy₂ single-molecule magnet. *J Am Chem Soc* 133(31):11948–11951. doi:[10.1021/ja205035g](https://doi.org/10.1021/ja205035g)
28. Guo Y-N, Chen X-H, Xue S et al (2012) Molecular assembly and magnetic dynamics of two novel Dy₆ and Dy₈ aggregates. *Inorg Chem* 51(7):4035–4042. doi:[10.1021/ic202170z](https://doi.org/10.1021/ic202170z)
29. Blagg RJ, Murny CA, McInnes EJJ et al (2011) Single pyramid magnets: Dy₅ pyramids with slow magnetic relaxation to 40 K. *Angew Chem Int Ed* 50(29):6530–6533. doi:[10.1002/anie.201101932](https://doi.org/10.1002/anie.201101932)
30. Woodruff DN, Tuna F, Bodensteiner M et al (2013) Single-molecule magnetism in tetrametallic terbium and dysprosium thiolate cages. *Organometallics* 32(5):1224–1229. doi:[10.1021/om3010096](https://doi.org/10.1021/om3010096)
31. Woodruff DN, Wimpenny REP, Layfield RA (2013) Lanthanide single-molecule magnets. *Chem Rev* 113:5110–5148. doi:[10.1021/cr400018q](https://doi.org/10.1021/cr400018q)
32. Zhang P, Guo Y-N, Tang J (2013) Recent advances in dysprosium-based single molecule magnets: structural overview and synthetic strategies. *Coord Chem Rev* 257(11–12):1728–1763. doi:[10.1016/j.ccr.2013.01.012](https://doi.org/10.1016/j.ccr.2013.01.012)
33. Lin P-H, Burchell TJ, Ungur L et al (2009) A polynuclear lanthanide single-molecule magnet with a record anisotropic barrier. *Angew Chem Int Ed* 48(50):9489–9492. doi:[10.1002/anie.200903199](https://doi.org/10.1002/anie.200903199)
34. Zhang P, Zhang L, Tang J (2013) Hydrazone-based dysprosium single molecule magnets. *Inorg Chem* 52(2):101–111. doi:[10.1021/ic30020005](https://doi.org/10.1021/ic30020005)
35. Yamashita A, Watanabe A, Akine S et al. (2011) Wheel-shaped Er^{III}Zn₃^{II} single-molecule magnet: a macrocyclic approach to designing magnetic anisotropy. *Angew Chem Int Ed* 50(17):4016–4019. doi:[10.1002/anie.201008180](https://doi.org/10.1002/anie.201008180)
36. Lin S-Y, Guo Y-N, Guo Y et al (2012) Macrocyclic ligand encapsulating dysprosium triangles: axial ligands perturbed magnetic dynamics. *Chem Commun* 48(55):6924–6926. doi:[10.1039/C2CC32827E](https://doi.org/10.1039/C2CC32827E)
37. Hewitt IJ, Lan Y, Anson CE et al (2009) Opening up a dysprosium triangle by ligand oximation. *Chem Commun* 44:6765–6767. doi:[10.1039/B908194A](https://doi.org/10.1039/B908194A)

38. Guo F-S, Liu J-L, Leng J-D et al (2011) Pure trinuclear 4f single-molecule magnets: synthesis, structures, magnetism and ab initio investigation. *Chem Eur J* 17(8):2458–2466. doi:[10.1002/chem.2011002296](https://doi.org/10.1002/chem.2011002296)
39. Liu C-S, Du M, Sanudo EC et al (2011) A luminescent linear trinuclear Dy^{III} complex exhibiting slow magnetic relaxation of single ion origin. *Dalton Trans* 40(37):9366–9369. doi:[10.1039/C1DT11039J](https://doi.org/10.1039/C1DT11039J)
40. Chilton NF, Deacon GB, Gazukin O et al (2014) Structure, magnetic behavior, and anisotropy of homoleptic trinuclear lanthanoid 8-quinolinolate complexes. *Inorg Chem* 53(5):2528–2534. doi:[10.1021/ic402672m](https://doi.org/10.1021/ic402672m)
41. Zheng Y-Z, Lan Y, Anson CE et al (2008) Anion-perturbed magnetic slow relaxation in planar Dy₄ clusters. *Inorg Chem* 47(23):10813–10815. doi:[10.1021/ic801672z](https://doi.org/10.1021/ic801672z)
42. Yan P-F, Lin P-H, Habib F et al (2011) Planar tetranuclear Dy(III) single-molecule magnet and its Sm(III), Gd(III), and Tb(III) analogues encapsulated by Salen-Type and β -diketonate ligands. *Inorg Chem* 50(15):7059–7065. doi:[10.1021/ic200566y](https://doi.org/10.1021/ic200566y)
43. Langley SK, Chilton NF, Gass IA et al (2011) Planar tetranuclear lanthanide clusters with the Dy₄ analogue displaying slow magnetic relaxation. *Dalton Trans* 40(47):12656–12659. doi:[10.1039/C1DT11750E](https://doi.org/10.1039/C1DT11750E)
44. Abbas G, Lan Y, Kostakis GE et al. (2010) Series of isostructural planar lanthanide complexes [Ln^{III}(μ_3 -OH)₂(mdeaH)₂(piv)₈] with single molecule magnet behavior for the Dy₄ analogue. *Inorg Chem* 49 (17):8067–8072. doi:[10.1021/ic1011605](https://doi.org/10.1021/ic1011605)
45. Liu C-M, Zhang D-Q, Zhu D-B (2013) A single-molecule magnet featuring a parallelogram [Dy₄(OCH₂)₄] core and two magnetic relaxation processes. *Dalton Trans* 42(41):14813–14818. doi:[10.1039/c3dt51785c](https://doi.org/10.1039/c3dt51785c)
46. Das S, Dey A, Biswas S et al (2014) Hydroxide-free cubane-shaped tetranuclear [Ln₄] complexes. *Inorg Chem* 53(7):3417–3426. doi:[10.1021/ic402827b](https://doi.org/10.1021/ic402827b)
47. Ke H, Gamez P, Zhao L et al (2010) Magnetic properties of dysprosium cubanes dictated by the M–O–M angles of the [Dy₄(μ_3 -OH)₄] Core. *Inorg Chem* 49(16):7549–7557. doi:[10.1021/ic101057e](https://doi.org/10.1021/ic101057e)
48. Gao YJ, Xu GF, Zhao L et al (2009) Observation of slow magnetic relaxation in discrete dysprosium cubane. *Inorg Chem* 48(24):11495–11497. doi:[10.1021/ic901806g](https://doi.org/10.1021/ic901806g)
49. Peng J-B, Ren Y-P, Kong X-J et al (2011) A series of di-, tri- and tetranuclear lanthanide clusters with slow magnetic relaxation for Dy₂ and Dy₄. *Cryst Eng Comm* 13(6):2084–2090. doi:[10.1039/C0CE00589D](https://doi.org/10.1039/C0CE00589D)
50. Lin P-H, Korobkov I, Wernsdorfer W et al (2011) A rare μ_4 -O centred Dy₄ tetrahedron with coordination-Induced local chirality and single-molecule magnet behaviour. *Eur J Inorg Chem* 10:1535–1539. doi:[10.1002/ejic.201100038](https://doi.org/10.1002/ejic.201100038)
51. Zhang L, Zhang P, Zhao L et al. (2013) Two locally chiral dysprosium compounds with salen-type ligands that show slow magnetic relaxation behavior. *Eur J Inorg Chem* 2013 (8):1351–1357. doi:[10.1002/ejic.201201336](https://doi.org/10.1002/ejic.201201336)
52. Ke H, Xu G-F, Guo Y-N et al (2010) A linear tetranuclear dysprosium(III) compound showing single-molecule magnet behaviour. *Chem Commun* 46(33):6057–6059. doi:[10.1039/C0CC01067G](https://doi.org/10.1039/C0CC01067G)
53. Lin S-Y, Zhao L, Ke H et al (2012) Steric hindrances create a discrete linear Dy₄ complex exhibiting SMM behaviour. *Dalton Trans* 41(11):3248–3252. doi:[10.1039/C2DT11539E](https://doi.org/10.1039/C2DT11539E)
54. Chen Y-H, Tsai Y-F, Lee G-H et al (2012) The synthesis, structure, magnetic and luminescent properties of a new tetranuclear dysprosium (III) cluster. *J Solid State Chem* 185:166–171. doi:[10.1016/j.jssc.2011.10.033](https://doi.org/10.1016/j.jssc.2011.10.033)
55. Koo BH, Lim KS, Ryu DW et al (2013) Synthesis, structures and magnetic characterizations of isostructural tetranuclear Ln₄ clusters (Ln = Dy, Ho, and Eu). *Dalton Trans* 42(19):7204–7209. doi:[10.1039/c3dt00056g](https://doi.org/10.1039/c3dt00056g)
56. Yang P-P, Gao X-F, Song H-B et al (2010) Slow magnetic relaxation in novel Dy₄ and Dy₈ compounds. *Inorg Chem* 50(3):720–722. doi:[10.1021/ic102164z](https://doi.org/10.1021/ic102164z)
57. Goura J, Walsh JPS, Tuna F et al (2014) Tetranuclear lanthanide(III) complexes in a seesaw geometry: synthesis, structure, and magnetism. *Inorg Chem* 53(7):3385–3391. doi:[10.1021/ic4027915](https://doi.org/10.1021/ic4027915)

58. Zou H-H, Wang R, Chen Z-L et al (2014) Series of edge-sharing bi-triangle Ln₄ clusters with a μ_4 -NO₃ bridge: syntheses, structures, luminescence, and the SMM behavior of the Dy₄ analogue. *Dalton Trans* 43(6):2581–2587. doi:[10.1039/c3dt52316k](https://doi.org/10.1039/c3dt52316k)
59. Sharples JW, Zheng Y-Z, Tuna F et al (2011) Lanthanide discs chill well and relax slowly. *Chem Commun* 47(27):7650–7652. doi:[10.1039/C1CC12252E](https://doi.org/10.1039/C1CC12252E)
60. Bi Y, Xu G, Liao W et al (2012) Calixarene-supported hexadysprosium cluster showing single molecule magnet behavior. *Sci China Chem* 55(6):967–972. doi:[10.1007/s11426-012-4570-5](https://doi.org/10.1007/s11426-012-4570-5)

Chapter 5

Hydrazone-Based Lanthanide Single-Molecule Magnets

Abstract To date, a great number of lanthanide SMMs have been reported through applying rigid mixed-donor hydrazone ligands which can be modified very easily by altering the hydrazide or aldehyde parts. This chapter first focuses on two typical polynuclear Dy complexes which greatly contribute to the elucidation of two-step relaxation model and are subsequently devoted to the constructions of lanthanide SMMs based on the different hydrazide parts and their magnetic analysis. Therefore, the assembly of hydrazone ligands with lanthanide salts under different conditions turns out to be an effective way to discover new lanthanide SMMs and to explore the origin of complicated magnetic dynamics.

Keywords Hydrazone ligands · Two-step relaxation · Keto-enol tautomerism · Hula hoop · Magnetic exchange

As seen in the third and fourth chapters, Schiff base ligands exhibit some advantages over other ligands in the assembly of polynuclear lanthanide SMMs. Generally speaking, such ligands incorporate a great number of coordinating donors such as N and O atoms with an affinity for lanthanide ions, thus leading to the polytopic coordination within a single ligand. More importantly, such donors are usually coupled into multiple dentate coordination pockets preferring chelating a single lanthanide center, which is favorable to self-assembly of lanthanide clusters. As a special class in Schiff base ligands, hydrazone ligands exhibit not only the common features of Schiff base ligands but also some special coordination characteristics, which have proven to be beneficial to achieve high-performance lanthanide SMMs. Therefore, considerable lanthanide SMMs have been obtained using hydrazone ligands which seem to be in great abundance and variety due to the various alternations of hydrazide and aldehyde reagents, as seen in Fig. 5.1.

the rigid ligand incorporates two bidentate and a tridentate coordination pockets, which leads to the easy formation of five-membered chelate rings when two antiparallel ligands coordinate to lanthanide centers. Herein, the presence of axial pentagonal bipyramidal and hula hooplike coordination geometries in Dy_2 complexes in Fig. 5.3a, b is well favorable of the observation of strong SMM behaviors, while no SMM behaviors were observed in the other two Dy_2 complexes (Fig. 5.3c, d). In addition, the ligand can generate several different conformations through keto-enol tautomerism, further leading to the different bridging modes through phenolate and enolate-O connections (Figs. 5.2 and 5.3), which seem to be a key factor in modulating the magnetic exchange between lanthanide centers. Herein, the most common conformation is the *syn* enolic form with an enolate oxygen atom as a bridge between two metal centers, resulting in the strong ferromagnetic interactions. Especially in the asymmetric Dy_2 SMM [3], the theoretical investigations reveal an important exchange-blocking regime at low temperature, which effectively slows down the QTM relaxation times and results in the observation of strong SMM behavior. Please refer to the original references for more detailed information on the structures and magnetism of the above-mentioned complexes [2, 3]. In summary, such a versatile hydrazone ligand turns out to be an excellent candidate for constructing strongly blocked lanthanide SMMs.

To date, a great number of lanthanide SMMs have been reported through applying different hydrazone ligands which can be modified very easily by altering the hydrazide or aldehyde part. Figure 5.1 has listed the two critical parts of hydrazone ligands used in lanthanide SMMs, and their combinations will give various

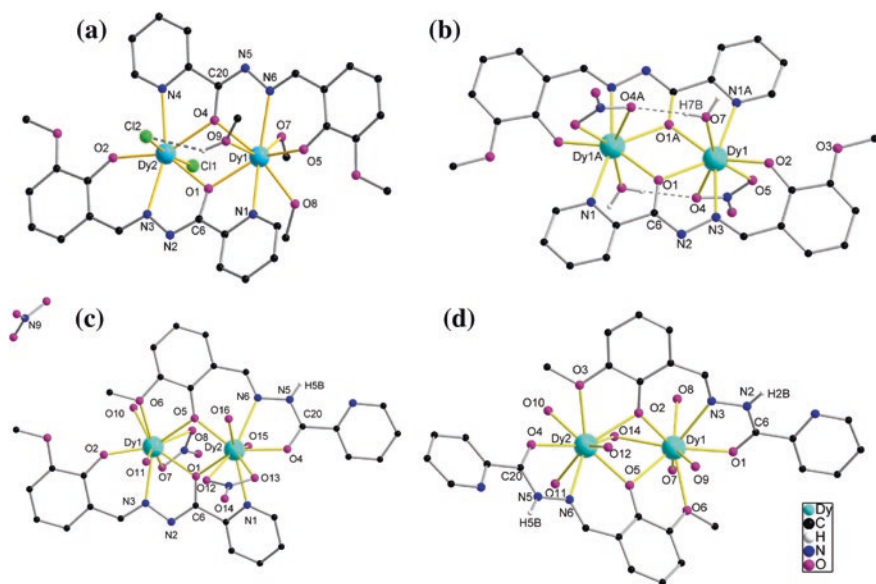


Fig. 5.3 Four typical Dy_2 compounds from *o*-vanillin picolinoylhydrazone ligand with the first two complexes showing the obvious ferromagnetic interactions and SMM behaviors

hydrazone ligands. The following parts firstly focus on two typical polynuclear Dy complexes which greatly contribute to the elucidation of two-step relaxation model and are subsequently devoted to the constructions of lanthanide SMMs based on the different hydrazone parts and their magnetic analysis.

5.2 Two Model Complexes for Two-Step Relaxation

In 2011, a linear Dy₄ SMM (Fig. 5.4) was reported by some of us through applying a hexadentate rigid hydrazone ligand, 2-hydroxy-3-methoxybenzoic acid [(2-hydroxy-3-methoxyphenyl)methylene] hydrazone [4, 5]. The centrosymmetric complex has a nearly linear Dy₄ core with Dy-Dy-Dy angles of 149.99(1)° and incorporates two unique crystallographic Dy ions showing the distorted bicapped trigonal-prismatic and monocapped square-prismatic geometry, respectively. Importantly, alternating current (ac) susceptibility exhibits two well-separated peaks for χ'' versus ν curves, suggesting the occurrence of a multiple relaxation process. Arrhenius analysis gave U_{eff} of 19.7 and 173 K and τ_0 of 7.8×10^{-6}

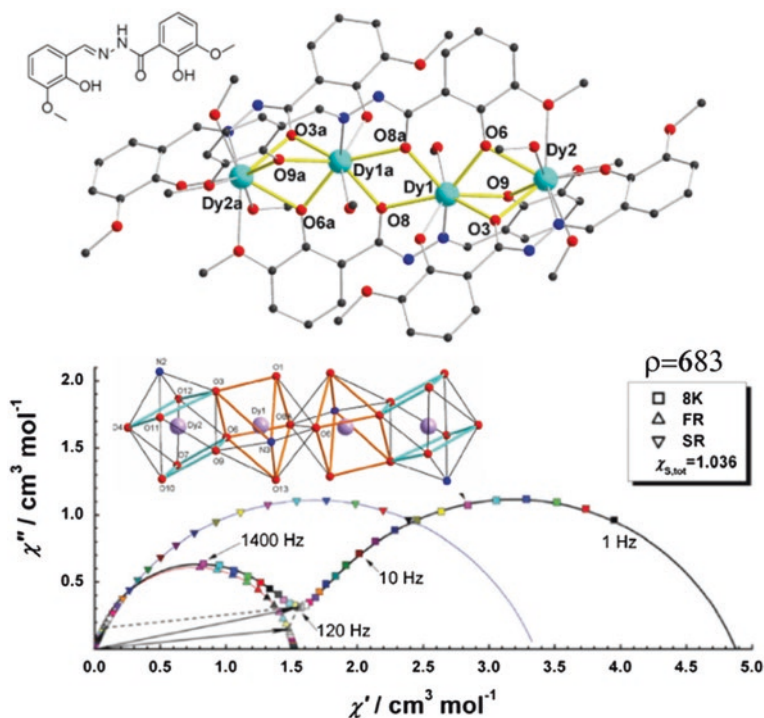


Fig. 5.4 The linear Dy₄ SMM from an *o*-vanilloyl hydrazone ligand and the fitting of its two-step relaxation process from the sum of two modified Debye functions. Reproduced from Ref. [5] by permission of The Royal Society of Chemistry

and 1.2×10^{-7} s for the FR and SR, respectively. Here, the sum of two modified Debye functions in Sect. 1.2.3 was firstly applied to describe the two-step relaxation process, and the presence of such two relaxation processes was ascribed to two distinct anisotropic centers present in the complex. As shown in Fig. 5.4, the Cole–Cole plot can be nicely resolved into two semicircles corresponding to the FR and SR processes at 8 K due to the large ρ value (683).

In addition, the magnetic properties of the asymmetric Dy₂ SMM in Fig. 5.3a have been discussed in Sect. 3.1, and a strongly blocked SMM behavior was observed in this complex [3]. Obviously, the χ'' versus ν plots showing broaden relaxation peaks cannot be fitted with single relaxation Debye model. As shown in Fig. 5.5, such broaden peaks at 6 and 10 K are indicative of the possible occurrence of two close relaxation processes, which are consistent with the presence of two different Dy centers. Therefore, the ac susceptibility data can be nicely described by the sum of two modified Debye functions, which resembles the case in above Dy₄ SMM, but very small ρ values (<10) were obtained, indicating the proximity of two relaxation processes. Naturally, two close effective barriers corresponding to two relaxation processes were also given to be 150 and 198 K.

The application of two different hydrazone ligands resulted in the discovery of two model complexes behaving as typical SMMs with two-step relaxation of magnetization, which can be elucidated through the sum of two modified Debye functions, thus improving our understanding of multiple relaxation processes in lanthanide SMM systems. It has been evidenced that such an in-depth exploration

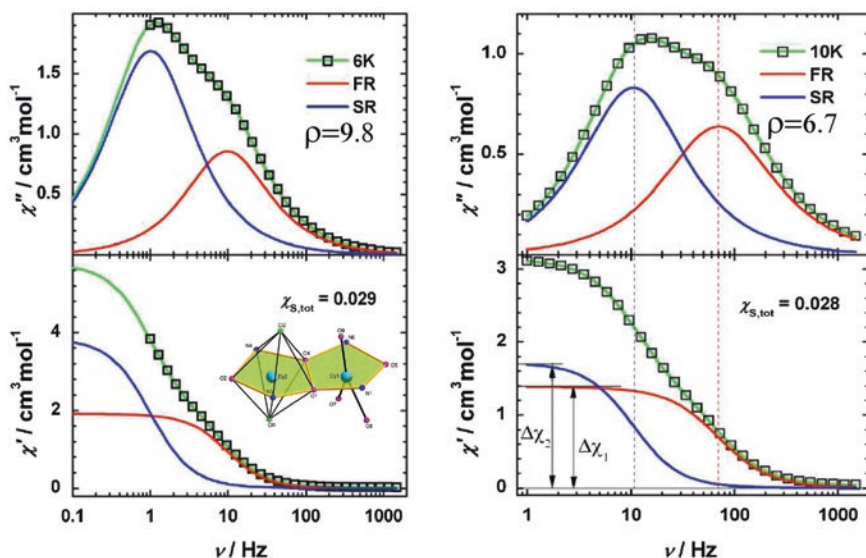


Fig. 5.5 The fitting of a two-step relaxation process with two close relaxations in the asymmetric Dy₂ SMM from *o*-vanillin picolinoylhydrazone ligand. Reprinted with the permission from Ref. [3]. Copyright 2011 American Chemical Society

into multiple relaxation processes stimulated much further work on the design of polynuclear lanthanide SMMs and that hydrazone ligands are a promising class in constructing lanthanide SMMs with high performance.

5.3 Hydrazone Ligands Based on Different Hydrazone Parts

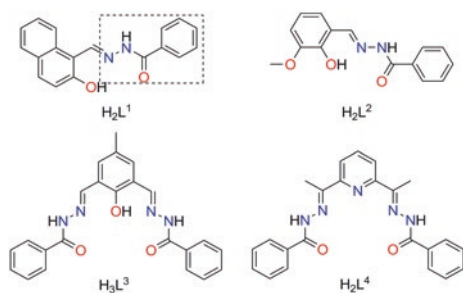
For the hydrazone parts in hydrazone ligands, the simplest type appears to be benzhydrazone, where no donor atom is present in the benzene ring. Subsequently, the alterations of phenyl group result in a variety of hydrazone derivatives, as shown in Fig. 5.1. In the following parts, we will give a systematic description on lanthanide SMMs based on different hydrazone derivatives.

5.3.1 Benzhydrazone Ligands

Two Dy₂ complexes [6, 7] with three bridges were assembled using two different benzhydrazone ligands H₂L¹ and H₂L² in Fig. 5.6, where phenolate-O atoms play the bridging role between two metal centers while keto-enol tautomerism does not occur in the acyl groups. Here, the extremely distorted coordination geometries were observed around Dy ions for both two complexes. Therefore, only weak SMM behaviors are present in two complexes under zero or nonzero applied field, as shown in Fig. 5.7.

In addition, two bis-acylhydrazone ligands arising from the condensation reactions of benzhydrazone and bis-aldehyde, H₂L³ and H₂L⁴ in Fig. 5.6, were used to prepare lanthanide SMMs by us and T. Mallah group, respectively. Here, the distinct features are demonstrated for the two ligands, one showing two tridentate pockets close enough to encapsulate two Dy ions, while the other displaying a large multidentate pocket chelating only one Dy ion, thus leading to the assembly of lanthanide complexes with different nuclearity. For ligand H₂L³,

Fig. 5.6 Hydrazone ligands from the reactions of benzhydrazone and different aldehyde/ketone



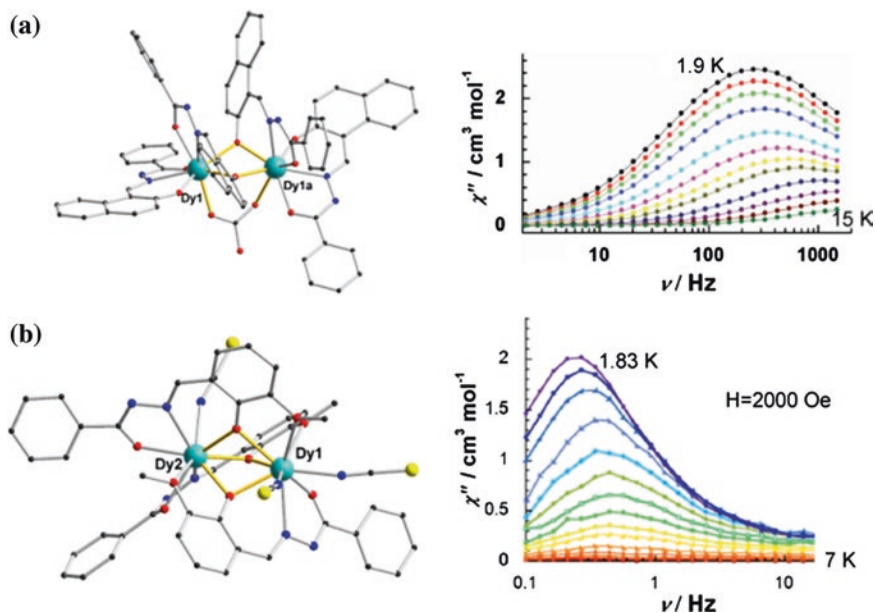


Fig. 5.7 Two Dy₂ complexes from ligands H₂L¹ and H₂L², and the corresponding SMM properties. **a** Reproduced from Ref. [6] by permission of The Royal Society of Chemistry; **b** Reprinted with the permission from Ref. [7]. Copyright 2014 American Chemical Society

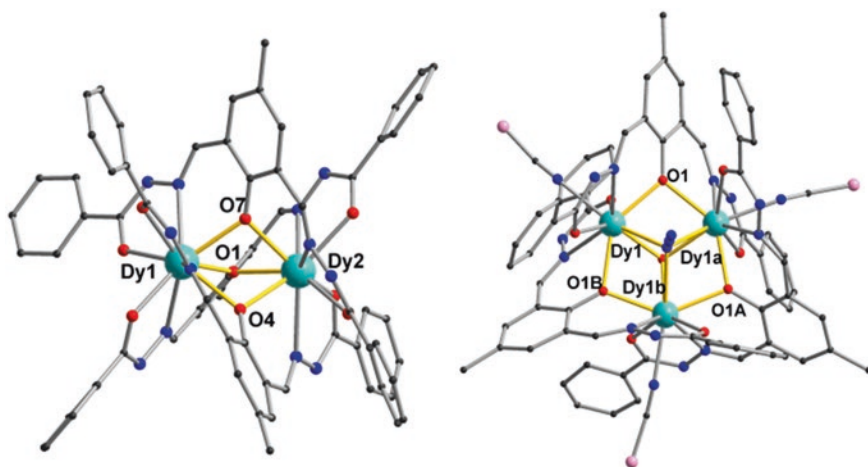


Fig. 5.8 The helical Dy₂ and Dy₃ complexes from bis-acylhydrazone ligand H₃L³

three Dy-based complexes with typical helical structures have been achieved and shown in Fig. 5.8. The Dy₂ complex reported in 2011 exhibits a triple-stranded helical structure with the coordination of three large ligands to two Dy ions in a crossing fashion [8]. Furthermore, such helical structures result in the presence of

two chiral configurations, i.e., Δ and Λ in the crystal. Here, no χ'' signals were observed under zero dc field, but the application of a 700 Oe dc field allows the observation of an obvious frequency-dependent ac signal, indicating the onset of the slow magnetization relaxation. In addition, two novel Dy₃ complexes displaying circular helicates were also prepared by some of us [9]. For them, a remarkable difference is located in the μ_3 -bridging atoms: One Dy₃ triangle is capped by two μ_3 -methoxy oxygens, while in the other one by one μ_3 -OH and one μ_3 -N₃⁻ above and below the plane. In addition, a close observation reveals the distinct coordination environments of the corresponding Dy ions between two Dy₃ molecules. Herein, one complex contains two distinct metal centers, with one nine-coordinate Dy in a distorted tricapped trigonal-prismatic geometry and two eight-coordinate Dy^{III} centers in the distorted bicapped trigonal-prismatic geometry, while the three Dy^{III} ions in the other complex are same nine-coordinate with a

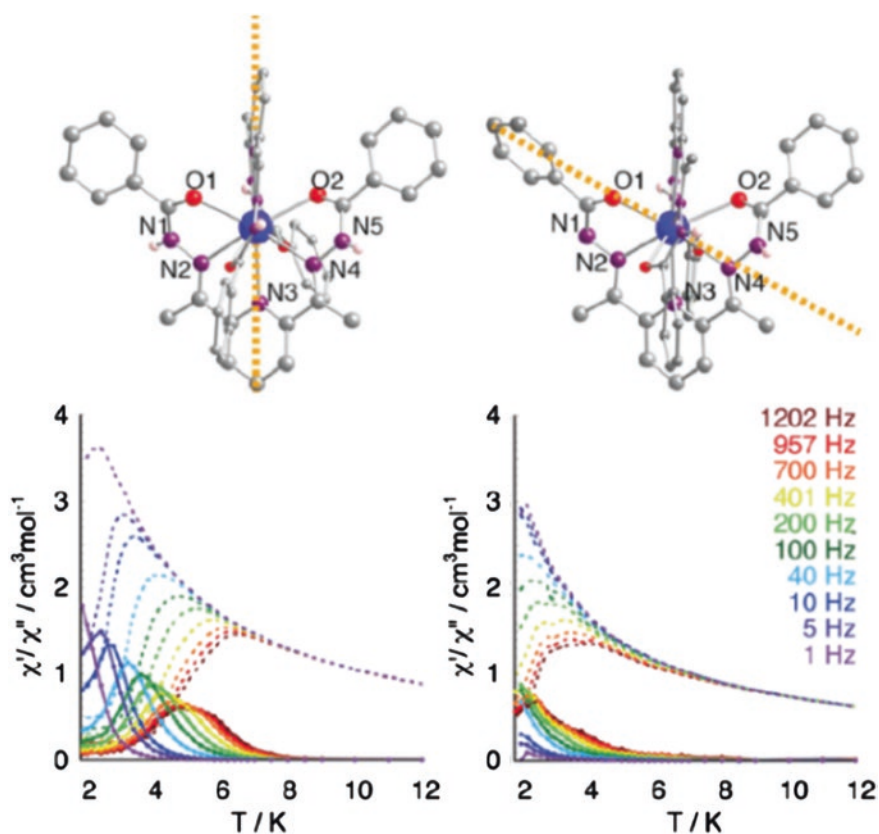


Fig. 5.9 Two mononuclear Dy DMMs from ligand H₂L⁴, and their corresponding SMM properties. The yellow dashed lines show the directions of anisotropic axes. Reproduced from Ref. [10] by permission of The Royal Society of Chemistry

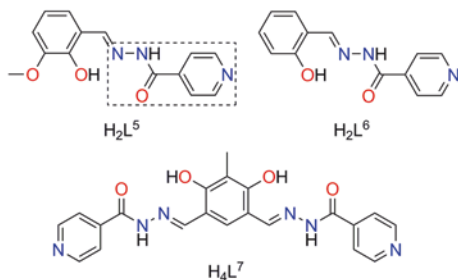
distorted tricapped trigonal-prismatic geometry. As a result, the distinct relaxation dynamics of magnetization appear in two complexes under either zero or nonzero applied field.

For ligand H_2L^4 , two structurally similar mononuclear Dy compounds $[Dy(H_2L^4)_2](NO_3)_3 \cdot 2.5H_2O$ and $[Dy(H_2L^4)(HL^4)](NO_3)_2 \cdot EtOH \cdot 4H_2O$ were assembled with the large coordination pocket accommodating only one Dy ion [10]. Here, Dy^{III} ion was wrapped by two interlocked chelate ligands in both complexes, leading to a distorted geometry of ten-coordinate bicapped square antiprism. However, the major difference between the two complexes is the deprotonation of the amino nitrogen atom (N1) of one of the ligands in the second complex, which results in the different charge distribution and local symmetry around Dy ions of two complexes and thus the different anisotropic tensors, as shown in Fig. 5.9. As a result, although both in-phase and out-of-phase magnetic susceptibility show the frequency-dependent maxima when applied a dc field for both complexes, the deprotonated Dy complex behaves as a weak SMM relative to the other one, which should be attributed to a large shift in the direction of the main magnetic axis.

5.3.2 Isonicotinohydrazone Ligands

In 2008, the application of ligand H_2L^5 (Fig. 5.10) led to the assembly of the Dy_2 complex in Fig. 5.11, where a structural motif similar to that in Fig. 5.3b is observed with Dy-O-Dy angles of 106.418° , but the phenoxido group plays a linking role between two Dy centers [11]. Importantly, the hula hooplike coordination geometries are kept around Dy centers. Furthermore, a 2D network of the Dy_2 complex was also obtained due to the changes of reaction conditions resulting in the further coordination of pyridyl N atoms to a Dy ion of neighboring complexes. Here, the almost identical ferromagnetic interactions between two Dy centers were observed for the two complexes. Furthermore, their ac susceptibility data reveal the frequency-dependent maximum of out-of-phase signals under zero dc field, signaling the typical SMM behavior but with a small difference in effective barriers (56 and 71 K).

Fig. 5.10 Hydrazone ligands from the reactions of isonicotinohydrazone and different aldehydes



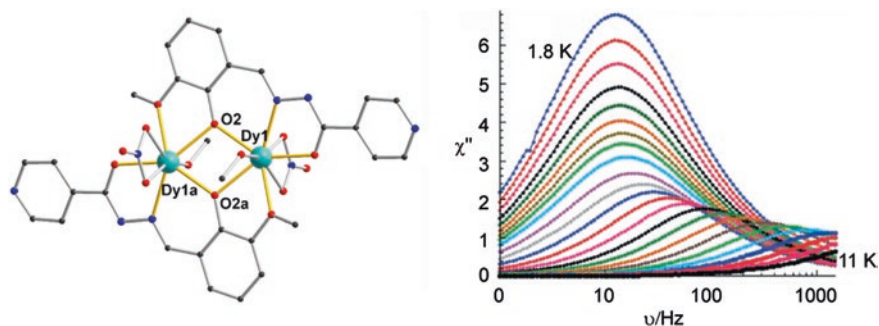


Fig. 5.11 The Dy₂ SMM from ligand H₂L⁵ and its SMM properties. Reproduced from Ref. [11] by permission of John Wiley & Sons Ltd.

In 2012, our group reported the magnetic study of a rare μ_4 -OH-centered square Dy₄ complex (Fig. 5.12), [Dy₄(μ_4 -OH)(HL⁶)₈](ClO₄)₃·2CH₃CN·MeOH·4H₂O, assembled by using ligand H₂L⁶, which was synthesized through substituting *o*-vanillin in H₂L⁵ with salicylaldehyde [12]. Herein, four Dy ions are linked by a central μ_4 -OH in a square fashion with the shortest Dy...Dy distance of 3.536 Å. All nine-coordinate Dy ions are located in the coordination geometry of near mono-capped square antiprism but with some slight differences for them. As a result, the multiple relaxation processes were observed under both zero and 1 kOe static field, as evidenced by the different linear regions in $\ln(\tau)$ versus T^{-1} plots (Fig. 5.12). It is noteworthy that, in high temperature region, the barrier under 1 kOe field is enhanced remarkably up to 92 K, presenting a threefold increase compared with 30 K in zero applied field.

A novel [2 × 2] nanosized Dy₄ metallogrid (Fig. 5.13) was constructed by the supramolecular strategy applying a long bis-acylhydrazone ligand H₄L⁷ (N', N'''E,

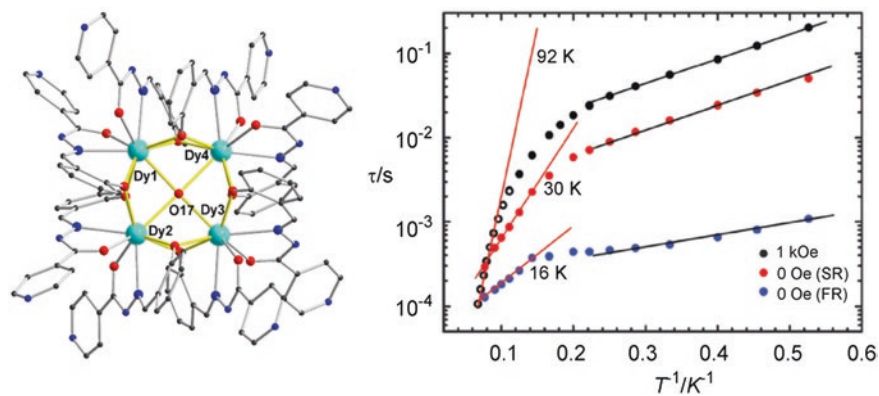


Fig. 5.12 The Dy₄ SMM from ligand H₂L⁶ and its SMM properties. Reproduced from Ref. [12] by permission of The Royal Society of Chemistry

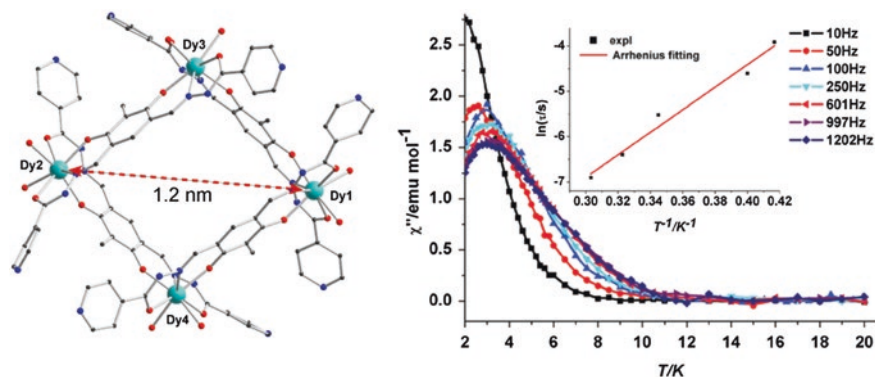


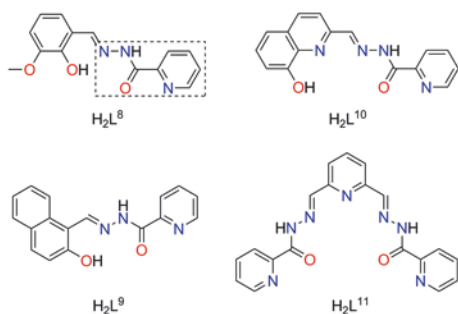
Fig. 5.13 The Dy₄ SMM from ligand H₄L⁷ and its SMM properties. Reproduced from Ref. [13] by permission of The Royal Society of Chemistry

N', N'''E)-N', N'''-((4,6-dihydroxy-5-methyl-1,3-phenylene)bis(methanylylidene)) di(isonicotinohydrazide)), and the large intramolecular Dy–Dy distances are in the range of 8.998–9.064 Å [13]. Each Dy^{III} ion is chelated by two ONO pockets from two ligands almost perpendicular to each other. Four doubly deprotonated ligands H₂L²⁻ arranged in two pairs above and below the mean plane of four metal centers. No obvious out-of-phase signal was observed under zero dc field, but frequency-dependent signals were clearly observed under an external dc field of 1 kOe with no peaks. Further out-of-phase susceptibility measurements under a 2 kOe dc field exhibit frequency-dependent peaks in the range of 2.4–3.3 K, typical of field-induced SMM behavior with an effective barrier of 25 K.

5.3.3 Picolinohydrazone Ligands

For ligand H₂L⁸ in Fig. 5.14, several typical Dy-based complexes have been discussed previously, containing four Dy₂ in Fig. 5.3 and one Dy₆ in Fig. 4.15, where the hula hooplike coordination geometry has proven to be greatly favorable to the

Fig. 5.14 Hydrazone ligands from the reactions of picolinohydrazide and different aldehydes



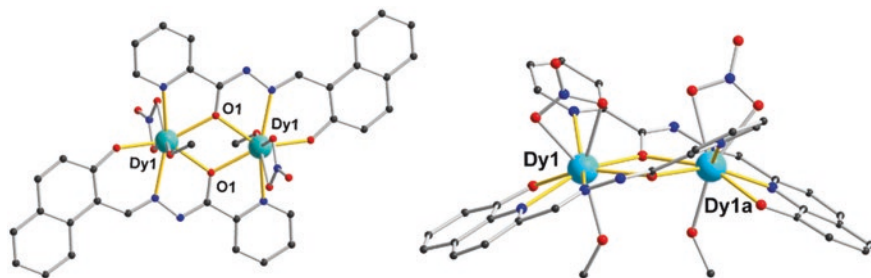


Fig. 5.15 Two Dy₂ complexes from ligands H₂L⁹ and H₂L¹⁰, respectively

occurrence of SMM behavior. Furthermore, a centrosymmetric Dy₂ similar to the one in Fig. 5.3b was constructed using ligand H₂L⁹ [6], and a hula hooplike geometry was also observed around Dy ion (Fig. 5.15 left). As a result, a typical SMM behavior was present in the complex, although its effective barrier ($U_{\text{eff}} = 41$ K) seems to be small compared with that of the Dy₂ in Fig. 5.3b ($U_{\text{eff}} = 69$ K). In contrast, the hydrazone ligand, H₂L¹⁰ in Fig. 5.14, deriving from the reaction of picolinohydrazide and 8-hydroxyquinoline-2-carboxaldehyde was applied to assemble lanthanide SMM, and hence, a distinct Dy₂ complex was obtained [14], as seen in Fig. 5.15 right. Here, two hydrazone ligands incorporate two Dy ions in an unparallel fashion, and thus, hula hooplike geometry is broken, leading to the disappearance of SMM behavior.

In addition, the reaction of dysprosium chloride with hydrazone ligand H₂L⁸ generated a Dy₈ compound with a tub conformation under a different condition from that in the assembly of Dy₆ SMM (Fig. 4.15) [15]. As shown in Fig. 5.16, the complex possesses a [Dy₈(μ_4 -CO₃²⁻)₄(μ_2 -O)₈] core and each carbonato ligand

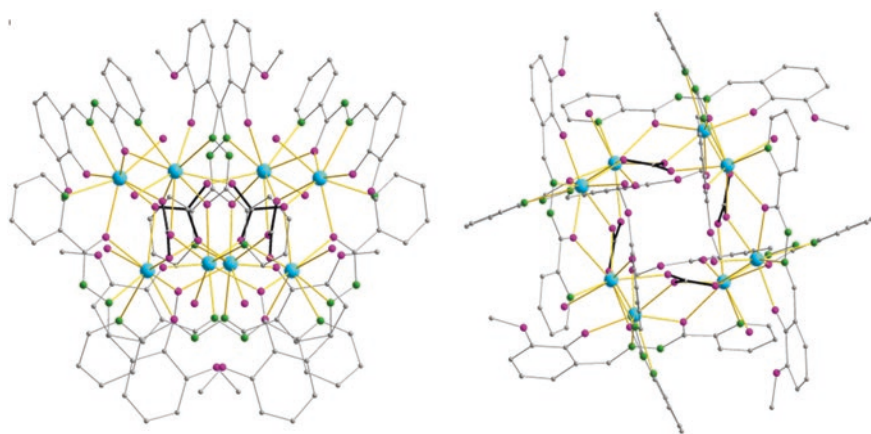


Fig. 5.16 Side view (a) and top view (b) of the molecular structure of the Dy₈ complex from ligand H₂L⁸

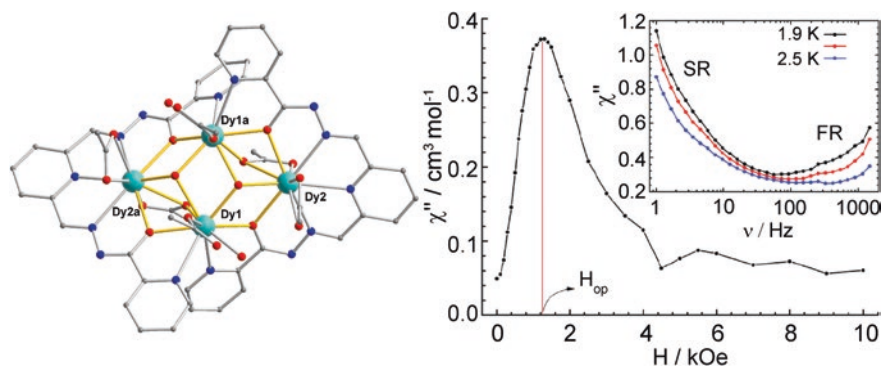


Fig. 5.17 The Dy₄ compound from ligand H₂L¹¹ and its magnetic dynamic properties. Reproduced from Ref. [16] by permission of The Royal Society of Chemistry

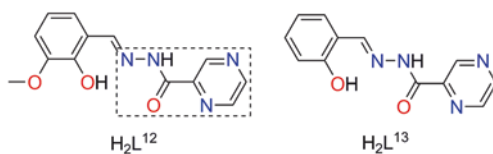
binds to four adjacent metal centers with a chelating and bridging $\mu_4\text{-}\eta^1\text{:}\eta^2\text{:}\eta^1\text{:}\eta^1$ fashion. However, the low-temperature ac susceptibility data only display the increasing χ'' signals without maxima below 15 K under zero dc field.

In 2011, a Dy₄ compound [16] from bis-acylhydrazone ligand H₂L¹¹ reported by our group demonstrates the linking of two edge-sharing Dy₃ triangle units, similar to the planar Dy₄, but with a dihedral of 154.5° between them, as shown in Fig. 5.17. Here although no χ'' ac signal was observed under zero dc field within the available frequency range, the application of a dc field $H = 1200$ Oe allows the presence of two relaxation signals, indicating the possible field-induced multiple relaxation behavior.

5.3.4 Pyrazine Acylhydrazone Ligands

The *o*-vanillin pyrazine acylhydrazone ligand H₂L¹² in Fig. 5.18 exhibits the same arrangement of coordination pockets to picolinohydrazone ligand H₂L⁸, and thus, the application of ligand H₂L¹² resulted in the assembly of some Dy complexes with similar structural motifs to the previous complexes with ligand H₂L⁸, such as Dy₆ complex with triangular prism arrangement [17] and Dy₈ complex with tub conformation [18], which will not be discussed detailedly here in spite of the slight differences of magnetic properties. Besides, two unique “butterfly-shaped” Dy₅ clusters

Fig. 5.18 Hydrazone ligands from the reactions of pyrazine acylhydrazone and different aldehydes



[19], namely $[\text{Dy}_5(\mu_3\text{-OH})_3(\text{L}^{12})_6(\text{H}_2\text{O})_3]\cdot 3\text{MeOH}\cdot 9\text{H}_2\text{O}$ and $[\text{Dy}_5(\mu_3\text{-OH})_3(\text{HL}^{12})_2(\text{L}^{12})_4(\text{MeOH})(\text{H}_2\text{O})_2]\cdot (\text{ClO}_4)_2\cdot 6\text{MeOH}\cdot 4\text{H}_2\text{O}$, have been successfully assembled by the reactions between the ligand and different dysprosium salts. Herein, for the first complex, five Dy^{III} ions are wrapped by a total of six doubly deprotonated acylhydrazone ligands $[\text{L}^{12}]^{2-}$ in their enolate form and further linked together by three $\mu_3\text{-OH}$ groups, resulting in a unique butterfly-shaped motif. The close inspection reveals four versatile and flexible coordination modes in the complex. The structure of the second compound is essentially isomorphous to the first one, with the main differences of two $[\text{HL}^{12}]^-$ ligands in the keto form and one different coordinated solvent molecule, as marked in the molecular structures in Fig. 5.19. Even so, the distinct relaxation dynamics were observed between the two compounds. The first compound presents the multiple slow relaxation processes, for which two effective barriers were given to be 8 and 38 K, while only a single relaxation process was noted for the second compound with an effective barrier of 197 K. These significant disparities are most likely ascribed to the versatile coordination modes of the hydrazone ligand with important keto-enol tautomerism, which alters the strength of the local crystal field and, hence, the nature of easy axes of anisotropic Dy ions.

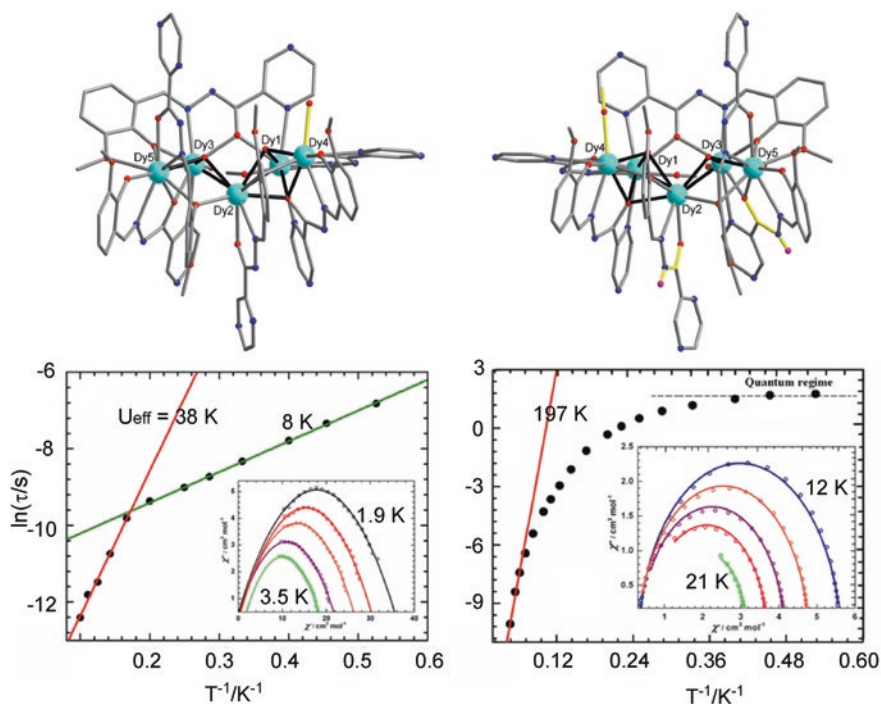


Fig. 5.19 Two Dy_5 compounds from ligand H_2L^{12} and the corresponding SMM properties. Reproduced from Ref. [19] by permission of John Wiley & Sons Ltd.

In addition, the employment of salicylaldehyde pyrazine acylhydrazone ligand H_2L^{13} generated an anomalous Dy_6 compound, $[Dy_6(\mu_3-OH)_3(\mu_3-CO_3)(\mu-Ome)(L^{13})_6(MeOH)_4(H_2O)_2] \cdot 3MeOH \cdot 2H_2O$, which can be seen as an aggregation of three capped triangular Dy_3 motifs with the incorporation of atmospheric CO_2 , and six ligands exhibit three different coordination modes in the enolate forms (Fig. 5.20) [20]. Obviously, the frequency-dependent out-of-phase ac signals are indicative of its typical SMM behavior with a possible multiple relaxation process, and two effective barriers were given to be 5.6 and 38 K.

5.3.5 Hydroxymethyl Picolinohydrazone Ligands

A new rhombus-shaped Dy_4 complex [21] was separated by Chandrasekhar's group using ligand H_3L^{14} in Fig. 5.21, which can be considered as the modification of picolinohydrazone ligand H_2L^{10} by hydroxymethyl group. Two metal centers are chelated by two different coordination pockets from the ligand to form a dinuclear subunit, and a pair of subunits is further coupled to each other by oxido bridges in an antiparallel fashion, resulting in the formation of the Dy_4O_6 core with the four dysprosium ions in the corners of a perfect rhombus (Fig. 5.22). The alternating current (ac) susceptibility measurements revealed two resolved frequency-dependent peaks, indicating the presence of two relaxation processes possibly related to the two distinct spheres of Dy^{III} ions. Therefore, the Arrhenius fitting afforded two effective barriers of 17 and 54 K.

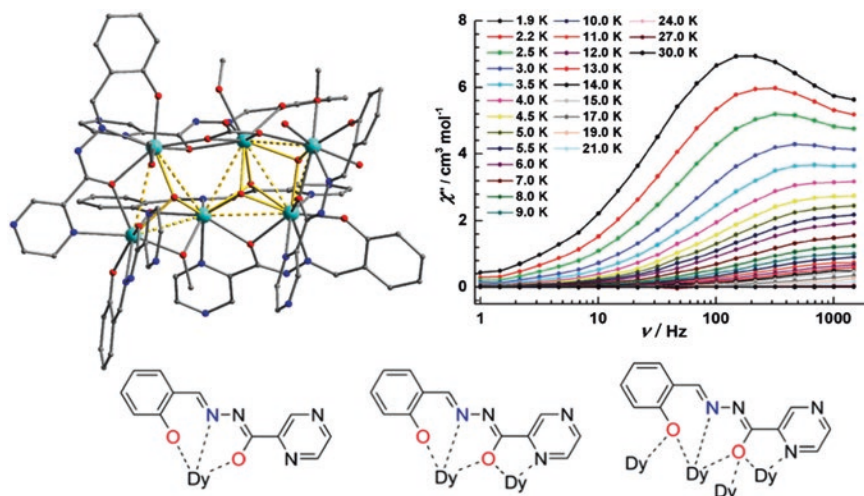


Fig. 5.20 The Dy_6 compound from ligand H_2L^{13} and the corresponding SMM property. Reprinted with the permission from Ref. [20]. Copyright 2011 American Chemical Society

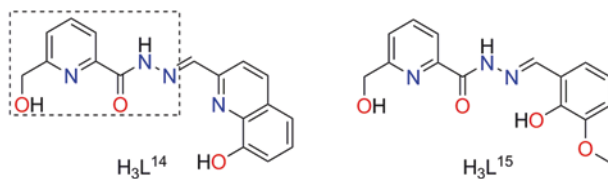


Fig. 5.21 Hydrazone ligands from the reactions of hydroxymethyl picolinohydrazone and different aldehydes

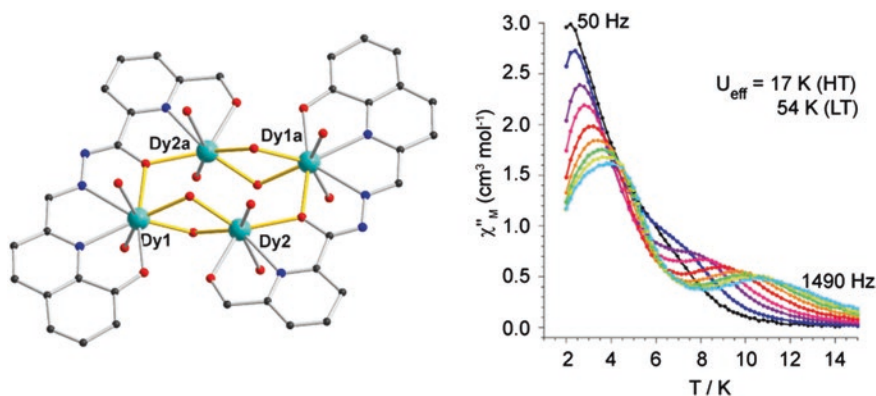


Fig. 5.22 The Dy_4 compound from ligand H_3L^{14} and the corresponding SMM property. Reprinted with the permission from Ref. [21]. Copyright 2013 American Chemical Society

In addition, the Dy_4 and Dy_6 compounds in Fig. 5.23 were obtained by applying hydrazone ligand H_3L^{15} (Fig. 5.21), where *o*-vanillin moiety substitutes the 8-hydroxyquinoline moiety in H_3L^{14} , thus adding another coordination pocket. The Dy_4 complex [22] incorporates two dimeric subunits, which are further linked together by two ligands resulting from the additional $-CH_2OH$ binding site and the C–C rotation. Herein, the asymmetric unit contains two different types of Dy^{III} ions with $[NO_7]$ coordination environment for eight-coordinate Dy^{III} ion and $[O_6N_3]$ for nine-coordinate Dy^{III} ion. Therefore, two series of out-of-phase ac peaks are observed under a 1000 Oe dc field, which is a characteristic of SMM behavior with multiple-step relaxation. Two effective barriers were extracted to be 26 and 63 K.

For the Dy_6 compound [23], $[Dy_6(L^{15})_2(\mu_3-OH)_4][MeOH]_2[H_2O]_6[Cl]_4 \cdot 8H_2O \cdot 4CH_3OH$, six Dy^{III} ions are tightly held together by two fully deprotonated nonadentate ligands $[L^{15}]^{3-}$ in a $\mu_4-\eta^2-\eta^1-\eta^2-\eta^1-\eta^2-\eta^1$ fashion and four μ_3-OH groups to form the Dy_6O_{12} core consisting of two triangular motifs with an edge-to-edge arrangement. Finally, two $[HL^{15}]^{2-}$ ligands function in a hexadentate $\mu_2-\eta^1-\eta^1-\eta^2-\eta^1-\eta^1$ binding mode to hold two terminal Dy^{III} ions. Analysis

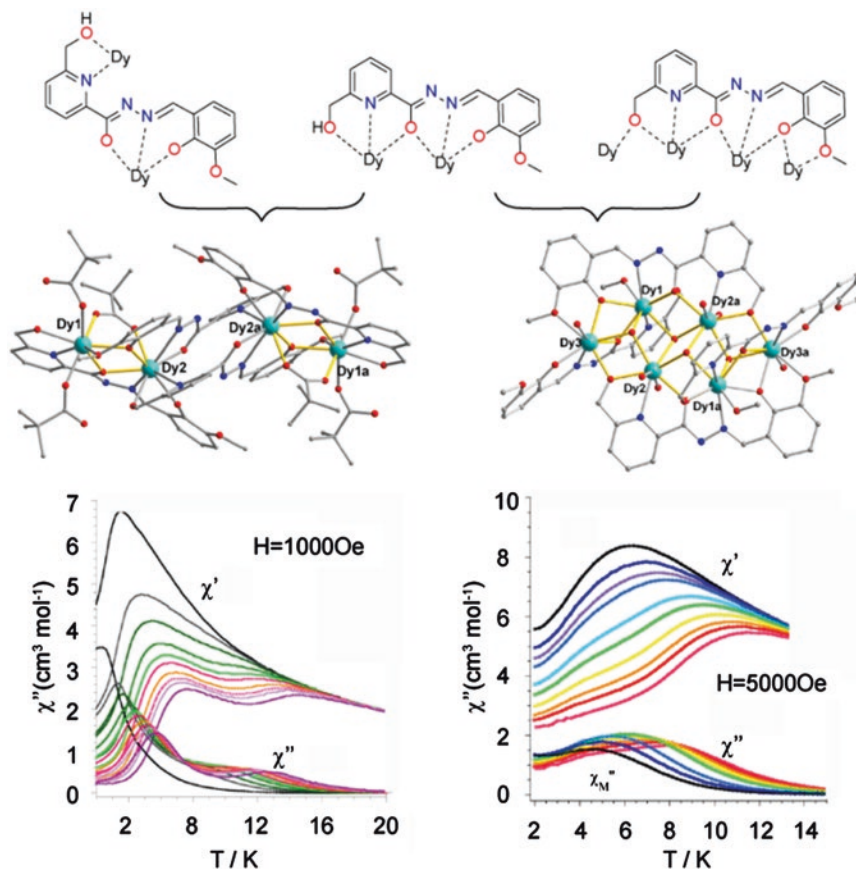


Fig. 5.23 The Dy₄ and Dy₆ compounds from ligand H₃L¹⁵ and the corresponding SMM properties. Reprinted with the permission from Refs. [22, 23]. Copyright 2013 and 2014 American Chemical Society

of the ac susceptibility data reveals that the Dy₆ complex features SMM behavior under a 1000 Oe external field with an effective energy barrier of 46 K and $\tau_0 = 2.85 \times 10^{-7}$ s.

5.3.6 *o*-Vanilloyl Hydrazone Ligands

The Dy₄ SMM (Fig. 5.4) from ligand H₃L¹⁶ and two Dy₃ SMMs (Fig. 4.4) from ligands H₃L¹⁷ and H₂L¹⁸ have been described previously containing their structural and magnetic properties, and subsequently, we will give a brief introduction to the Dy-based SMMs from ligands L¹⁹ to L²¹.

For ligand H_2L^{19} in Fig. 5.24, an unprecedented Y-shaped Dy_4 compound was isolated in 2014 by the assembly of the versatile ligand with $Dy(ClO_4)_3 \cdot 6H_2O$ [24]. As shown in Fig. 5.25, four Dy^{III} ions are surrounded by four deprotonated H_2L^{19} ligands in their coordination modes A, B, C, and D (Fig. 5.25) to form the Y-shaped metal topology, which can be regarded as two μ_3 -hydroxo bridged triangle (Dy_2 , Dy_3 and Dy_4), connected to another metal center Dy_1 through the alkoxido and phenoxido atoms from three ligands. Here, the versatility of the mixed-donor hydrazone ligands appears to play a critical role in the formation of the metal cluster. The further magnetic investigations for relaxation dynamics revealed that the novel Dy_4 complex behaves as a typical SMM, showing a multiple relaxation process with two effective barriers of 8 and 84 K. Such a relaxation process is probably attributed to the presence of different Dy centers within the molecule.

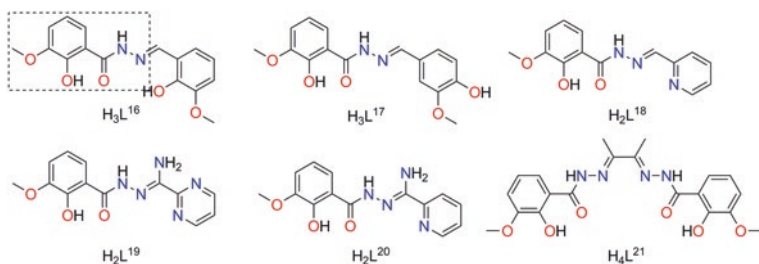


Fig. 5.24 Hydrazone ligands from *o*-vanilloyl hydrazide

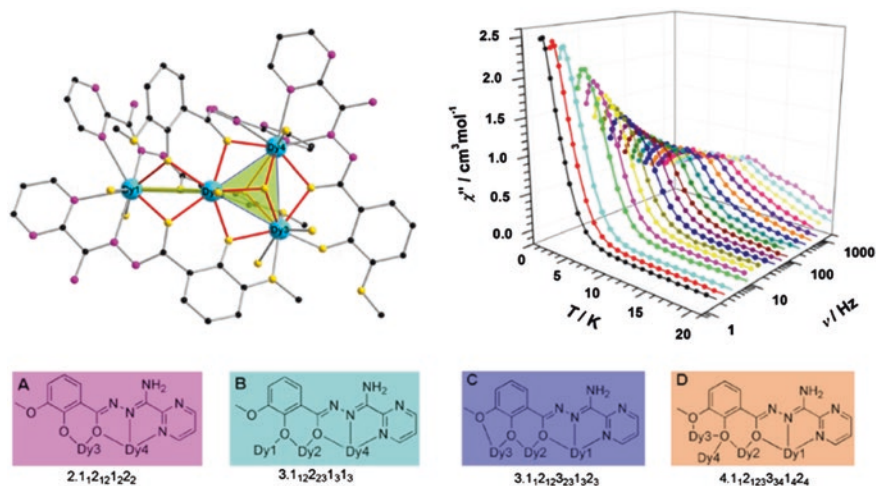


Fig. 5.25 The Dy_4 compound from ligand H_2L^{19} and the corresponding SMM property. Reproduced from Ref. [24] by permission of The Royal Society of Chemistry

In addition, the ligand H_2L^{20} with a slight difference from ligand H_2L^{19} was also applied to construct lanthanide SMM, but a distinct cluster, $[Dy_6(L^{20})_4(HL^{20})_4(CO_3)_2(SCN)_2] \cdot 6CH_3CN \cdot 8CH_3OH \cdot 2H_2O$ (Fig. 5.26), was separated [25]. Here, six Dy^{III} ions are distributed into two well-differentiated and symmetry-related groups of Dy_3 moieties, behaving as a Dy_3 molecular cluster pair (MCP). Each Dy_3 motif is enveloped by three H_2L^{20} ligands with distinct coordinate modes (Fig. 5.26a–c). Further, both Dy_3 fragments were linked in a long distance by two other H_{2apovh} ligands, which adopt an anticongformation with two types of pockets (d in Fig. 5.26). Thus, the coordination versatility of the mixed-donor hydrazone ligands is exhibited perfectly. Alternating current (ac) susceptibility measurements reveal the appearance of an out-of-phase χ'' signal below 15 K. An effective relaxation barrier of $U_{eff} = 29$ K can be extracted with $\tau_0 = 1.2 \times 10^{-6}$ s. In addition, the application of a field of 700 Oe has no practical effect on the dynamics within the frequency window. Such SMM-like MCP will serve as the basis for the investigation of related quantum superpositions of their spin wave functions, with the aim to explore their potential as two-qubit quantum gates.

The application of a bis-acylhydrazone ligand H_4L^{21} resulted in the construction of the first Dy_4 grid exhibiting slow magnetic relaxation [26]. As shown in Fig. 5.27, the ligands adopt a $\mu_3-\eta^4:\eta^2:\eta^1$ fashion in one side to bridge three Dy centers through their hydrazone-O and phenoxide-O atoms, and thus, the self-assembly of four Dy ions and four ligands leads to the formation of a Dy_4 unit with windmill-type motif. No ac signal (χ'') was observed below 20 K under zero dc field, suggesting the absence of a SMM behavior. However, applying a 900 Oe dc field induces the occurrence of out-of-phase ac signals with frequency-dependent peaks, indicating the field-induced SMM behavior.

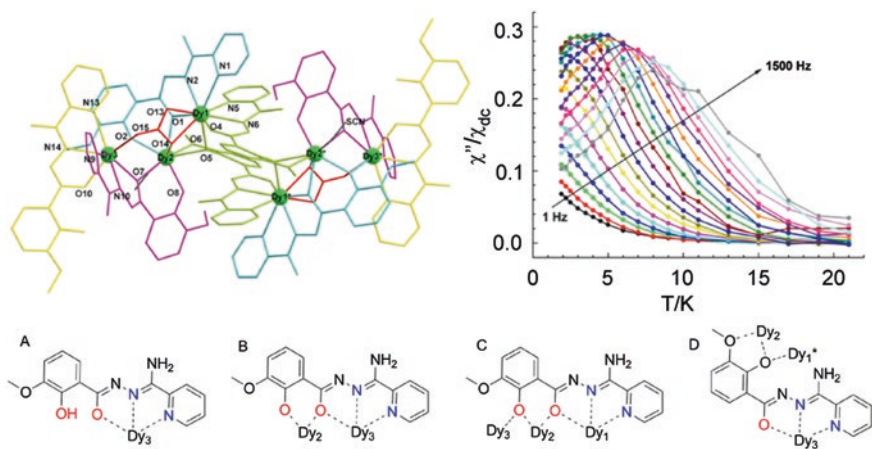


Fig. 5.26 The Dy_6 compound from ligand H_2L^{20} and the corresponding SMM property. Reproduced from Ref. [25] by permission of The Royal Society of Chemistry

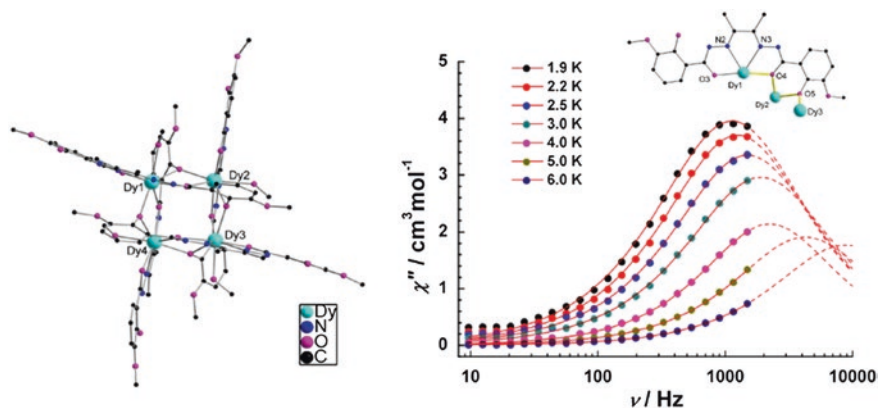


Fig. 5.27 The Dy₄ compound from ligand H₄L²¹ and the corresponding SMM property. Reproduced from Ref. [26] by permission of The Royal Society of Chemistry

5.3.7 Hydrazone–Oxime Ligands

In order to obtain better lanthanide SMMs, two hydrazone–oxime ligands (Fig. 5.28) incorporating three functional ligand components, i.e., aldehyde, hydrazide, and oxime moieties have been successfully applied to assemble Dy-based clusters, which exhibit some novel structural motifs, such as the expanded fused triangular and cyclooctadiene-like conformations. In fact, such ligands have proven to be very suitable for the assembly of polynuclear metal clusters in transition metal compounds, such as the assembly of polynuclear Mn clusters [27].

For ligand H₃L²², two Dy-based complexes have been reported by Thompson [28], one being mononuclear with formula of [Dy(H₂L²²)(NO₃)₂(DMF)₂](DMF) and the other being hexanuclear with [Dy₆(H₂L²²)₆(O)(CH₃COO)₆](HNEt₃)(H₂O)₁₆(CH₃OH)₁₄. Their structures were demonstrated in Fig. 5.29. In mononuclear compound, the nine-coordinate Dy center exhibits a distorted puckered pentagonal array of donor atoms from the ligand and two coordinated DMF molecules at equatorial position. The obvious field-induced SMM behavior was observed with an effective barrier of 36 K in the complex. Remarkably, the Dy₆ complex presents a fascinating structural motif (Fig. 5.29), where six Dy ions are arranged in a flat, expanded fused triangular conformation. Here, six hydrazone ligands

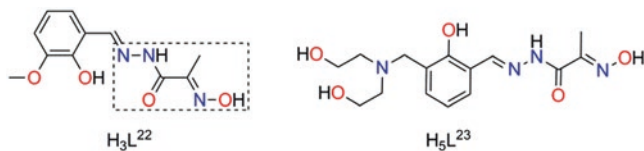


Fig. 5.28 Hydrazone ligands from the reactions of oxime-based hydrazide and different aldehydes

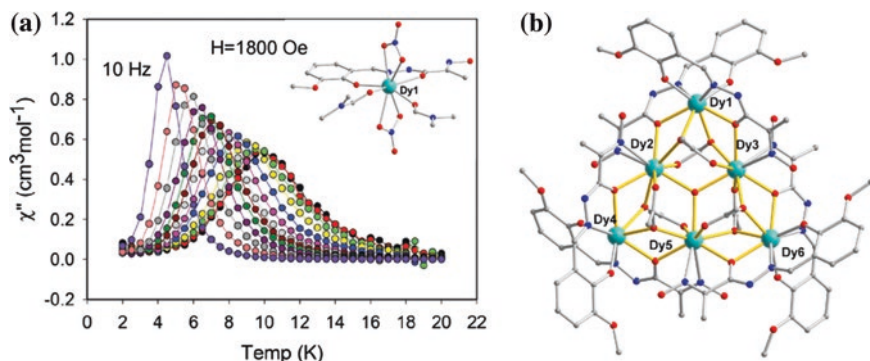


Fig. 5.29 The Dy₁ and Dy₆ compounds from ligand H₃L²² and the corresponding SMM properties. Reproduced from Ref. [28] by permission of The Royal Society of Chemistry

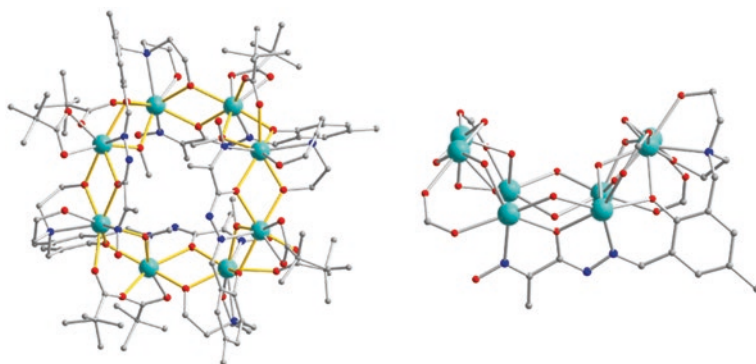


Fig. 5.30 The Dy₈ compounds from ligand H₅L²³

surround the Dy₆ metal core around the periphery, and all hydrazone-O atoms provide a bridging role. Furthermore, the corner Dy^{III} ions are eight-coordinate N₂O₆ centers and the side sites have N₂O₇ coordination spheres. However, such a compound only displays a weak frequency dependence of ac signals without χ'' peaks above 2 K.

An unprecedented macrocyclic Dy₈ complex [29] has been isolated using the new multidentate ligand H₅L²³ along with pivalic acid, as shown in Fig. 5.30. Here, ligand H₅L²³ features two unsymmetrically disposed arms with one arm of a diethanolamine group and the other of a hydrazone built by the condensation reaction about 2-hydroxyiminopropanehydrazide. Four triply deprotonated [H₂L²³]³⁻ ligands bridged eight Dy^{III} ions and arranged on the outer surface of the octanuclear wheel, creating a 16-membered macrocyclic central core. Interestingly, all Dy^{III} ions are distributed on the eight vertices of an octagon adopting a puckered configuration, which can be described as a cyclooctadiene ring core. Each [H₂L²³]³⁻ ligand simultaneously coordinated to four Dy^{III}

ions in a $\mu_4\text{-}\eta^1:\eta^2:\eta^1:\eta^2:\eta^1:\eta^1:\eta^2$ binding mode. No SMM behavior was observed under zero applied field for the complex, but the application of a 1000 Oe dc field allowed the observation of slow relaxation of magnetization above 2 K.

5.3.8 Hydrazone Ligands from Bis-Acylhydrazide

The extension of mono-hydrazide to symmetric bis-hydrazide can result in the production of bis-hydrazone ligand, which creates two symmetrically appended hydrazone fragments and thus more extended coordination ability [30, 31]. Such polytopic ligands have proven very effective in producing large numbers of grid-like compounds with first-row transition metal ions. Typically, ligand H_2L^{24} in Fig. 5.31 as a linear tritopic entity formed self-assembled square [3×3] compounds with transition metal ions (Mn^{II} , Cu^{II} , Zn^{II} et al.) in high yield, due to an exact match between the coordination requirements of the nine six-coordinate metal ions and the available complement of donor sites provided by the six ligands [32]. Therefore, such a directed and programmed approach is also expected to apply in the assembly of lanthanide grid-like complexes, but only few examples are successful to date, as a possible result of the variable charge number and ionic radii. The ligands used in assembly of lanthanide SMMs are listed in Fig. 5.31.

The application of ligand H_2L^{24} led to the production of a linear Dy_3 compound [33] (Fig. 5.32a), where two ligands bind the three Dy^{III} ions in the same relative tridentate coordination pockets in each ligand; thus, the central Dy ions are bridged to the outer Dy ions through $\mu\text{-O}$ hydrazone bridges with bridge angles in the range $116.55(9)^\circ\text{--}117.78(9)^\circ$. The putative grids were not formed

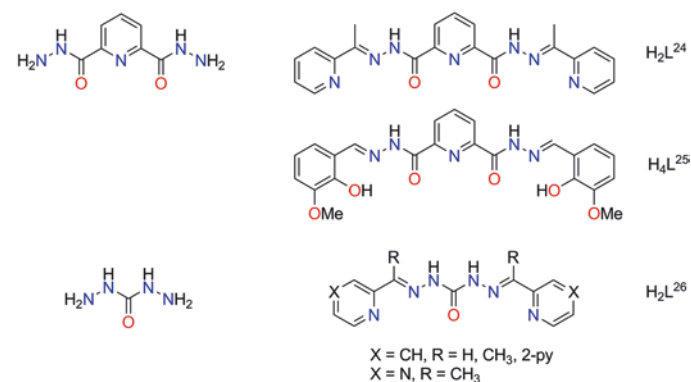


Fig. 5.31 Hydrazone ligands from bis-acylhydrazide

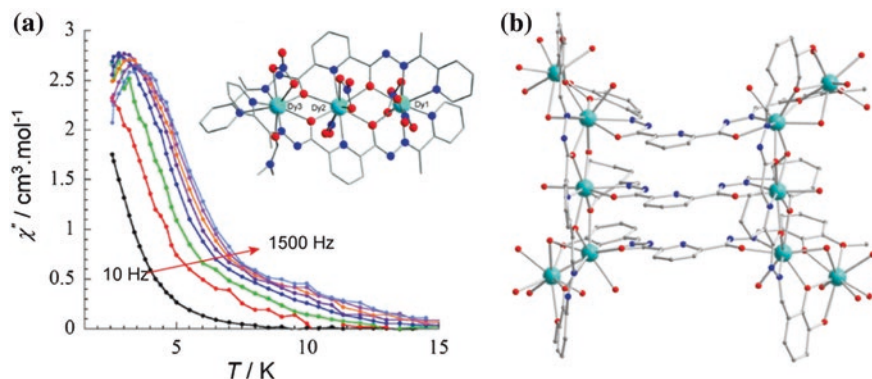


Fig. 5.32 The Dy₃ and Dy₁₀ compounds from ligand H₂L²⁴ and H₄L²⁵, respectively, and the corresponding SMM properties. **a** Reprinted with the permission from Ref. [33]. Copyright 2011 American Chemical Society

probably due to the fact that the larger size results in the protrusion of the Dy ions from their respective ligand sites. Ac magnetic measurements revealed a frequency-dependent ac signal but without full peaks below 10 K under zero dc field for the complex. Furthermore, the application of an 1800 Oe dc field allowed the observation of χ'' peaks, and an effective barrier was given to be 14 K. Remarkably, a Dy₁₀ compound with a double rectangular grid-like structure (Fig. 5.32b) was constructed through applying ligand H₄L²⁵ containing *o*-vanillin moieties [34]. Here, two Dy₅ subunits, where five Dy ions occupy all coordination pockets within a single ligand, are further linked by three terminally bound ligands in a *syn* conformation. Although the ideal [3 × 3] grid-like complex has not been obtained, such an example of polynuclear lanthanide complex suggests a great promise in constructing lanthanide grid-like complex using the above ligands.

To date, the most successful example in grid-like lanthanide SMM should be the assembly of [2 × 2] Dy₄ square grids using ditopic carbohydrazone ligand H₂L²⁶ in Fig. 5.31. In 2012, two similar Dy₄ square grids were constructed firstly with some important differences being the absence or presence of the central μ_4 -O atom and the bridging atoms at each side [35]. In the Dy₄ grid in Fig. 5.33b, four Dy centers are fixed by a central μ_4 -O atom with Dy-O-Dy angles in the range 88.9–91.4°, indicating that the Dy₄(μ_4 -O) subunit is almost planar. The further structural comparison between two complexes reveals that the μ -OH bridge at each edge in Fig. 5.33a is substituted by μ -N₃⁻ with the Dy-N₃-Dy angles in the range of 99.5–99.3° in Fig. 5.33b. Therefore, such different structural features promote their distinct SMM properties. Herein, no SMM behavior was detected in the Dy₄ grid in Fig. 5.33a, while the one in Fig. 5.33b exhibits two relaxation processes with $U_{\text{eff}} = 51$ K and 91 K in the absence of an external field and one relaxation process with $U_{\text{eff}} = 270$ K in the presence of a 1600 Oe optimum field (Fig. 5.33c).

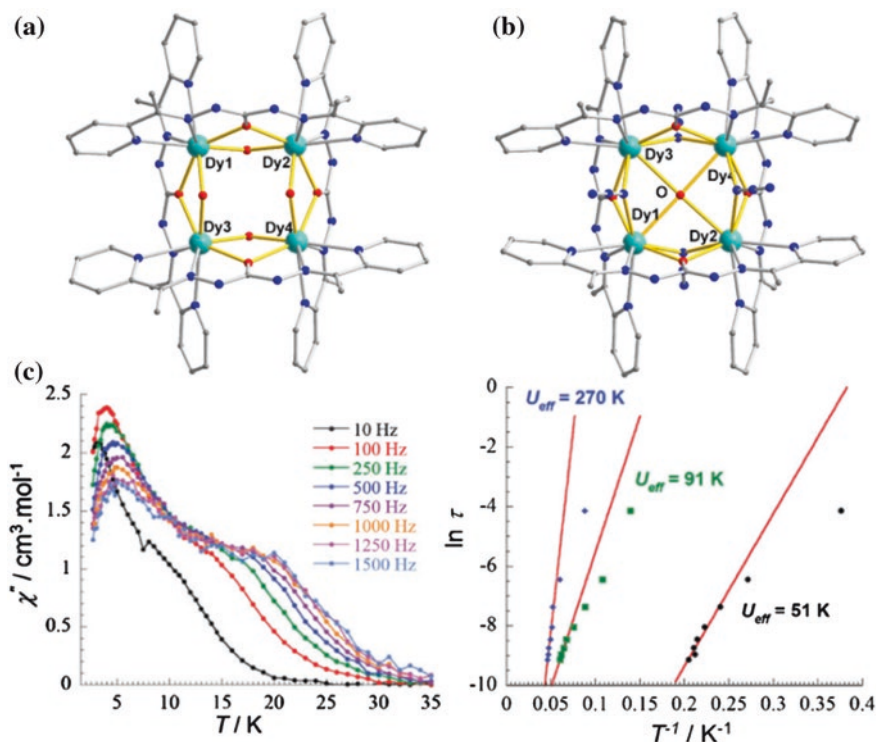


Fig. 5.33 Two Dy₄ compounds from ligand H₂L²⁶ and the SMM properties of the one in (b). Reproduced from Ref. [35] by permission of The Royal Society of Chemistry

In addition, the employment of a terephthalohydrazone ligand H₄L²⁷ effectively promoted the connecting of two mononuclear lanthanide SMMs based on benzhydrazone ligands [36], which were demonstrated in Fig. 5.34. Herein, the mononuclear Dy SMM resembles the one in Fig. 5.29a and exhibits an effective barrier of 34 K under a dc field of 1800 Oe. Furthermore, the connecting of two subunits appears to exert a small influence on their SMM behavior, which is probably due to the large separation between the two Dy ions. The effective barrier of 42 K under 1800 Oe exhibits a slight increase compared with that of the mononuclear complex. Therefore, such an example presents a useful methodology to promote formation of larger molecules while retaining their magnetic properties via controlled ligand modification.

In conclusion, the assembly of the rigid mixed-donor hydrazone ligands with lanthanide salts under different conditions turns out to be an effective way to discover new lanthanide SMMs and to explore the origin of complicated magnetic dynamics. In future, some novel hydrazone ligands, especially the modifications to original ligands, should be designed to rationally improve the magnetic properties compared to the existing SMM and better understand the relation between the electronic structure and relaxation process.

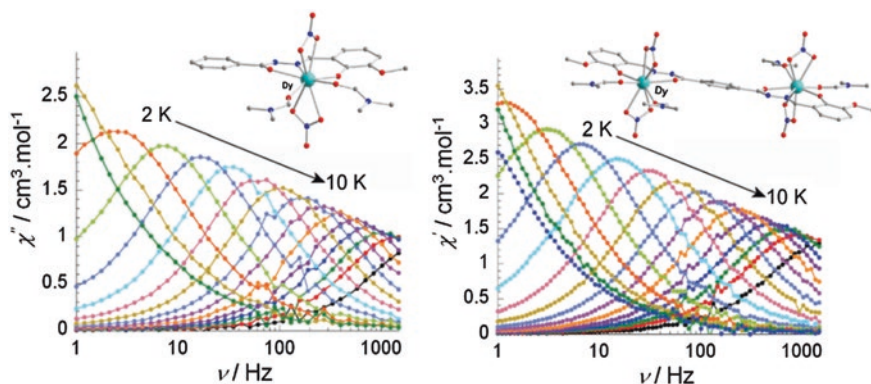


Fig. 5.34 The Dy₁ and Dy₂ compounds from ligand H₂L² and H₄L²⁷, respectively, and the corresponding SMM properties. Reproduced from Ref. [36] by permission of The Royal Society of Chemistry

References

- Zhang P, Zhang L, Tang J (2013) Hydrazone-based dysprosium single molecule magnets. *Curr Inorg Chem* 3(2):101–111. doi:[10.2174/1877944111303020005](https://doi.org/10.2174/1877944111303020005)
- Guo Y-N, Chen X-H, Xue S, Tang J (2011) Modulating magnetic dynamics of three Dy₂ complexes through keto-enol tautomerism of the *o*-vanillin picolinoylhydrazone ligand. *Inorg Chem* 50:9705–9713. doi:[10.1021/ic2014978](https://doi.org/10.1021/ic2014978)
- Guo Y-N, Xu G-F, Wernsdorfer W, Ungur L, Guo Y, Tang J, Zhang H-J, Chibotaru LF, Powell AK (2011) Strong axiality and ising exchange interaction suppress zero-field tunneling of magnetization of an asymmetric Dy₂ single-molecule magnet. *J Am Chem Soc* 133(31):11948–11951. doi:[10.1021/ja205035g](https://doi.org/10.1021/ja205035g)
- Guo Y-N, Xu G-F, Gamez P, Zhao L, Lin S-Y, Deng R, Tang J, Zhang H-J (2010) Two-step relaxation in a linear tetranuclear dysprosium(III) aggregate showing single-molecule magnet behavior. *J Am Chem Soc* 132(25):8538–8539. doi:[10.1021/ja103018m](https://doi.org/10.1021/ja103018m)
- Guo Y-N, Xu G-F, Guo Y, Tang J (2011) Relaxation dynamics of dysprosium(III) single molecule magnets. *Dalton Trans* 40(39):9953–9963. doi:[10.1039/C1DT10474H](https://doi.org/10.1039/C1DT10474H)
- Zou L, Zhao L, Chen P, Guo Y-N, Guo Y, Li Y-H, Tang J (2012) Phenoxido and alkoxido-bridged dinuclear dysprosium complexes showing single-molecule magnet behaviour. *Dalton Trans* 41(10):2966–2971. doi:[10.1039/c2dt12235a](https://doi.org/10.1039/c2dt12235a)
- Hutchings A-J, Habib F, Holmberg RJ, Korobkov I, Murugesu M (2014) Structural rearrangement through lanthanide contraction in dinuclear complexes. *Inorg Chem* 53(4):2102–2112. doi:[10.1021/ic402682r](https://doi.org/10.1021/ic402682r)
- Lin S-Y, Xu G-F, Zhao L, Guo Y-N, Guo Y, Tang J (2011) Observation of slow magnetic relaxation in triple-stranded lanthanide helicates. *Dalton Trans* 40(32):8213–8217. doi:[10.1039/c1dt10729a](https://doi.org/10.1039/c1dt10729a)
- Lin S-Y, Zhao L, Guo Y-N, Zhang P, Guo Y, Tang J (2012) Two new Dy₃ triangles with trinuclear circular helicates and their single-molecule magnet behavior. *Inorg Chem*. doi:[10.1021/ic300371m](https://doi.org/10.1021/ic300371m)
- Batchelor LJ, Cimatti I, Guillot R, Tuna F, Wernsdorfer W, Ungur L, Chibotaru LF, Campbell VE, Mallah T (2014) Chemical tuning of the magnetic relaxation in dysprosium(III) mononuclear complexes. *Dalton Trans* 43(32):12146–12149. doi:[10.1039/c4dt00846d](https://doi.org/10.1039/c4dt00846d)

11. Lin P-H, Burchell TJ, Cl rac R, Murugesu M (2008) Dinuclear dysprosium(III) single-molecule magnets with a large anisotropic barrier. *Angew Chem Int Ed* 47(46):8848–8851. doi:[10.1002/anie.200802966](https://doi.org/10.1002/anie.200802966)
12. Xue S, Zhao L, Guo Y-N, Chen X-H, Tang J (2012) Field enhanced thermally activated mechanism in a square Dy₄ aggregate. *Chem Commun* 48(56):7031–7033. doi:[10.1039/C2CC31864D](https://doi.org/10.1039/C2CC31864D)
13. Wu S-Q, Xie Q-W, An G-Y, Chen X, Liu C-M, Cui A-L, Kou H-Z (2013) Supramolecular lanthanide metallogrids exhibiting field-induced single-ion magnetic behavior. *Dalton Trans* 42(13):4369–4372. doi:[10.1039/c3dt50265a](https://doi.org/10.1039/c3dt50265a)
14. Zhang P, Zhang L, Lin S-Y, Xue S, Tang J (2013) Modulating magnetic dynamics of Dy₂ system through the coordination geometry and magnetic interaction. *Inorg Chem* 52(8):4587–4592. doi:[10.1021/ic400150f](https://doi.org/10.1021/ic400150f)
15. Guo Y-N, Chen X-H, Xue S, Tang J (2012) Molecular assembly and magnetic dynamics of two novel Dy₆ and Dy₈ aggregates. *Inorg Chem* 51(7):4035–4042. doi:[10.1021/ic202170z](https://doi.org/10.1021/ic202170z)
16. Xue S, Zhao L, Guo Y-N, Deng R, Guo Y, Tang J (2011) A series of tetranuclear lanthanide complexes comprising two edge-sharing triangular units with field-induced slow magnetic relaxation for Dy₄ species. *Dalton Trans* 40(33):8347–8352. doi:[10.1039/c1dt10654f](https://doi.org/10.1039/c1dt10654f)
17. Tian H, Wang M, Zhao L, Guo Y-N, Guo Y, Tang J, Liu Z (2012) A discrete dysprosium trigonal prism showing single-molecule magnet behaviour. *Chem Eur J* 18(2):442–445. doi:[10.1002/chem.201102547](https://doi.org/10.1002/chem.201102547)
18. Tian H, Zhao L, Guo Y-N, Guo Y, Tang J, Liu Z (2012) Quadruple-CO₃²⁻ bridged octanuclear dysprosium(III) compound showing single-molecule magnet behaviour. *Chem Commun* 48(5):708–710. doi:[10.1039/C1CC15814G](https://doi.org/10.1039/C1CC15814G)
19. Tian H, Zhao L, Lin H, Tang J, Li G (2013) Butterfly-shaped pentanuclear dysprosium single-molecule magnets. *Chem Eur J* 19(39):13235–13241. doi:[10.1002/chem.201301313](https://doi.org/10.1002/chem.201301313)
20. Tian H, Guo Y-N, Zhao L, Tang J, Liu Z (2011) Hexanuclear dysprosium(III) compound incorporating vertex- and edge-sharing Dy₃ triangles exhibiting single-molecule-magnet behavior. *Inorg Chem* 50(18):8688–8690. doi:[10.1021/ic201121p](https://doi.org/10.1021/ic201121p)
21. Chandrasekhar V, Hossain S, Das S, Biswas S, Sutter J-P (2013) Rhombus-shaped tetranuclear [Ln₄] complexes [Ln = Dy(III) and Ho(III)]: synthesis, structure, and SMM behavior. *Inorg Chem* 52(11):6346–6353. doi:[10.1021/ic302848k](https://doi.org/10.1021/ic302848k)
22. Chandrasekhar V, Das S, Dey A, Hossain S, Sutter J-P (2013) Tetranuclear lanthanide(III) complexes containing dimeric subunits: single-molecule magnet behavior for the Dy₄ analogue. *Inorg Chem* 52(20):11956–11965. doi:[10.1021/ic401652f](https://doi.org/10.1021/ic401652f)
23. Das S, Hossain S, Dey A, Biswas S, Sutter J-P, Chandrasekhar V (2014) Molecular magnets based on homometallic hexanuclear lanthanide(III) complexes. *Inorg Chem* 53(10):5020–5028. doi:[10.1021/ic500052v](https://doi.org/10.1021/ic500052v)
24. Xue S, Guo Y-N, Zhao L, Zhang P, Tang J (2014) Unique Y-shaped lanthanide aggregates and single-molecule magnet behaviour for the Dy₄ analogue. *Dalton Trans* 43(4):1564–1570. doi:[10.1039/c3dt52444b](https://doi.org/10.1039/c3dt52444b)
25. Xue S, Zhao L, Guo Y-N, Zhang P, Tang J (2012) The use of a versatile *o*-vanilloyl hydrazone ligand to prepare SMM-like Dy₃ molecular cluster pair. *Chem Commun* 48(71):8946–8948. doi:[10.1039/C2CC34737G](https://doi.org/10.1039/C2CC34737G)
26. Xue S, Zhao L, Guo Y-N, Tang J (2012) A novel windmill-type Dy^{III} [2 × 2] grid exhibiting slow magnetic relaxation. *Dalton Trans* 41:351–353. doi:[10.1039/c1dt11883h](https://doi.org/10.1039/c1dt11883h)
27. Anwar MU, Dawe LN, Thompson LK (2011) Approaching polymetallic ‘assemblies of assemblies’ using ligands with multiple functionality—novel Mn₁₀M₂ (M = alkali metal) chains with ‘ionophoric’ end cavities. *Dalton Trans* 40(32):8079–8082. doi:[10.1039/c1dt11067e](https://doi.org/10.1039/c1dt11067e)
28. Anwar MU, Dawe LN, Tandon SS, Bunge SD, Thompson LK (2013) Polynuclear lanthanide (Ln) complexes of a tri-functional hydrazone ligand—mononuclear (Dy), dinuclear (Yb, Tm), tetranuclear (Gd), and hexanuclear (Gd, Dy, Tb) examples. *Dalton Trans* 42(21):7781–7794. doi:[10.1039/c3dt32732a](https://doi.org/10.1039/c3dt32732a)

29. Chandrasekhar V, Bag P, Colacio E (2013) Octanuclear $\{\text{Ln}(\text{III})_8\}$ (Ln = Gd, Tb, Dy, Ho) macrocyclic complexes in a cyclooctadiene-like conformation: manifestation of slow relaxation of magnetization in the Dy(III) derivative. *Inorg Chem* 52(8):4562–4570. doi:[10.1021/ic400091j](https://doi.org/10.1021/ic400091j)
30. Dawe LN, Shuvaev KV, Thompson LK (2009) Polytopic ligand directed self-assembly-polymetallic $[n \times n]$ grids versus non-grid oligomers. *Chem Soc Rev* 38(8):2334–2359. doi:[10.1039/b807219c](https://doi.org/10.1039/b807219c)
31. Dawe LN, Abedin TSM, Kelly TL, Thompson LK, Miller DO, Zhao L, Wilson C, Leech MA, Howard JAK (2006) Self-assembled polymetallic square grids ($[2 \times 2]$ M₄, $[3 \times 3]$ M₉) and trigonal bipyramidal clusters (M₅)-structural and magnetic properties. *J Mater Chem* 16(26):2645–2659. doi:[10.1039/B602595A](https://doi.org/10.1039/B602595A)
32. Dawe LN, Abedin TSM, Thompson LK (2008) Ligand directed self-assembly of polymetallic $[n \times n]$ grids: rational routes to large functional molecular subunits? *Dalton Trans* 13:1661–1675. doi:[10.1039/B716114J](https://doi.org/10.1039/B716114J)
33. Anwar MU, Tandon SS, Dawe LN, Habib F, Murugesu M, Thompson LK (2011) Lanthanide complexes of tritopic bis(hydrazone) ligands: single-molecule magnet behavior in a linear Dy₃^{III} complex. *Inorg Chem* 51 (2):1028–1034. doi:[10.1021/ic2022006](https://doi.org/10.1021/ic2022006)
34. Adhikary A, Jena HS, Khatua S, Konar S (2014) Synthesis and characterization of two discrete Ln₁₀ nanoscopic ladder-type cages: magnetic studies reveal a significant cryogenic magnetocaloric effect and slow magnetic relaxation. *Chem Asian J* 9(4):1083–1090. doi:[10.1002/asia.201301619](https://doi.org/10.1002/asia.201301619)
35. Anwar MU, Thompson LK, Dawe LN, Habib F, Murugesu M (2012) Predictable self-assembled $[2 \times 2]$ Ln(III)₄ square grids (Ln = Dy, Tb)-SMM behaviour in a new lanthanide cluster motif. *Chem Commun* 48(38):4576–4578. doi:[10.1039/c2cc17546k](https://doi.org/10.1039/c2cc17546k)
36. Lin P-H, Korobkov I, Burchell TJ, Murugesu M (2012) Connecting single-ion magnets through ligand dimerisation. *Dalton Trans* 41(44):13649–13655. doi:[10.1039/c2dt31226c](https://doi.org/10.1039/c2dt31226c)

Chapter 6

Conclusion and Perspective

Abstract As a new type of lanthanide SMMs, the novel endohedral metallofullerene (EMF) SMMs are introduced in the first part of this chapter. Furthermore, a survey of the organization of SMMs on surfaces and molecular spintronics is provided with an emphasis focusing on the applications of double-decker phthalocyanine lanthanide SMMs in spintronics. Herein, [LnPc₂] SMMs were not only used to fabricate three-terminal spin transistor, but its combination with carbon-based nanostructures led to the successful design of supramolecular spin valve. Remarkably, the nuclear spin of Tb atom embedded in [TbPc₂] SMM can be read out electronically through detecting the conductance jump, indicating the great promise of lanthanide SMMs in future applications.

Keywords Endohedral metallofullerene · Au surface · Molecular spintronics · Spin transistor · Spin valve · Nuclear spin

Naturally, the ultimate goal of SMM research is to develop future devices for possible applications in information storage and quantum computing. Therefore, now considerable efforts in some research groups have been devoted to the anchoring and organization of SMMs on surfaces as well as the design of molecular spintronics using SMMs. In contrast to traditional magnetic nanoparticles, the magnetic molecular clusters possess a well-defined structure and behave like perfectly monodisperse nanomagnets, which allow us to design a target molecule-based device. Nevertheless, one critical problem is the poor stability against water and temperature for most reported SMMs, especially lanthanide SMMs, and thus developing new type of SMM family is still necessary to obtain feasible SMMs with structural and magnetic stability when anchoring them on surfaces. Undoubtedly, a new era of collaborative research has been starting among synthetic chemists, physicists, and theorists [1]. This chapter will be devoted to this aspect.

6.1 New Type of Lanthanide SMM— $\text{Dy}_n\text{Sc}_{3-n}\text{N}@C_{80}$ ($n = 1, 2, 3$)

Endohedral metallofullerenes (EMFs) are of increasing interest since 1990s due to their fascinating structural, electronic, physical, and chemical properties different from the empty fullerenes [2]. The first metal-nitride cluster fullerene (NCF) was isolated and characterized in 1999, and the internal Sc_3N displays an equilateral triangle with a nitrogen atom in the center of the planar cluster [3]. Subsequently, a great diversity of such molecules was isolated due to the significant progress in the synthetic and separation procedures, and their spectroscopic properties and electronic structure were widely investigated through NMR, ESR, and vibrational spectroscopy. In particular, the electronic structure of NCFs on surfaces has been also studied via STM/STS and HRTEM [2]. Nevertheless, the exploration of SMM properties for them just started in 2012, when $\text{DySc}_2\text{N}@C_{80}$ molecule was revealed to behave as a strong SMM with long relaxation times [4]. Herein, although magnetization hysteresis loops were observed at a relatively high temperature (<6 K, Fig. 6.1), the lack of remanence and coercivity is still indicative of the fast QTM relaxation at zero dc field.

Remarkably, *ab initio* calculations performed by L.F. Chibotaru et al. in 2013 provided a theoretical prediction for the SMM performance of $\text{Dy}_n\text{Sc}_{3-n}\text{N}@C_{80}$ ($n = 2, 3$) complexes [5]. The results suggest that the dysprosium complex would behave as the best SMM rather than the tridysprosium one as a main result of the different exchange ground states arising from magnetic interactions (Fig. 6.2). For the complex with $n = 2$, the ground states exhibit double degeneracy with two reverse magnetic configurations, and thus, simultaneous reversal of magnetic moments on both Dy centers is necessary to induce the quantum tunneling between them. This seems to be rather difficult due to a very small transversal magnetic moment at each Dy site. As a result, the QTM relaxation within ground

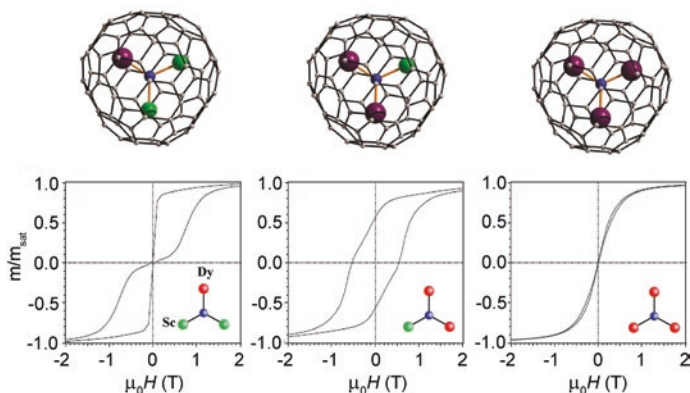
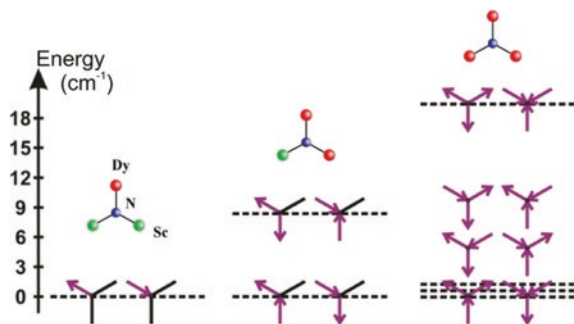


Fig. 6.1 The structures of $\text{Dy}_n\text{Sc}_{3-n}\text{N}@C_{80}$ ($n = 1, 2, 3$) and their corresponding magnetic properties. *Top* Reprinted with the permission from Ref. [5]. Copyright 2013 American Chemical Society. *Bottom* Reprinted with the permission from Ref. [6]. Copyright 2014 American Physical Society

Fig. 6.2 The magnetic structure of the corresponding Ising-like states for $\text{Dy}_n\text{Sc}_{3-n}\text{N}@C_{80}$ ($n = 1, 2, 3$) SMMs. Reprinted with the permission from Ref. [5]. Copyright 2013 American Chemical Society

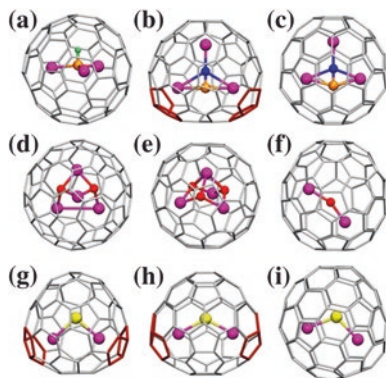


states should be suppressed effectively, possibly leading to strong SMM behavior in the dysprosium complex. In contrast, for the complex with $n = 3$, the similar magnetic interactions between three Dy centers result in three low-lying Kramers doublets with small splitting gaps ($<1 \text{ cm}^{-1}$). All three low-lying doublets are equally populated within the investigated temperature domain and therefore can be considered degenerate, which brings about magnetic frustration in the complex. Significantly, each magnetic configuration from the ground manifold is connected with other two by a single flip of the magnetic moment on one of the Dy sites. Consequently, a high QTM rates would be observed in the complex.

In 2014, the experimental investigations on $\text{Dy}_n\text{Sc}_{3-n}\text{N}@C_{80}$ ($n = 2, 3$) complexes were performed by Greber and coworkers [6]. Hence, a magnetization hysteresis loop with large remanence and coercivity at 2 K was observed in the complex with $n = 2$, while the tridysprosium complex only exhibited a small opening of the hysteresis curve (Fig. 6.1), which is well in agreement with the above predicted results by ab initio calculations.

Unfortunately, the SMM properties were explored only for $\text{Dy}_n\text{Sc}_{3-n}\text{N}@C_{80}$ ($n = 1, 2, 3$) system in the fascinating EMF family to date. In fact, different kinds of EMF molecules have been reported in recent years due to the progress of synthetic and separating techniques, and those molecules demonstrate the various structural motifs linked by different bridging atoms [2], as shown in Fig. 6.3,

Fig. 6.3 The various structural motifs linked by different bridging atoms in EMF family. Reprinted with the permission from Ref. [2]. Copyright 2013 American Chemical Society



which thus provides plentiful resource for discovering new SMMs with higher blocking temperatures. More importantly, the previous studies of surface layers of such fullerene molecules on different substrates afford the predominant advantage for developing the envisaged technological applications such as information storage and quantum computing devices. Furthermore, the future exploration into other new types of lanthanide SMMs is needed to achieve better SMM systems suitable for the final application in devices.

6.2 The Organization of SMMs on Surfaces

The organization of SMMs on surfaces seems to be the first step toward single-molecule experiments and final applications. Although a great number of SMM systems have been developed to date containing pure transition metal and lanthanide SMMs as well as their combinations $3d-4f$ SMMs, the systems suitable for the organization on surfaces are very rare due to the poor stability against water, temperature, or other factors. Up to now, the main investigations in this respect are concentrated on transition metal SMMs, especially for Mn_{12} and Fe_4 complexes, which exhibit stable inorganic core structure when changing the SMM peripheral organic groups [7, 8]. A substitution of the peripheral acetate ligands in archetypal Mn_{12} cluster allows its incorporation into different environments, such as Langmuir–Blodgett (LB) films [9, 10], mesoporous silica [11, 12], polymeric matrices, ultrathin films [13, 14], and so on (Fig. 6.4). Herein, the fascinating is the incorporating of magnetic molecules to single-molecule break-junctions, extended conducting surfaces or carbon-based nanostructures including carbon nanotube and graphene (Fig. 6.5), which were devised and studied only after 2003 [8, 15]. Here, the probing and characterization for individual molecules on surfaces seem to be a critical subject in ensuring the presence of intact SMMs on the

Fig. 6.4 Representation of the investigated Mn_{12} SMM into the non-crystalline environments including LB films, mesoporous silica, and Au surface. Reproduced from Ref. [14] by permission of John Wiley & Sons Ltd.

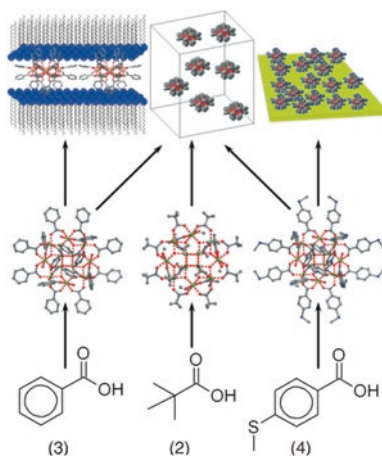
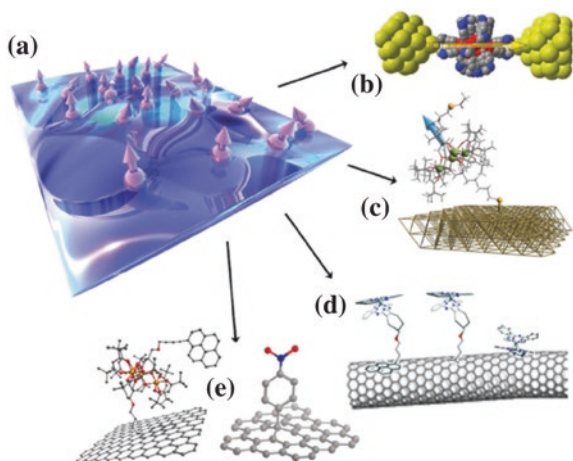


Fig. 6.5 Representation of the investigated SMM onto single-molecule break-junctions, extended conducting surfaces or carbon-based nanostructures including carbon nanotube and graphene. Reproduced from Ref. [15] by permission of The Royal Society of Chemistry



surface. The review article by R. Sessoli et al. in 2011 has given a detailed discussion on the chemical, structural, and magnetic characterizations on SMMs on surfaces through a wide class of surface analysis techniques, such as STM, AFM, XAS, and XMCD [8]. Notably, as a high-sensitivity magneto-optical technique, MCD measurement was first applied by L. Bogani et al. to probe the surface magnetic properties of SMMs in 2007 [14], thus providing the reliable information on the magnetic behavior of Mn_{12} SMM on surfaces, which is almost impossible to be achieved for the conventional magnetic measurements such as SQUIDS or μ -Hall probes due to a very tiny amount of magnetic molecules on surfaces.

6.2.1 Transition Metal SMMs on Au Surface

To anchor magnetic molecules to a solid substrate, some specific molecule–substrate interactions can be used such as electrostatic interactions, van der Waals forces, and specific chemical interactions, which depends on different substrates with different chemical reactivity [8, 15], as seen in Fig. 6.5. In recent years, the graft of SMMs on a Au(111) substrate have been the focus of the largest number of studies [14, 16–22] due to the high conductivity and ultraflat surface of gold substrate which allow the addressing of individual SMM molecules with monolayer or submonolayer coverage. Another important reason is the strong affinity of S atoms to the Au surface, and hence, the strategy used widely is to functionalize the magnetic molecules with thiol or thioether groups. For example, two main strategies were usually adopted for the deposition of Mn_{12} SMMs on Au surface, which is the earliest attempt to explore the surface-grafted SMMs. As shown in Fig. 6.6, one approach is to pre-functionalize the Au surface using the ligands with both thiol and carboxylic groups which allows the substitution with the peripheral moieties of Mn_{12} on the surface, while the other one is to tailor the Mn_{12} peripheral groups to thiol or thioether groups which will

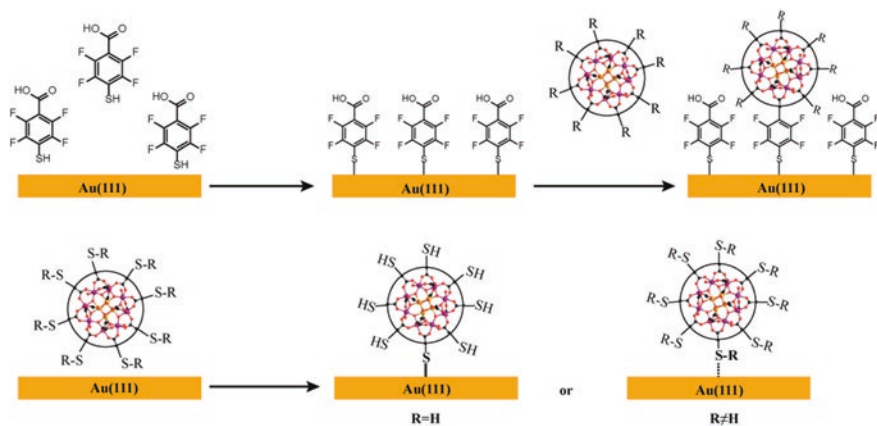


Fig. 6.6 Schematic representations of two main strategies for the deposition of Mn_{12} SMMs on Au surfaces

promote a selective incorporation on Au surface [8, 23]. Therefore, the subsequent STM investigations demonstrate the formation of a submonolayer of SMMs, indicating the validity of the above approaches.

The above description gave only a fundamental step toward molecular-scale spintronic devices, and subsequently, the control of magnetic properties of individual molecule on a surface seems to be a more significant point to the final application. In particular, all molecules in the layers should be oriented in a unique way, and ideally, the anisotropic axes of magnetization could be perpendicular to the surface, which thus request the ligands of magnetic molecules to be functionalized at the special sites [8]. This should be a challenging task for synthetic chemists, especially for Mn_{12} SMMs, where site-selective functionalization seems to be very difficult due to the wide distribution of carboxylate ligands around metal core. In contrast to Mn_{12} SMMs, site selection is much easier in the family of Fe_4 SMMs [24, 25], as seen in Fig. 6.7a, where two tripodal ligands functionalized by S-containing moiety aggregate four Fe centers in axial positions at opposite sides of the plane, thus providing the advantage of grafting them to the surface in a unique way. Initially, the Fe_4 SMM with long alkyl chains (C9) was successfully anchored on Au surface and retained hysteresis in the magnetization from XMCD [26], but further XPS analysis indicated that the S atoms of either one or both ligands can bind the surface since the alkyl chains are long enough (Fig. 6.7b) [27]. As a result, the anisotropic axes of Fe_4 SMMs were still oriented randomly on the surface. Nevertheless, further theoretical and experimental studies revealed that the reduction of long alkyl chains allowed a preferential orientation of Fe_4 complexes on an Au surface. In particular, the changing hysteresis loops dependent on the applied field direction provide direct evidence that the molecules are preferentially oriented with their easy magnetization axes perpendicular to the surface (Fig. 6.7c) [28]. Therefore, the present example demonstrates that, as a critical step to the final application, molecular orientation can be controlled effectively through elaborate chemical tailoring of magnetic molecules.

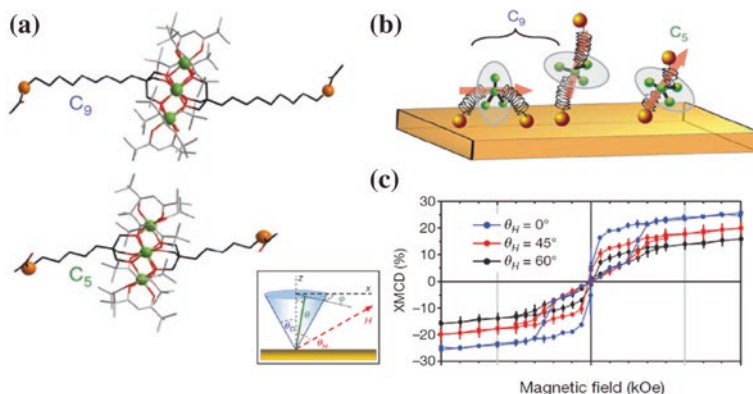


Fig. 6.7 The molecular structure of the Fe_4C_9 and Fe_4C_5 systems (a), sketch of the grafting modes expected on surfaces (b), and the measured angle-resolved hysteresis loops of Fe_4C_5 on Au surface from XMCD (c). Reprinted by permission from Macmillan Publishers Ltd.: Ref. [26], copyright 2010

6.2.2 $[LnPc_2]$ SMMs on Surfaces

As seen in the previous chapters, a tremendous number of lanthanide SMMs have been obtained by synthetic chemists and most of them even exhibit higher anisotropic barriers and blocking temperatures than transition metal SMMs, but the lanthanide SMM systems suitable for the organization on a surface are still rare with the most important example being double-decker phthalocyanine lanthanide SMMs ($[LnPc_2]$) to date. Strikingly, this kind of complexes demonstrates a rare chemical stability in ultrahigh vacuum (UHV), which allows them to be deposited on metal substrates in UHV conditions. In fact, some single plane Pc molecules, such as Pc, CoPc, and FePc, have shown excellent film growth properties on different substrates [29]. Figure 6.8 exhibits the deposition process of $[TbPc_2]$ on Cu(111) surface using a dry imprint technique in UHV, which was performed by V. Lucia and coworkers in 2008 [30]. Importantly, the STM topograph (Fig. 6.8c) clearly presents 8 molecular lobes with an apparent height of about 3 Å, suggesting that $[TbPc_2]$ molecules can be transferred in a flat lying configuration to a Cu(111) surface without damage. Remarkably, in 2010, the magnetic properties of isolated $[TbPc_2]$ molecules supported on a Cu(100) surface are investigated through XAS and XMCD by S. Stepanow and coworkers, revealing that the ligand field and hence magnetic properties remain unaltered despite the strong interactions between Pc ligand with the Cu substrate [31].

Furthermore, in 2009, M. Yamashita et al. demonstrated a direct deposition of neutral $[LnPc_2]$ on Au(111) surface using the thermal evaporation in UHV [32]. Here the 8-lobe molecules were still observed in STM images (Fig. 6.9), indicating the successful adsorption of $[LnPc_2]$ molecules onto Au surface. However, 4 molecular lobes were also present in the STM images, and further studies indicated

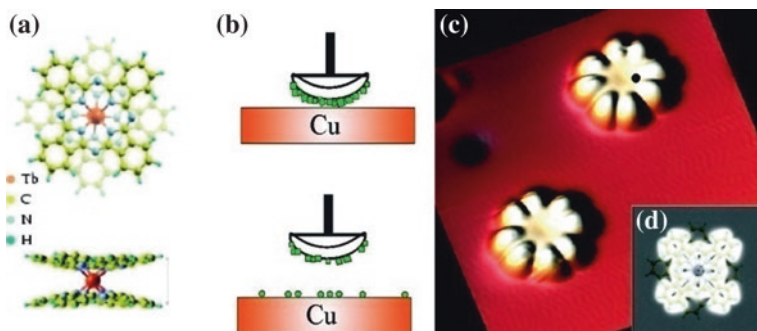


Fig. 6.8 **a** Structure of the $[\text{TbPc}_2]$ molecule. **b** Scheme of the dry-imprinting technique. **c** Constant current topograph of two isolated $[\text{TbPc}_2]$ molecules supported by the $\text{Cu}(111)$ surface. Reprinted with the permission from Ref. [30]. Copyright 2008 American Chemical Society

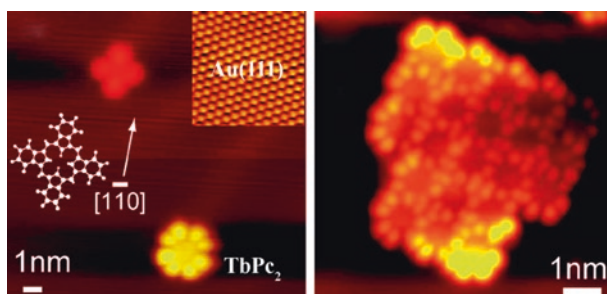


Fig. 6.9 STM images of isolated $[\text{TbPc}_2]$, $[\text{TbPc}]$ and monolayer film incorporating $[\text{LnPc}_2]$ molecules. Reprinted with the permission from Ref. [32]. Copyright 2009 American Chemical Society

that the 4-lobe molecule can be related to $[\text{LnPc}]$ species which derives from a cracking of the $[\text{LnPc}_2]$ molecule in the sublimation process. High-resolution STS spectra indicated that the 4-lobe $[\text{TbPc}]$ molecules present a Kondo temperature (T_K) of 250 K near the Fermi level, while no clear Kondo peak was observed for the isolated $[\text{LnPc}_2]$ molecule. Interestingly, a 2D ordered domain, i.e., monolayer film incorporating $[\text{LnPc}_2]$ molecules, was self-assembled onto Au surface, as seen in Fig. 6.9 right. The STS analysis on $[\text{LnPc}_2]$ molecules in the monolayer film revealed clear Kondo features with a T_K of 31 K when the tip was positioned over one of the lobes, and such features almost disappears with the tip being placed over the center of the molecule [33]. This suggests that the delocalized unpaired spin in Pc ligands rather than the local magnetic moment of the metal ion contributes to the Kondo effect. Importantly, M. Yamashita et al. further demonstrated that the Kondo effect can be switched on or off by modulating the spin states through rotating the Pc ligand of a single $[\text{TbPc}_2]$ molecule under a current from an STM, which potentially allows information to be coded at the single-molecule level [33].

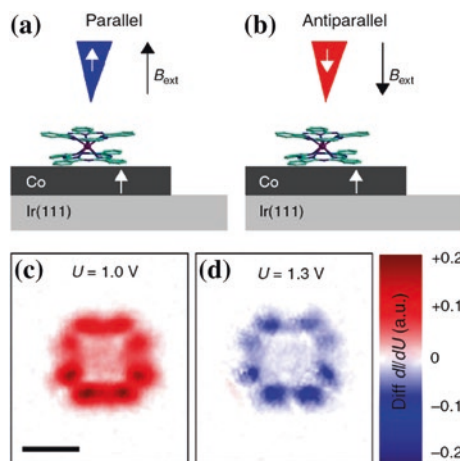


Fig. 6.10 Schematic diagram of SP-STM experiments (**a**, **b**), where the magnetization direction of the tip is aligned either parallel or antiparallel by applying an external magnetic field, while Co nanostructure is a hard magnet with a given magnetization direction. **c**, **d** Differences of maps of spin-resolved differential tunneling conductance, showing opposite spin polarization. Reprinted by permission from Macmillan Publishers Ltd.: Ref. [34], copyright 2012

As a great progress, the [TbPc₂] molecules were further deposited onto a ferromagnetic cobalt nanostructure in an isolated fashion in 2012, and the spin character of molecular orbitals interacting with ferromagnetic leads was investigated in detail via spin-polarized STM (SP-STM) [34]. As seen in Fig. 6.10a, b, the scanning tip exhibits parallel or antiparallel magnetization to that of the cobalt nanostructure, thus giving the different tunneling current. In particular, to determine the spin character of the LUMO orbital, the spin-resolved normalized differential tunneling conductance was measured for antiparallel and parallel alignment under the point spectroscopy mode, and their difference exhibits the almost opposite spin character suggesting the presence of spin-split LUMO orbital. Furthermore, the maps of the spin polarization of the molecular orbitals at the given voltages display the same 8-lobe spatial distribution, but opposite spin polarization, which is consistent with the features of LUMO π -orbital. Therefore, the studies represent an important advancement in the understanding of the molecular coupling at the electrode interfaces and will further promote the control of spin in molecular electronics. Moreover, the magnetic properties of [TbPc₂] molecules deposited onto ferromagnetic Ni layer [35] and antiferromagnetic Mn and CoO layers [36] were studied through element-resolved XMCD, leading to the observation of different magnetic phenomena.

Due to the specific electronic and transport properties of carbon-based nanostructures including carbon nanotube and graphene [37, 38], their applications in sensing and nanoelectronics have been explored widely in recent years [39–41]. Of course, such investigations have also been proceeding in the field of spintronic devices with molecular nanomagnets and yielded some fascinating results especially the successful design of spin transistor and spin valves, which will be introduced in the next

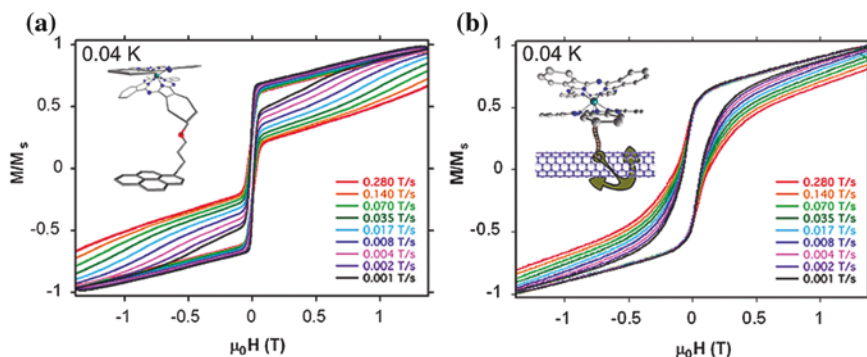


Fig. 6.11 Comparison of the micro-SQUID hysteresis cycles of **a** the powder sample of pyrenyl-substituted heteroleptical $[\text{TbPc}_2]$ SMM and **b** the SMM-SWNT conjugate recorded for different scan rates. Reprinted with the permission from Ref. [42]. Copyright 2009 American Chemical Society

part. Here, we focus on the organization of double-decker Pc lanthanide SMMs on carbon-based materials, where a key point is still to functionalize those magnetic molecules through tailoring the Pc ligands at the periphery. In 2009, L. Bogani and his coworkers demonstrated that a pyrenyl-substituted heteroleptical $[\text{TbPc}_2]$ SMM was successfully anchored on single-walled carbon nanotubes (SWNTs) through a strong π - π interaction between the pyrenyl moiety and SWNT, as shown in Fig. 6.11 inset [42]. Such SMM-SWNTs hybrids were confirmed by HRTEM, AFM, and emission spectroscopy. Significantly, an enhanced SMM behavior was observed in the hybrid system in contrast to the bulk material, as evidenced by the more open hysteresis loops in Fig. 6.11. In addition, D.B. Amabilino et al. reported in 2011 that an acetal protected $[\text{TbPc}_2]$ complex was organized on the highly oriented pyrolytic graphite (HOPG) [43], but AFM images and molecular dynamics simulations demonstrated that those $[\text{TbPc}_2]$ molecules on the surface form highly regular rectangular 2D nanocrystals, as shown in Fig. 6.12. Obviously, an opening magnetization hysteresis was also recorded through XMCD measurements.

Now, we have given an overview on the organization of SMMs on a surface with particular focus on how to anchor the phthalocyanine lanthanide SMMs on metal- or carbon-based surfaces, which is the first step toward final applications. The following part will be devoted to the design of molecular spintronics, which have shown a great achievement due to the collaborative researches.

6.3 Molecular Spintronics

Molecular spintronics combining spintronics and molecular electronics is not only an appealing issue of fundamental interest to exploit the rich diversity and functionality of molecules, but also of critical importance for the use of magnetic molecules in information technology [33, 44]. As a representative family in molecule-based

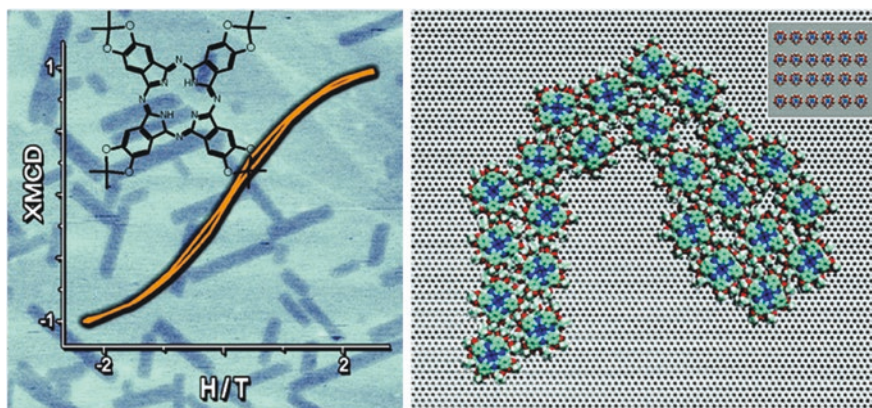


Fig. 6.12 AFM images and molecular dynamics simulations of the organization of an acetal protected [TbPc₂] on the highly oriented pyrolytic graphite (HOPG). *Inset* the Pc ligand and hysteresis loops from XMCD. Reprinted with the permission from Ref. [43]. Copyright 2011 American Chemical Society

magnetic material, SMMs have proved to be a promising family as critical magnetic building blocks of the device owing to its long relaxation time and rich quantum behaviors [26], which were clearly revealed in previous chapters. In 2008, the review article on molecular spintronics using SMMs from L. Bogani and W. Wernsdorfer identified them into three classes including molecular spin-transistor, molecular spin-valve, and molecular multidot device [44], as shown in Fig. 6.13. Nevertheless, the first three-terminal SMM-based molecular spin transistor has been reported by Heersche et al. in 2006 [45]. Here, the devices were organized through fabricating individual Mn₁₂ SMM into Au break-junction using electromigration, and the differential conductance as a function of gate voltage (V_g) and bias voltage (V_b) indicating electron transport through Mn₁₂ molecule was measured successfully, revealing current suppression and negative differential conductance on the energy scale of the anisotropy barrier. Subsequently, the magnetic-field dependence of the transport spectroscopy reported by H. Park et al. enables to identify signatures of magnetic states and their associated magnetic anisotropy [46]. Remarkably, a series of investigations on Fe₄ SMMs in three-terminal device geometry revealed the small but critical changes in the orientation and magnitude of the anisotropy in different charge states [47–49]. In contrast to the above transition metal SMMs, the development of lanthanide SMMs started later in this respect, but considerable breakthrough has been achieved for [LnPc₂] SMMs in recent years, which mainly benefits from its stable structural and magnetic features, stable redox state of the Tb^{III} ion as well as strong π conjugated property. Herein, [LnPc₂] SMMs were not only used to fabricate three-terminal spin transistor, but its combination with carbon-based nanostructures led to the successful design of supramolecular spin valve [50].

In 2012, W. Wernsdorfer and his coworkers reported the molecular spin transistor fabricated using a [TbPc₂] SMM [51]. Here, they not only measured the

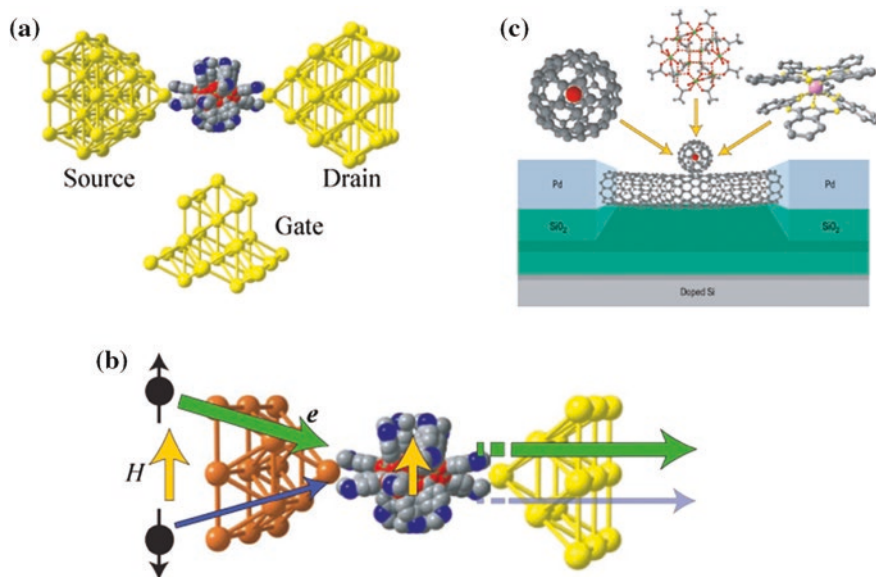


Fig. 6.13 Schematic representations of three kinds of molecular electronics. **a** Three-terminal molecular spin transistor. **b** Molecular spin-valve with parallel configuration of the magnetic source electrode (*orange*) and molecular magnetization. **c** Molecular multidot device. Reprinted by permission from Macmillan Publishers Ltd.: Ref. [44], copyright 2008

electron transport properties through the [TbPc₂] molecule, but also demonstrated that the nuclear spin of Tb metal atom embedded in [TbPc₂] SMM can be read out electronically through detecting the conductance jump (Fig. 6.14c) when sweeping the magnetic field at constant bias and gate voltages. As shown in Fig. 6.14d, the histogram of switching field obtained for 11,000 field sweeps gives four preferential field values corresponding to the four avoided energy-level crossings in Fig. 6.14b. The further detailed investigations revealed time trajectories for an individual nuclear spin and the individual relaxation times (T_1) for four nuclear spin states were up to several tens of seconds [52]. Importantly, a more striking breakthrough is that the single nuclear spin can be manipulated using electric fields only through the hyperfine Stark effect [53]. Therefore, the electrical manipulation allows fast switching and spatially confined spin control, which opens up a new path toward using nuclear-spin-based quantum bits.

In 2011, a supramolecular spin valve was demonstrated through coupling the [TbPc₂] SMMs on SWNT under supramolecular interactions [54]. Here, [TbPc₂] molecules were functionalized by one pyrene group and six hexyl groups on one of the two Pc rings (Fig. 6.15a) to increase van der Waals interactions with SWNT. The scheme of the supramolecular spin-valve device is shown in Fig. 6.15b containing the similar building blocks to spin transistor. Therefore, the electronic-transport characteristics can be measured under zero and nonzero external magnetic field, revealing the obvious Coulomb blockade regime. Importantly,

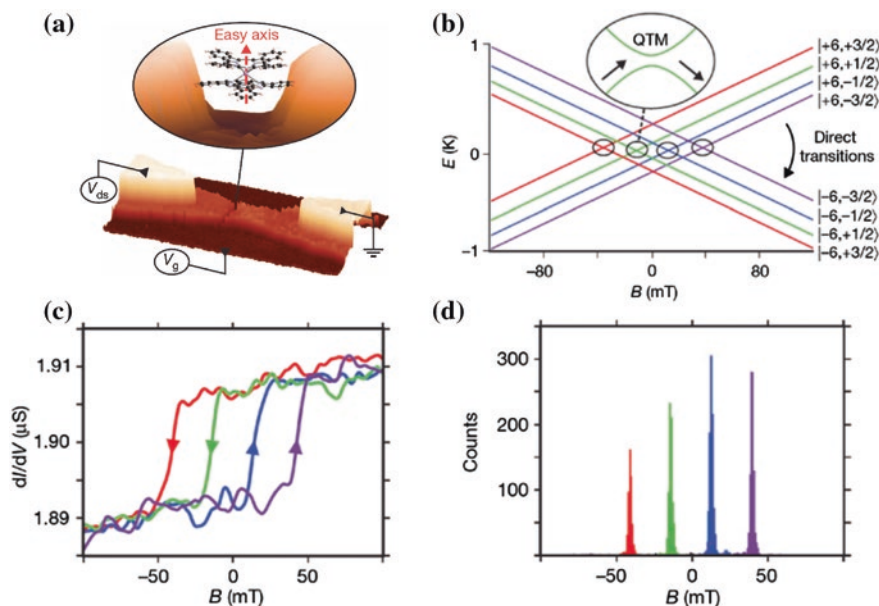


Fig. 6.14 **a** Schematic representations of molecular spin transistor fabricated using a [TbPc₂] SMM. **b** Zeeman diagram presenting the energy of the two ground states as a function of the magnetic field (B). **c** dI/dV measurements for a given working point ($V_g = -0.9$ V; $V_{ds} = 0$ V) as function of the magnetic field. **d** Histogram of switching field obtained for 11,000 field sweeps showing four preferential field values. Reprinted by permission from Macmillan Publishers Ltd.: Ref. [51], copyright 2012

the measurement of zero-bias conductance through sweeping the magnetic field revealed an obvious jump and hysteresis loops around zero field below 0.6 K (Fig. 6.15c), which is consistent with QTM regime of [TbPc₂] SMM. Such a typical magnetoresistance effect is considered as a fingerprint of standard spin valve. In addition, such a [TbPc₂] molecule was also anchored onto graphene surface and further applied to spintronic devices, thus exhibiting the similar electronic-transport characteristics to the above sample, as shown in Fig. 6.15 d, e [55].

Up to now, we have introduced systematically the research of lanthanide SMMs, from the basic investigations of relaxation dynamics to the most up-to-date progresses of molecular spintronics. In lanthanide SIMMs (Chap. 2), high symmetry seems to be rather critical to block the magnetization as efficient as possible, since the asymmetric factors are closely correlated with the transversal components of anisotropy which facilitate the underbarrier QTM process. In contrast, the case is different in multinuclear lanthanide SMMs (Chaps. 3–5), where the magnetic coupling between magnetic ions has been playing a major role in controlling the low-temperature QTM process, although SMM behaviors are still attributed to single-ion anisotropy of individual magnetic center in most examples. Herein, the coupling effects were elucidated in detail in dinuclear lanthanide SMMs in Chap. 3,

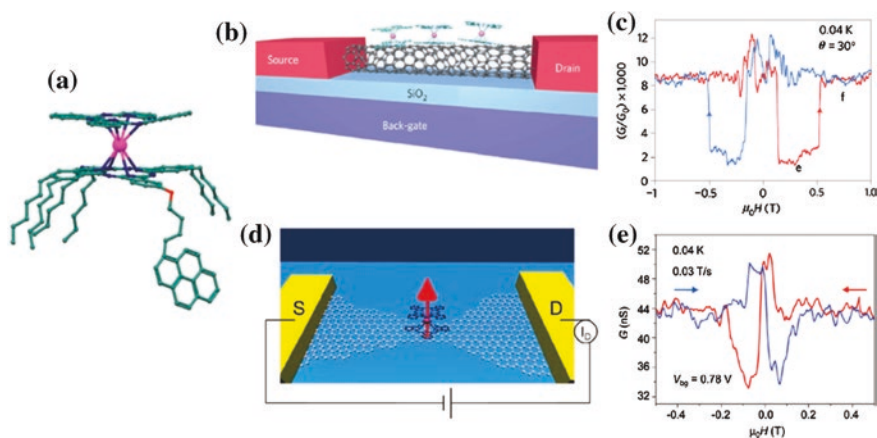


Fig. 6.15 **a** The molecular structure of the functionalized [TbPc₂] SMM. **b, d** Schematic representations of molecular spintronics arising from the coupling of [TbPc₂] molecules with SWNT and grapheme. **c, e** Zero-bias conductance measured as a function of the magnetic field for spintronics (**b**) and (**d**), respectively. **a, b, c** Reprinted with permission from Macmillan Publishers Ltd.: Ref. [54], copyright 2011. **d, e** Reprinted with the permission from Ref. [55]. Copyright 2011 American Chemical Society

where the relatively strong magnetic coupling can achieve a strong exchange coupling regime between strongly anisotropic metal ions thus enhancing the magnetization blocking, but a weak coupling usually leads to perturbing field to the neighboring metal ions, causing fast QTM at temperatures higher than exchange splitting. Ultimately, the design of new SMM systems, the organization of SMMs on surfaces, and molecular spintronics were clearly demonstrated, suggesting the great promise of lanthanide SMMs in future applications. We believe that this book will not only serve as a valuable resource in the basic knowledge about relaxation mechanism for new researchers, but also guide further research efforts to fine-tune the properties of the existing lanthanide SMMs and design new SMMs.

References

1. Dunbar KR (2012) Editorial for the virtual issue on quantum molecular magnets. *Inorg Chem* 51(22):12055–12058. doi:10.1021/ic302312m
2. Popov AA, Yang S, Dunsch L (2013) Endohedral fullerenes. *Chem Rev* 113(8):5989–6113. doi:10.1021/cr300297r
3. Stevenson S, Rice G, Glass T et al (1999) Small-bandgap endohedral metallofullerenes in high yield and purity. *Nature* 401(6748):55–57. doi:10.1038/43415
4. Westerström R, Dreiser J, Piamonteze C et al (2012) An endohedral single-molecule magnet with long relaxation times: DySc₂N@C₈₀. *J Am Chem Soc* 134(24):9840–9843. doi:10.1021/ja301044p
5. Vieru V, Ungur L, Chibotaru LF (2013) Key role of frustration in suppression of magnetization blocking in single-molecule magnets. *J Phys Chem Lett* 4(21):3565–3569. doi:10.1021/jz4017206

6. Westerström R, Dreiser J, Piamonteze C et al (2014) Tunneling, remanence, and frustration in dysprosium-based endohedral single-molecule magnets. *Phys Rev B* 89(6):060406. doi:[10.1103/PhysRevB.89.060406](https://doi.org/10.1103/PhysRevB.89.060406)
7. Gatteschi D, Cornia A, Mannini M et al (2009) Organizing and addressing magnetic molecules. *Inorg Chem* 48(8):3408–3419. doi:[10.1021/ic8013283](https://doi.org/10.1021/ic8013283)
8. Cornia A, Mannini M, Sainctavit P et al (2011) Chemical strategies and characterization tools for the organization of single molecule magnets on surfaces. *Chem Soc Rev* 40(6):3076–3091. doi:[10.1039/c0cs00187b](https://doi.org/10.1039/c0cs00187b)
9. Clemente-León M, Soyer H, Coronado E et al (1998) Langmuir-blodgett films of single-molecule nanomagnets. *Angew Chem Int Ed* 37(20):2842–2845. doi:[10.1002/\(sici\)1521-3773\(19981102\)37:20<2842:aid-anie2842>3.0.co;2-b](https://doi.org/10.1002/(sici)1521-3773(19981102)37:20<2842:aid-anie2842>3.0.co;2-b)
10. Clemente-León M, Coronado E, Forment-Aliaga A et al (2003) Organized assemblies of magnetic clusters. *C R Chimie* 6(7):683–688. doi:[10.1016/S1631-0748\(03\)00121-8](https://doi.org/10.1016/S1631-0748(03)00121-8)
11. Coradin T, Larionova J, Smith AA et al (2002) Magnetic nanocomposites built by controlled incorporation of magnetic clusters into mesoporous silicates. *Adv Mater* 14(12):896–898. doi:[10.1002/1521-4095\(20020618\)14:12<896:aid-adma896>3.0.co;2-e](https://doi.org/10.1002/1521-4095(20020618)14:12<896:aid-adma896>3.0.co;2-e)
12. Clemente-Leon M, Coronado E, Forment-Aliaga A et al (2003) Incorporation of Mn₁₂ single molecule magnets into mesoporous silica. *J Mater Chem* 13(12):3089–3095. doi:[10.1039/b310408g](https://doi.org/10.1039/b310408g)
13. Ruiz-Molina D, Mas-Torrent M, Gómez J et al (2003) Isolated single-molecule magnets on the surface of a polymeric thin film. *Adv Mater* 15(1):42–45. doi:[10.1002/adma.200390006](https://doi.org/10.1002/adma.200390006)
14. Bogani L, Cavigli L, Gurioli M et al (2007) Magneto-optical investigations of nanostructured materials based on single-molecule magnets monitor strong environmental effects. *Adv Mater* 19(22):3906–3911. doi:[10.1002/adma.200700594](https://doi.org/10.1002/adma.200700594)
15. Cervetti C, Heintze E, Bogani L (2014) Interweaving spins with their environment: novel inorganic nanohybrids with controllable magnetic properties. *Dalton Trans* 43(11):4220–4232. doi:[10.1039/c3dt52650j](https://doi.org/10.1039/c3dt52650j)
16. Cornia A, Fabretti AC, Pacchioni M et al (2003) Direct observation of single-molecule magnets organized on gold surfaces. *Angew Chem Int Ed* 42(14):1645–1648. doi:[10.1002/anie.200350981](https://doi.org/10.1002/anie.200350981)
17. Naitabdi A, Bucher JP, Gerbier P et al (2005) Self-assembly and magnetism of Mn₁₂ nanomagnets on native and functionalized gold surfaces. *Adv Mater* 17(13):1612–1616. doi:[10.1002/adma.200401623](https://doi.org/10.1002/adma.200401623)
18. Zobbi L, Mannini M, Pacchioni M et al (2005) Isolated single-molecule magnets on native gold. *Chem Commun* 1640–1642. doi:[10.1039/b418072k](https://doi.org/10.1039/b418072k)
19. Coronado E, Forment-Aliaga A, Romero FM et al (2005) Isolated Mn₁₂ single-molecule magnets grafted on gold surfaces via electrostatic interactions. *Inorg Chem* 44(22):7693–7695. doi:[10.1021/ic0508021](https://doi.org/10.1021/ic0508021)
20. Pineider F, Mannini M, Sessoli R et al (2007) Solvent effects on the adsorption and self-organization of Mn₁₂ on Au(111). *Langmuir* 23(23):11836–11843. doi:[10.1021/la7016837](https://doi.org/10.1021/la7016837)
21. Mannini M, Pineider F, Sainctavit P et al (2009) X-ray magnetic circular dichroism picks out single-molecule magnets suitable for nanodevices. *Adv Mater* 21(2):167–171. doi:[10.1002/adma.200801883](https://doi.org/10.1002/adma.200801883)
22. Saywell A, Magnano G, Satterley CJ et al (2010) Self-assembled aggregates formed by single-molecule magnets on a gold surface. *Nat Commun* 1:75. doi:[10.1038/ncomms1075](https://doi.org/10.1038/ncomms1075)
23. Voss S, Burgert M, Fonin M et al (2008) A comparative study on the deposition of Mn₁₂ single molecule magnets on the Au(111) surface. *Dalton Trans* 499–505. doi:[10.1039/b712371j](https://doi.org/10.1039/b712371j)
24. Cornia A, Fabretti AC, Garrisi P et al (2004) Energy-barrier enhancement by ligand substitution in tetrairon(III) single-molecule magnets. *Angew Chem Int Ed* 43(9):1136–1139. doi:[10.1002/anie.200352989](https://doi.org/10.1002/anie.200352989)
25. Accorsi S, Barra A-L, Caneschi A et al (2006) Tuning anisotropy barriers in a family of tetrairon(III) single-molecule magnets with an S = 5 ground state. *J Am Chem Soc* 128(14):4742–4755. doi:[10.1021/ja0576381](https://doi.org/10.1021/ja0576381)

26. Mannini M, Pineider F, Danieli C et al (2010) Quantum tunnelling of the magnetization in a monolayer of oriented single-molecule magnets. *Nature* 468(7322):417–421. doi:[10.1038/nature09478](https://doi.org/10.1038/nature09478)
27. Pineider F, Mannini M, Danieli C et al (2010) Deposition of intact tetrairon(III) single molecule magnet monolayers on gold: an STM, XPS, and ToF-SIMS investigation. *J Mater Chem* 20(1):187–194. doi:[10.1039/b916895h](https://doi.org/10.1039/b916895h)
28. Mannini M, Pineider F, Sainctavit P et al (2009) Magnetic memory of a single-molecule quantum magnet wired to a gold surface. *Nat Mater* 8(3):194–197. doi:[10.1038/nmat2374](https://doi.org/10.1038/nmat2374)
29. Peisert H, Schwieger T, Auerhammer JM et al (2001) Order on disorder: copper phthalocyanine thin films on technical substrates. *J Appl Phys* 90(1):466–469. doi:[10.1063/1.1375017](https://doi.org/10.1063/1.1375017)
30. Vitali L, Fabris S, Conte AM et al (2008) Electronic structure of surface-supported bis(phthalocyaninato) terbium(III) single molecular magnets. *Nano Lett* 8(10):3364–3368. doi:[10.1021/nl801869b](https://doi.org/10.1021/nl801869b)
31. Stepanow S, Honolka J, Gambardella P et al (2010) Spin and orbital magnetic moment anisotropies of monodispersed bis(Phthalocyaninato) terbium on a copper surface. *J Am Chem Soc* 132(34):11900–11901. doi:[10.1021/ja105124r](https://doi.org/10.1021/ja105124r)
32. Katoh K, Yoshida Y, Yamashita M et al (2009) Direct observation of lanthanide(III)-phthalocyanine molecules on Au(111) by using scanning tunneling microscopy and scanning tunneling spectroscopy and thin-film field-effect transistor properties of Tb(III)- and Dy(III)-phthalocyanine molecules. *J Am Chem Soc* 131(29):9967–9976. doi:[10.1021/ja902349t](https://doi.org/10.1021/ja902349t)
33. Komeda T, Isshiki H, Liu J et al (2011) Observation and electric current control of a local spin in a single-molecule magnet. *Nat Commun* 2:217. doi:[10.1038/ncomms1210](https://doi.org/10.1038/ncomms1210)
34. Schwöbel J, Fu Y, Brede J et al (2012) Real-space observation of spin-split molecular orbitals of adsorbed single-molecule magnets. *Nat Commun* 3:953. doi:[10.1038/ncomms1953](https://doi.org/10.1038/ncomms1953)
35. Lodi Rizzini A, Krull C, Balashov T et al (2011) Coupling single molecule magnets to ferromagnetic substrates. *Phys Rev Lett* 107(17):177205. doi:[10.1103/PhysRevLett.107.177205](https://doi.org/10.1103/PhysRevLett.107.177205)
36. Lodi Rizzini A, Krull C, Balashov T et al (2012) Exchange biasing single molecule magnets: coupling of TbPc₂ to antiferromagnetic layers. *Nano Lett* 12(11):5703–5707. doi:[10.1021/nl302918d](https://doi.org/10.1021/nl302918d)
37. Charlier J-C, Blase X, Roche S (2007) Electronic and transport properties of nanotubes. *Rev Mod Phys* 79(2):677–732. doi:[10.1103/RevModPhys.79.677](https://doi.org/10.1103/RevModPhys.79.677)
38. Bekyarova E, Sarkar S, Wang F et al (2012) Effect of covalent chemistry on the electronic structure and properties of carbon nanotubes and graphene. *Acc Chem Res* 46(1):65–76. doi:[10.1021/ar300177q](https://doi.org/10.1021/ar300177q)
39. Schwierz F (2010) Graphene transistors. *Nat Nanotechnol* 5(7):487–496. doi:[10.1038/nnano.2010.89](https://doi.org/10.1038/nnano.2010.89)
40. Bogani L, Danieli C, Biavardi E et al (2009) Single-molecule-magnet carbon-nanotube hybrids. *Angew Chem Int Ed* 48(4):746–750. doi:[10.1002/anie.200804967](https://doi.org/10.1002/anie.200804967)
41. Giusti A, Charron G, Mazerat S et al (2009) Magnetic bistability of individual single-molecule magnets grafted on single-wall carbon nanotubes. *Angew Chem Int Ed* 48(27):4949–4952. doi:[10.1002/anie.200901806](https://doi.org/10.1002/anie.200901806)
42. Kyatskaya S, Mascarós JRG, Bogani L et al (2009) Anchoring of rare-earth-based single-molecule magnets on single-walled carbon nanotubes. *J Am Chem Soc* 131(42):15143–15151. doi:[10.1021/ja906165e](https://doi.org/10.1021/ja906165e)
43. Gonidec M, Biagi R, Corradini V et al (2011) Surface supramolecular organization of a terbium(III) double-decker complex on graphite and its single molecule magnet behavior. *J Am Chem Soc* 133(17):6603–6612. doi:[10.1021/ja109296c](https://doi.org/10.1021/ja109296c)
44. Bogani L, Wernsdorfer W (2008) Molecular spintronics using single-molecule magnets. *Nat Mater* 7(3):179–186. doi:[10.1038/nmat2133](https://doi.org/10.1038/nmat2133)
45. Heersche HB, de Groot Z, Folk JA et al (2006) Electron transport through single Mn₁₂ molecular magnets. *Phys Rev Lett* 96(20):206801. doi:[10.1103/PhysRevLett.96.206801](https://doi.org/10.1103/PhysRevLett.96.206801)
46. Jo M-H, Grose JE, Baheti K et al (2006) Signatures of molecular magnetism in single-molecule transport spectroscopy. *Nano Lett* 6(9):2014–2020. doi:[10.1021/nl061212i](https://doi.org/10.1021/nl061212i)

47. Zyazin AS, van den Berg JWG, Osorio EA et al (2010) Electric field controlled magnetic anisotropy in a single molecule. *Nano Lett* 10(9):3307–3311. doi:[10.1021/nl1009603](https://doi.org/10.1021/nl1009603)
48. Zyazin AS, van der Zant HSJ, Wegewijs MR et al (2011) High-spin and magnetic anisotropy signatures in three-terminal transport through a single molecule. *Synth Met* 161(7–8):591–597. doi:[10.1016/j.synthmet.2010.11.050](https://doi.org/10.1016/j.synthmet.2010.11.050)
49. Burzurí E, Zyazin AS, Cornia A et al (2012) Direct observation of magnetic anisotropy in an individual Fe₄ single-molecule magnet. *Phys Rev Lett* 109(14):147203. doi:[10.1103/PhysRevLett.109.147203](https://doi.org/10.1103/PhysRevLett.109.147203)
50. Hong K, Kim WY (2013) Fano-resonance-driven spin-valve effect using single-molecule magnets. *Angew Chem Int Ed* 52(12):3389–3393. doi:[10.1002/anie.201208816](https://doi.org/10.1002/anie.201208816)
51. Vincent R, Klyatskaya S, Ruben M et al (2012) Electronic read-out of a single nuclear spin using a molecular spin transistor. *Nature* 488(7411):357–360. doi:[10.1038/nature11341](https://doi.org/10.1038/nature11341)
52. Thiele S, Vincent R, Holzmann M et al (2013) Electrical readout of individual nuclear spin trajectories in a single-molecule magnet spin transistor. *Phys Rev Lett* 111(3):037203. doi:[10.1103/PhysRevLett.111.037203](https://doi.org/10.1103/PhysRevLett.111.037203)
53. Thiele S, Balestro F, Ballou R et al (2014) Electrically driven nuclear spin resonance in single-molecule magnets. *Science* 344(6188):1135–1138. doi:[10.1126/science.1249802](https://doi.org/10.1126/science.1249802)
54. Urdampilleta M, Klyatskaya S, Cleuziou JP et al (2011) Supramolecular spin valves. *Nat Mater* 10(7):502–506. doi:[10.1038/nmat3050](https://doi.org/10.1038/nmat3050)
55. Candini A, Klyatskaya S, Ruben M et al (2011) Graphene spintronic devices with molecular nanomagnets. *Nano Lett* 11(7):2634–2639. doi:[10.1021/nl2006142](https://doi.org/10.1021/nl2006142)